The Impact of Vegetation Morphology on Turbulence and Bedload Transport

By

Tian Zhao

B. Sc., Nanjing University (2017)

Submitted to the Department of Civil and Environmental Engineering
in partial fulfillment of the requirements for the degree(s) of

Doctor of Philosophy

at the

Massachusetts Institute of Technology

September 2024

Authored by: Tian Zhao
Department of Civil and Environmental Engineering
August 9, 2024

Certified by: Heidi Nepf
Donald and Martha Harleman Professor of Civil and Environmental Engineering
Thesis supervisor

Accepted by: Heidi Nepf
Donald and Martha Harleman Professor of Civil and Environmental Engineering
Chair, Graduate Program Committee

The Impact of Vegetation Morphology on Turbulence and Bedload Transport

By

Tian Zhao

Submitted to the Department of Civil and Environmental Engineering on August 9, 2024
in partial fulfillment of the requirements for the degree of
Doctor of Philosophy

Abstract

By promoting sediment deposition and retention, aquatic vegetation can contribute to river bank stabilization, biodiversity, as well as carbon sequestration. The morphology and distribution of aquatic plants influence the velocity field, turbulence intensity, and sediment transport in wetlands, which impacts the erosion and deposition processes. By combining physical and numerical experiments, this thesis quantified how vegetation geometry impacts turbulence and sediment transport near the bed.

In aquatic canopies, turbulence generated at the stem scale, and for submerged canopies, also in the canopy shear layer, could contribute to the near-bed turbulence. Results of flume experiments using a constant channel average velocity revealed that bedload transport was predominantly correlated with near-bed turbulence, but was also weakly correlated with near-bed velocity. First, in emergent canopies, if vegetation was not clustered, turbulent kinetic energy (TKE) and bedload transport did not depend on the arrangement and stem diameter(s) and can be predicted from plant biomass and velocity. If vegetation was clustered in patches, TKE and bedload transport decreased with increased clustering and can be predicted from plant biomass, patch geometry, and velocity. Second, in submerged canopies, for constant channel velocity, submerged canopies could enhance or reduce bedload transport, depending on their degree of submergence. With increasing submergence, H/h (defined as the ratio of flow depth H to canopy height h), the near-bed velocity and TKE decreased, and the source of near-bed turbulence shifted from stem wake to the shear layer at the canopy top. A model to predict near-bed TKE in submerged canopies was developed and used to explore bedload transport under more realistic conditions with constant energy slope and flexible vegetation. For a constant energy slope, the denser the canopy, and/or the larger fraction of flow depth occupied by the canopy (decreasing H/h), the greater the sediment transport was reduced compared to unvegetated beds. This thesis provides essential parameterizations of vegetation to hydrodynamic and morphodynamic models, which can be used to predict the vegetation conditions that promote or diminish erosion, offering a useful guide for river and coastal restoration.

Thesis supervisor: Heidi Nepf
Title: Donald and Martha Harleman Professor of Civil and Environmental Engineering

Acknowledgments

The completion of this thesis is under financial support from MIT (Linde Presidential Fellowship, CEE Teaching Assistantship, Teaching Development Fellowship, and MathWorks Fellowship) and NSF EAR 1854564, which are hereby gratefully acknowledged.

First and foremost, I would like to sincerely thank my advisor, Heidi Nepf. This thesis would not have been possible without her unwavering guidance and support. A role model herself who defines excellence, Professor Heidi Nepf is a source of inspiration for her students to pursue excellence in both research and teaching. As a researcher, Heidi is enthusiastic, knowledgeable, and rigorous. As a mentor, she shows great patience, flexibility, and sympathy to mentees. As a teacher, she consistently delivers effective, enjoyable, and enlightening lectures with cutting-edge knowledge. Her careful and patient work approach has set a high standard that I aspire to emulate. I would also like to thank my doctoral committee members, Michael Howland and Taylor Perron. Thank you for your insightful questions and constructive feedback, which have encouraged me to think more about the theoretical assumptions and big picture, and to carefully examine and iterate my work with more technical details and potential field applications.

Second, many thanks go to the fellow members of the Nepf Lab: Qingjun (Judy) Yang, Jiarui (Gary) Lei, Isabella Schalko, Yuqi Shan, Chao Liu, Yuan Xu, Hyoungchul Park, Rachel Schaefer, In Him (Ernie) Lee, Autumn Deitrick, Jiao (Caroline) Zhang, James Vincent Brice, Chuyan Zhao, Xiaoxia Zhang, Yuanheng (Aki) Zhang, and Thomas van Veelen. I am fortunate to have the opportunity to work with two outstanding undergraduate researchers, Jade Ishii and Rovi Porter. The broader Environmental Fluid Mechanics community is a source of support and ideas, in which I would like to particularly thank Tong Bo, Yilang Xu, Adrian Garcia, Dayang (Cindy) Wang, Ishita Shrivastava, Rose Palermo, Souha El Mousadik, Kirby Heck, and Liying Qiu. I also thank Andy Ryan, Steve Rudolph, Scott Spence, and Andy Gallant for the maintenance of experimental facilities, Brenda Pepe, Denise Stewart, Jay Matthews, Lili Zhu, and Sal Netherton for assistance with purchases and logistics, and Kiley Clapper and Sarah Smith for administrative assistance.

Third, I thank the people I have met at MIT and beyond who have shown me a wide spectrum of expertise, ideas, lives, and possibilities. In CEE – Tong Bo, Yilang Xu, Yunpo Li, Xiaoyu Shan, Jie Yun, Yue (Olivia) Meng, Ruijiao Sun, Adrian Garcia, Lucas Medeiros, Yu Qiu, Baichuan Mo, Yunhan Zheng, Chuliang Song, Jingqiu Liao, Ke Xu, Lurong Yang, Dayang (Cindy) Wang, Na Chen, Kirby Heck, Haoran Cai, Ruofei Jia, Jie Deng, and Wei Lu. I thank Souha El Mousadik, a CEE Communication Lab Fellow who patiently helped me polish up my conference presentations and fellowship statement. At MIT – special thanks go to all the folks who bettered my teaching and communication skills: Meghan Moriarty for hosting my Kaufman Teaching Certificate Program, Ben Hansberry for the opportunity to let me serve as the Teaching Development Fellow for CEE in Academic Year 2022-2023, students in Heidi's courses (1.061/1.61 and 1.106) for letting me practice and refine my teaching skills (and for endorsing me for the

Maseeh Award!), and Diana Chien and Amanda Cornwall for hosting the Research Mentoring Certificate Program. I also thank MIT Libraries for their convenient literature delivery services. At Harvard – thanks go to Professor Nick Trefethen for his insights on numerical analysis/scientific computation and collegiate teaching, and his book *An Applied Mathematician's Apology*. From Nanjing University – Qian Yu, Yunwei Wang, Zhiyun Du, Hangjie Lin, and Yun Peng for their continued company in research and life, and Ze-Xun Lin, Yang Chen, Ge Yu, Xiaofan Xu, Yunhan Chen, Pai-Hung Lin, Yihang She, Tianyi Tang, Mengyang Zhou, and Hongming Huang for continued friendship. Lastly, my childhood friends Han Bao and Chao Zhang, for your support throughout my doctoral journey.

Finally, I thank my parents for raising me up and for respecting and supporting my decisions. We learn from each other and grow together.

Contents

This page intentionally left blank

List of Figures

List of Tables

Chapter 1 Introduction

Aquatic vegetation plays a crucial role in floodplain and coastal ecosystems. It slows the flow by increasing flow resistance, which promotes sediment deposition and stabilizes river banks (Afzalimehr & Dey, 2009; Hackney et al., 2020; Pollen-Bankhead & Simon, 2010; Tal & Paola, 2007). Vegetation also dissipates wave energy, thereby reducing the wave intensity onshore and discouraging erosion (Barbier et al., 2011). Additionally, aquatic vegetation can improve water quality by removing nutrients (e.g., Chambers & Prepas, 1994; Wilcock et al., 1999) and pollutants (e.g., Dhir et al., 2009), and by producing oxygen through photosynthesis (e.g., Sand-Jensen, 1989). In aquatic canopies, enhanced water quality, along with low-flow zones create sheltered nursery habitat, which is important for fisheries and enhances biodiversity (Costanza et al., 1997; Crowder & Diplas, 2002; Kemp et al., 2000). Although occupying no more than 0.2% of global seabed, coastal vegetation is estimated to contribute to 10% of annual organic carbon burial in the oceans (Fourqurean et al., 2012).

Aquatic vegetation is categorized into three common types: emergent, submerged, and floating (Figure 1-1; e.g., Massachusetts Department of Conservation and Recreation, 2016). Emergent vegetation is rooted to the bed, with stiff stems, and penetrates through the water surface, i.e., the plant height is greater than the water depth. Common species include *Spartina* (cordgrass), *Juncus* (rushes), *Salicornia* (pickleweed), and *Typha* (cattails), as well as the mangroves *Rhizophora* (true mangroves), *Avicennia* (black mangrove), *Laguncularia racemosa* (white mangrove), and *Conocarpus erectus* (buttonwood). Submerged vegetation is rooted in the bed sediment, and is usually softer and more flexible than emergent vegetation, but its shoots (e.g., leaves/blades and stems) are fully submerged underwater. Common submerged plants include *Elodea* (waterweeds), *Vallisneria* (eelgrass), *Zostera* (marine eelgrass), and *Posidonia* (Mediterranean tapeweed). Floating vegetation grows on the water surface and may or may not be rooted. Common species include *Nymphaea* (water lilies), *Lemna* (duckweeds), *Sargassum*, and *Pontederia crassipes* (water hyacinth). All aquatic vegetation exhibits flexibility to different degrees, leading to different reconfiguration, i.e., changes in posture, in response to the incoming flow (Vogel, 1994). The dimensions

of their stems, leaves/blades, and roots also vary depending on their growth stage, bed type, light and nutrient availability, temperature, as well as local hydrodynamics.

Emergent aquatic plants

Sporobolus alterniflorus (formerly known as *Spartina alterniflora*)

Juncus roemerianus

Salicornia europaea

Typha latifolia

Rhizophora mangle

Avicennia marina

Laguncularia racemosa

Conocarpus erectus

Submerged aquatic plants

Elodea canadensis

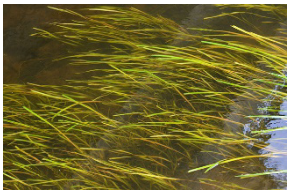

Vallisneria spiralis

Zostera marina

Posidonia oceanica

Floating aquatic plants

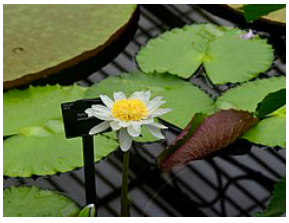

Nymphaea immutabilis

Lemna minor

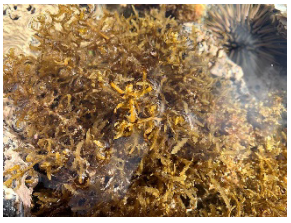

Sargassum polyphyllum

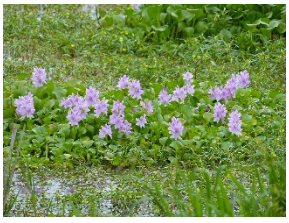

Pontederia crassipes

Figure 1-1. Examples of aquatic vegetation. Image source: Wikimedia Commons.

In addition to their various morphological features, aquatic vegetation also forms different distribution patterns. First, aquatic vegetation often exhibits zonation along the bed profile (e.g., Minnesota Department of Natural Resources, 2021), in which emergent and floating species dominate in shallow regions, whereas submerged plants are more common in deep regions. Second, aquatic vegetation may form patches, i.e., clusters of vegetation, due to seed dispersal (Orth et al., 1994), reproduction (e.g., Wang et al., 2005; McLain & Ross, 2005), as well as natural disturbances (Collins & Glenn, 1997; Lake, 2000; Luisa, 2012), which in turn reshapes the local physical, chemical, and ecological environment.

Aquatic vegetation can act as a nature-based solution for global climate change, i.e., they can "protect, sustainably manage, or restore natural ecosystems, that address societal challenges such as climate change, human health, food and water security, and disaster risk reduction effectively and adaptively, simultaneously providing human wellbeing and biodiversity benefits" (World Bank, 2022). Seeking nature-based solutions can further accomplish the 17 Sustainable Development Goals (United Nations, 2015), specifically sustainable cities and communities (#11), climate action (#13), and life below water (#14).

1.1 Flow and Turbulence in Vegetated Channels

Flow through vegetation is a type of canopy flow, for which fluid moves through and/or around a porous canopy of obstacles (roughness elements). When fluid flows past an individual obstacle, the velocity directly behind the obstacle is reduced. The area downstream of the object, where the flow patterns are influenced by the presence of the object, is called the wake. The flow accelerates on both sides of the obstacle, creating regions of enhanced velocity, whereas the velocity in the wake region is low, leading to a spatial gradient in velocity, which is called velocity shear. The velocity shear produces chaotic fluid motion, which is called turbulence (Figure 1-2). In a submerged canopy, additionally, flow tends to bypass the underlying canopy, thus the overflow layer above the canopy has a greater velocity than that in the canopy layer, which also produces shear and turbulence (Figures 1-5 & 1-6). The production of turbulence facilitates mass and

momentum exchange (Finnigan, 2000; Nepf, 2012a), thus playing an important role in gas (e.g., Tseng & Tinoco, 2021), nutrient (e.g., Okamoto & Nezu, 2010), and particle (e.g., Neary et al., 2012) transport.

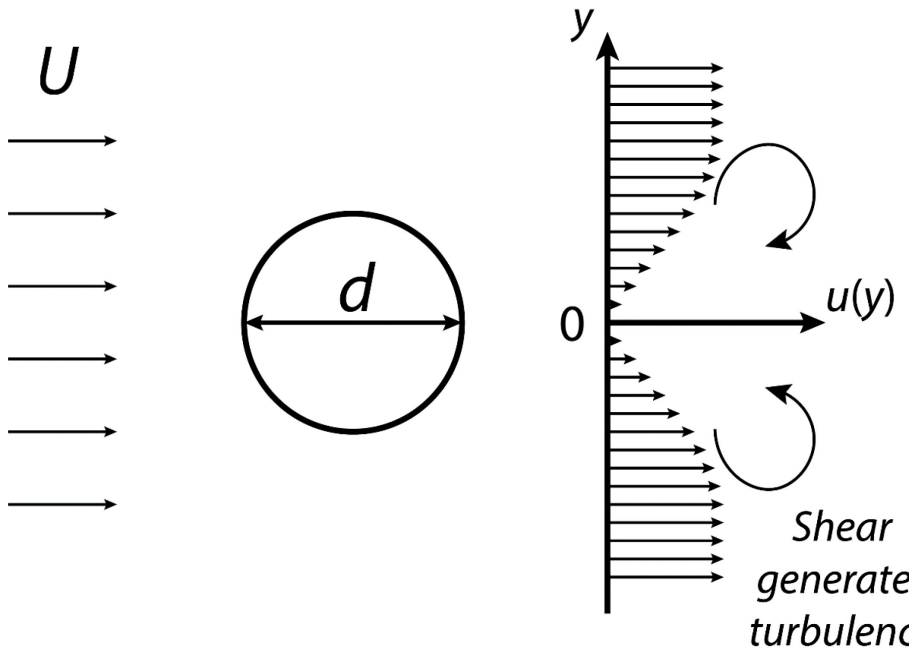

Figure 1-2. Flow past a cylinder of diameter *d* and uniform into the page. Upstream uniform velocity is *U*. Arrows indicate flow direction and magnitude. Turbulence is generated in the cylinder wake when the stem Reynolds number $Re_{\mathrm{d}} = \frac{Ud}{\nu} > 120$, in which ν is the kinematic viscosity.

The scale of turbulence depends on the dimensions of the shear region, which is related to the geometry of the roughness elements. In aquatic canopies, the scales of turbulence production range from individual roughness elements (e.g., stems, leaves, or roots; Tanino & Nepf, 2008), clusters of roughness elements (e.g., bunches of leaves or vegetation patches; Nicolle & Eames, 2011), to canopy height (e.g., Raupach et al., 1986). First, for individual vegetation elements, the scale of turbulence is set by the wake dimension (Tanino & Nepf, 2008). In a sparse array in which wakes are allowed to grow with sufficient space, the scale is the dimension of individual vegetation elements, e.g., stem diameter. In a dense array in which wake growth is limited by the element spacing, the scale is such spacing (Figure 1-3).

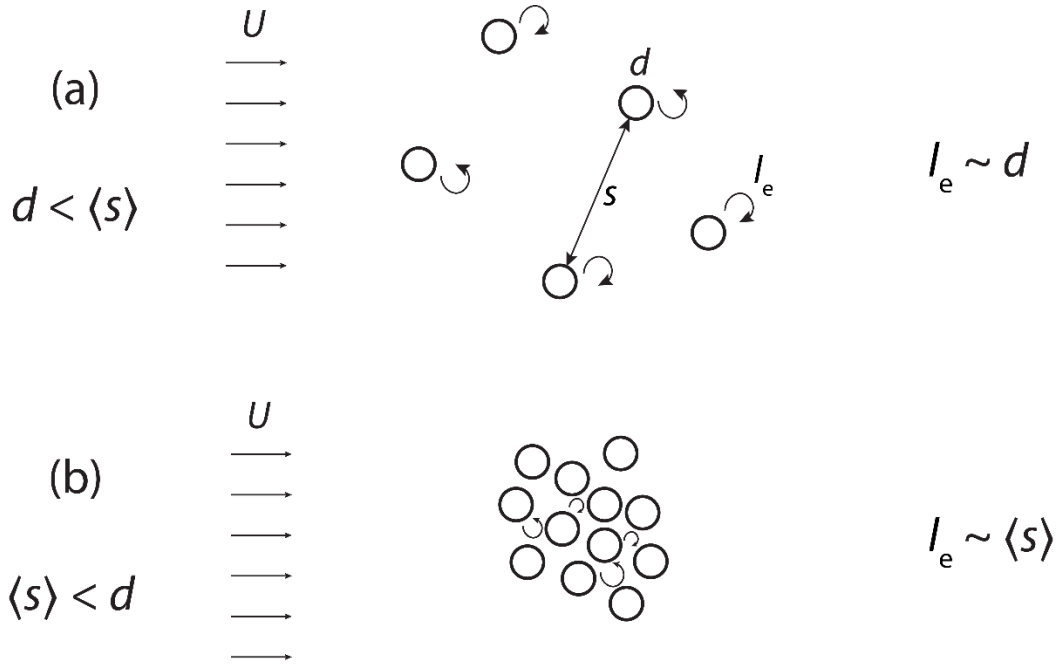

Figure 1-3. Turbulent eddies of size l_e generated in a cylinder array of uniform stem diameter d and random surface-to-surface spacing s. Angle brackets indicate spatial average. (a) Sparse array, in which eddy size scales with cylinder diameter, i.e., $l_e \sim d$. (b) Dense array, in which eddy size scales with cylinder spacing, i.e., $l_e \sim \langle s \rangle$. Modified from Tanino and Nepf (2008).

Second, for emergent vegetation clustered in patches, in addition to the element-scale turbulence, patch-scale turbulence may be generated for $\phi > 0.04$ (ϕ: solid volume fraction) downstream of the patch due to the wake formed downstream of the patch (Nicolle & Eames, 2011; Zong & Nepf, 2012). However, the patch-scale turbulence will be only observed five to ten times patch diameter (5D to 10D) downstream of the patch. If the solid volume within the patch is higher than 0.2, then the wake of the circular patch approximates that of a solid cylinder (Figure 1-4).

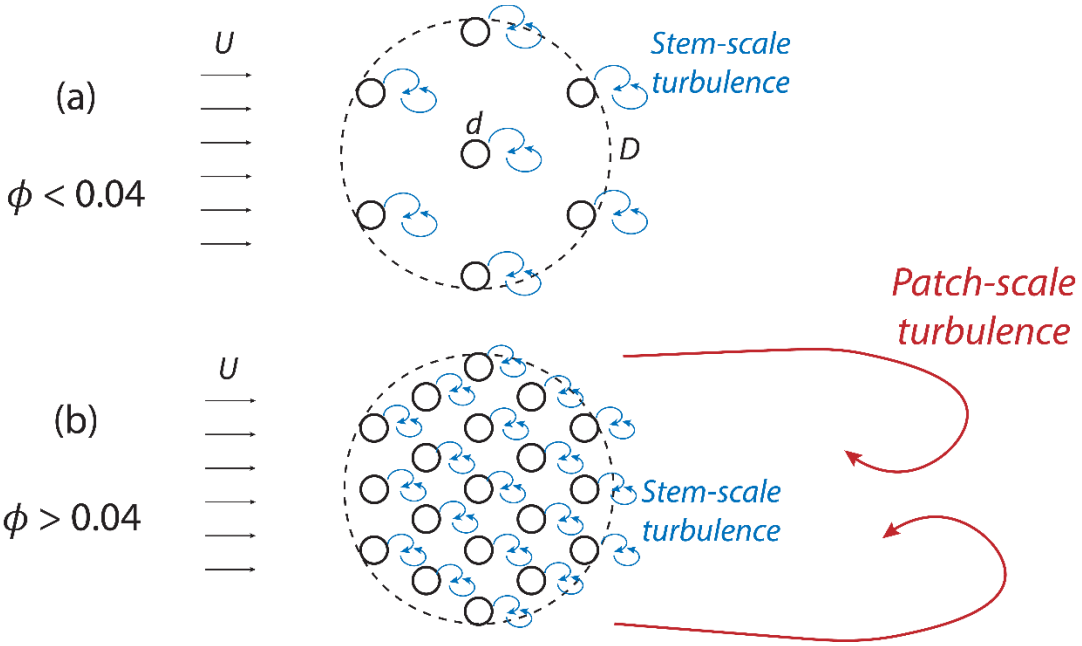

Figure 1-4. Scales of turbulence in a patch of cylinders. The cylinders have a uniform stem diameter d, and the patch has a diameter of D. ϕ is the solid volume fraction within the patch. (a) Sparse patch. No patch-scale turbulence is triggered. (b) Dense patch. Patch-scale turbulence is present. Modified from Nicolle and Eames (2011).

Third, aquatic canopies may experience different degrees of submergence. Different from terrestrial canopies, in which the canopy only occupies O (1%) of the atmospheric boundary layer thickness (Forseth, 2010; Monin, 1970), aquatic canopies can occupy a large fraction of the flow depth, thus impacting the entire flow domain (Nepf, 2012a). The submergence ratio of a canopy, H/h, is defined as the ratio of flow depth (H) to canopy height (h). In aquatic canopies, H/h ranges from 1 (emergent) to O(10), which is limited because light is required for vegetation growth (e.g., Duarte, 1991). In terrestrial canopies, $H/h >$ O(10). For emergent canopies, turbulence primarily arises from stem wakes and patch wakes, and for $\phi > 0.01$, vegetation-induced drag and turbulence are dominant over bed drag and turbulence (Belcher et al., 2003; Yang & Nepf, 2019). For long submerged canopies, due to the canopy drag, the vertical velocity profile adjusts downstream from upstream of the canopy leading edge and becomes fully developed (Figure 1-5; Belcher et al., 2003; Chen et al., 2013). The length scale of in-canopy flow adjustment, X_D (subscript "D" for deflection and deceleration, Chen et al., 2013), is

$$X_{\mathrm{D}} = (1 + \alpha C_{\mathrm{D}} a h)\beta L_{\mathrm{C}} \tag{1.1}$$

in which C_{D} is the canopy drag coefficient, a the frontal canopy area per unit volume, h the canopy height, $L_{\mathrm{C}} = \frac{2}{C_{\mathrm{D}} a(1-\phi)}$ is the canopy drag length scale, and coefficients $\alpha = 2.3 \pm 0.2$ and $\beta = 1.5 \pm 0.2$ are based on empirical fits presented on Figure 6 in Chen et al. (2013). A shear layer develops downstream around the canopy top and becomes fully developed at a larger length scale X_* (Chen et al., 2013):

$$X_* = \gamma \frac{U_{\mathrm{canopy}} + U_{\mathrm{of}}}{2} \frac{L_{\mathrm{s}}}{u_*} \tag{1.2}$$

in which U_{canopy} and U_{of} (subscript "of" for "overflow") represent the average velocity within and above the canopy in the fully developed region, respectively, shear length scale $L_{\mathrm{s}} \approx \delta_{\mathrm{e}}$ (penetration length, discussed below), and u_* the friction velocity. Coefficient $\gamma = 8 \pm 2$ is based on empirical fits presented on Figure 11 in Chen et al. (2013).

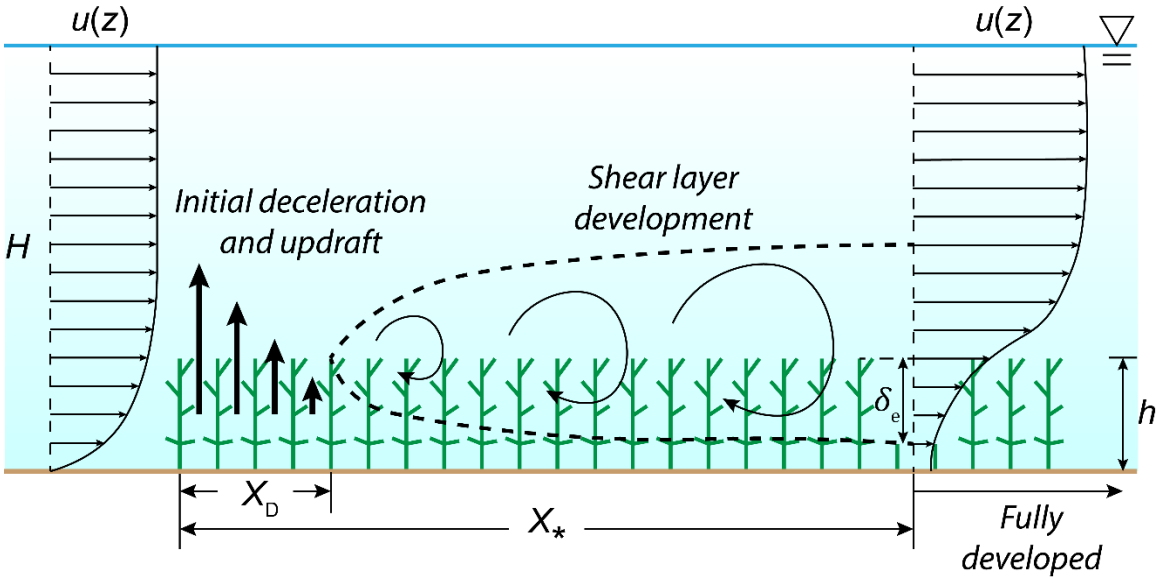

Figure 1-5. Flow adjustment in a submerged vegetation canopy. Modified from Chen et al. (2013). In a canopy of height h, the velocity profile $u(z)$ adjusts over the adjustment length X_{D}, and a shear layer grows downstream over X_* until fully developed, where the distance between its lower limit and the canopy top is defined as the penetration length δ_e. H is the flow depth.

When the canopy density is sufficiently large ($ah > 0.1$), an inflection point in the velocity profile coincides with the canopy top (Figure 1-6; Belcher et al., 2003), which induces canopy-scale turbulence that directly penetrates into the canopy over the penetration length δ_e. δ_e is inversely proportional to the product of canopy drag coefficient, C_D, and frontal canopy area per unit volume, a, i.e. $\delta_e \approx \frac{1}{3}(C_D a)^{-1}$, which was verified for model rigid and flexible aquatic canopies, model terrestrial and urban canopies, coral reefs, and dense porous media, with $0.1 < C_D ah < 4$ (Ghisalberti, 2009, Figure 4). However, the penetration length is also restricted by the bed ($\delta_e = h$) and the water surface ($\delta_e = H - h$, Nepf & Vivoni, 2000), such that

$$\delta_e = \min\left\{\frac{1}{3}(C_D a)^{-1},\ h,\ H - h\right\}. \tag{1.3}$$

This implies that, if not limited by the water surface, in a sparse canopy ($0.1 < ah < 0.3$), canopy turbulence penetrates throughout the canopy to the bed, whereas for dense canopies ($ah > 0.3$), the production of shear layer turbulence does not extend to the bed (Figure 1-6). All the types of turbulence listed above, with scales ranging from element, patch to canopy, can in turn impact the hydrodynamic forces and velocity within the canopy, which influences sediment transport in vegetated channels.

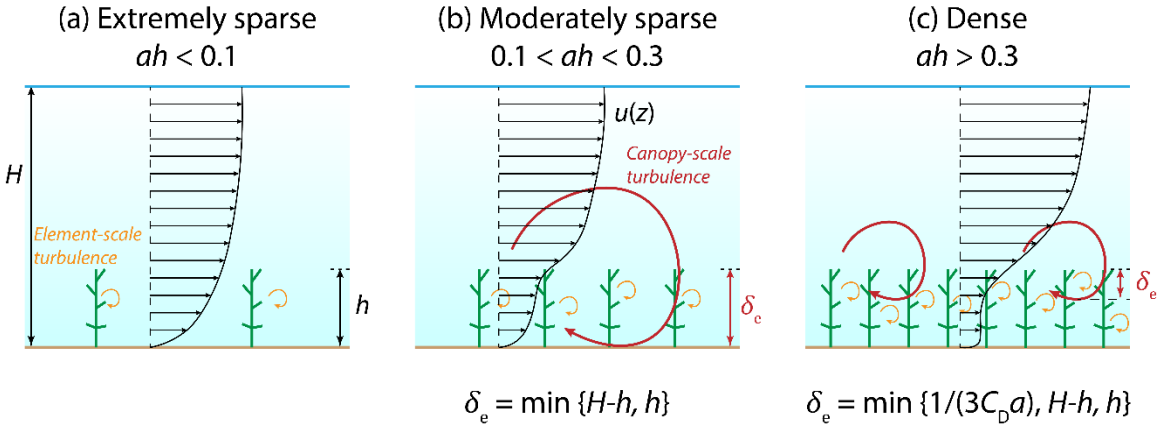

Figure 1-6. Scales of turbulence in submerged vegetation canopies. Element-scale turbulence is present in all cases. (a) Extremely sparse canopy ($ah < 0.1$), in which canopy-scale turbulence is not triggered. (b) Moderately sparse canopy ($0.1 < ah < 0.3$), in which the growth of canopy-scale turbulence is limited by the bottom boundary. (c) Dense canopy ($ah > 0.3$), in which the growth of canopy-scale turbulence is limited by the canopy density (ah). Modified from Nepf (2012a).

The magnitude of vegetation turbulence depends on the magnitude of velocity shear, which is also related to the vegetation geometry. The turbulent kinetic energy (TKE), k_t, is set by both the vegetation density (solid volume fraction) and the length scale of turbulence. Tanino and Nepf (2008) proposed a model of channel average TKE in emergent arrays of rigid circular cylinders:

$$\frac{k_t}{U^2} = \begin{cases} 1.2\left[C_{Df}\frac{2\phi}{\pi(1-\phi)}\right]^{\frac{2}{3}} & d < 0.56s_n \\ 0.77\left[C_{Df}\frac{s_n}{d}\frac{2C_{Df}\phi}{\pi(1-\phi)}\right]^{\frac{2}{3}} & d \geq 0.56s_n \end{cases} \tag{1.4}$$

in which the channel average TKE is normalized by the channel-averaged velocity U, C_{Df} is the form drag coefficient, ϕ is the solid volume fraction, d is the stem diameter, and s_n is the average surface-to-surface distance between a cylinder and its nearest neighbor in the vegetation array. The normalized channel average TKE increases almost linearly with increasing solid volume fraction in the sparse regime ($d < 0.56s_n$, i.e., $\phi < 0.1$), but approaches a nearly constant value in the dense regime ($d \geq 0.56s_n$, i.e., $\phi \geq 0.1$; see Figure 14 & 15 in Tanino & Nepf, 2008). Note that this model is only valid for emergent plants with cylindrical morphology, e.g., reeds and mangrove pneumatophores.

In the discussions above, the model vegetation consisted of rigid cylinders of uniform cylindrical morphology, which mimics the shape of erect main stems. In addition to the stems that may or may not branch, aquatic plants have other structures including leaves and roots (e.g., mangrove pneumatophores) that exert drag on the flow. For example, see *Rhizophora mangle* in Figure 1-1. In this case, the vertical distribution of vegetation frontal area is not uniform. An equivalent diameter, d_e, may be defined based on the geometry of plant elements (e.g., stem diameter and leaf/blade width) to be used as an input in the turbulence model derived based on simple morphology (circular cylinders). For example, for emergent vegetation, Xu and Nepf (2020) defined an effective diameter (d_e) of a cylinder spanning water depth H with the same submerged total frontal area A_f:

$$d_e = A_f/H. \tag{1.5}$$

In the field, aquatic vegetation species exhibit different degrees of flexibility. In response to the flow, flexible plants will bend, which reduces their height and consequently frontal area. This process is called reconfiguration (Figure 1-7). For a single flexible blade tied to a stem with negligible height, Luhar and Nepf (2011, 2013) proposed a model to predict the ratio of deflected canopy height, h, to the blade length (i.e., the height of canopy at erection), l:

$$\frac{h}{l} = 1 - \frac{1 - Ca^{-\frac{1}{4}}}{1 + Ca^{-\frac{3}{5}}\left(4 + B^{\frac{3}{5}}\right) + Ca^{-2}(8 + B^2)}, \tag{1.6}$$

in which the Cauchy number

$$Ca = \frac{1}{2}\frac{\rho C_D b U_{\text{hor}}^2 l^3}{EI} \tag{1.7}$$

is the ratio of inertial force to elastic restoring force, and the buoyancy parameter

$$B = \frac{|\rho - \rho_{veg}| g b t l^3}{EI} \tag{1.8}$$

is the ratio of buoyant restoring force to elastic restoring force. ρ and ρ_{veg} are the density of water and vegetation, respectively. b is the blade width, t the blade thickness, l the blade length, U_{hor} the horizontal velocity (assumed vertically uniform in their study, i.e., $U_{\text{hor}} = U$), g the gravitational acceleration, E the Young's modulus of the blade, and $I = \frac{bt^3}{12}$ the moment of inertia of area of the blade.

Luhar and Nepf (2011) also defined an effective blade length, l_{eff}, as the height of erect rigid blade that produces the same total drag as a reconfiguring flexible blade, may be defined to characterize the drag reduction by reconfiguration:

$$\frac{l_{\text{eff}}}{l} = 1 - \frac{1 - 0.9Ca^{-\frac{1}{3}}}{1 + Ca^{-\frac{3}{2}}\left(8 + B^{\frac{3}{2}}\right)}. \tag{1.9}$$

Flexible plants may also perform wavy motion (known as *monami*; Japanese: 藻波, lit. "water weed wave", Ackerman & Okubo, 1993; Okamoto & Nezu, 2009; Wang et al., 2022) that leads to temporal changes in their height and frontal area.

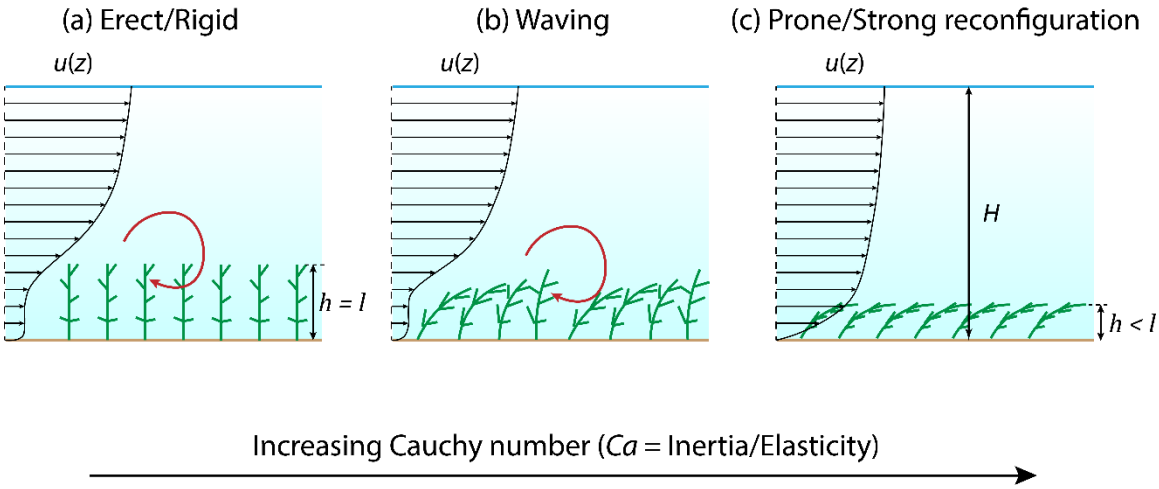

Figure 1-7. Reconfiguration of flexible aquatic vegetation, with increasing Cauchy number *Ca*. When the flexible canopy is prone, no canopy-scale vortices were observed. Modified from Okamoto et al. (2016) and Tschisgale et al. (2021).

1.2 Sediment Transport

Aquatic vegetation has the potential to act as a nature-based solution for global climate change. Projects of wetland protection and restoration can be implemented to exploit this potential, which requires understanding of the flow and sediment transport processes in wetlands where aquatic vegetation resides (Paola et al., 2011; Fagherazzi et al., 2017). Specifically, the erosion and deposition of sediment bed (e.g., seabed, riverbed, lakebed, delta, desert, floodplain) is reflected by the bed level change and determined by the divergence of sediment flux:

$$\frac{\partial \eta}{\partial t} = -\frac{1}{1-\lambda_p} \nabla \cdot \overrightarrow{q_s}, \tag{1.10}$$

in which η is bed elevation, t is time, λ_p is bed porosity, and $\overrightarrow{q_s} = (q_{s,x}, q_{s,y}, q_{s,z})$ is the sediment transport rate vector. Equation 1.10 is called the Exner equation (Exner, 1920, 1925). To protect the wetland, we require a non-negative change in bed elevation ($\frac{\partial \eta}{\partial t} \geq 0$), which may be attributed to increased sediment supply from upstream and/or reduced local erosion, both leading to convergence of sediment transport ($\nabla \cdot \overrightarrow{q_s} \leq 0$).

Sediment transport refers to the movement of sediment particles, which is often driven by turbulent fluid flow (e.g., water or air; Julien, 2010) and which can reshape the landscape of earth and other planets (Pähtz et al., 2020). Coasts and riverbanks with limited sediment supply undergo erosion, i.e., the removal of sediment through sediment transport, which can lead to severe property and ecological damages. For example, according to the U.S. Climate Resilience Toolkit (2021), every year in the U.S., $500 million of coastal property loss is due to coastal erosion and $150 million is spent on erosion control by the federal government. In addition, aside from beach erosion, more than 300 km^2 of coastal wetlands, crucial habitats for many coastal species ranging from birds, fish, crabs to frogs, are lost annually.

The classic view of sediment transport in bare channels holds that bed sediments enter motion when the applied fluid boundary shear stress exceeds a threshold value (Julien, 2010), which is a function of grain size and specific weight. The threshold of sediment motion has been recorded empirically in the Shields (1936) diagram (Figure 1-8; Whitehouse et al., 2000; Guo, 2020), which shows the applied shear stress observed to initiate the motion of grains of a specific size. Sediment in motion is divided into bedload and suspended load (Figure 1-9; Julien, 2010). Bedload maintains close contact with the bed as it moves downstream, whereas suspended load remains in suspension in the water column, not in frequent contact with the bed. The focus of this thesis is bedload transport in vegetated channels. For suspended load transport in vegetated channels, readers are invited to refer to Xu (2022) and Tseng (2022)'s theses.

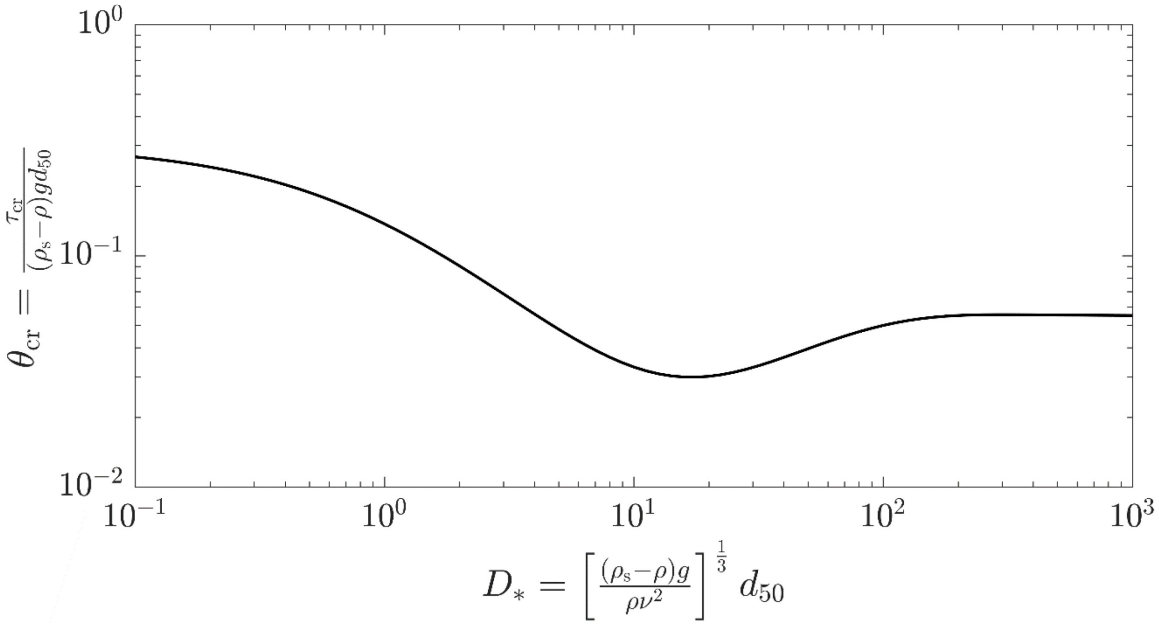

Figure 1-8. Shields diagram. This diagram shows the corresponding critical shear stress (in dimensionless form $\theta_{\mathrm{cr}} = \frac{\tau_{\mathrm{cr}}}{(\rho_s-\rho)gd_{50}}$) for a given sediment grain size (in dimensionless form $D_* = \left[\frac{(\rho_s-\rho)g}{\rho\nu^2}\right]^{\frac{1}{3}} d_{50}$). The curve is Soulsby (1997)'s fit of experimental results.

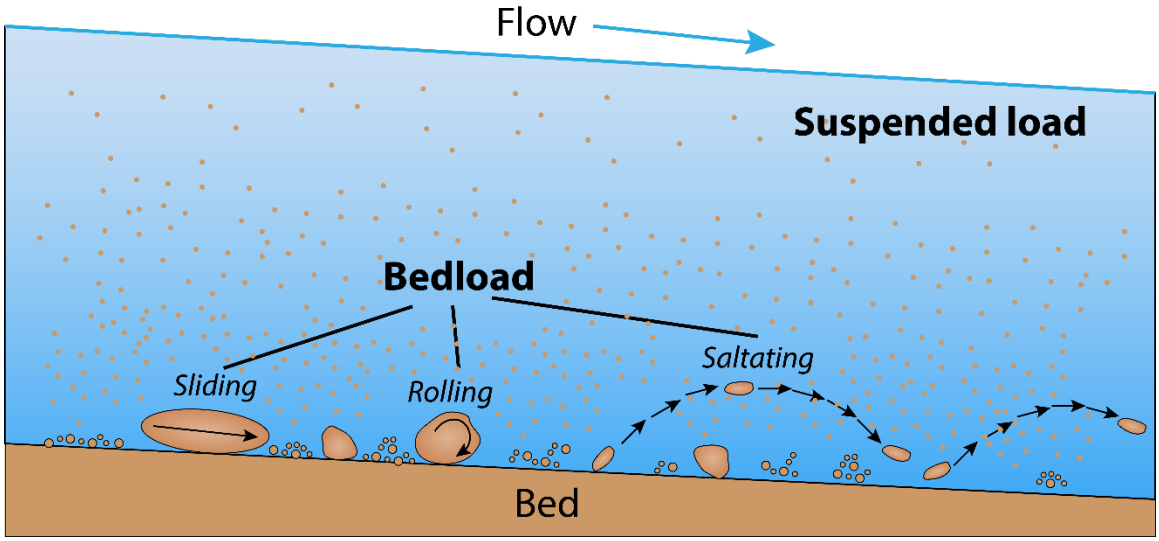

Figure 1-9. Illustration of bed load and suspended load. Bed load maintains close contact with the bed while in motion (rolling, sliding, and saltation). Suspended load is kept in suspension by fluid turbulence.

In classic sediment transport studies, bedload transport rate (sediment mass per unit channel width and time) is described as a function of time-mean channel average bed shear stress (e.g., Einstein, 1942; Engelund & Hansen, 1967). A critical bed shear stress associated with the median grain size of bed sediment is often included in the function (e.g., Meyer-Peter & Müller, 1948; Shields, 1936). While this approach can predict bedload transport rate in many scenarios, it does not directly account for turbulence that is also important in initiating and maintaining sediment transport (Yager et al., 2018). Turbulence causes instantaneous fluctuations in both the magnitude and direction of bed shear stress through ejection ($u' < 0$, $w' > 0$) and sweep events ($u' > 0$, $w' < 0$) that create short pulses of higher-than-average bed shear stress (Nelson et al., 1995) and favorable pressure fields for particle motion (Shih et al., 2017), both of which enhance sediment transport (Sumer et al., 2003; Noguchi & Nezu, 2009; Tinoco & Coco, 2016; Salim et al., 2017; Tseng & Tinoco, 2021). The enhancement of sediment transport by turbulence is more important near the motion threshold (Yang et al., 2016; Benavides et al., 2022). Not only the magnitude but also the duration of stress fluctuations is important to sediment transport. Both the stress magnitude and the impulse, i.e., product of magnitude and duration of a fluctuation, contribute to the onset of grain motion (Diplas et al., 2008; Celik et al., 2010).

In vegetated channels, the shear-stress-based models have been shown to underestimate bedload transport by several orders of magnitude (Yager & Schmeeckle, 2013; Yang & Nepf, 2018), not only because they do not account for vegetation-generated turbulence, but also due to the difficulty of quantifying total bed shear stress in the presence of vegetation (Nepf, 2012b). In unvegetated channels, bed shear stress is usually extrapolated from a linear Reynolds stress profile (e.g., Nezu & Rodi, 1986; Stacey et al., 1999), or inferred from a correlation between the near-bed TKE and bed shear stress (Soulsby, 1983). However, in vegetated channels, the Reynolds stress profile is not a good predictor for the bed shear stress (Yang et al., 2015; Conde-Frias et al., 2023), and TKE has been shown to provide a better prediction than bed shear stress for the sediment motion threshold (Yang et al., 2016), the resuspension threshold (Tinoco & Coco, 2018; Liu et al., 2021), sediment pickup rate (Xu et al., 2022), and bedload transport rate (Yang & Nepf, 2018, 2019). This raises the question: can we predict

bedload transport solely from the intensity of near-bed turbulence? Previous studies have suggested that bedload transport rate can be described as the product of grain velocity, which is correlated with fluid velocity, and the number of grains in motion, which is correlated with turbulence (Ancey et al., 2008), but that net sediment transport is predominantly controlled by the number of grains in motion (e.g., Radice & Ballio, 2008; Roseberry et al., 2012). Both the near-bed TKE and velocity may be required for modeling bedload transport. Laboratory experiments are designed to explore this question.

1.3 Thesis Structure

This thesis explored how different vegetation geometries control near-bed turbulence and bedload sediment transport. Chapter 2 examines turbulence and bedload transport in channels with randomly distributed emergent patches of model vegetation. With constant channel velocity and solid volume fraction, TKE and bedload transport decreased with increased clustering. The channel average TKE better predicted sediment transport than channel average bed shear stress.

Chapter 3 explores whether stem diameter and element arrangement of emergent model vegetation influence channel turbulence and bedload transport. For vegetation canopies that are not clustered, bedload transport did not depend on the arrangement and stem diameter(s), which was explained by the impulse model for sediment entrainment. The classic Meyer-Peter-Müller bedload transport model was recast in terms of TKE to predict sediment transport in channels with emergent vegetation. In addition, this chapter outlines how to predict the channel average TKE from plant biomass and velocity, offering an important step toward predicting turbulence and sediment transport in vegetation canopies of real morphology in the field.

Chapter 4 explores the turbulence and bedload transport in canopies of submerged model vegetation. For constant channel velocity, submerged canopies could enhance or reduce bedload transport, depending on their degree of submergence. With increasing submergence H/h, the near-bed velocity and TKE decreased, and the source of near-bed turbulence shifted from stem wake to the shear layer at the canopy top. For high

submergence ratio ($H/h > 2$), TKE was insensitive to changes in H/h and ah. Bedload transport was predominantly correlated with near-bed turbulence but also weakly correlated with near-bed velocity, so bedload transport monotonically decreased with increasing H/h. A model to predict near-bed TKE in submerged canopies was developed and used to explore bedload transport with constant energy slope and flexible vegetation, commonly seen in the field. In the modeled scenarios, canopies reduced sediment transport compared to unvegetated cases. Because of the important contribution of canopy-shear-generated turbulence, with constant energy slope, the highest sediment transport rates occurred for vegetation with the greatest submergence ratio and the smallest canopy density.

Chapter 5 describes the bedform migration observed during the experiment within a submerged model vegetation canopy. The rate of bedform migration was inferred from photographs. The migration of bedforms explained the observed cyclical variation in channel-averaged sediment transport rates. Finally, Chapter 6 summarizes this dissertation and offers several research directions.

Chapter 1 References

Ackerman, J. D., & Okubo, A. (1993). Reduced mixing in a marine macrophyte canopy. *Functional Ecology*, 7, 305-309. doi:10.2307/2390209

Afzalimehr, H., & Subhasish, D. E. Y. (2009). Influence of bank vegetation and gravel bed on velocity and Reynolds stress distributions. *International Journal of Sediment Research*, 24(2), 236-246. doi:10.1016/S1001-6279(09)60030-5

Ancey, C., Davison, A. C., Böhm, T., Jodeau, M., & Frey, P. (2008). Entrainment and motion of coarse particles in a shallow water stream down a steep slope. *Journal of Fluid Mechanics*, 595, 83–114. doi:10.1017/S0022112007008774

Barbier, E.B., Hacker, S.D., Kennedy, C., Koch, E.W., Stier, A.C. & Silliman, B.R. (2011). The value of estuarine and coastal ecosystem services. *Ecological Monographs*, 81: 169–193. doi:10.1890/10-1510.1

Belcher, S. E., Jerram, N., & Hunt, J. C. R. (2003). Adjustment of a turbulent boundary layer to a canopy of roughness elements. *Journal of Fluid Mechanics*, 488: 369–398. doi:10.1017/S0022112003005019

Benavides, S. J., Deal, E., Rushlow, M., Venditti, J. G., Zhang, Q., Kamrin, K., & Perron, J. T. (2022). The impact of intermittency on bed load sediment transport. *Geophysical Research Letters*, 49(5), e2021GL096088. doi:10.1029/2021GL096088

Celik, A. O., Diplas, P., Dancey, C. L., & Valyrakis, M. (2010). Impulse and particle dislodgement under turbulent flow conditions. *Physics of Fluids*, 22(4), 46601. doi:10.1063/1.3385433

Chambers, P. A., & Prepas, E. E. (1994). Nutrient dynamics in riverbeds: the impact of sewage effluent and aquatic macrophytes. *Water Research*, 28(2), 453-464. doi:10.1016/0043-1354(94)90283-6

Chen, Z., Jiang, C., & Nepf, H. (2013). Flow adjustment at the leading edge of a submerged aquatic canopy. *Water Resources Research*, 49(9), 5537–5551. doi:10.1002/wrcr.20403

Collins, S. L., & Glenn, S. M. (1997). Intermediate disturbance and its relationship to within-and between-patch dynamics. *New Zealand Journal of Ecology*, 21(1), 103-110.

Conde-Frias, M., Ghisalberti, M., Lowe, R.J., Abdolahpour, M., & Etminan, V. (2023). The Near-Bed Flow Structure and Bed Shear Stresses Within Emergent Vegetation. *Water Resources Research*, 59(4), e2022WR032499. doi:10.1029/2022WR032499

Costanza, R., d'Arge, R., de Groot, R., Farber, S., Grasso, M., Hannon, B., ... & van den Belt, M. (1997). The value of the world's ecosystem services and natural capital. *Nature*, 387(6630), 253–260. doi:10.1038/387253a0

Crowder, D. W., & Diplas, P. (2002). Assessing Changes in Watershed Flow Regimes with Spatially Explicit Hydraulic Models. *Journal of the American Water Resources Association*, 38(2), 397-408. doi:10.1111/j.1752-1688.2002.tb04325.x

Dhir, B., Sharmila, P., & Saradhi, P. P. (2009). Potential of aquatic macrophytes for removing contaminants from the environment. *Critical Reviews in Environmental Science and Technology*, 39(9), 754-781. doi:10.1080/10643380801977776

Diplas, P., Dancey, C. L., Celik, A. O., Valyrakis, M., Greer, K., & Akar, T. (2008). The Role of Impulse on the Initiation of Particle Movement Under Turbulent Flow Conditions. *Science*, 322(5902), 717–720. doi:10.1126/science.1158954

Duarte, C. M. (1991). Seagrass depth limits. *Aquatic botany*, 40(4), 363-377. doi:10.1016/0304-3770(91)90081-F

Einstein, H. A. (1942). Formulas for the Transportation of Bed Load. *Transactions of the American Society of Civil Engineers*, 107(1), 561–577.

Engelund, F., & Hansen, E. (1967). *A monograph on sediment transport in alluvial streams*. Teknisk Forlag.

Fagherazzi, S., Bryan, K., & Nardin, W. (2017). Buried Alive or Washed Away: The Challenging Life of Mangroves in the Mekong Delta. *Oceanography*, 30(3), 48–59. doi:10.5670/oceanog.2017.313

Finnigan, J. (2000). Turbulence in plant canopies. *Annual review of fluid mechanics*, 32(1), 519-571. doi:10.1146/annurev.fluid.32.1.519

Forseth, I. (2010) Terrestrial Biomes. *Nature Education Knowledge,* 3(10):11

Fourqurean, J. W., Duarte, C. M., Kennedy, H., Marbà, N., Holmer, M., Mateo, M. A., ... & Serrano, O. (2012). Seagrass ecosystems as a globally significant carbon stock. *Nature Geoscience*, 5(7), 505–509. doi:10.1038/ngeo1477

Ghisalberti, M. (2009). Obstructed shear flows: similarities across systems and scales. *Journal of Fluid Mechanics*, 641, 51–61. doi:10.1017/S0022112009992175

Guo, J. (2020). Empirical model for shields diagram and its applications. *Journal of Hydraulic Engineering*, 146(6), 04020038. doi:10.1061/(ASCE)HY.1943-7900.0001739

Hackney, C.R., Darby, S.E., Parsons, D.R., Leyland, J., Best, J.L., Aalto, R., ... & Houseago, R.C. (2020). River bank instability from unsustainable sand mining in the lower Mekong River. Nature Sustainability, 3(3), 217–225. doi:10.1038/s41893-019-0455-3

Julien, P. Y. (2010). *Erosion and Sedimentation* (2nd ed.). Cambridge University Press. doi: 10.1017/CBO9780511806049

Kemp, J. L., Harper, D. M., & Crosa, G. A. (2000). The habitat-scale ecohydraulics of rivers. *Ecological engineering*, 16(1), 17-29. doi:10.1016/S0925-8574(00)00073-2

Lake, P. S. (2000). Disturbance, patchiness, and diversity in streams. *Journal of the North American Benthological Society*, 19(4), 573-592. doi:10.2307/1468118

Luhar, M., & Nepf, H. M. (2011). Flow-induced reconfiguration of buoyant and flexible aquatic vegetation. *Limnology and Oceanography*, 56(6), 2003-2017. doi:10.4319/lo.2011.56.6.2003

Luhar, M., & Nepf, H. M. (2013). From the blade scale to the reach scale: A characterization of aquatic vegetative drag. *Advances in Water Resources*, 51, 305-316. doi:10.1016/j.advwatres.2012.02.002

Luisa, B. G. (2012). *The ecology of natural disturbance and patch dynamics*. Academic press. doi:10.1016/C2009-0-02952-3

Massachusetts Department of Conservation and Recreation, (2016). *A Guide to Aquatic Plants in Massachusetts*. https://www.mass.gov/doc/dcr-guide-to-aquatic-plants-in-massachusetts/download

McLain, D. C., & Ross, M. R. (2005). Reproduction based on local patch size of Alasmidonta heterodon and dispersal by its darter host in the Mill River, Massachusetts, USA. *Journal of the North American Benthological Society*, 24(1), 139-147. doi:10.1899/0887-3593(2005)024<0139:RBOLPS>2.0.CO;2

Meyer-Peter, E., & Müller, R. (1948). Formulas for Bed Load Transport. In *Proceedings of 2nd meeting of the International Association for Hydraulic Structures Research*, Stockholm, Appendix 2, 39–64.

Minnesota Department of Natural Resources, (2021). Where aquatic plants grow. Retrieved July 13, 2024, from https://www.dnr.state.mn.us/shorelandmgmt/apg/wheregrow.html

Monin, A. S. (1970). The atmospheric boundary layer. *Annual Review of Fluid Mechanics*, 2(1), 225-250. doi:10.1146/annurev.fl.02.010170.001301

Neary, V. S., Constantinescu, S. G., Bennett, S. J., & Diplas, P. (2012). Effects of vegetation on turbulence, sediment transport, and stream morphology. *Journal of Hydraulic Engineering*, 138(9), 765-776. doi:10.1061/(ASCE)HY.1943-7900.0000168

Nelson, J. M., Shreve, R. L., McLean, S. R., & Drake, T. G. (1995). Role of Near-Bed Turbulence Structure in Bed Load Transport and Bed Form Mechanics. *Water Resources Research*, 31(8), 2071–2086. doi:10.1029/95WR00976

Nepf, H. M. (2012). Flow and Transport in Regions with Aquatic Vegetation. *Annual Review of Fluid Mechanics*, 44(1), 123–142. doi:10.1146/annurev-fluid-120710-101048

Nepf, H. M. (2012). Hydrodynamics of vegetated channels. *Journal of Hydraulic Research*, *50*(3), 262-279. doi:10.1080/00221686.2012.696559

Nepf, H.M., & Vivoni, E.R. (2000). Flow structure in depth-limited, vegetated flow. *Journal of Geophysical Research: Oceans*, 105(C12), 28547–28557. doi:10.1029/2000JC900145

Nezu, I., & Rodi, W. (1986). Open-channel Flow Measurements with a Laser Doppler Anemometer. *Journal of Hydraulic Engineering*, 112(5), 335–355. doi:10.1061/(ASCE)0733-9429(1986)112:5(335)

Nicolle, A., & Eames, I. (2011). Numerical study of flow through and around a circular array of cylinders. *Journal of Fluid Mechanics*, 679, 1-31. doi:10.1017/jfm.2011.77

Noguchi, K., & Nezu, I. (2009). Particle–turbulence interaction and local particle concentration in sediment-laden open-channel flows. *Journal of Hydro-environment Research*, 3(2), 54-68. doi:10.1016/j.jher.2009.07.001

Okamoto, T. A., & Nezu, I. (2009). Turbulence structure and "Monami" phenomena in flexible vegetated open-channel flows. *Journal of Hydraulic Research*, 47(6), 798-810. doi:10.3826/jhr.2009.3536

Okamoto, T. A., & Nezu, I. (2010). Large eddy simulation of 3-D flow structure and mass transport in open-channel flows with submerged vegetations. *Journal of Hydro-environment Research*, 4(3), 185-197. doi:10.1016/j.jher.2010.04.015

Orth, R. J., Luckenbach, M., & Moore, K. A. (1994). Seed dispersal in a marine macrophyte: implications for colonization and restoration. *Ecology*, 75(7), 1927-1939. doi:10.2307/1941597

Pähtz, T., Clark, A. H., Valyrakis, M., & Durán, O. (2020). The physics of sediment transport initiation, cessation, and entrainment across aeolian and fluvial environments. *Reviews of Geophysics*, 58(1), e2019RG000679. doi:10.1029/2019RG000679

Paola, C., Twilley, R.R., Edmonds, D.A., Kim, W., Mohrig, D., Parker, G., ... & Voller, V.R. (2011). Natural Processes in Delta Restoration: Application to the Mississippi Delta. *Annual Review of Marine Science*, 3(1), 67–91. doi:10.1146/annurev-marine-120709-142856

Pollen-Bankhead, N., & Simon, A. (2010). Hydrologic and hydraulic effects of riparian root networks on streambank stability: Is mechanical root-reinforcement the whole story?. *Geomorphology*, 116(3-4), 353-362. doi:10.1016/j.geomorph.2009.11.013

Radice, A., & Ballio, F. (2008). Double-average characteristics of sediment motion in one-dimensional bed load. *Acta Geophysica*, 56(3), 654–668. doi:10.2478/s11600-008-0015-0

Raupach, M. R., Coppin, P. A., & Legg, B. J. (1986). Experiments on scalar dispersion within a model plant canopy part I: The turbulence structure. *Boundary-Layer Meteorology*, 35, 21-52. doi:10.1007/BF00117300

Roseberry, J. C., Schmeeckle, M. W., & Furbish, D. J. (2012). A probabilistic description of the bed load sediment flux: 2. Particle activity and motions. *Journal of Geophysical Research: Earth Surface*, 117(F3), F03032. doi:10.1029/2012JF002353

Salim, S., Pattiaratchi, C., Tinoco, R., Coco, G., Hetzel, Y., Wijeratne, S., & Jayaratne, R. (2017). The influence of turbulent bursting on sediment resuspension under unidirectional currents. *Earth Surface Dynamics*, 5(3), 399–415. doi:10.5194/esurf-5-399-2017

Sand-Jensen, K. A. J. (1989). Environmental variables and their effect on photosynthesis of aquatic plant communities. *Aquatic Botany*, 34(1-3), 5-25. doi:10.1016/0304-3770(89)90048-X

Shields, A. (1936). *Anwendung der Aehnlichkeitsmechanik und der Turbulenzforschung auf die Geschiebebewegung* [*Application of similarity mechanics and turbulence research on shear flow*]. Mitteilungen der Preußischen Versuchsanstalt für Wasserbau (in German). 26. Berlin: Preußische Versuchsanstalt für Wasserbau.

Shih, W., Diplas, P., Celik, A. O., & Dancey, C. (2017). Accounting for the role of turbulent flow on particle dislodgement via a coupled quadrant analysis of velocity and pressure sequences. *Advances in water resources*, 101, 37-48. doi:10.1016/j.advwatres.2017.01.005

Soulsby, R. L. (1983). The bottom boundary layer of shelf seas. In *Elsevier oceanography series* (Vol. 35, pp. 189–266). Elsevier.

Soulsby, R. L. (1997). *Dynamics of marine sands: A manual for practical applications*. Thomas Telford.

Stacey, M. T., Monismith, S. G., & Burau, J. R. (1999). Measurements of Reynolds stress profiles in unstratified tidal flow. *Journal of Geophysical Research: Oceans*, 104(C5), 10933–10949. doi:10.1029/1998JC900095

Sumer, B. M., Chua, L. H. C., Cheng, N.-S., & Fredsøe, J. (2003). Influence of Turbulence on Bed Load Sediment Transport, *Journal of Hydraulic Engineering*, 129(8), 585–596. doi:10.1061/(ASCE)0733-9429(2003)129:8(585)

Tal, M., Paola, C. (2010). Effects of vegetation on channel morphodynamics: results and insights from laboratory experiments. Earth Surface Proc. and Land. 35: 1014–1028. https://doi.org/10.1002/esp.1908

Tanino, Y., & Nepf, H.M. (2008). Lateral dispersion in random cylinder arrays at high Reynolds number. *Journal of Fluid Mechanics*, 600, 339–371. doi:10.1017/S0022112008000505

Tinoco, R., and Coco, G. (2016). A laboratory study on sediment resuspension within arrays of rigid cylinders. *Advances in Water Resources*, 92, 1-9. doi:10.1016/j.advwatres.2016.04.003

Tinoco, R.O., & Coco, G. (2018). Turbulence as the Main Driver of Resuspension in Oscillatory Flow Through Vegetation. *Journal of Geophysical Research: Earth Surface*, 123(5), 891–904. doi:10.1002/2017JF004504

Tseng, C. Y. (2022). *From substrate to surface: An integrated study on the Interfacial transfer and sediment suspension based on a turbulence perspective in vegetated flows* [Doctoral thesis, University of Illinois at Urbana-Champaign]. IDEALS@Illinois University Library. https://www.ideals.illinois.edu/items/124822

Tseng, C., & Tinoco, R. O. (2021). A Two-Layer Turbulence-Based Model to Predict Suspended Sediment Concentration in Flows with Aquatic Vegetation. *Geophysical Research Letters*, 48(3), e2020GL091255. doi:10.1029/2020GL091255

U.S. Climate Resilience Toolkit (2021, Apr 1). *Coastal Erosion*. https://toolkit.climate.gov/topics/coastal-flood-risk/coastal-erosion

United Nations (2015). *Resolution adopted by the General Assembly on 25 September 2015*. https://undocs.org/en/A/RES/70/1

Vogel, S. (1994). *Life in moving fluids: the physical biology of flow-revised and expanded second edition*. Princeton university press.

Wang, J., He, G., Dey, S., & Fang, H. (2022). Fluid–structure interaction in a flexible vegetation canopy in an open channel. *Journal of Fluid Mechanics*, 951, A41. doi:10.1017/jfm.2022.899

Wang, Y., Wang, Q. F., Guo, Y. H., & Barrett, S. C. (2005). Reproductive consequences of interactions between clonal growth and sexual reproduction in Nymphoides peltata: a distylous aquatic plant. *New Phytologist*, 165(1), 329-336. doi:10.1111/j.1469-8137.2004.01234.x

Whitehouse, R. J. S., Soulsby, R. L., & Damgaard, ‚J. S. (2000). Discussion of "Inception of Sediment Transport on Steep Slopes". *Journal of Hydraulic Engineering*, 126(7), 553–555. doi:10.1061/(ASCE)0733-9429(2000)126:7(553.2)

Wilcock, R. J., Champion, P. D., Nagels, J. W., & Croker, G. F. (1999). The influence of aquatic macrophytes on the hydraulic and physico-chemical properties of a New Zealand lowland stream. *Hydrobiologia*, 416, 203-214. doi:10.1023/A:1003837231848

World Bank. (2022, May 19). *What You Need to Know About Nature-Based Solutions to Climate Change*. https://www.worldbank.org/en/news/feature/2022/05/19/what-you-need-to-know-about-nature-based-solutions-to-climate-change

Xu, Y. (2022). 刚性挺水植被作用下水流及泥沙运动特性研究 [*Impacts of Emergent Rigid Vegetation on Flow and Sediment Movement*]. Doctoral thesis, Tsinghua University (in Chinese).

Xu, Y., & Nepf, H. (2020). Measured and Predicted Turbulent Kinetic Energy in Flow Through Emergent Vegetation With Real Plant Morphology. *Water Resources Research*, 56(12), e2020WR027892. doi:10.1029/2020WR027892

Xu, Y., Li, D., & Nepf, H. (2022). Sediment Pickup Rate in Bare and Vegetated Channels. *Geophysical Research Letters*, 49(21), e2022GL101279. doi:10.1029/2022GL101279

Yager, E. M., & Schmeeckle, M. W. (2013). The influence of vegetation on turbulence and bed load transport. *Journal of Geophysical Research: Earth Surface*, 118(3), 1585–1601. doi:10.1002/jgrf.20085

Yager, E. M., Venditti, J. G., Smith, H. J., & Schmeeckle, M. W. (2018). The trouble with shear stress. *Geomorphology*, 323, 41-50. doi:10.1016/j.geomorph.2018.09.008

Yang, J. Q., & Nepf, H. M. (2018). A Turbulence-Based Bed-Load Transport Model for Bare and Vegetated Channels. *Geophysical Research Letters*, 45(19), 10,428–10,436. doi:10.1029/2018GL079319

Yang, J. Q., & Nepf, H. M. (2019). Impact of Vegetation on Bed Load Transport Rate and Bedform Characteristics. *Water Resources Research*, 55(7), 6109–6124. doi:10.1029/2018WR024404

Yang, J. Q., Chung, H., & Nepf, H. M. (2016). The onset of sediment transport in vegetated channels predicted by turbulent kinetic energy. *Geophysical Research Letters*, 43(21), 11,261–11,268. doi:10.1002/2016GL071092

Yang, J. Q., Kerger, F., & Nepf, H. M. (2015). Estimation of the bed shear stress in vegetated and bare channels with smooth beds. *Water Resources Research*, 51(5), 3647-3663. doi:10.1002/2014WR016042

Zong, L., & Nepf, H. (2012). Vortex development behind a finite porous obstruction in a channel. *Journal of Fluid Mechanics*, 691, 368-391. doi:10.1017/jfm.2011.479

Exner, F. M. (1920), Zur physik der dünen [*On the Physics of Dunes*], Akad. Wiss. Wien Math. Naturwiss. Klasse, 129(2a), 929-952.

Exner, F. M. (1925), Über die wechselwirkung zwischen wasser und geschiebe in flüssen [*On the Interaction between Water and Bedload in Rivers*], Akad. Wiss. Wien Math. Naturwiss. Klasse, 134(2a), 165-204.

This page intentionally left blank

Chapter 2 Turbulence and Bedload Transport in Channels with Randomly Distributed Vegetation Patches*

Laboratory experiments explored the impact of vegetation patchiness on channel-averaged turbulence and sediment transport. Stems were clustered into 16 randomly distributed circular patches of decreasing diameter. For the same channel velocity, the sediment transport increased with total stem number but decreased as stems were clustered into smaller patch diameters, occupying a smaller fraction of the bed area. The channel-averaged turbulence, which also declined with increased clustering, was shown to be a good predictor for sediment transport at the channel scale. Previous models for uniform vegetation were adapted to predict both the channel-averaged turbulence and sediment transport as a function of the total number of stems and degree of clustering, represented by the fraction of bed covered by patches. This provides a way for numerical modelers to represent the impact of subgrid-scale vegetation patchiness on sediment transport.

2.1 Introduction

Vegetation is often present in rivers and on floodplains, altering the velocity and turbulence intensity, which in turn alters sediment transport and bed morphology (e.g., Bywater-Reyes et al., 2018; Rominger et al., 2010; Sukhodolov & Sukhodolova, 2010; Yang & Nepf, 2019). Some channel restoration projects use vegetation to stabilize banks and floodplains (Surian et al., 2015; Tal & Paola, 2010), but to do so effectively, it is crucial to understand how vegetation impacts sediment transport (e.g., Larsen & Harvey,

* This chapter is part of the following published article:
Shan, Y., Zhao, T., Liu, C., & Nepf, H. (2020). Turbulence and Bed Load Transport in Channels With Randomly Distributed Emergent Patches of Model Vegetation. *Geophysical Research Letters*, 47(12), e2020GL087055. doi:10.1029/2020GL087055

2010; Reed et al., 1999). While vegetation can reduce local velocity, which promotes sediment retention, recent studies have highlighted how vegetation-generated turbulence may also enhance resuspension and sediment transport (Tinoco & Coco, 2016, 2018; Yager & Schmeeckle, 2013; Yang et al., 2016; Yang & Nepf, 2018). Further, when vegetation-generated turbulence is present, sediment transport models based on bed shear stress, τ, do not provide good estimates of sediment transport (Yager & Schmeeckle, 2013; Yang & Nepf, 2018). Recent studies have suggested that near-bed turbulence, k_t, may be a better predictor of sediment transport. For example, the initiation of both bed load and suspended load transport in vegetated channels can be better described by a threshold value of k_t than of τ (Tang et al., 2019; Tinoco & Coco, 2018; Yang et al., 2016).

The turbulent kinetic energy per fluid mass, k_t, includes bed-generated turbulence, $k_{\mathrm{t,b}}$, and vegetation-generated turbulence, $k_{\mathrm{t,v}}$. Bed-generated turbulence is correlated with the bed shear stress, $\tau = \rho C_\mathrm{f} U^2$, with fluid density, ρ, velocity, U, and bed drag coefficient, C_f (e.g., Biron et al. 2004). Specifically, $k_{\mathrm{t,b}} = \tau/\omega$, with scale factor $\omega = 0.20 \pm 0.01$ (Soulsby, 1981). The vegetation-generated turbulence, $k_{\mathrm{t,v}}$, can be estimated from $k_\mathrm{t} = \gamma^2 \left[\left(C_{\mathrm{D,form}} \frac{\phi}{1-\phi} \frac{2}{\pi}\right)^{2/3} U^2\right]$ (Tanino & Nepf, 2008a), in which γ is an empirical coefficient and ϕ is the solid volume fraction of the vegetation. Yang et al. (2016) and Yang and Nepf (2019) combined these two models to predict the total turbulence, k_t, in a channel with emergent vegetation:

$$k_\mathrm{t} = \underbrace{\frac{C_\mathrm{f} U^2}{\omega}}_{k_{\mathrm{t,b}}} + \underbrace{\gamma^2 \left[\left(C_{\mathrm{D,form}} \frac{\phi}{1-\phi} \frac{2}{\pi}\right)^{2/3} U^2\right]}_{k_{\mathrm{t,v}}}. \tag{2.1}$$

Because only form drag contributes to turbulence generation, Equation 2.1 uses a form drag coefficient, $C_{\mathrm{D,form}} = 2[(0.46 \pm 0.11) + (3.8 \pm 0.5)\,\phi]$, described for random arrays in Equation (2.10) in Tanino and Nepf (2008a). The second term in Equation 2.1 is only valid when the stem wakes are turbulent, that is, $Re_\mathrm{d} = Ud/\nu > 120$, with stem diameter d and kinematic viscosity ν (Liu & Nepf, 2016). Finally, Equation 2.1 is valid for stem spacing greater than the stem diameter (Tanino & Nepf, 2008a).

The Einstein-Brown equation, based on measurements in a bare channel, provides an empirical description of bedload transport as a function of bed shear stress (Brown, 1950; Einstein, 1950). Yang and Nepf (2018) suggested that this relationship could be converted to a k_t-based model (Equation 2.2 below) using the expression provided above ($k_{t,b} = \tau/\omega$). They verified that bedload transport rate per channel width, q_s, could be predicted from near-bed turbulence in both vegetated and bare channels. Specifically, the nondimensional bedload transport, q_s^* ($= \frac{q_s}{\rho_s\sqrt{(\rho_s/\rho-1)g{d_s}^3}}$, in which ρ_s is the sediment density, d_s is the sediment diameter, and g is the acceleration of gravity), can be predicted from the non-dimensional turbulence, k_t^* ($= \frac{k_t}{(\rho_s/\rho-1)gd_s}$):

$$q_s^* = \begin{cases} 2.15e^{\beta/k_t^*}, & k_t^* < 0.95 \\ 0.27{k_t^*}^3, & 0.95 < k_t^* < 2.74 \end{cases} \quad (2.2)$$

in which β = -2.06 is the original scale factor in the Einstein-Brown equation adapted by Yang and Nepf (2018) (see also Julien, 2010). Yang and Nepf (2018, 2019) validated the turbulence (Equation 2.1) and bedload transport (Equation 2.2) models using experiments with model vegetation consisting of staggered arrays of circular cylinders distributed uniformly across the channel width, for which the velocity averaged over distances greater than the stem spacing was uniform over the channel width (see Figures 4 and 5 in Yang & Nepf, 2019). However, in nature, vegetation often exists in individual patches of limited width and length. For example, the patch size in rivers has been observed to fall between 0.5 and 5 m, smaller than the channel width (e.g., Cornacchia et al., 2018; Sand-Jensen & Pedersen, 2008; Schoelynck et al., 2012). The horizontal distribution of patches is constrained by feedbacks between hydrodynamic, morphologic, and biologic processes, which often results in patches of vegetation within which velocity is lower separated by unvegetated regions in which the velocity is higher (e.g., Montgomery et al., 2018; Temmerman et al., 2007). The present study sought to understand how the patchy distribution of vegetation within a channel would influence bed load transport. A model was proposed to predict the spatial mean turbulence. The new turbulence model was combined with Equation 2.2 to predict bedload transport.

2.2 Theory: Turbulence in a Channel with Patchy Vegetation

In this study, a heterogeneous distribution of vegetation will be represented by an idealized configuration of circular patches with bare channel between them. Consider M circular patches of vegetation, each of diameter D (grey circles in Figure 2-1) that are randomly distributed in an L-m long and B-m wide section of channel. The fraction of bed occupied by patches is $\phi_{\mathrm{p}} = \frac{\pi}{4}\frac{MD^2}{LB}$. It is used to describe the weighted average contribution of the patches to channel-averaged velocity and turbulence (see Equations 2.3, 2.6, and 2.7 below).Within each patch, the vegetation is represented by a random distribution of cylindrical stems with diameter d and stem density m (stems / bed area), such that the solid volume fraction within the patch is $\phi = \frac{\pi}{4}md^2$, which is used to describe the in-patch turbulence generation (see Equation 2.7 below). The channel-averaged solid volume fraction is $\phi_c = \frac{\pi}{4}\frac{n_{\mathrm{total}}}{LB}d^2$, with n_{total} the total number of stems in the section $L \times B$.

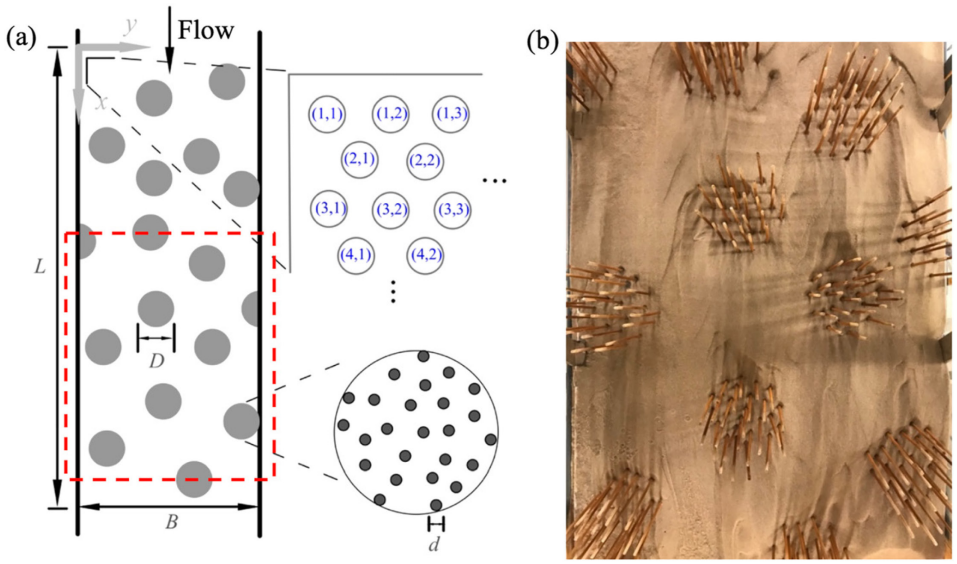

Figure 2-1. (a) Randomly distributed model vegetation patches in an L-m-long and B-m-wide channel section. Gray circles indicate patches within which cylinders were randomly distributed. The white area indicates bare sand bed. The individual cylinders were inserted into predrilled holes in the baseboard. The staggered array of holes was labeled with a coordinate system (c_x,c_y), a portion of which is shown in the inset above. Within the test section, c_x = 1 to 190 and c_y = 1 to 80. (b) Patch Case 2.4, in which each patch had a diameter D = 20 cm and contained 25 dowels. The photo shows the area denoted by a red dashed box in subplot (a), in which full and half patches were included.

A channel with patches of vegetation may have three sources of turbulence: bed shear, stem wake, and patch wake. The generation of turbulence within individual stem wakes has been observed for both vegetation mimics (rigid cylinders, Nepf & Vivoni, 2000; Poggi et al., 2004; Tanino & Nepf, 2008a) and real vegetation (King et al., 2012), and it occurs when the stem Reynolds number, $Re_d(=\frac{Ud}{\upsilon})$, > 120 (Liu & Nepf, 2016). Patch-scale vortices can form in the wake of a porous patch when ϕ > 0.05. Because the porosity of the patch allows bleed flow into the wake, the patch-scale vortices appear five to ten diameters downstream from the patch (Nicolle & Eames, 2011; Zong & Nepf, 2012). The present study considered a distribution of patches spaced at distances of no more than six patch diameters, in which case the flow was redirected by neighboring patches before the patch wake developed vortices, so that patch-scale turbulence was not generated. This was confirmed by flow visualization, which is described and illustrated in Figure A1-1 in the Appendices. For this reason, patch-scale turbulence will be not considered here. The channel-averaged turbulent kinetic energy, $\langle k_t \rangle$, is defined as the area-weighted average of the turbulence generated in the bare channel and within the patches. The brackets denote the spatial average.

Because the vegetation contributes to flow resistance, the average velocity within a patch, U_p, is smaller than the spatially averaged velocity in the bare channel, U_b. These velocities are related to the channel-averaged velocity, U_o, by the conservation of mass:

$$U_o = U_b(1 - \phi_p) + U_p\phi_p. \tag{2.3}$$

U_p is defined as the average of the velocity entering, assumed to be U_b, and exiting, U_e, each patch; that is,

$$U_p = (U_b + U_e)/2 \tag{2.4}$$

The velocity exiting the patch, U_e, is estimated from Equation (5) in Chen et al. (2012), which describes the velocity exiting an individual patch:

$$\frac{U_e}{U_b} = 1 - \mu\frac{D}{L_p}, \tag{2.5}$$

in which $\mu = 0.42 \pm 0.03$. $L_\mathrm{p} = \left[\left(\frac{2(1-\phi)}{C_\mathrm{D} a}\right)^2 + \left(\frac{D}{2}\right)^2\right]^{1/2}$ is the flow adjustment length scale within the patch (Rominger & Nepf, 2011), and a (= md) is the frontal area per volume inside the patch, and C_D is the drag coefficient, which is a function of ϕ and $Re_{\mathrm{d,p}} = U_\mathrm{p} d/\upsilon$, as described for random cylinder distributions in Tanino and Nepf (2008b). Since U_p is required for $Re_{\mathrm{d,p}}$, an iterative solution of Equations 2.3-2.5 is needed. Starting from C_D = 1, L_p was estimated and used to obtain U_e from Equation 2.5, which in turn was used in Equation 2.4 to estimate U_p. Next, $Re_{\mathrm{d,p}}$ and ϕ were used to estimate a new C_D (Tanino & Nepf, 2008b). The iteration was repeated until consecutive estimates of C_D differed by less than 5%.

The bed-generated turbulence in Equation 2.1 is modified to be a weighted average of the bare and patch regions, with ϕ_p defining the area occupied by vegetation. The channel-averaged bed-generated turbulence is then

$$\langle k_{\mathrm{t,b}} \rangle = \underbrace{\frac{C_\mathrm{f}}{\omega} U_\mathrm{b}^2 \left(1 - \phi_\mathrm{p}\right)}_{\text{bare channel}} + \underbrace{\frac{C_\mathrm{f}}{\omega} U_\mathrm{p}^2 \phi_\mathrm{p}}_{\text{inside patches}} \tag{2.6}$$

The stem turbulence is described by the second term in Equation 2.1 using the patch velocity, U_p. The stem contribution to the channel average is then

$$\langle k_{\mathrm{t,v}} \rangle = \gamma^2 \left[\left(C_{\mathrm{D,form}} \frac{\phi}{1-\phi} \frac{2}{\pi}\right)^{2/3} U_\mathrm{p}^2\right] \phi_\mathrm{p} \tag{2.7}$$

Finally, the channel-averaged turbulent kinetic energy, $\langle k_\mathrm{t} \rangle$, is the sum of Equations 2.6 and 2.7.

2.3 Experimental Methods

Experiments were designed to explore how the vegetation patchiness impacts bedload transport and to test the models for channel-averaged turbulence (Equations 2.6 and 2.7) and bedload transport (Equation 2.2). Vegetation clustering was increased by distributing the same number of stems into patches of smaller patch diameter, D, which resulted in a smaller value of ϕ_p, the fraction of bed covered by vegetation patches. That is, a higher clustering corresponded to a smaller patch diameter. The experiments were performed in a 10-m-long and 1-m-wide flume with a horizontal bed, which recirculated water and sediment through separate pipes. The flow depth was H = 12.0 ± 0.4 cm, and the channel-averaged velocity was U_o = 30.0 ± 0.5 cm/s. The Reynolds number Re (= $U_o R/v$, with the hydraulic radius R) was 29,000, and the Froude number, Fr (= $U_o/\sqrt{gH}$), = 0.3 < 1, indicating that the flow was turbulent and subcritical.

The model vegetation consisted of circular cylinders arranged in randomly distributed patches (Figure 2-1) or in a uniform random distribution that covered the entire test section (Figure A1-2). The cylinders do not represent a specific macrophyte but resemble the morphology of a reed, the base of a tree, or a mangrove root (e.g., Lightbody & Nepf, 2006; Liu et al., 2018; Shan et al., 2019; Tinoco & Coco, 2016; Zhang et al., 2018). The cylinder diameter, d = 0.6 cm, was chosen based on the range of scales found in reeds, and young plants on floodplains, d = 0.2 to 1.2 cm (e.g. Lightbody & Nepf, 2006; Manners et al., 2015). The cylinders extended through the water depth, modeling emergent vegetation. The channel-averaged solid volume fraction, ϕ_c = 0.005, 0.015, and 0.02, were chosen based on the observed range on a reed bed, ϕ_c = 0.001 to 0.04 (Coon et al., 2000; Grace & Harrison, 1986). The control case (Case 1.1) was with a bare bed, that is, no cylinders.

In each case with patches, M = 16 circular patches were randomly distributed within the test section (2.4 m × 1 m, Figure 1a). The patch diameter, D, was varied from 6.5 to 30 cm, resulting in patch area fractions ϕ_p = 0.01 to 0.24. The length of the test section was limited by the position of the sediment return. Because the flow adjusts to (deflects around) each patch, a fully developed flow was not present in the test section.

Predrilled holes in the baseboards were used to determine the patch positions. The streamwise, lateral, and vertical directions were denoted as x, y, and z, respectively, with the origin at the right sidewall at the leading edge of the test section. The test section had c_x = 1 to 190 holes in the x direction and c_y = 1 to 80 holes in the y direction. The hole closest to the origin was $(c_x, c_y) = (1, 1)$, as shown in Figure 2-1a. The center position (hole) of each patch was determined using the MATLAB random number generator. To avoid overlapping patches, a minimum distance of D was allowed between the centers of any two patches. Half patches were constructed if the distance between the patch center and the side wall was less than $D/2$. Patch distributions for Cases 2.1 to 4.3 (Table 2.1) are shown in Figures A1-3 to A1-5. For the uniform random array, the position of each cylinder was randomly selected.

A 5-cm thick layer of sand was placed on top of the baseboards and manually flattened. The mean sand grain diameter was d_s= 0.5 mm, and the sand density was ρ_s = 2.65 g/cm^3. The sediment transport rate was measured by using a T-valve to divert sediment from the sand recirculation pipe into a mesh bag for a measured collection time. The mesh bag was hung to drain and shook to remove excess water. The sand was then placed into a container with 5 L of water, and the displacement of water provided a measure of the sediment volume (V) and mass ($\rho_s V$). The transport rate per unit channel width, q_s (g m^{-1} s^{-1}), was calculated as the collected sand mass divided by the collection time and the width of the channel. Four replicate measurements were used to estimate the mean q_s and standard error, σ_{q_s}. This was repeated every 3 hr until the measured q_s ($\pm\sigma_{q_s}$) was the same as the previous, indicating that the bedload transport had reached equilibrium, which required 14 to 30 hours of running time.

After transport equilibrium was achieved, a Nortek Vectrino with a side-looking probe was used to measure the instantaneous velocities $u(t), v(t)$ and $w(t)$, corresponding to the (x, y, z) directions, respectively, along lateral transects with a 5-cm interval between measurements. The velocity was measured at mid-depth (z = 6 cm). Vertical profiles confirmed that measurements at mid-depth provided representative values of depth-averaged velocity (see Figure A1-6a). Further, the mid-depth turbulence was similar to the near-bed turbulence (see Figure A1-6b). Specifically, the ratio of near-

bed to mid-depth turbulence was 1.1 ± 0.3, indicating bedforms did not contribute significantly to turbulence. MATLAB code was used to extract time-averaged ($\bar{u}$, $\bar{v}$ and $\bar{w}$) and fluctuating (u', v' and w') velocities. The turbulent kinetic energy was defined as $k_\mathrm{t} = 0.5\left(\overline{u'^2} + \overline{v'^2} + \overline{w'^2}\right)$. The noise in the velocity and turbulence measurements was 0.1 cm/s and 0.15 cm^2/s^2, respectively, determined from measurements in still water. For each condition, a lateral profile of velocities was measured at two streamwise positions. The channel-averaged turbulent kinetic energy was determined as the average over both transects, which was denoted as $\langle k_\mathrm{t} \rangle$. A channel-averaged $\langle k_\mathrm{t} \rangle$ based on eight transects differed by only 6% from one based on two transects, confirming that two transects were sufficient (Figure A1-7b). The maximum value of turbulent kinetic energy within the two transects was denoted $k_{\mathrm{t,max}}$. For patchy cases, transects of time mean velocity and turbulent kinetic energy are summarized in Table A1-1.

Table 2.1: Summary of Experimental Parameters

Case pattern	Case	D (m)	m (m^{-2})	n_{total}	n_{patch}	ϕ_c	ϕ_p	ϕ	U_b (cm/s)	U_p (cm/s)	$q_s \pm \sigma_{q_s}$ (g m^{-1} s^{-1})	$\langle k_t \rangle \pm \sigma_{k_t}$ (cm^2/s^2)	$k_{t,max}$ (cm^2/s^2)
Bare channel	1.1	-	-	0	0	0	-	-	30.0	30.0	0.20 ± 0.04	14 ± 1	-
Patches	2.1a	0.065	7,538	400	25	0.005	0.02	0.24	30.3	17.9	1.0 ± 0.3	23 ± 3	54
	2.2a	0.1	3,185	400	25	0.005	0.05	0.10	30.5	21.3	1.2 ± 0.3	21 ± 2	35
	2.3	0.15	1,415	400	25	0.005	0.12	0.05	30.7	24.8	1.9 ± 0.5	23 ± 3	97
	2.4a	0.2	796	400	25	0.005	0.21	0.03	31.0	26.5	1.6 ± 0.3	26 ± 4	92
	2.5a	0.3	354	400	25	0.005	0.47	0.01	32.1	27.9	2.5 ± 0.3	39 ± 5	96
	3.1	0.15	4,246	1,200	75	0.015	0.12	0.14	31.6	18.4	3.7 ± 1.0	25 ± 3	92
	3.2	0.2	2,389	1,200	75	0.015	0.21	0.08	32.7	20.2	5.2 ± 0.5	25 ± 3	81
	3.3	0.3	1,061	1,200	75	0.015	0.47	0.03	36.2	23.3	6.5 ± 0.4	32 ± 3	61
	4.1	0.2	3,185	1,600	100	0.02	0.21	0.10	33.0	18.8	4.6 ± 0.8	26 ± 3	85
	4.2	0.25	2,038	1,600	100	0.02	0.33	0.07	34.9	20.2	7.0 ± 0.6	30 ± 5	160
	4.3	0.3	1,415	1,600	100	0.02	0.47	0.05	37.8	21.6	9.8 ± 1.0	32 ± 3	86
Uniform random distribution	5.1	-	-	400	-	0.005	1	-	30.2	30.2	2.8 ± 0.6	25 ± 5	126
	5.2	-	-	1,200	-	0.015	1	-	30.5	30.5	8.4 ± 0.5	43 ± 3	62
	5.3	-	-	1,600	-	0.02	1	-	30.6	30.6	13 ± 1	48 ± 4	126

Note: D is the patch diameter; m is the cylinder density in the patch; n_{total} is the total number of cylinders in the test section; n_{patch} is the number of cylinders per patch; ϕ_c ($= \frac{\pi}{4}\frac{n_{total}}{LB}d^2$) is the channel-averaged solid volume fraction, with bed area LB and cylinder diameter d; ϕ_p ($= \frac{\pi}{4}\frac{MD^2}{LB}$) is the patch area fraction, with n = 6.67 m^{-2} the number of patches per unit bed area; $\phi (= \frac{\pi}{4}md^2)$ is the solid volume fraction inside the patch; U_b and U_p are the spatial mean velocities in the bare channel and in a patch, respectively, using Equations 2.3-2.5. q_s is the sediment transport rate per channel width. $\langle k_t \rangle$ and $k_{t,max}$ are the mean and maximum turbulent kinetic energy measured over two transects, respectively.

[a]Cases for which two realizations were performed with different patch distributions. For each patch case, sixteen circular patches were constructed in the test section.

2.4 Results and Discussion

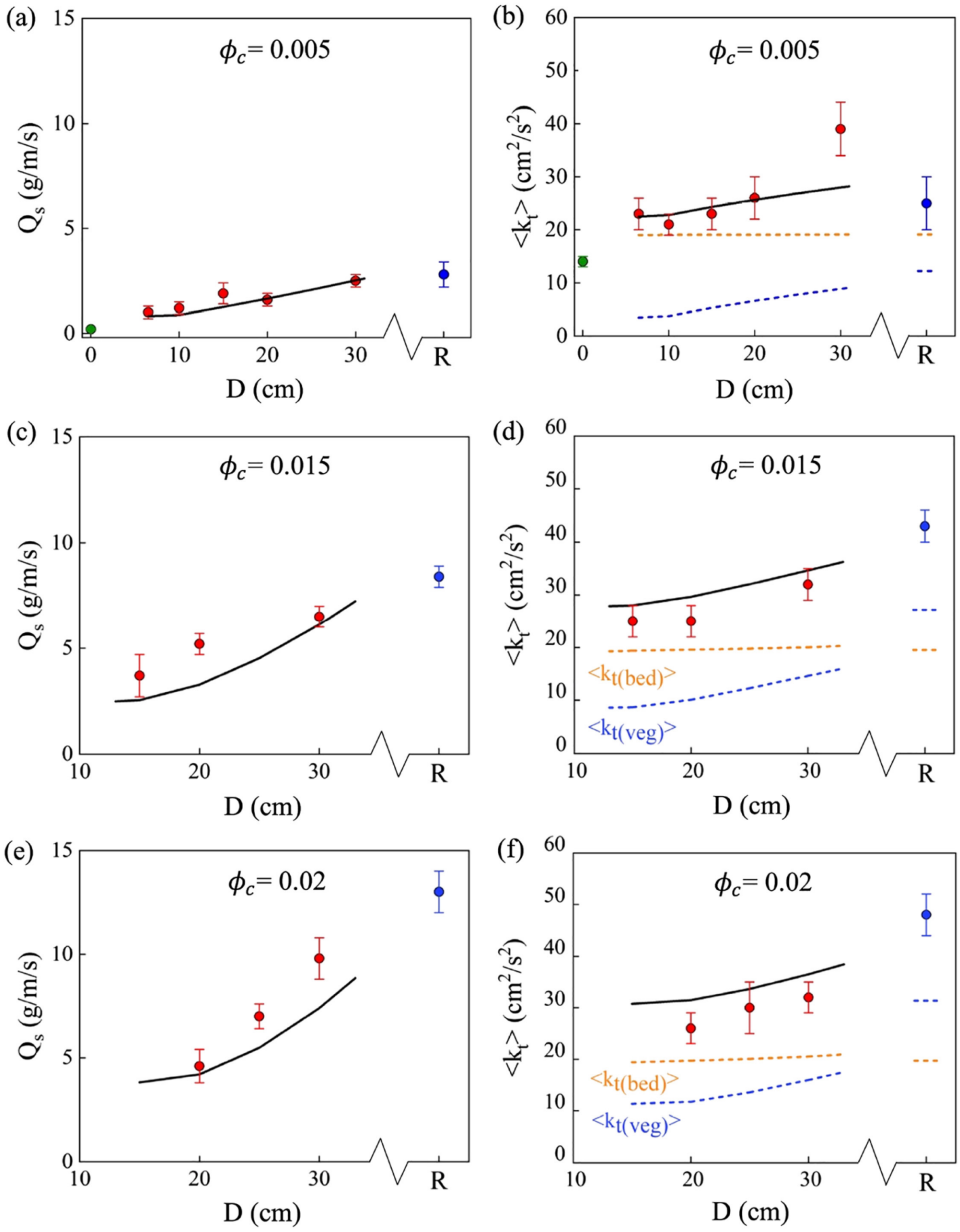

Figure 2-2. (a, c, and e) Measured (red symbols) and predicted (solid curve, Equations 2.2, 2.6, and 2.7) bedload transport, q_s, as a function of patch diameter, D. (b, d, and f) Measured (red symbols) and predicted (Equations 2.6, and 2.7) channel-averaged turbulent kinetic energy, $\langle k_t \rangle$. $\langle k_{t,b} \rangle$ is predicted from Equation 2.6 using $C_f = 0.004$, U_b, U_p, and ϕ_p (orange dashed line), and $\langle k_{t,v} \rangle$ is predicted from Equation 2.7 using $\gamma = 0.8$, ϕ, U_p, and ϕ_p (blue dashed lines). All parameters are summarized in Table 2.1. The blue symbols above the axis label "R" indicate uniform random distributions ($\phi_p = 1$). The red symbols indicate randomly distributed patches. The green symbols in (a) and (b) indicate the bare channel case. Channel-averaged solid volume fractions are (a, b) $\phi_c = 0.005$, (c, d) $\phi_c = 0.015$, and (e, f) $\phi_c = 0.02$.

The channel-averaged turbulent kinetic energy predicted from Equations 2.6 and 2.7 was compared to the measured values (Figure 2-2a). The bed drag coefficient was C_f = 0.004 ± 0.001, based on $C_f = [5.75 \log (2H/d_s)]^{-2}$ from Julien (2010). The scale coefficient ω = 0.22 ± 0.01 was determined from the bare bed condition (green dot in Figure A1-8a), which was consistent with previous estimates (0.20 ± 0.01 in Soulsby, 1981). For cases with patches, the scale constant γ = 0.8 ± 0.4 (95% CI) was determined using a least squares fit of predicted $\langle k_t \rangle$ to measured values from all cases in Table 2.1. This value was consistent with previous measurements in uniform random arrays (γ = 1.1, Tanino & Nepf, 2008a). Note that Yang and Nepf (2019) fit a slightly smaller value (γ = 0.6) to measurements of turbulence in uniform staggered arrays, suggesting that staggered arrays produce slightly less turbulence, possibly due to the influence of upstream, in-line wakes.

The predicted turbulent kinetic energy was used to predict the sediment transport rate using Equation 2.2, which was then fit to the measured sediment transport rate (Table 2.1) with β = -1.6 ± 0.3 (Figure A1-8). The combined prediction of $\langle k_t \rangle$ (Equations 2.6 and 2.7) and q_s (Equation 2.2) worked across all cases with randomly arranged cylinders (this study, Figure A1-8b) and for most cases with staggered cylinders from Yang and Nepf (2019, diamonds in Figure A1-8b) with similar flow depth h (=10 to 12 cm), channel velocity U_o (= 21 to 43 cm/s), and sediment size (0.5 mm) to this study. An overprediction in staggered arrays was noted at low values of sediment transport. This is likely due to the fact that the turbulence model used here (with γ = 0.8) over predicted the turbulence in the staggered array (with γ = 0.6), and the overprediction of $\langle k_t \rangle$ contributed to an overprediction of q_s.

For each channel-averaged stem density (ϕ_c), the bedload transport was highest for the uniform, random distribution (blue dots in Figure 2-2) and decreased as patches were formed and decreased in size (Figures 2-2a, 2-2c, and 2-2e). The sediment transport rate was highest and the impact of clustering (decreasing patch size) was greatest for the highest channel-averaged stem density (ϕ_c = 0.02, Figure 2e). The trends in q_s were generally consistent with the trends in measured turbulence. Specifically, for ϕ_c = 0.015 and 0.02, the peak turbulence was associated with the uniform random distribution and

turbulence level decreased as patches formed and decreased in size. The smallest bedload transport rate and turbulence level were observed in the bare channel (green points in Figures 2-2a and 2-2b).

By describing the relative contributions of bed- and vegetation- generated turbulence, Equations 2.6 and 2.7 provided insight into the changes in bedload transport associated with changes in the total number of stems and patch size. Specifically, the trends in turbulence, and by association in sediment transport, were due mostly to changes in vegetation-generated turbulence. As the stem distribution changed, the bed-generated turbulence ($\langle k_{t,b} \rangle$, orange dashed lines in Figure 2-2) had almost no change (less than 5%), whereas the vegetation-generated turbulence ($\langle k_{t,v} \rangle$, blue dashed lines in Figure 2-2) approximately tripled between the smallest patch size (smallest ϕ_p) and the uniform random distribution. The relative contributions of bed- and vegetation- generated turbulence also depended on the total amount of vegetation present. For example, for the randomly distributed stems at the smallest channel-averaged stem density (ϕ_c = 0.005), the vegetation-generated turbulence was smaller than the bed-generated turbulence (Figure 2-2b). Because of this, clustering the vegetation into patches did not have a significant impact on channel-averaged turbulence (Figure 2-2b) or bedload transport (Figure 2-2a). In contrast, for the higher stem densities (ϕ_c = 0.015 and 0.02), vegetation-generated turbulence exceeded bed-generated turbulence in the random distribution, so that when clustering was introduced, the drop in vegetation-generated turbulence had a significant impact on channel-averaged turbulence (Figure 2-2d and 2-2f) and bedload transport (Figures 2-2c and 2-2e). The clustering of vegetation into patches decreased the velocity impacting individual stems, which decreased the stem-generated turbulence (Equation 2.7). Specifically, as the patches became more clustered (smaller D and higher ϕ), the velocity within the patch, U_p, declined (Table 2.1). The decrease in U_p could be more pronounced if the patch was placed directly in the wake of the upstream patch (e.g., Ghani et al., 2019). In addition, as clustering increased (decreasing D), a smaller fraction of bed area contained patches (smaller ϕ_p). These two trends led to a decline in $\langle k_{t,v} \rangle$.

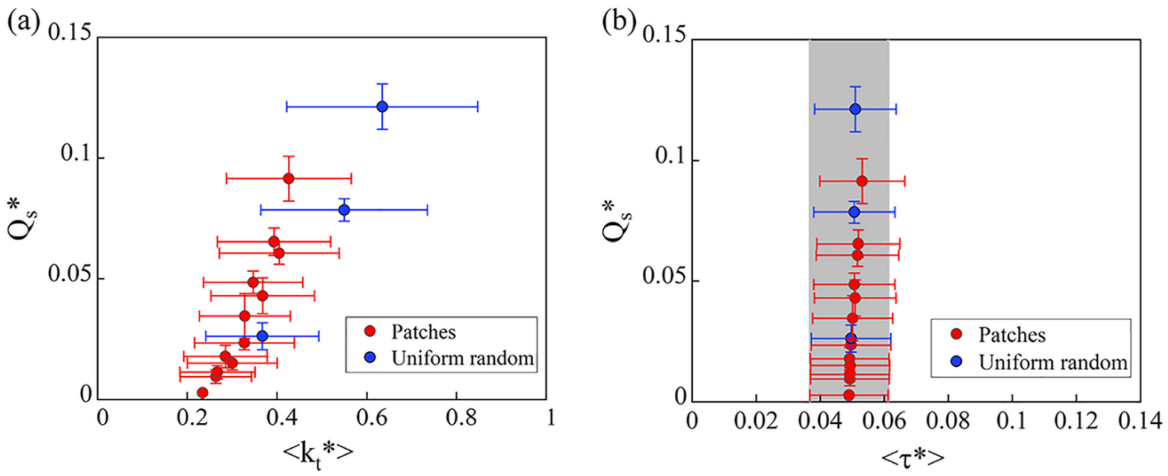

Figure 2-3. Measured sediment transport rate, $q_s^* = \frac{q_s}{\rho_s\sqrt{(\rho_s/\rho-1)g{d_s}^3}}$, versus (a) channel-averaged turbulent kinetic energy, $\langle k_t^* \rangle = \frac{\langle k_t \rangle}{(\rho_s/\rho-1)gd_s}$, from Equations 2.6 and 2.7, and versus (b) channel-averaged bed shear stress, $\langle \tau^* \rangle = \frac{\langle \tau \rangle}{(\rho_s/\rho-1)gd_s}$, with $\langle \tau \rangle = C_f U_b^2(1-\phi_p) + C_f U_p^2 \phi_p$. The vertical gray bar denotes $\langle \tau \rangle = C_f U_o^2$ with bar width indicating the uncertainty due to the propagated uncertainty of C_f and U_o. Patch cases are shown with red circles, and uniform random distributions are shown with blue circles.

The variation in measured bedload transport, q_s, exhibited a dependence on channel-averaged turbulence, but no dependence on channel-averaged bed-shear stress, which was estimated as $\langle \tau \rangle = C_f U_b^2(1-\phi_p) + C_f U_p^2 \phi_p$ (Figure 2-3). The bedload transport increased with increasing $\langle k_t \rangle$, but had no clear dependence on $\langle \tau \rangle$. Specifically, across the range of patch conditions, the bed shear stress was unchanged within uncertainty, yet the bedload transport exhibited a more than tenfold change (Figure 2-3b and Table 2.1). Further, the bedload transport had little dependence on peak turbulence, $k_{t,max}$, because $k_{t,max}$ did not vary consistently with the spatial average $\langle k_t \rangle$. Specifically, $k_{t,max}/\langle k_t \rangle$ exhibited a wide range of value (between 1.4 and 5.4) that did not vary systematically with either the channel-scale vegetation density, ϕ_c, or the fraction of channel occupied by vegetation patches, ϕ_p (see Figure A1-9). In order to impact the channel-averaged sediment transport directly, $k_{t,max}$ would need to occur over a spacing smaller than or equal to the individual sediment excursions. It appears that this condition was not met in our study.

The results above may be applied to hydrodynamic and morphodynamic models, which is further discussed in Shan et al. (2020).

2.5 Summary

This study measured sediment transport in a channel with model vegetation and considered both uniform random distributions of individual stems and heterogeneous distributions with stems clustered into patches separated by bare bed. For the same channel velocity, the highest turbulence and bed load transport was observed with the uniform random distribution, and both turbulence and bed load transport decreased as stems were clustered into progressively smaller patch diameters, associated with a smaller fraction of bed area occupied by stems (smaller ϕ_p). For both uniform and clustered distributions of model vegetation the channel-averaged turbulence was shown to be a better predictor for sediment transport than channel-averaged bed shear stress. A model was developed to predict the channel-averaged turbulence and sediment transport as a function of channel-averaged vegetation density (ϕ_c) and degree of clustering, represented by vegetation patch area fraction (ϕ_p). This provides a way for numerical modelers to represent the impact of subgrid-scale heterogeneity in vegetation distribution on sediment transport.

Chapter 2 References

Brown, C. (1950). Sediment transportation. Engineering Hydraulics, 12, 769–857.

Biron, P., Robson, C. Lapointe, M., and Gaskin, S. (2004). Comparing different methods of bed shear stress estimates in simple and complex flow fields, Earth Surf. Processes Landforms, 29(11), 1403–1415. https://doi.org/10.1002/esp.1111

Bywater-Reyes, S., Diehl, R., and Wilcox, A. (2018). The influence of a vegetated bar on channel-bend flow dynamics. Earth Surface Dynamics, 6(2), 487-503. https://doi.org/10.5194/esurf-6-487-2018

Cornacchia, L., Van De Koppel, J., Van Der Wal, D., Wharton, G., Puijalon, S., Bouma, T.J., (2018). Landscapes of facilitation: how self-organized patchiness of aquatic macrophytes promotes diversity in streams. Ecology 99 (4), 832–847. https://doi. org/10.1002/ecy.2177.

Chen, D., and Jirka, G. (1995). Experimental study of plane turbulent wakes in a shallow water layer. Fluid dynamics research, 16(1), 11-41.

Chen, Z., Ortiz, A., Zong, L., and Nepf, H. (2012). The wake structure behind a porous obstruction and its implications for deposition near a finite patch of emergent vegetation. Water Resources Research, 48(9), W09517. https://doi.org/10.1029/2012WR012224.

Coon, W., Bernard, J., Seischab, F. (2000). Effects of a Cattail Wetland on Water Quality of Irondequoit Creek near Rochester, New York (No. 2000-4032). US Geological Survey.

Diplas, P., Dancey, C., Celik, A., Valyrakis, M., Greer, K., and Akar, T. (2008). The role of impulse on the initiation of particle movement underturbulent flow conditions. Science, 322(5902), 717–720.

Einstein, H. (1950). The bed-load function for sediment transportation in open channel flows (Technical Bulletin No 1026). Washington, DC: US Department of Agriculture.

Grace, J., and Harrison, J. (1986). The biology of Canadian weeds, Typha latifolia L., Typha angustifolia, L., and Typha xglauca Godr., Canadian Journal of Plant Science, 66, 361-37, https://doi.org/10.4141/cjps86-051

Julien, P. (2010). Erosion and Sedimentation, 2nd edition, Cambridge University Press [p198]

Larsen, L., and Harvey, J. (2010). How vegetation and sediment transport feedbacks drive landscape change in the Everglades and wetlands worldwide. The American Naturalist, 176(3), E66-E79.

Liu, C, Nepf, H. (2016). Sediment deposition within and around a finite patch of model vegetation over a range of channel velocity. Water Res. Res., 2016, 52(1): 600-612. https://doi.org/10.1002/2015WR018249.

Liu, C, Hu, Z., Lei, J., Nepf, H. (2018). Vortex structure and sediment deposition in the wake behind a finite patch of model submerged vegetation. J. Hydr. Eng., 144(2), 04017065. https://doi.org/10.1061/(ASCE)HY.1943-7900.0001408.

Lightbody, A., and Nepf H. (2006). Prediction of velocity profiles and longitudinal dispersion in emergent salt marsh vegetation, Limnol. Oceanogr., 51(1), 218–228. https://doi.org/10.4319/lo.2006.51.1.0218.

Manners, R., Wilcox, A., Kui, L., Lightbody, A., Stella, J., and Sklar, L. (2015). When do plants modify fluvial processes? Plant-hydraulic interactions under variable flow and sediment supply rates, JGR - Earth Surf., 120, 325–345, doi:10.1002/ 2014JF003265.

Reed, D., Spencer, T., Murray, A., French, J., and Leonard, L. (1999). Marsh surface sediment deposition and the role of tidal creeks: Implications for created and managed coastal marshes. J. Coastal Conservation, 5(1), 81-90. https://xs.scihub.ltd/https://doi.org/10.1007/BF02802742

Rominger, J., Lightbody, A., and Nepf, H. (2010). The effects of vegetation on sand bar stability and stream hydrodynamics. J. Hydr. Eng. 136(12):994-1002, doi:10.1061/(ASCE)HY.1943-7900.0000215

Rominger, J., Nepf, H. (2011). Flow adjustment and interior flow associated with a rectangular porous obstruction. J. Fluid Mech., 680, 636–659. https://doi.org/10.1017/jfm.2011.199.

Shan Y., Chao, L., Nepf, H. (2019). Comparison of drag and velocity in model mangrove forests with random and in-line tree distributions. J. Hydrology, 568: 735-746. https://doi.org/10.1016/j.jhydrol.2018.10.077

Sukhodolov, A., Sukhodolova, T. (2010). Case study: effect of submerged aquatic plants on turbulence structure in a lowland river. J. Hydraul. Eng. 136 (7), 434–446. https://doi.org/10.1061/(ASCE)HY.1943-7900.0000195.

Schoelynck, J., De Groote, T., Bal, K., Vandenbruwaene, W., Meire, P., and Temmerman, S. (2012). Self-organized patchiness and scale-dependent bio-geomorphic feedbacks in aquatic river vegetation. Ecography 35 (8), 760–768. https://doi.org/10.1111/j.1600-0587.2011.07177.x.

Sand-Jensen, K., Pedersen, M. (2008). Streamlining of plant patches in streams. Freshwater Biol. 53 (4), 714–726. https://doi.org/10.1111/j.1365-2427.2007. 01928.x.

Surian, N., Barban, M., Ziliani, L., Monegato, G., Bertoldi, W., and Comiti, F. (2015). Vegetation turnover in a braided river: frequency and effectiveness of floods of different magnitude. Earth Surface Processes and Landforms, 40(4), 542-558. https://doi.org/10.1002/esp.3660

Soulsby, R. (1981). Measurement of the Reynolds stress components close to a marine sand bank, Marine Geology, 42: 35-47. https://doi.org/10.1016/0025-3227(81)90157-2

Tang, C., Lei, J. and Nepf, H. (2019). The Impact of a Vegetation-generated Turbulence on the Critical Wave-velocity for Sediment Resuspension. Water Res. Res., 55, 5904–5917. https://doi.org/10.1029/2018WR024335

Tanino, Y., and Nepf, H. (2008). Lateral dispersion in random cylinder arrays at high Reynolds number. J. Fluid Mechanics, 600, 339-371. https://doi.org/10.1017/S0022112008000505

Tal, M., Paola, C. (2010). Effects of vegetation on channel morphodynamics: results and insights from laboratory experiments. Earth Surface Proc. and Land. 35: 1014–1028. https://doi.org/10.1002/esp.1908

Tinoco, R., and Coco, G. (2016). A laboratory study on sediment resuspension within arrays of rigid cylinders. Advances in Water Resources, 92, 1-9. https://doi.org/10.1016/j.advwatres.2016.04.003

Widdows, J., Pope, N., and Brinsley, M. (2008). Effect of Spartina anglica stems on near-bed hydrodynamics, sediment erodability and morphological changes on an intertidal mudflat. Marine Ecol. Prog. Ser., 362, 45-57. https://doi.org/10.3354/meps07448

Yang, J. Q., Chung, H., & Nepf, H. M. (2016). The onset of sediment transport in vegetated channels predicted by turbulent kinetic energy. Geophysical Research Letters, 43(21), 11-261. https://doi.org/10.1002/2016GL071092

Yang, J. Q., and Nepf, H. (2018). A Turbulence-Based Bed-Load Transport Model for Bare and Vegetated Channels. Geophys. Res. Letters, 45(19), 10-428. https://doi.org/10.1029/2018GL079319

Yang, J. Q., and Nepf, H. (2019). Impact of vegetation on bedload transport rate and bedform characteristics. Water Res. Res., 55, 6109–6124. https://doi.org/10.1029/2018WR024404

Yager, E., and Schmeeckle, M. (2013). The influence of vegetation on turbulence and bed load transport. JGR - Earth Surface, 118, 1585–1601. https://doi.org/10.1002/jgrf.20085

Zhang, Y., Tang, C., and Nepf, H. (2018). Turbulent kinetic energy in submerged model canopies under oscillatory flow. Water Res. Res., 54, doi.org/10.1002/2017WR021732

This page intentionally left blank

Chapter 3 Turbulence Dictates Bedload Transport in Vegetated Channels without Dependence on Stem Diameter and Arrangement[†]

Vegetation provides habitat and nature-based solutions to coastal flooding and erosion, drawing significant interest in its restoration, which requires an understanding of sediment transport and retention. Laboratory experiments examined the influence of stem diameter and arrangement on bedload sediment transport by considering arrays of different stem diameter and mixed diameters. Bedload transport rate was observed to depend on turbulent kinetic energy (TKE), with no dependence on stem diameter, which was shown to be consistent with the impulse model for sediment entrainment. Existing predictors of bedload transport for bare beds, based on bed shear stress, were recast in terms of turbulence. The new turbulence-based model predicted sediment transport measured in model canopies across a range of conditions drawn from several previous studies. A prediction of turbulence based on biomass and velocity was also described, providing an important step toward predicting turbulence and bedload transport in canopies of real vegetation morphology.

3.1 Introduction

Aquatic vegetation is a crucial part of wetland and floodplain ecosystems. It stabilizes river banks (Hackney et al., 2020), protects coasts from waves and storm surges (Barbier et al., 2011), and provides habitat for fisheries (Costanza et al., 1997). Wetlands sustain themselves partially through their ability to retain and accrete sediment. However, the influence of vegetation on water motion and sediment transport is complex. On the one hand, vegetation provides additional drag, which reduces current (Kouwen & Unny, 1973), facilitating sediment deposition (Abt et al., 1994) and increasing bed elevation. On

[†] This chapter is published as:

Zhao, T., & Nepf, H. M. (2021). Turbulence Dictates Bedload Transport in Vegetated Channels Without Dependence on Stem Diameter and Arrangement. *Geophysical Research Letters*, 48(21), e2021GL095316. doi:10.1029/2021GL095316

the other hand, vegetation generates turbulence (Tanino & Nepf, 2008; Xu & Nepf, 2020), which can enhance erosion (Niño & Garcia, 1996), alter the vertical distribution of suspended sediment (Tseng & Tinoco, 2021), and decrease bed elevation in the vicinity of vegetation (Yagci et al., 2016; Norris et al., 2021). Recent studies have proposed ways to incorporate the impacts of vegetation on bedload transport by considering the related process of scour hole formation (Wu et al., 2021), or by modifying the parameters of the Einstein (1950) probabilistic model (Armanini & Cavedon, 2019). A deeper understanding of sediment transport within aquatic ecosystems is still critical (Fagherazzi et al., 2017) to facilitate wetland protection and restoration projects (Paola et al., 2011).

3.2 Background and Theory

This study considered the impact of vegetation on bedload transport, in which sediment maintains close contact with the bed. Most previous studies of bedload (e.g., Shields, 1936; Einstein, 1942; Meyer-Peter & Müller, 1948; Engelund & Hansen, 1967) relate sediment mass transport rate, q_s, to the time-averaged bed shear stress, τ. For example, the Meyer-Peter-Müller formula (MPM, 1948) is a commonly used τ-based model:

$$q_s^* = 8(\theta - \theta_{cr})^{1.5}, \tag{3.1}$$

in which $q_s^* = \frac{q_s}{\rho_s w_s d_{50}}$ is the dimensionless sediment transport rate and $\theta = \frac{\tau}{(\rho_s - \rho) g d_{50}}$ is the dimensionless skin bed shear stress, with τ the skin bed shear stress, θ_{cr} the dimensionless critical shear stress, ρ_s the sediment density, ρ the fluid density, w_s the sediment settling velocity, g the gravitational acceleration, and d_{50} the median grain size of bed sediment.

Several studies have shown that turbulence contributes to the entrainment and mobility of individual grains (Celik et al., 2010; Shih & Diplas, 2018) as well as net sediment transport at the bed scale (Niño & Garcia, 1996; Sumer et al., 2003; Salim et al., 2017). Over a bare flat bed, the near-bed turbulent kinetic energy (TKE, k_t) is generated by bed shear and thus proportional to the bed shear stress (Soulsby, 1983), so that the impact of turbulence is implicitly embedded in the τ-based sediment transport models.

However, large roughness elements, including vegetation and bedforms, produce additional turbulence that also impacts sediment transport (Nelson et al., 1995; Yager & Schmeeckle, 2013; Yang & Nepf, 2018), but which are not captured by τ-based models. Consequently, the τ-based models significantly underestimate sediment transport in channels with obstacles (Nelson et al., 1995; Schmeeckle, 2015). Recent work has suggested that within regions of vegetation, turbulence is a better predictor than bed stress for incipient motion (Yang et al., 2016), resuspension (Tinoco & Coco, 2018; Liu et al., 2021), and bedload transport (Yang & Nepf, 2018, 2019). Therefore, we have recast the MPM formula in terms of TKE. Specifically, for the flat bare beds considered in MPM, bed stress is directly correlated with near-bed turbulence. We apply the conversion suggested by Soulsby (1983) based on flow measurements in atmospheric and marine boundary layers:

$$k_\mathrm{t} = 5.3\tau/\rho, \tag{3.2}$$

in which k_t is the near-bed TKE. Using this, we recast Equation 3.1 in terms of TKE,

$$q_s^* = 0.66\left(k_\mathrm{t}^* - k_{\mathrm{t,cr}}^*\right)^{1.5}, \tag{3.3}$$

in which $k_\mathrm{t}^* = \frac{k_\mathrm{t}}{(\rho_s/\rho-1)gd_{50}} = 5.3\,\theta$ is the dimensionless TKE. Previous studies have shown that the critical TKE for sediment entrainment, $k_{\mathrm{t,cr}}$, is the same for vegetated and unvegetated channels (Yang et al., 2016; Liu et al., 2021). Based on this, we propose that $k_{\mathrm{t,cr}}$ can be estimated from previously determined critical bed shear stress for bare bed, i.e., in dimensionless form, $k_{\mathrm{t,cr}}^* = 5.3\,\theta_{cr}$ (based on Equation 3.2).

In application, Equation 3.3 uses the spatial-averaged turbulence $\langle k_\mathrm{t}\rangle$, which can be predicted within an emergent canopy of circular stems as a combination of bed-generated ($k_{\mathrm{t,b}}$) and vegetation-generated ($k_{\mathrm{t,v}}$) turbulence (Yang & Nepf, 2019; see A2.1 in Appendices for model details). For canopy solid volume fraction (SVF) $\phi < 0.1$,

$$\langle k_\mathrm{t}\rangle = \underbrace{\frac{C_\mathrm{f}U^2}{0.19}}_{k_{\mathrm{t,b}}} + \underbrace{\delta_{k_\mathrm{t}}\left[\frac{2C_{\mathrm{D,form}}\,\phi}{\pi(1-\phi)}\right]^{\frac{2}{3}}U^2}_{k_{\mathrm{t,v}}}, \tag{3.4}$$

in which C_f is the bed drag coefficient. $C_{\mathrm{D,form}}$ is the stem form drag coefficient, and δ_{k_t} is an O(1) scale constant. Equation 3.4 is valid if the velocity U is sufficient to produce

stem turbulence, i.e. stem Reynolds number $Re_{\mathrm{d}} = \frac{Ud}{\nu} > 120$ (Liu & Nepf, 2016). A combination of Equations 3.3 and 3.4 predicts bedload based only on U and ϕ, which could be estimated from canopy biomass. The prediction has no dependence on stem diameter. This is somewhat surprising, because the stem diameter sets the scale of vegetation-generated turbulence (Tanino & Nepf, 2008; King et al., 2012), and we expect larger eddies to be more effective in mobilizing sediment. The lack of dependence on stem size needs justification and testing, which is the main point of this study.

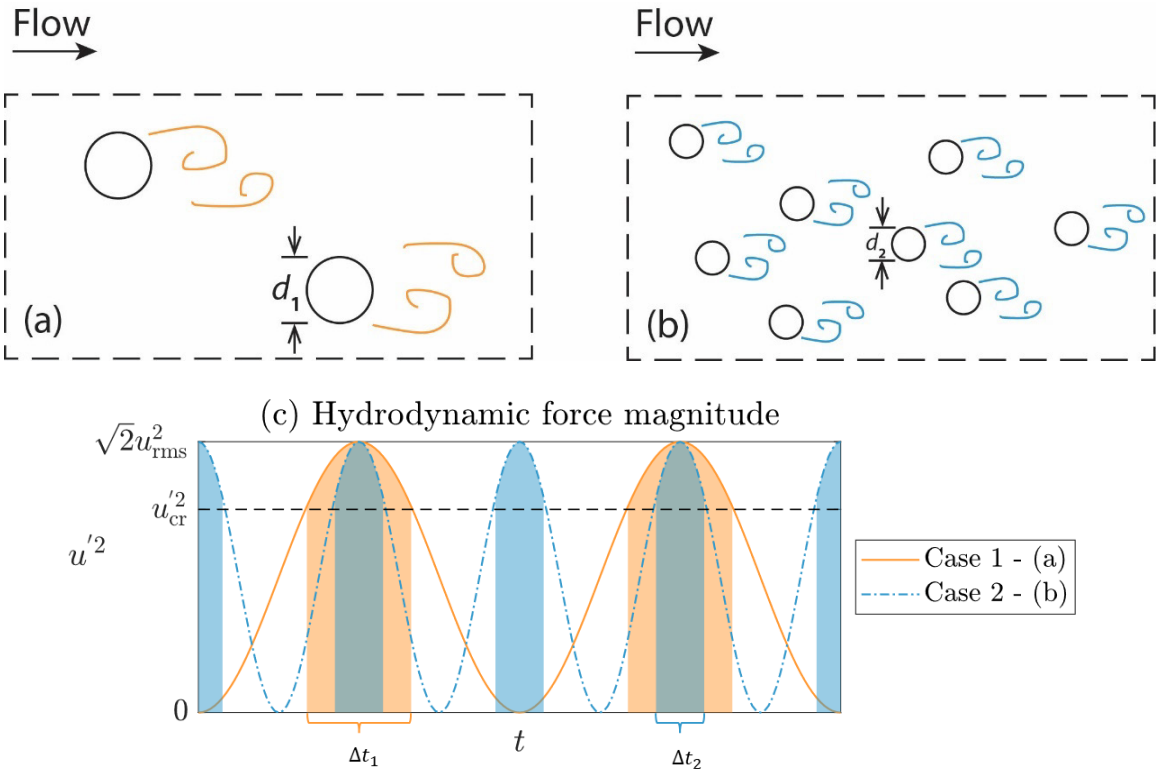

Figure 3-1. For canopies with same solid volume fraction and velocity, cumulative impulse does not depend on stem size. (a) and (b) Top view of sparse cylinder arrays with the same solid volume fraction, ϕ, but different stem diameter and eddy length scale $l_{\mathrm{e}} \sim d$. The arrays are exposed to the same velocity, and thus have the same k_{t} (Eqn. 4) and same peak hydrodynamic force $\sqrt{2}u^2_{rms} \sim k_t$. (c) Temporal variation in hydrodynamic force ($\sim u'^2$) generated by the eddies. The duration of a single turbulent event, Δt, associated with force magnitude above the threshold for incipient motion (u'^2_{cr}), is proportional to the stem diameter, d. However, the event frequency is inversely proportional to d, so that the two arrays generate the same total impulse (area of shaded region).

Bedload transport reflects the sum of individual grain dislodgement events (Niño & Garcia, 1996) and depends on the cumulative influence of hydrodynamic forces, set by

both the magnitude and duration of the lift and drag interacting with the particle, which can be characterized by impulse (Diplas et al., 2008), work (Lee et al., 2012), or stream power (Shih & Diplas, 2018). These models suggest that larger eddies, which interact with a bed particle for a longer duration, are more effective in initiating particle motion during a single event. However, the number of stems producing eddies is also important. Consider two arrays of circular stems with the same ϕ, the same sediment d_{50}, exposed to the same channel-averaged velocity, U, and flow depth, h, but consisting of different stem diameter, d (Figure 3-1). The array with larger d (Figure 3-1a) produces larger but fewer eddies, compared to the array with smaller d (Figure 3-1b). This trade-off between number (frequency) and size (duration) of turbulent interactions with the bed produces the same channel-averaged impulse in both channels, if turbulence intensity, which sets the force magnitude, is the same (Figure 3-1c). Within these constraints, we expect the same channel-averaged impulse and sediment transport rate, regardless of stem size. The present study used laboratory experiments to validate this conclusion. A more quantitative description of how the impulse model supports this conclusion is given in A2.2 and A2.3.

3.3 Methods

Laboratory experiments were conducted in a 1-m-wide and 10.4-m-long flume, with water and sediment recirculated separately. Velocity and sediment transport rate were measured for similar channel velocity and SVF, but different cylinder sizes (d = 0.64, 2.5, or 5.1 cm) and in both random and staggered emergent arrays (see A2, Table A2.2 for experimental conditions and Section A2.4 for photographs). Two randomly distributed arrays were constructed with mixed cylinder diameters (d = 1.3 and 1.9 cm, and d = 1.3, 1.9, and 5.1 cm). The random distributions were generated using the randperm() function in MATLAB to select the cylinder position. The number of cylinders per bed area were m = 0 to 775 m^{-2}, corresponding to vegetation frontal area per volume $a = md$ = 0 to 4.9 m^{-1}, and $\phi = \pi ad/4$ = 0 to 0.049. These ranges were chosen based on marsh plants, mangrove pneumatophores, and young floodplain trees (Nepf, 2012; Manners et al., 2015; Norris et al, 2017). The 3-m-long array of cylinders occupied

the entire channel width. A 9-cm layer of manually flattened sand (d_{50} = 0.6 mm, ρ_s = 2650 kg/m^3, see A2.5 for grain size distribution) was added within the array. The water depth was h = 12.0 cm above the sand layer, measured with a ruler mid-length along the array.

The sediment transport rate was measured four to six times every four hours using a butterfly valve to divert flow from the sediment recirculating pipe to a mesh bag (Figure A2-1). The collected sediment weighed at least 50 g and the duration of collection was at least 1 min, but no more than 30 min. The number of collections (4 to 6) was smaller when longer collection time was required, and a larger number was used when sediment transport showed considerable temporal variability. This was continued for up to 70 hours, until the measured sediment transport reached equilibrium, which was defined once the sediment transport rate of the last two measurement sets agreed within the standard error within each set, typically smaller than 10% of the mean value.

After the bed reached equilibrium, a Nortek Vectrino recorded instantaneous velocity components $u(t)$, $v(t)$, and $w(t)$. Spherical glass (Potters Industries Inc. 110P8, median grain size d_{50} = 10 μm) was added to enhance the backscatter signal. At each position, a 150-second record was measured at 200 Hz. The sampling duration was confirmed by a convergence test of mean and turbulent flow statistics (Figure A2-2). For staggered arrays, the channel-averaged velocity, U, was measured using a lateral transect at mid-depth and 2 m downstream from the array leading edge. A vertical profile was made at the point where the time-mean velocity matched the transect average. In a random array, two lateral transects provided an accurate estimate of U and $\langle k_t \rangle$. Specifically, the velocity statistics converged to a constant value after averaging two complete transects chosen randomly along the array (see SI in Shan et al., 2020). Along each transect, two locations whose time-mean streamwise velocity and TKE were closest to the transect mean were selected for a vertical profile. The vertical profiles confirmed that mid-depth measurements reasonably represented near-bed flow conditions (Figure A2-3).

The velocity records were processed using the Goring and Nikora (2002) method to remove spikes, with the acceleration and velocity thresholds set to λ_a = 1 and k = 1.5,

respectively. After despiking, TKE was calculated at each position as $k_t = \frac{1}{2}\overline{(u'^2 + v'^2 + w'^2)}$, and its spatial average was denoted $\langle k_t \rangle$. The integral time scale of turbulence, Λ_t, was estimated using the autocorrelation function (Kundu et al. 2016):

$$\Lambda_t = \int_0^{+\infty} \frac{\overline{v(t)v(t+\tau)}}{\overline{[v'(t)]^2}} d\tau \approx \int_0^{t_c} \frac{\overline{v(t)v(t+\tau)}}{\overline{[v'(t)]^2}} d\tau, \quad (3.5)$$

in which t_c is the first zero-crossing of the autocorrelation function. The lateral velocity, $v(t)$, was used because the identification of the zero crossing was more precise, although similar values were obtained from the streamwise component. At each position, the local integral length scale was defined as $l_e = \bar{u}\Lambda_t$, with $\bar{u}$ the local time-averaged velocity. The spatial-averaged (across the transects) eddy length scale was denoted $\langle l_e \rangle$.

3.4 Results

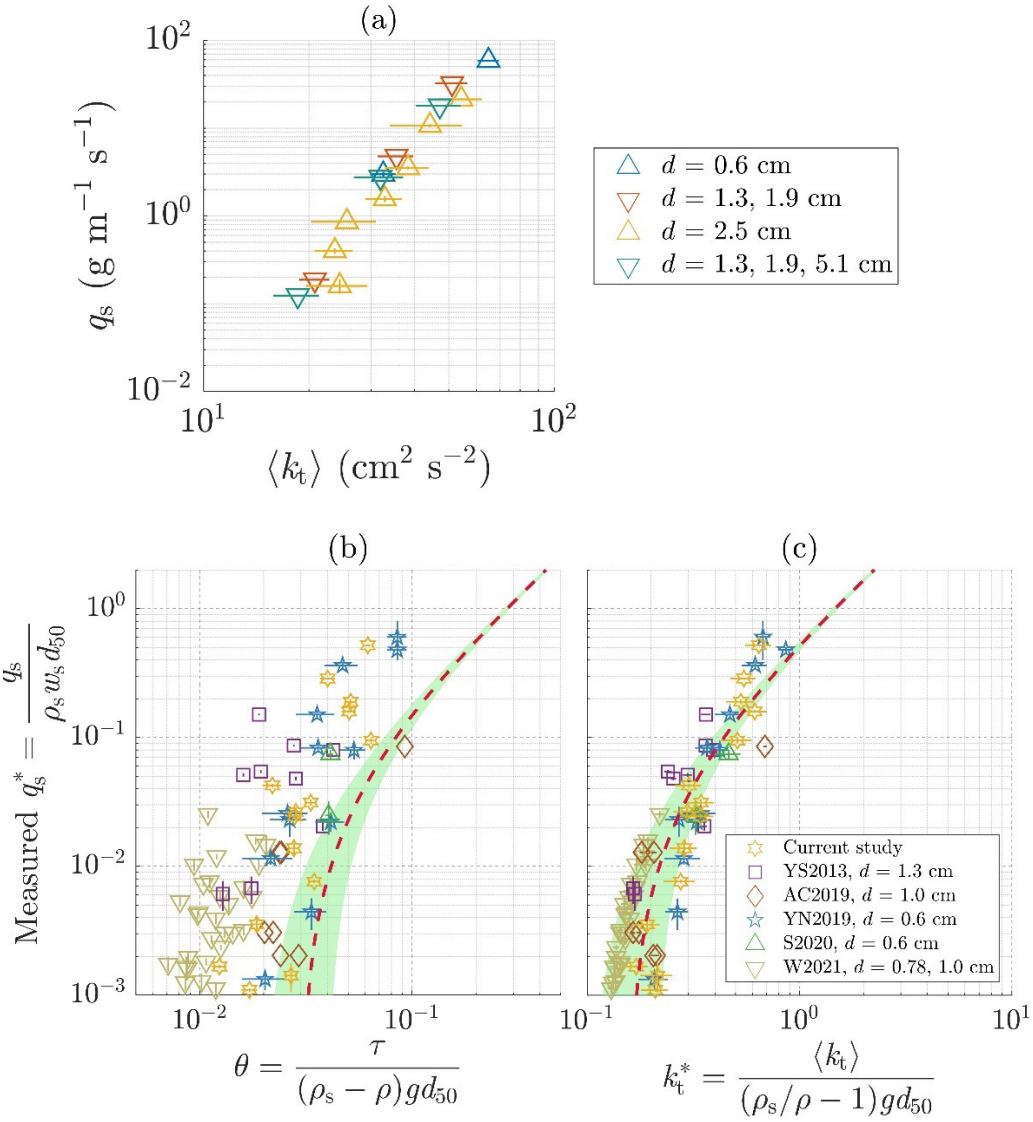

Figure 3-2. (a) Measured sediment transport rate q_s versus measured turbulent kinetic energy $\langle k_t \rangle$. Error bars denote standard error of multiple measurements in two transects for TKE and in time for q_s. The error in q_s was smaller than the symbol size. (b) and (c) Measured dimensionless sediment transport rate $q_s^* = \frac{q_s}{\rho_s w_s d_{50}}$ versus (b) dimensionless bed stress $\theta = \frac{\tau}{(\rho_s - \rho) g d_{50}}$ predicted using Equation 3.10, and (c) dimensionless turbulent kinetic energy $k_t^* = \frac{\langle k_t \rangle}{(\rho_s/\rho - 1) g d_{50}}$ predicted using Equation 3.8 and $\delta_{k_t} = 0.52 \pm 0.07$ (95% CI). The median grain size $d_{50} = 0.6\ mm$ in the current study and in Yang and Nepf (2019) and Shan et al. (2020); $d_{50} = 0.5\ mm$ in Yager and Schmeeckle (2013), Armanini and Cavedon (2019); and $d_{50} = 0.93$ mm in Wu et al. (2021). The dashed line represents MPM (Eqns. 1 and 3) using $\theta_{cr} = 0.03$ in subplot (b) and $k_{t,cr}^* = 5.3\theta_{cr} = 0.16$ in subplot (c). The shaded regions bound the range θ_{cr} = 0.02 to 0.04 and $k_{t,cr}^*$ = 0.11 to 0.21, respectively, as discussed in the text.

3.4.1 Bedload Sediment Transport

Considering a five-fold variation in stem diameter (0.64 to 2.5 cm), the measured bedload transport rate, q_s, did not exhibit a dependence on the stem diameter, d, but increased with spatial-averaged TKE $\langle k_t \rangle$ (Figure 3-2a). These results support the conclusion drawn from the impulse model, i.e., sediment transport rate depended primarily on TKE and not stem size, such that q_s may be predicted from channel-averaged turbulence alone. Further, the arrays consisting of multiple stem diameters (downward triangles in Figure 3-2a) exhibited the same dependence on $\langle k_t \rangle$ as the single-diameter arrays, indicating that the impulse description for single-diameter arrays (Figure 3-1) extends to arrays with multiple diameters.

3.4.2 Integral Length Scale

For arrays with mixed cylinder size, an average diameter $\langle d \rangle$ was defined that preserved the frontal area. This choice was made because turbulent eddies are expected to scale with the projected width of the plant elements, which has been confirmed for plants of real morphology (Xu & Nepf, 2020). Within a mixed array, each stem diameter, d_i, occurs at area density m_i (stems per bed area). The total frontal area per canopy volume is

$$\langle a \rangle = \sum_{i=1}^{p} m_i d_i = \left(\sum_{i=1}^{p} m_i\right)\langle d \rangle, \tag{3.6}$$

from which we define

$$\langle d \rangle = \frac{\langle a \rangle}{\sum_{i=1}^{p} m_i} = \frac{\sum_{i=1}^{p} m_i d_i}{\sum_{i=1}^{p} m_i}. \tag{3.7}$$

Within both staggered and random arrays of both uniform and mixed diameter, $\langle l_e \rangle$ was proportional to $\langle d \rangle$. Specifically, $\langle l_e \rangle = (0.43 \pm 0.02)\langle d \rangle$ (Figure A2-4). This was consistent with Tanino and Nepf (2008, Figure 12, d = 0.6 cm), who also found l_e proportional to d within a sparse array ($\Delta s/d > 2$). All cases in this study fell in the sparse array regime. Note that Tanino and Nepf (2008) measured a larger scale coefficient, l_e/d

≈ 1, which might be attributed to the smaller Reynolds numbers in that study ($Re_d < 600$, versus $Re_d \geq 1000$ in this study).

3.4.3 Turbulence

Although the turbulence arises from stem wakes at a scale proportional to d, Equation 3.4 does not include the stem diameter, d. This is due to the cylindrical geometry of the plant model, such that the same vegetation length scale (d) determines both the scale of turbulence, $l_e \sim d$, and the SVF $\phi = \frac{\pi}{4} m d^2$ (see details in Tanino & Nepf, 2008). To accommodate canopies of mixed element scale, we follow Xu and Nepf (2020), who predicted depth-averaged TKE using the depth-averaged values of a and l_e. It is reasonable to expect that a similar spatial average can be used in the horizontal plane to accommodate variations in stem diameter and to make the substitution $\langle l_e \rangle \sim \langle d \rangle$, as shown in 3.4.2, such that the spatial-averaged TKE within heterogeneous arrays can be described from $\langle a \rangle$ and $\langle d \rangle$:

$$\langle k_t \rangle = \underbrace{\frac{C_f U^2}{0.19}}_{k_{t,b}} + \underbrace{\delta_{k_t} \left[\frac{C_{D,form} \langle a \rangle \langle d \rangle}{2(1-\phi)} \right]^{\frac{2}{3}} U^2}_{k_{t,v}}. \quad (3.8)$$

For $Re_d \geq 200$, Etminan et al. (2018) showed that $C_{D,form} \approx 0.9\, C_D$, with C_D the total drag coefficient, which can be predicted following Etminan et al. (2017):

$$C_D = \left(\frac{1-\phi}{1-\sqrt{2\phi/\pi}} \right)^2 \left[1 + 10 Re_d^{-2/3} \left(\frac{1-\phi}{1-\sqrt{2\phi/\pi}} \right)^{-2/3} \right]. \quad (3.9)$$

A least-squares fit of Equation 3.8 with measured $\langle k_t \rangle$ yielded $\delta_{k_t} = 0.52 \pm 0.07$ (95% CI, Figure A2-5). When a canopy consists of a single diameter, Equation 3.8 is equivalent to Equation 3.4. Given this, the scale constant for Equation 3.8 was consistent with Yang and Nepf (2019), who found $\delta_{k_t} = 0.4 \pm 0.3$ (95% CI) for an array with a single diameter (d = 0.6 cm).

3.5 Discussion

3.5.1 Comparison of Stress-Based and Turbulence-Based Predictions of q_s

Measurements from previous studies were combined with the current study to both contrast the predictive capability of bed stress and TKE within vegetated regions and to validate the prediction of bedload transport using Equations 3.3 and 3.8 (Equation 6 in Yang & Nepf, 2018):

$$\tau = \begin{cases} \frac{4\rho\nu U}{d} & Re_{\mathrm{d}} < \frac{4}{C_{\mathrm{f}}} \\ \rho C_{\mathrm{f}} U^2 & Re_{\mathrm{d}} \geq \frac{4}{C_{\mathrm{f}}} \end{cases}, \tag{3.10}$$

which reflects the reduction of the viscous sublayer due to vegetation-generated turbulence. For each case, including the present study, the bed stress and TKE were predicted from the measured channel-averaged velocity and array characteristics (details in A2.6).

First, the measured bedload transport rate (symbols in Figure 3-2b, 3-2c) had only a weak dependence on bed stress (Figure 3-2b), with q_s^* varying by up to two orders of magnitude for conditions with the same θ. In contrast, q_s^* collapsed into a clear monotonic trend when plotted versus ${k_t}^*$ (Figure 3-2c). This demonstrated that bedload transport in vegetated channels was better described as a function of TKE, which echoes Figure 3 in Yang and Nepf (2018; also see A2.6). However, this study extended the result to arrays of different stem diameter (d = 0.6 to 5.1 cm) and to arrays of mixed stem sizes.

Second, this study considered the MPM model, which includes a threshold for sediment motion. This is in contrast to Yang and Nepf (2018), who used the Einstein-Brown (1942, 1950) model (SI, S6), which describes bedload as the sum of individual grain dislodgement events related to a probabilistic distribution, for which a threshold of sediment motion is not defined. However, for the timescale of interest in typical experiments, 10^0 to 10^2 min, and for many applications of monitoring and predicting bed evolution, 10^0 to 10^3 hr, a critical threshold makes physical and practical sense.

The MPM model (Equation 3.1) was recast in terms of TKE (Equation 3.3), which required a prediction of $k_{\mathrm{t,cr}}$. Previous studies have shown that the threshold for

grain motion can be described in terms of TKE, and that $k_{\mathrm{t,cr}}$ is the same for vegetated and unvegetated channels with the same bed sediment (Yang et al., 2016; Tinoco & Coco, 2018; Liu et al., 2021). Hence, we proposed that the threshold of sediment motion documented for bare beds in terms of θ_{cr} can be used to estimate the turbulence threshold, $k^*_{\mathrm{t,cr}} = 5.3\,\theta_{cr}$, using Equation 3.2. For the included studies, d_{50} = 0.5, 0.6 and 0.93 mm, for which θ_{cr} = 0.03 was estimated from the Shields diagram, using the fitted curve in Soulsby (1997). The corresponding $k^*_{\mathrm{t,cr}}$ = 0.16. The red dashed curves in Figure 3-2 correspond to these critical values. We note that measurements of incipient motion exhibit significant spread, which has been attributed to factors including bed characteristics (Lamb et al., 2008) and the different definitions for incipient motion (Buffington & Montgomery, 1997). From the spread in the Shields diagram, but considering only unidirectional flow conditions (e.g., Soulsby, 1997; Buffington & Montgomery, 1997; Whitehouse et al., 2000), we extracted a minimum (θ_{cr} = 0.02) and maximum (θ_{cr} = 0.04), corresponding to $k^*_{\mathrm{t,cr}}$ = 0.11 and 0.21, respectively. These values were used to define the green shaded region in Figure 3-2b and 3-2c, respectively. Note that Yang et al. (2016) used visual observation to determine $k^*_{\mathrm{t,cr}} = 0.15$ for grain size d_s = 0.6 – 0.85 mm within arrays of different ϕ (Figure 3 in Yang et al., 2016). This corresponded to θ_{cr} = 0.028, consistent with the range of critical shear stress extracted from the Shields diagram. This agreement supports the proposal that $k^*_{\mathrm{t,cr}}$ can be estimated from archived measurements of θ_{cr}.

Finally, the stress-based MPM formula did poorly predicting sediment transport within model vegetation (Figure 3-2b), underpredicting the measured transport rate by up to three orders of magnitude. In contrast, when MPM was recast in terms of TKE, using $k^*_{\mathrm{t,cr}} = 5.3\,\theta_{cr}$, the prediction matched the measurement more closely, with only a factor-four maximum deviation from the measurement.

3.5.2 Model Limitations

The equations for predicting bedload transport (Equations 3.3, 3.4, and 3.8) have some limitations. First, bed-generated turbulence is characterized by C_f defined by a

logarithmic profile over an unvegetated bed. Within a canopy, the velocity profile is more uniform, and the bed shear stress may be elevated due to thinning of the viscous sublayer by vegetation turbulence (Yang et al., 2015; Etminan et al., 2018). In addition, bed-generated turbulence can be broken down by stems, shifting turbulent energy from depth-scale (bed turbulence) to the stem-scale l_e, making it difficult to strictly partition bed and vegetation contributions. Despite these issues, Equations 3.4 and 3.8 performed well in predicting canopy turbulence, in part because the vegetation-generated turbulence is often the dominant term. Specifically, laboratory experiments (Yang & Nepf, 2019, Figure 4b) and numerical simulation (Etminan et al., 2018, Figure 11) indicate that bed-generated turbulence is small compared to vegetation-generated turbulence for $\phi > 0.01$, making weaknesses in $k_{t,b}$ prediction unimportant. Second, the model assumes $l_e \sim d$, which is valid for $\phi < 0.1$ and 0.06 for a regular and random array, respectively (Tanino & Nepf, 2008). For $\phi \geq 0.1$, the turbulence length scale is constrained by stem spacing, i.e. $l_e \sim \Delta s$, which modifies the form of Equation 3.4 (Tanino & Nepf, 2008). Third, the model assumes an emergent canopy. If the canopy is submerged, turbulence may be additionally generated in the shear layer at canopy top (e.g., Zhang et al., 2020). Canopy-scale turbulence forms when the non-dimensional meadow density $ah_v > 0.1$, with h_v the canopy height (Nepf, 2012). If the canopy is not too dense ($ah_v \leq 0.5$), this turbulence may reach the bed and influence sediment transport (e.g., Figure 3 in Luhar et al., 2008), a process that is not represented in the present model. Finally, grain-to-grain interaction can also influence sediment transport, including grain arrangement (Masteller & Finnegan, 2017) and collective grain entrainment (Lee & Jerolmack, 2018). These factors were not considered within the model, and the obstruction provided by the vegetation may alter these effects from those observed in bare channels.

3.5.3 Extension to More Complex Plant Morphology

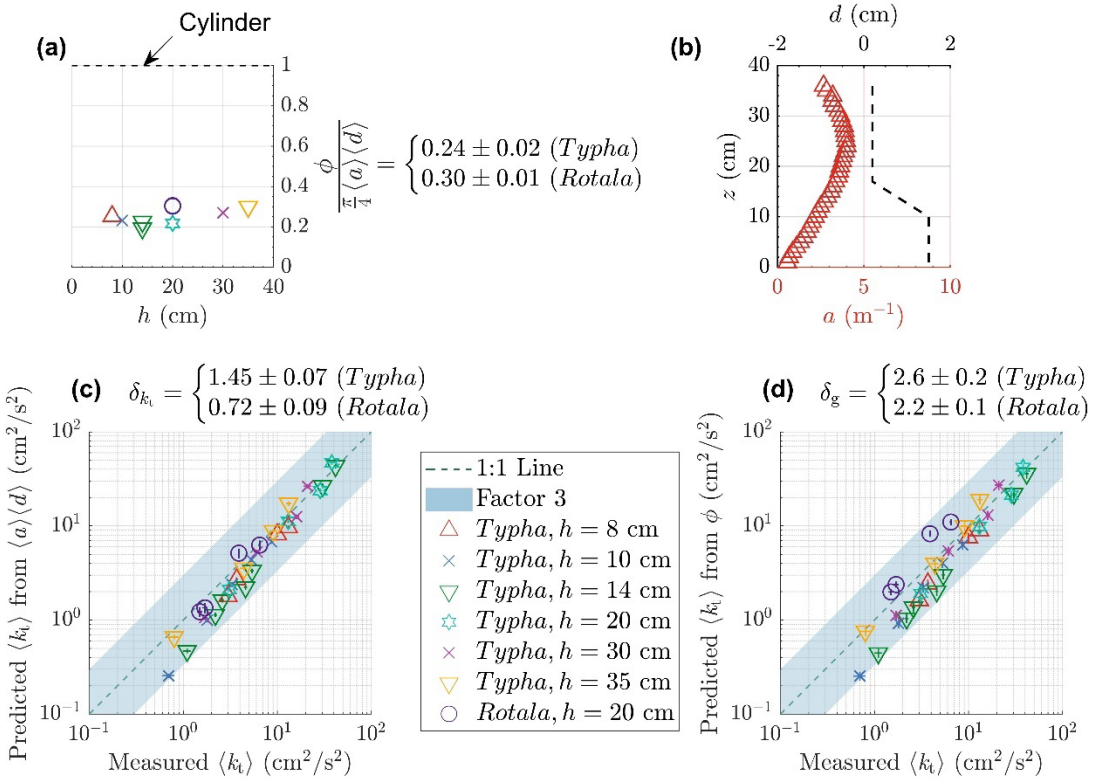

Figure 3-3. (a) Morphology ratio $\frac{\phi}{\frac{\pi}{4}\langle a\rangle\langle d\rangle}$ for *Typha* and *Rotala* for different flow depths. Black dashed line corresponds to cylindrical stems. (b) Vertical profiles of frontal area per unit volume, a, and characteristic width, d, (Equation 16 in Xu & Nepf, 2020) for *Typha*. For *Rotala*, d = 0.68 ± 0.13 cm (SE). (c) and (d) Predicted channel-averaged turbulent kinetic energy, $\langle k_t\rangle$ for *Typha* and *Rotala* using Equation 3.8 (subplot c) and Equation 3.11 (subplot d) versus measured values. All data from Xu and Nepf (2020).

Vegetation density is often characterized in terms of biomass $B = \rho_v \phi h_v$ (mass/bed area), which is directly related to solid volume fraction (ϕ), with ρ_v the plant bulk density. Therefore, it is useful to consider a prediction of TKE and bedload using B to infer ϕ. As an example, we considered two plant species with different morphology (A2.7 in SI), *Typha latifolia* (with branching leaves emerging from a short cylindrical culm) and *Rotala indica* (with decussate leaves distributed along the stem in orthogonal pairs). Even for these complex morphologies, l_e scales with the characteristic width of plant element, d, following the morphological variation over depth (Figure 12 in Xu &

Nepf, 2020). Therefore, we retain the assumption in Equations 3.4 and 3.8 that the canopy-averaged turbulence scale is proportional to the canopy average plant element width, i.e., $\langle l_e \rangle = \langle d \rangle$.

For a canopy of cylindrical stems, $\phi = \frac{\pi}{4} ad$, which makes Equations 3.4 and 3.8 equivalent. However, for real plant morphology with flat elements like leaves, $\phi < \frac{\pi}{4}\langle a \rangle \langle d \rangle$, so that Equation 3.4 will underpredict turbulence, compared to Equation 3.8. Specifically, $\frac{\phi}{\frac{\pi}{4}\langle a \rangle \langle d \rangle} = 0.24 \pm 0.02$ (*Typha*, SE) and 0.30 ± 0.01 (*Rotala*, SE), compared to $\frac{\phi}{\frac{\pi}{4}\langle a \rangle \langle d \rangle} = 1$ for cylinders. Conveniently, this morphology ratio is not a function of water depth (Figure 3-3a). This was expected for *Rotala*, which has a vertically uniform frontal area (Figure 1f in Xu & Nepf, 2020). In contrast, *Typha* has a nonuniform frontal area. However, its characteristic width d varies in a complementary trend with a (Figure 3-3b), such that the product ad has little vertical variation.

Xu and Nepf (2020) validated Equation 3.8 for the prediction of TKE within canopies of *Typha* and *Rotala* (repeated in Figure 3-3c). Here, we considered a modification of Eqn. 8 cast in terms of ϕ, derived using the morphology ratio (Figure 3-3a). The plant-specific morphology ratio $\frac{\phi}{\frac{\pi}{4}\langle a \rangle \langle d \rangle}$ was used to replace $\langle a \rangle \langle d \rangle$ in Equation 3.8, and the constants incorporated into a pre-factor δ_g (2.6 ± 0.2 for *Typha* and 2.2 ± 0.1 for *Rotala*) in $k_{t,v}$:

$$\langle k_t \rangle = \underbrace{\frac{C_f U^2}{0.19}}_{k_{t,b}} + \underbrace{\delta_g \delta_{k_t} \left[\frac{2C_{D,form}\,\phi}{\pi(1-\phi)}\right]^{\frac{2}{3}} U^2}_{k_{t,v}}. \tag{3.11}$$

Within the *Typha* and *Rotala* canopies, the bed contribution $\frac{k_{t,b}}{U^2} = 0.019 \pm 0.002$ (SE) was estimated from bare-bed measurements, and measured $C_D = 1.62 \pm 0.11$ for *Typha* and $C_D = 1.75 \pm 0.15$ for *Rotala* (SE), all reported in Xu and Nepf (2020, Figure 5b). The $\langle k_t \rangle$ predicted by Equation 3.11 agreed with the measured $\langle k_t \rangle$ to within factor 3 (Figure 3-3d). To apply this in the field, one could use measurements of biomass (B) to estimate SVF, $\phi = \frac{B}{\rho_v h_v}$.

3.6 Conclusions

In canopies of different stem size and of mixed stem size, bedload transport rate was a function of turbulent kinetic energy alone, with no dependence on stem size or distribution. This was consistent with the impulse model, which describes sediment entrainment as a function of both the duration and magnitude of turbulent events. Specifically, canopies of comparable solid volume fraction and velocity (producing the same TKE magnitude) but different stem sizes produce similar impulse, due to a trade-off between number (frequency) and size (duration) of turbulent interactions with the bed. Based on this, indirect methods for predicting turbulence (e.g., through measured or predicted energy gradients) may be used to predict sediment transport, without requiring specific descriptions of plant morphology. Further, the Meyer-Peter-Müller bedload equation was recast in terms of TKE, with critical TKE inferred from the Shields diagram. By accounting for the morphology-dependent ratios of non-dimensional frontal area $\langle a \rangle \langle d \rangle$ and SVF, one can predict TKE and thus sediment transport from biomass, flow depth, and flow velocity. This represents an important step in the description of turbulence and bedload transport within vegetated regions, enabling prediction of coastal and riverbank evolution.

Chapter 3 References

Abt, S., Clary, W., & Thornton, C. (1994). Sediment deposition and entrapment in vegetated streambeds. *Journal of Irrigation and Drainage Engineering*, 120(6), 1098–1110. doi:10.1061/(ASCE)0733-9437(1994)120:6(1098)

Armanini, A., & Cavedon, V. (2019). Bed-load through emergent vegetation. *Advances in Water Resources*, 129, 250–259. doi:10.1016/j.advwatres.2019.05.021

Barbier, E.B., Hacker, S.D., Kennedy, C., Koch, E.W., Stier, A.C. & Silliman, B.R. (2011). The value of estuarine and coastal ecosystem services. *Ecological Monographs*, 81: 169–193. doi:10.1890/10-1510.1

Brown, C. B. (1950). Sediment transportation. In H. Rouse (Ed.), *Engineering hydraulics* (pp. 769–857). Wiley & Sons.

Buffington, J.M., & Montgomery, D.R. (1997). A systematic analysis of eight decades of incipient motion studies, with special reference to gravel-bedded rivers. *Water Resources Research*, 33(8), 1993–2029. doi:10.1029/96WR03190

Celik, A. O., Diplas, P., Dancey, C. L., & Valyrakis, M. (2010). Impulse and particle dislodgement under turbulent flow conditions. *Physics of Fluids*, 22(4), 46601. doi:10.1063/1.3385433

Costanza, R., d'Arge, R., de Groot, R., Farber, S., Grasso, M., Hannon, B., ... & van den Belt, M. (1997). The value of the world's ecosystem services and natural capital. *Nature*, 387(6630), 253–260. doi:10.1038/387253a0

Diplas, P., Dancey, C. L., Celik, A. O., Valyrakis, M., Greer, K., & Akar, T. (2008). The Role of Impulse on the Initiation of Particle Movement Under Turbulent Flow Conditions. *Science*, 322(5902), 717–720. doi:10.1126/science.1158954

Einstein, H. A. (1942). Formulas for the Transportation of Bed Load. *Transactions of the American Society of Civil Engineers*, 107(1), 561–577.

Einstein, H. A. (1950). *The bed-load function for sediment transportation in open channel flows* (No. 1026). US Government Printing Office.

Engelund, F., & Hansen, E. (1967). *A monograph on sediment transport in alluvial streams*. Teknisk Forlag.

Etminan, V., Lowe, R.J., & Ghisalberti, M. (2017). A new model for predicting the drag exerted by vegetation canopies. *Water Resources Research*, 53(4), 3179–3196. doi: 10.1002/2016WR020090

Etminan, V., Ghisalberti, M., & Lowe, R. J. (2018). Predicting Bed Shear Stresses in Vegetated Channels. *Water Resources Research*, 54(11), 9187–9206. doi:10.1029/2018WR022811

Fagherazzi, S., Bryan, K., & Nardin, W. (2017). Buried Alive or Washed Away: The Challenging Life of Mangroves in the Mekong Delta. *Oceanography*, 30(3), 48–59. doi:10.5670/oceanog.2017.313

Goring, D. G., & Nikora, V. I. (2002). Despiking Acoustic Doppler Velocimeter Data. *Journal of Hydraulic Engineering*, 128(1), 117–126. doi:10.1061/(ASCE)0733-9

Hackney, C.R., Darby, S.E., Parsons, D.R., Leyland, J., Best, J.L., Aalto, R., ... & Houseago, R.C. (2020). River bank instability from unsustainable sand mining in the lower Mekong River. *Nature Sustainability*, 3(3), 217–225. doi:10.1038/s41893-019-0455-3

King, A.T., Tinoco, R.O., & Cowen, E.A. (2012). A k–ε turbulence model based on the scales of vertical shear and stem wakes valid for emergent and submerged vegetated flows. *Journal of Fluid Mechanics*, 701, 1–39. doi:10.1017/jfm.2012.113

Kouwen, N., & Unny, T. (1973). Flexible Roughness in Open Channels, *Journal of the Hydraulics Division*. 99(5), 713–728.

Kundu, P. K., Cohen, I. M., & Dowling, D. R. (2016). *Fluid Mechanics* (6th ed.). Academic Press. doi:10.1016/C2012-0-00611-4

Lamb, M.P., Dietrich, W.E., & Venditti, J.G. (2008). Is the critical Shields stress for incipient sediment motion dependent on channel-bed slope?. *Journal of Geophysical Research*, 113(F2), F02008. doi:10.1029/2007JF000831

Lee, D.B., & Jerolmack, D. (2018). Determining the scales of collective entrainment in collision-driven bed load. *Earth Surface Dynamics*, 6(4), 1089–1099. doi:10.5194/esurf-6-1089-2018

Lee, H., Ha, M.Y., & Balachandar, S. (2012). Work-based criterion for particle motion and implication for turbulent bed-load transport. *Physics of Fluids*, 24(11), 116604. doi:/10.1063/1.4767541

Liu, C., & Nepf, H. (2016). Sediment deposition within and around a finite patch of model vegetation over a range of channel velocity. *Water Resources Research*, 52(1), 600–612. doi:10.1002/2015WR018249

Liu, C., Shan, Y., & Nepf, H. (2021). Impact of Stem Size on Turbulence and Sediment Resuspension Under Unidirectional Flow. *Water Resources Research*, 57(3), e2020WR028620. doi:10.1029/2020WR028620

Luhar, M., Rominger, J., & Nepf, H. (2008). Interaction between flow, transport and vegetation spatial structure. *Environmental Fluid Mechanics*, 8(5-6), 423–439. doi:10.1007/s10652-008-9080-9

Manners, R.B., Wilcox, A.C., Kui, L., Lightbody, A.F., Stella, J.C., & Sklar, L.S. (2015). When do plants modify fluvial processes? Plant-hydraulic interactions under variable flow and sediment supply rates. *Journal of Geophysical Research: Earth Surface*, 120(2), 325–345. doi:10.1002/2014JF003265

Masteller, C.C., & Finnegan, N.J. (2017). Interplay between grain protrusion and sediment entrainment in an experimental flume. *Journal of Geophysical Research: Earth Surface*, 122(1), 274–289. doi:10.1002/2016JF003943

Meyer-Peter, E., & Müller, R. (1948). Formulas for Bed Load Transport. In *Proceedings of 2nd meeting of the International Association for Hydraulic Structures Research*, Stockholm, Appendix 2, 39–64.

Nelson, J. M., Shreve, R. L., McLean, S. R., & Drake, T. G. (1995). Role of Near-Bed Turbulence Structure in Bed Load Transport and Bed Form Mechanics. *Water Resources Research*, 31(8), 2071–2086. doi:10.1029/95WR00976

Nepf, H.M. (2012). Flow and Transport in Regions with Aquatic Vegetation. *Annual Review of Fluid Mechanics*, 44(1), 123–142. doi:10.1146/annurev-fluid-120710-101048

Niño, Y., & Garcia, M.H. (1996). Experiments on particle-turbulence interactions in the near-wall region of an open channel flow: implications for sediment transport. *Journal of Fluid Mechanics*, 326, 285–319. doi:10.1017/S0022112096008324

Norris, B.K., Mullarney, J.C., Bryan, K.R., & Henderson, S.M. (2017). The effect of pneumatophore density on turbulence: A field study in a *Sonneratia*-dominated mangrove forest, Vietnam. *Continental Shelf Research*, 147, 114–127. doi:10.1016/j.csr.2017.06.002

Norris, B.K., Mullarney, J.C., Bryan, K.R., & Henderson, S.M. (2021). Relating millimeter-scale turbulence to meter-scale subtidal erosion and accretion across the fringe of a coastal mangrove forest. *Earth Surface Processes and Landforms*, 46(3), 573–592. doi:10.1002/esp.5047

Paola, C., Twilley, R.R., Edmonds, D.A., Kim, W., Mohrig, D., Parker, G., ... & Voller, V.R. (2011). Natural Processes in Delta Restoration: Application to the Mississippi Delta. *Annual Review of Marine Science*, 3(1), 67–91. doi:10.1146/annurev-marine-120709-142856

Salim, S., Pattiaratchi, C., Tinoco, R., Coco, G., Hetzel, Y., Wijeratne, S., & Jayaratne, R. (2017). The influence of turbulent bursting on sediment resuspension under unidirectional currents. *Earth Surface Dynamics*, 5(3), 399–415. doi:10.5194/esurf-5-399-2017

Schmeeckle, M. W. (2015). The role of velocity, pressure, and bed stress fluctuations in bed load transport over bed forms: numerical simulation downstream of a backward-facing step. *Earth Surface Dynamics*, 3(1), 105–112. doi:esurf-3-105-2015

Shan, Y., Zhao, T., Liu, C., & Nepf, H. (2020). Turbulence and Bed Load Transport in Channels With Randomly Distributed Emergent Patches of Model Vegetation. *Geophysical Research Letters*, 47(12), e2020GL087055. doi:10.1029/2020GL087055

Shields, A. (1936). *Anwendung der Aehnlichkeitsmechanik und der Turbulenzforschung auf die Geschiebebewegung* [*Application of similarity mechanics and turbulence research on shear flow*]. Mitteilungen der Preußischen Versuchsanstalt für Wasserbau (in German). 26. Berlin: Preußische Versuchsanstalt für Wasserbau.

Shih, W., & Diplas, P. (2018). A Unified Approach to Bed Load Transport Description Over a Wide Range of Flow Conditions via the Use of Conditional Data Treatment. *Water Resources Research*, 54(5), 3490–3509. doi:10.1029/2017WR022373

Soulsby, R. L. (1983). The bottom boundary layer of shelf seas. In *Elsevier oceanography series* (Vol. 35, pp. 189–266). Elsevier.

Soulsby, R. L. (1997). *Dynamics of marine sands: A manual for practical applications*. Thomas Telford.

Sumer, B. M., Chua, L. H. C., Cheng, N.-S., & Fredsøe, J. (2003). Influence of Turbulence on Bed Load Sediment Transport, *Journal of Hydraulic Engineering*, 129(8), 585–596. doi:10.1061/(ASCE)0733-9429(2003)129:8(585)

Tanino, Y., & Nepf, H.M. (2008). Lateral dispersion in random cylinder arrays at high Reynolds number. *Journal of Fluid Mechanics*, 600, 339–371. doi:10.1017/S0022112008000505

Tinoco, R.O., & Coco, G. (2018). Turbulence as the Main Driver of Resuspension in Oscillatory Flow Through Vegetation. *Journal of Geophysical Research: Earth Surface*, 123(5), 891–904. doi:10.1002/2017JF004504

Tseng, C., & Tinoco, R.O. (2021). A Two-Layer Turbulence-Based Model to Predict Suspended Sediment Concentration in Flows With Aquatic Vegetation. *Geophysical Research Letters*, 48(3), e2020GL091255. doi:10.1029/2020GL091255

Whitehouse, R. J. S., Soulsby, R. L., & Damgaard, ‚J. S. (2000). Discussion of "Inception of Sediment Transport on Steep Slopes". *Journal of Hydraulic Engineering*, 126(7), 553–555. doi:10.1061/(ASCE)0733-9429(2000)126:7(553.2)

Wu, H., Cheng, N., & Chiew, Y. (2021). Bed-Load Transport in Vegetated Flows: Phenomena, Parametrization, and Prediction. *Water Resources Research*, 57(4), e2020WR028143. doi:10.1029/2020WR028143

Xu, Y., & Nepf, H. (2020). Measured and Predicted Turbulent Kinetic Energy in Flow Through Emergent Vegetation With Real Plant Morphology. *Water Resources Research*, 56(12), e2020WR027892. doi:10.1029/2020WR027892

Yagci, O., Celik, M.F., Kitsikoudis, V., Ozgur Kirca, V., Hodoglu, C., Valyrakis, M., ... & Kaya, S. (2016). Scour patterns around isolated vegetation elements. *Advances in Water Resources*, 97, 251–265. doi:10.1016/j.advwatres.2016.10.002

Yager, E. M., & Schmeeckle, M. W. (2013). The influence of vegetation on turbulence and bed load transport. *Journal of Geophysical Research: Earth Surface*, 118(3), 1585–1601. doi:10.1002/jgrf.20085

Yang, J. Q., Chung, H., & Nepf, H. M. (2016). The onset of sediment transport in vegetated channels predicted by turbulent kinetic energy. *Geophysical Research Letters*, 43(21), 11,261–11,268. doi:10.1002/2016GL071092

Yang, J. Q., & Nepf, H. M. (2018). A Turbulence-Based Bed-Load Transport Model for Bare and Vegetated Channels. *Geophysical Research Letters*, 45(19), 10,428–10,436. doi:10.1029/2018GL079319

Yang, J. Q., & Nepf, H. M. (2019). Impact of Vegetation on Bed Load Transport Rate and Bedform Characteristics. *Water Resources Research*, 55(7), 6109–6124. doi:10.1029/2018WR024404

This page intentionally left blank

Chapter 4 Turbulence and Bedload Transport in Submerged Vegetation Canopies[‡]

Depending on the degree of submergence, aquatic vegetation can either enhance or reduce bedload transport and thus erosion. Using the same channel average velocity U, flume experiments investigated how canopy density (ah, with canopy frontal area per unit volume a, and canopy height h) and submergence ratio (H/h, with H the flow depth) impacted near-bed velocity, turbulence, and bedload transport within a submerged canopy of rigid model vegetation. For $H/h < 2$, as ah increased, both the near-bed turbulent kinetic energy (TKE) and bedload transport rate (q_s) increased. The near-bed TKE was predominantly stem-generated. For $H/h > 2$, the near-bed TKE was insensitive to ah and H/h, because of a trade-off between stem-generated turbulence and the turbulence originated from canopy shear. While the near-bed TKE was insensitive to ah for $H/h > 2$, the near-bed velocity declined with increasing ah and H/h, such that q_s also declined, highlighting that both TKE and velocity were important in setting the bedload transport. A model to predict the near-bed velocity and TKE was developed and validated with measurements. This model was used to explore bedload transport under more realistic conditions with constant energy slope (S) and flexible vegetation. For a constant S, the channel average velocity, U, increased as ah decreased and as H/h increased, which in turn influenced the near-bed velocity and TKE. The highest q_s occurred with the greatest H/h and the smallest ah, because of the contribution of canopy-shear-generated turbulence and because these conditions were associated with the highest U.

4.1 Introduction

Aquatic vegetation facilitates several wetland ecosystem services, such as slowing floods and storm surge (Barbier et al., 2011), capturing and fixing carbon (Fourqurean et al., 2012), and enhancing biodiversity (Costanza et al., 1997). Wetland ecosystems are

[‡] This chapter is submitted to *Water Resources Research* with manuscript number 2024WR037694, and is currently under major revision at the time this thesis is published.

sustained through sediment retention (Clarke, 2002), which is influenced by vegetation morphology and distribution (e.g., Nardin & Edmonds, 2014; Xu et al., 2022). A better understanding of sediment transport in vegetated regions is needed to guide existing and future projects of wetland protection and restoration (Paola et al., 2011; Fagherazzi et al., 2017). While many previous studies have considered sediment transport through emergent vegetation (e.g., Jordanova & James, 2003; Tang et al., 2013; Armanini & Cavedon, 2019), few have considered submerged vegetation. Submerged vegetation is likely to provide greater protection from erosion, compared to emergent vegetation, because as flow is routed over the submerged canopy, the velocity and turbulence near the bed are reduced.

This study focused on bedload transport. Classic studies relate bedload transport rate to the time-averaged bed shear stress (e.g., Einstein, 1942; Engelund & Hansen, 1967; Meyer-Peter & Müller, 1948; Shields, 1936). However, several studies have shown that turbulence facilitates the mobility of individual particles (Celik et al., 2010; Shih & Diplas, 2018) and enhances channel-average sediment transport (Niño & Garcia, 1996; Salim et al., 2017; Sumer et al., 2003; Tseng & Tinoco, 2021). Vegetation can generate turbulence (Nepf, 2012), and when the canopy is sufficiently dense, the vegetation-generated turbulence dominates turbulence generated by bed shear stress, such that, in regions with vegetation, near-bed turbulence, rather than bed shear stress, better predicts the sediment motion threshold (Yang et al., 2016), the resuspension threshold (Tinoco & Coco, 2018; Liu et al., 2021), the sediment pickup rate (Xu et al., 2022), and bedload transport rate (Yang & Nepf, 2018, 2019).

Within canopies, the near-bed TKE is influenced by vegetation morphology. Previous studies have investigated the role of plant density (Poggi et al., 2004; Tanino & Nepf, 2008; Yager & Schmeeckle, 2013), stem diameter (Zhao & Nepf, 2021), clustering (Sukhodolov & Sukhodolova, 2010; Shan et al., 2020), and branching (Maza et al., 2017; Xu & Nepf, 2020) in shaping the near-bed turbulence, but the model vegetation used in each of these studies was emergent, i.e., taller than the water surface. Submerged aquatic vegetation is also common in the field. In addition to turbulence generated by vegetation elements, such as stems, leaves, and roots, for submerged canopies of sufficient density, canopy-scale turbulence is also created by the velocity shear generated by the drag

discontinuity at the top of the canopy (Raupach et al., 1996). The canopy shear production may contribute directly to the near-bed turbulence, or indirectly through turbulent transport (King et al., 2012). The penetration length scale, δ_e, which is inversely related to canopy density, describes the distance from the canopy top that turbulent momentum flux enhances the velocity, resulting in velocity shear and shear production of turbulence near the canopy top. If the shear layer production penetrates to the bed, it can directly enhance near-bed turbulence (King et al., 2012; Zhang et al., 2020), which might enhance sediment transport. For example, a significant shift in resuspension within a seagrass meadow was observed to occur when the canopy density was small enough to permit the penetration of shear layer turbulence to the bed (Moore, 2004, as discussed in Luhar et al., 2008). However, even in canopies with shear production isolated at the top of the canopy ($\delta_e/h < 1$), turbulent transport may carry turbulence produced in the shear layer toward the bed (King et al., 2012).

The present study investigated near-bed turbulence and bedload transport rate within a submerged canopy of model vegetation. Canopy density (ah, defined by the frontal area per unit volume a and canopy height h) and submergence ratio (H/h, defined as the ratio of flow depth H to the canopy height h) were chosen to compare conditions for which shear layer turbulence had different degrees of influence near the bed. Conditions were compared for two constraints, either with the channel average velocity (U) or with the energy slope (S) held constant. In the laboratory experiments, the channel average velocity U was held constant, because U was easier to adjust than S. Sections 4.3.1 – 4.3.3 describe the flume experiments, which were used to develop a near-bed turbulence model and a model to predict bedload transport. The models were used to explore the influence of vegetation flexibility on turbulence and bedload transport. Section 4.3.4 considers field scenarios, in which energy slope S was kept constant, while the canopy parameters were varied. Readers should note that the same U does not necessarily mean the same S, and vice versa. Their relationship is discussed in detail in Section 4.3.

4.2 Methods

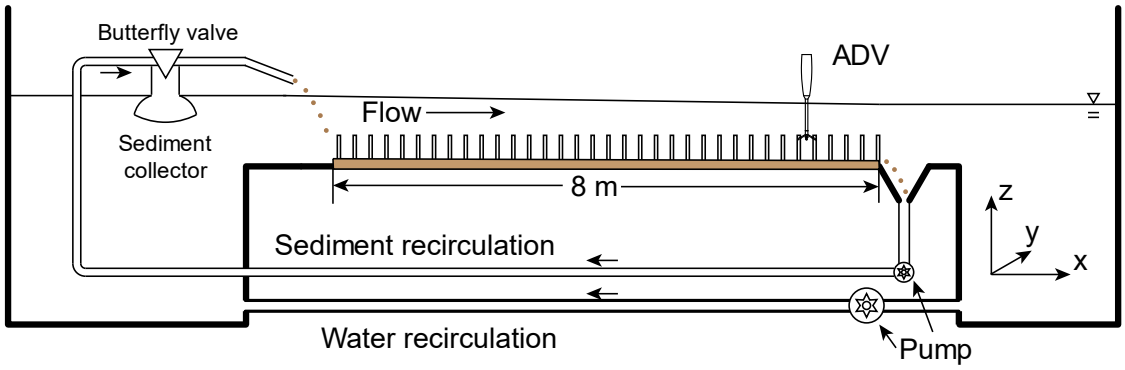

Figure 4-1. Side view of sediment recirculating flume, with sand layer (brown) within an array of submerged cylinders. Brown dots represent sediment in motion. The right-handed coordinates are x (streamwise), y (lateral), and z (vertical).

A submerged array of cylinders (diameter d = 1.27 cm) in a staggered arrangement was constructed in a 1-m wide and 10.4-m long test section of a sediment recirculating flume (Figure 4-1). The cylinder diameter was chosen both to be consistent with the stem diameter of submerged aquatic vegetation (Sukhodolov & Sukhodolova, 2006) and to ensure that cylinder-scale turbulence could be resolved by the 0.6-cm control volume of the velocity measurement. The array length (8 m) was sufficient for the velocity field to reach a fully developed condition (Chen et al., 2013). A sand bed (density ρ_s = 2650 kg/m^3, median grain size d_{50} = 0.35 mm) with an initial thickness of 7.8 cm was installed along the test section. Initially, the canopy height was h = 10 cm above the top of the sand layer. To consider different contributions of shear layer turbulence at the bed, the dimensionless canopy density was set to ah = 0.11 ($\delta_e = h$, which will be called the sparse canopy) and 0.49 ($\delta_e < h$, which will be called the dense canopy). The targeted channel-averaged velocity U was 40 cm/s, but it varied by up to 15% as the bed level adjusted during specific flow and canopy conditions. The flow depth (H) was varied to produce a range of submergence ratio H/h = 1.5 to 3.5.

Starting from level, the bed profile evolved before reaching an equilibrium state. To observe the evolution of the bed, a tripod-mounted Canon D7500 camera captured images of a side section of the channel every 15 min. Once the bed elevation varied by

less than 5 mm per hour, direct measurements of sediment transport rate were made to confirm that the bed had reached equilibrium. Sediment was collected by diverting sediment from the recirculation pipe (Figure 4-1) into a mesh bag for 20 min. If the collected sediment weighed more than 50 g, the collection time was decreased, but to no shorter than 2 min. Each measurement was followed by a 15-min break and was repeated four times. If the standard error within a 1-hr measurement set was less than 15% of the set average, the bed was considered to have reached equilibrium. The time to reach equilibrium was between 30 and 160 hours.

The sediment transport rate was normalized for comparison with other studies. Specifically, the dimensionless sediment transport rate is:

$$q_s^* = \frac{q_s}{\rho_s w_s d_{50}}, \tag{4.1}$$

in which q_s is the mass transported per unit width per time, and w_s is the settling velocity estimated by Rubey's equation (1933):

$$w_s = \left[\sqrt{\frac{2}{3} + \frac{36\nu^2}{(\rho_s/\rho - 1)g d_{50}^3}} - \sqrt{\frac{36\nu^2}{(\rho_s/\rho - 1)g d_{50}^3}}\right]\sqrt{(\rho_s/\rho - 1)g d_{50}}, \tag{4.2}$$

which yielded w_s = 0.047 m/s for the quartz sediment (d_{50} = 0.35 mm) used in this study.

After equilibrium was reached, a vertical profile of instantaneous velocity (u, v, and w, corresponding to streamwise, lateral, and vertical velocities, respectively) was measured 7 m downstream of the array leading edge, where the flow was fully developed. The profile was taken close to the channel centerline (y = 46.8 cm or 47.6 cm) and midway between two adjacent cylinder rows and columns. Based on preliminary measurements and previous studies, at this position, the velocity and turbulent kinetic energy respectively matched their spatial average to within 10% error (Figure A3-1; also see Figure 2 in Chen et al., 2013 and Figures 4 & 13 in Conde-Frias et al., 2023). The difference between the Reynolds stress at this point and the spatial average was less than 30% (Figure A3-1; Figure 4 & 13, Conde-Frias et al., 2023). At each point, velocity was recorded for 150 seconds at 200 Hz by a down-looking Nortek Vectrino. The region within 5 cm of the water surface was measured with a side-looking probe. Seeding

material (Potters Industries Inc. Spherical Glass 110P8, d_{50} = 10 μm) was added to enhance the backscatter signal.

The following protocol was used to process the velocity records. First, as suggested by Nortek (2021), data points with signal-to-noise ratio smaller than 10 (none in this study) or signal correlation smaller than 70% (observed in near-bed velocity data in dense canopy) were removed. Second, the Goring and Nikora (2002) spike removal algorithm was applied, with the acceleration and velocity thresholds set to $\lambda_a = 1$ and $k = 1.5$, respectively. For each velocity component, the temporal average (denoted by overbar), $\bar{X} = \frac{1}{T}\int_0^T X(t)\,\mathrm{dt}$, and fluctuation (denoted by prime), $X'(t) = X(t) - \bar{X}$, were calculated. Here X is a velocity component, t is time, and T is the sampling duration (150 s). The root-mean-square velocity (X_{rms}), Reynolds stress (τ_{Re}), and turbulent kinetic energy (k_t) were calculated, respectively, as:

$$X_{\mathrm{rms}} = \sqrt{\frac{1}{T}\int_0^T [X'(t)]^2\,\mathrm{dt}} \tag{4.3}$$

$$\tau_{\mathrm{Re}} = -\rho\overline{u'w'} \tag{4.4}$$

$$k_t = \frac{1}{2}\left(\overline{u'^2} + \overline{v'^2} + \overline{w'^2}\right) = \frac{1}{2}\left(u_{\mathrm{rms}}^2 + v_{\mathrm{rms}}^2 + w_{\mathrm{rms}}^2\right) \tag{4.5}$$

The canopy average was denoted by angle brackets, $\langle\square\rangle = \frac{1}{h}\int_0^h(\,)\,\mathrm{dz}$. After finishing the velocity measurements, the sediment transport rate was measured for another four consecutive times to confirm stationary conditions.

Because the canopy was submerged, the vertical profiles of velocity and turbulence had significant variation with distance from the bed. However, for bedload transport, the conditions near the bed were the most relevant. Thus, we defined a near-bed region within 2 cm from the bed, excluding the region of significant shear in the upper canopy. The near-bed average was defined as $(\square)_{\mathrm{nb}} = \frac{1}{2\ \mathrm{cm}}\int_0^{2\ \mathrm{cm}}(\,)\,\mathrm{dz}$.

4.3 Results and Discussion

Table 4.1: Summary of Experimental Cases

Case	#	1.1	1.2	1.3	2.1	2.2	2.3
a	(m^{-1})	1.1	1.1	1.1	4.9	4.9	4.9
h	(cm)	13.3	11.8	10.9	16.7	11.6	10.5
ah	(-)	0.15	0.13	0.12	0.82	0.57	0.51
H	(cm)	18.9	26.8	32.3	24.5	26.8	36.5
H/h	(-)	1.4	2.3	3.0	1.5	2.3	3.5
δ_e	(cm)	6.7	9.5	9.0	7.0	6.5	5.6
$\delta(\delta_e)$	(cm)	0.3	0.4	0.4	1.4	1.0	0.2
δ_e/h	(-)	0.50	0.81	0.83	0.42	0.56	0.53
$\delta(\delta_e/h)$	(-)	0.03	0.05	0.05	0.08	0.09	0.03
q_s	($g\ m^{-1}\ s^{-1}$)	3.8	0.85	0.265	8.2	0.86	0.036
SE(q_s)	($g\ m^{-1}\ s^{-1}$)	0.5	0.06	0.01	0.2	0.02	0.003
U	(cm/s)	38.1	41.2	38.9	39.3	45.8	38.4
SE(U)	(cm/s)	1.1	1.3	1.2	2.5	1.8	1.6
U_{nb}	(cm/s)	28.8	20.1	15.6	18.7	12.2	7.15
SE(U_{nb})	(cm/s)	0.8	1.5	1.5	0.3	0.2	0.16
U_{canopy}	(cm/s)	32.7	27.0	21.2	26	19.6	12.0
SE(U_{canopy})	(cm/s)	0.9	1.2	1.1	2	1.8	1.2
$k_{t,nb}$	(cm^2/s^2)	18.1	16.4	14.2	29	24	15.6
SE($k_{t,nb}$)	(cm^2/s^2)	0.5	0.4	0.3	3	3	1.5
$k_{t,canopy}$	(cm^2/s^2)	44	43	34	93	87	52
SE($k_{t,canopy}$)	(cm^2/s^2)	4	4	4	12	11	7
$\tau_{Re,nb}$	(N/m^2)	0.17	0.090	0.06	0.20	0.13	0.038
SE($\tau_{Re,nb}$)	(N/m^2)	0.03	0.015	0.02	0.05	0.07	0.015
$\tau_{Re}\|_{z=h}$	(N/m^2)	1.96	1.69	1.1	5.55	3.4	2.8
SE($\tau_{Re}\|_{z=h}$)	(N/m^2)	0.06	0.10	0.3	0.17	0.2	0.9

Notes

(1) Nomenclature

a: Frontal area per unit volume
h: Canopy height
ah: Canopy density
H: Flow depth
H/h: Submergence ratio
δ_e: Penetration length
U: Channel average velocity
U_{nb}: Near-bed velocity
U_{canopy}: Canopy-averaged velocity
$k_{t,nb}$: Near-bed turbulent kinetic energy
$k_{t,canopy}$: Canopy-averaged turbulent kinetic energy
SE: Standard error

(2) Uncertainties (denoted by $\boldsymbol{\delta}$)

$\frac{\delta a}{a} = \frac{\delta d}{d} = 8\%$, $\delta h = \delta H = 0.5$ cm.

4.3.1 Time-mean and Turbulent Velocity Statistics

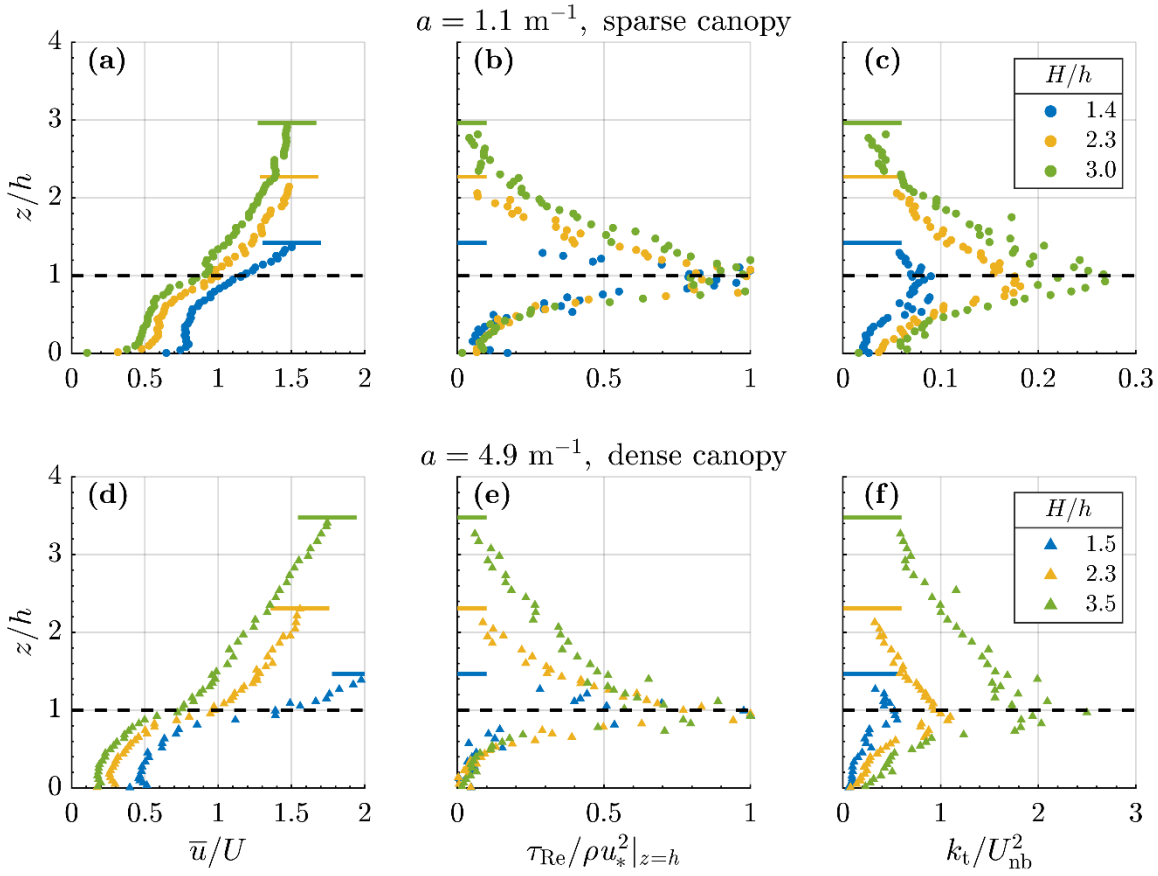

Figure 4-2. Vertical profiles of streamwise velocity (a, d), Reynolds stress (b, e), and turbulent kinetic energy (TKE, c, f) for frontal area per canopy volume a = 1.1 m^{-1} (first row, a – c, denoted as sparse in this paper) and a = 4.9 m^{-1} (second row, d – f, denoted as dense in this paper). Vertical coordinate (z), local time-average velocity ($\overline{u}$), Reynolds stress (RS, $\tau_{\mathrm{Re}} = -\rho\overline{u'w'}$), and TKE ($k_t$) are respectively normalized by canopy height above sand bed (h), channel average velocity (U), Reynolds stress at canopy top ($\rho u_*^2|_{z=h}$), and the near-bed velocity ($U_{\mathrm{nb}} = \frac{1}{2\ \mathrm{cm}}\int_0^{2\ \mathrm{cm}} \overline{u}(z)\,dz$). Submergence ratio ($H/h$) is indicated by symbol color in legend, with corresponding water surface position denoted by a horizontal line of the same color. Black dashed lines indicate the top of canopy ($z = h$). Measurement errors are smaller than the symbol size.

The vertical profiles of velocity (Figure 4-2a, 4-2d) were similar to those measured in other submerged canopies (e.g., Raupach et al. 1996; Ghisalberti, 2009; King et al., 2012), with velocity diminished within the canopy, relative to above the canopy, producing a shear layer with an inflection point near the canopy top (z/h = 1, Figure 4-2). The in-canopy velocity decreased both with an increase in canopy density (compare a = 1.1 m^{-1} and 4.9 m^{-1}, shown in Figure 4-2a and 4-2d, respectively) and with

an increase in the depth of submergence (e.g., compare H/h = 1.5 and 3.5 in Figure 4-2d). These trends were consistent with predictions from two-layer models based on conservation of mass and momentum (e.g., Huthoff et al., 2007; Chen et al., 2013).

The peak Reynolds stress (RS) occurred at the canopy top, coincident with the velocity inflection point (Figure 4-2b, 4-2e). Above the canopy, the RS profiles were linear, decreasing toward zero at the free surface, which was consistent with stress profiles over an unvegetated bed (e.g., Nezu & Rodi, 1986; Stacey et al., 1999). Because canopy drag inhibited downward turbulent momentum flux ($-\rho\overline{u'w'}$) into the canopy, RS decreased from the canopy top toward the bed (Figure 4-2b, 4-2e). The distance that turbulent momentum flux penetrates into the canopy, denoted δ_e, has been experimentally defined as the distance from the canopy top at which RS decreases to a value 10% of its peak value at the canopy top, i.e., normalized stress value of 0.1 (Nepf & Vivoni, 2000; Ghisalberti, 2009). Previous studies have shown $\delta_e \approx \frac{1}{3}(C_D a)^{-1}$ (Ghisalberti, 2009), with C_D the canopy drag coefficient. The penetration length is also restricted by the bed ($\delta_e = h$), and the water surface ($\delta_e = H - h$, Nepf & Vivoni, 2000). Combining these constraints,

$$\delta_e = \min\left\{\frac{1}{3}(C_D a)^{-1},\ h,\ H - h\right\}. \quad (4.6)$$

The water surface constraint was observed in the sparse canopy (a = 1.1 m^{-1}, Figure 2a) at submergence ratio H/h = 1.4 (blue dots), for which the penetration length was limited by the free surface (horizontal blue line), such that $\delta_e = H - h$ (Table 4.1, Figure 4-2b). In this case $\delta_e < h$, such that turbulent stress did not penetrate to the bed, creating a near-bed region with vertically uniform velocity (Figure 4-2a). Compared to the sparse canopy at a similar submergence ratio, in the dense canopy (a = 4.9 m^{-1}) the near-bed velocity was reduced to a greater degree (Figure 4-2d), leading to a stronger velocity shear and Reynolds stress at the top of the canopy (Table 4.1). Further, the dense canopy had a penetration length smaller than the canopy height ($\delta_e = \frac{1}{3}(C_D a)^{-1} < h$, Table 4.1), for all values of submergence ratio, resulting in a near-bed region unaffected by turbulent stress and thus having vertically uniform velocity (Figure 4-2d).

Turbulent kinetic energy, k_t, had a maximum value near the canopy top, associated with shear production in the canopy shear layer (Figure 4-2c, 4-2f). For both canopy densities, the normalized near-bed TKE increased as the submergence ratio increased (blue to yellow to green symbols), suggesting enhancement of near-bed turbulence by the shear layer turbulence. Note that TKE was enhanced even in regions without shear production, i.e., regions below the penetration distance ($z < h - \delta_e$), within which both RS and shear, and thus shear production ($P_s = -\rho\overline{u'w'}\frac{\partial\langle\overline{u}\rangle}{\partial z}$), were negligible (Figure 4-2c, 4-2f, & Figure A3-2). This suggested that the turbulent transport of turbulence played a role in elevating the near-bed turbulence by transporting turbulence produced in the shear layer toward the bed. A similar conclusion can be drawn from Figure 7 in Nepf and Vivoni (2000), which showed that the TKE normalized by the square of local velocity was elevated, relative to the emergent (H/h = 1) condition, when H/h > 1.75, indicating that near-bed turbulence was elevated by turbulent transport from the canopy shear layer.

4.3.2 Near-bed Velocity, Turbulence, and Sediment Transport

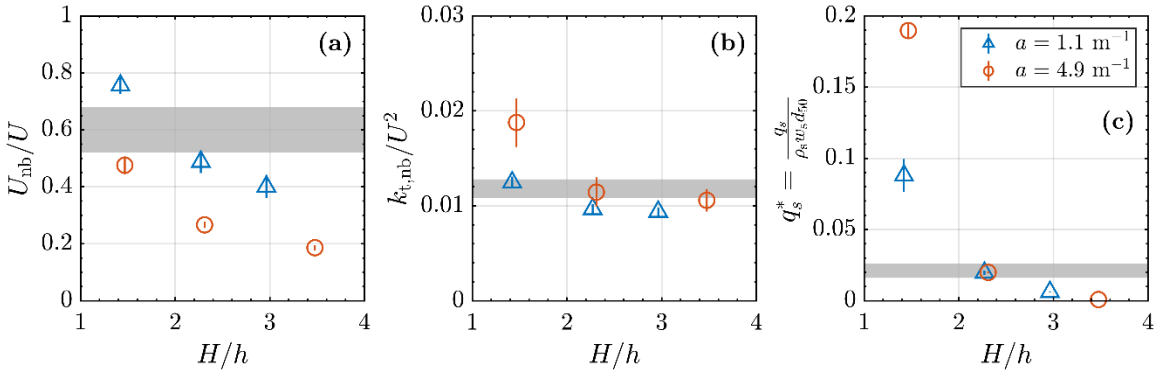

Figure 4-3. (a) Normalized near-bed velocity, U_{nb}/U, (b) normalized near-bed TKE, $k_{t,nb}/U^2$, and (c) dimensionless sediment transport rate, $q_s^* = \frac{q_s}{\rho_s w_s d_{50}}$, versus submergence ratio (H/h). Triangles represent sparse array (a = 1.1 m^{-1}), and circles represent dense array (a = 4.9 m^{-1}). Shaded band denotes conditions for an unvegetated bed with same channel average velocity and bed material (U = 0.4 m/s, d_{50} = 0.35 mm) estimated from measurements made by Ishii (2023), who used the same flume and sediment as this study.

The near-bed velocity, U_{nb}, normalized by channel average velocity, U, decreased as submergence ratio, H/h, increased, and for the same H/h, U_{nb}/U decreased as ah increased (Figure 4-3a), consistent with a two-layer momentum model (e.g., Chen et al., 2013, see Figure 4-5b). For $H/h > 2$, U_{nb}/U was smaller than the unvegetated bed (shaded band). The near-bed turbulence, $k_{t,nb}$, normalized by U^2, exhibited two regimes (Figure 4-3b). First, at the shallowest submergence ($H/h < 2$), $k_{t,nb}/U^2$ achieved the highest observed values and was higher for the denser canopy. This was consistent with a dominance of stem-generated turbulence, which is proportional to $aU_{nb}{}^2$ (Tanino & Nepf, 2008). Specifically, in the denser canopy, compared to the sparser canopy, $(U_{nb}/U)^2$ was smaller, but a was larger, leading to a higher $k_{t,nb}/U^2$ value. Second, for $H/h > 2$, $k_{t,nb}/U^2$ was not a function of canopy density or submergence, but exhibited a constant value of 0.0103 ± 0.0004, which was only slightly smaller than the value for unvegetated bed (0.0118 ± 0.0010).

For both canopy densities, the bedload transport rate decreased as H/h increased (Figure 4-3c). For $H/h < 2$, the sediment transport rate was higher than that associated with the bare bed and was also higher for the denser canopy (red circle) than the sparser canopy (blue triangle). Both of these trends were consistent with the dense canopy having the highest near-bed turbulence (Figure 4-3b). Similarly, emergent canopies ($H/h = 1$) have been consistently shown to produce higher bedload transport, compared to the bare channels, if the channel average velocity is the same (e.g., Yager & Schmeeckle, 2013; Yang & Nepf, 2018; Wu et al., 2021). For $H/h > 2$, the dimensionless sediment transport rate was similar for both canopy densities and lower than that associated with a bare bed.

Figure 4-3 suggests that bedload transport was positively correlated with both near-bed turbulence and velocity. First, compare Cases 1.2 (blue triangle at $H/h = 2.3$) and 2.1 (orange circle at $H/h = 1.5$), which have the same near-bed velocity within uncertainty (Figure 4-3a), but the normalized near-bed TKE of Case 1.2 was half of that of Case 2.1 (Figure 4-3b), leading to much weaker sediment transport (Figure 4-3c). Next, compare Case 1.2 (blue triangle at $H/h = 2.3$) and Case 1.3 (blue triangle at $H/h = 3.0$), which have the same near-bed TKE within uncertainty (Figure 4-3b), but the near-bed velocity was higher in Case 1.2 (Figure 4-3a), yielding higher sediment transport (Figure 4-3c). The dependence of sediment transport on a combination of velocity and

turbulence has been noted in previous studies. Specifically, in bare channels, bedload transport has been described as the product of grain velocity, correlated with fluid velocity, and the number of grains in motion, correlated with turbulence (Ancey et al., 2008), but bedload is predominantly controlled by the number of grains in motion (e.g., Radice & Ballio, 2008; Roseberry et al., 2012). Similar observations have been made in vegetated channels, with the number of grains in motion shown to have a positive correlation with a linear combination of time-mean and turbulent velocity (Yang & Nepf, 2019; Lu et al., 2021). Consistent with Yang and Nepf (2019), we found a strong correlation between sediment transport and a linear combination of time-mean and turbulence velocity, $f = \frac{\left(U_{\mathrm{nb}}+\alpha\sqrt{k_{\mathrm{t,nb}}}\right)^2}{\left(\frac{\rho_s}{\rho}-1\right)gd_{50}}$. Specifically,

$$q_s^* = \beta f^n, \tag{4.7}$$

with $\alpha = 10$ (as given in Yang & Nepf, 2019), and $\beta = 7.8\times10^{-11}$ (95% CI: [5.1×10^{-12}, 1.2×10^{-9}]) and $n = 4.5$ (95% CI: [3.9, 5.1]), based on data in Yang and Nepf (2019), Zhao and Nepf (2021) and this study (see Figure 4-4). This hybrid function of near-bed time-mean velocity and turbulence captures two modes of sediment mobilization, due to time-mean stress and due to impulse. When turbulence is low (e.g., flat beds without vegetation) or conditions far above the threshold of motion, time-mean stress is more important, which is correlated with time-mean velocity. When turbulence is high (e.g., beds with roughness elements, such as vegetation) or conditions close to the threshold of motion, turbulent fluctuations in bed stress or turbulent pressure can provoke sediment mobility, even when the time-mean bed stress is below the critical value. In these conditions, turbulence plays a more important role in sediment mobility. In this study (d_{50} = 0.35 mm) and in Yang and Nepf (2019, d_{50} = 0.60 mm), the constant $\alpha = 10$, indicating that turbulence becomes dominant only when $\sqrt{k_{\mathrm{t,nb}}} > 0.1\ U_{\mathrm{nb}}$. It is interesting to note that for bare beds the turbulence intensity is typically $\sqrt{k_{\mathrm{t,nb}}}/U_{\mathrm{nb}} \approx 0.1$ (e.g., Nezu & Rodi, 1986), indicating a condition for which turbulence would only weakly mediate the relationship between sediment mobility and time-mean bed stress, which is consistent with the large literature correlating sediment transport rate with time-mean bed stress in bare channels (e.g., Einstein, 1942; Engelund & Hansen, 1967; Meyer-Peter & Müller,

1948; Shields, 1936). Further, we note that the value $\alpha = 10$ has only been estimated for non-cohesive sediment in the range of medium sand (d_{50} = 0.35 to 0.60 mm). The value of α could be a function of both the grain size and the length scale of turbulence. For example, in a gravel-bed river with reed-scale vegetation, the diameter of vegetation elements (≈ 0.5 cm) could be much smaller than the grain size (4 to 6 cm), such that the vegetation-generated turbulence may not be large enough or act on the bed long enough to mobilize the sediment (e.g., Deitrick et al., 2024). Therefore, for gravel-bed rivers, α may be smaller than 10, or even zero.

Previously, to incorporate the role of vegetation turbulence in bedload transport, Zhao and Nepf (2021) recast the Meyer-Peter-Müller model (Meyer-Peter & Müller, 1948) in terms of TKE:

$$q_s^* = 0.66\left(k_{t,nb}^* - k_{t,cr}^*\right)^{1.5}. \tag{4.8}$$

in which the critical dimensionless TKE, $k_{t,cr}^*$ = 0.095 and 0.16 for d_{50} = 0.35 mm (Ishii, 2023) and 0.6 mm (Yang et al., 2016; Zhao & Nepf, 2021), respectively. While this model predicts sediment transport well for cases with strong channel turbulence, it overpredicts sediment transport by more than one order of magnitude with weak turbulence, because it did not account for the role of near-bed velocity (Figure 4-4b). Compared to Equation 4.8, which only considers near-bed TKE, Equation 4.7, which incorporates both velocity and TKE, provided a better description of sediment transport, cutting the root-mean-square error in half (Figure 4-4). This illustrates how the hybrid function in Equation 4.7 captures the role of TKE, when TKE is high, and that the time-mean velocity is only important when TKE is small.

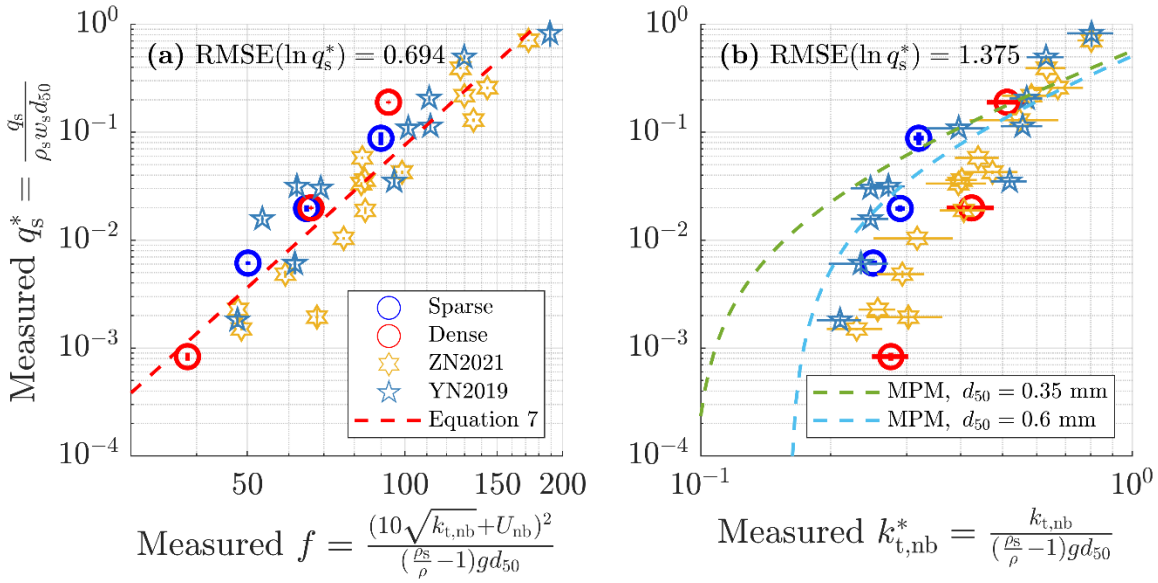

Figure 4-4. Measured dimensionless sediment transport rate $q_s^* = \frac{q_s}{\rho_s w_s d_{50}}$ versus (a) measured flow parameter $f = \frac{(U_{nb}+10\sqrt{k_{t,nb}})^2}{(\frac{\rho_s}{\rho}-1)gd_{50}}$ and (b) measured dimensionless near-bed TKE $k_{t,nb}^* = \frac{k_{t,nb}}{(\frac{\rho_s}{\rho}-1)gd_{50}}$. The present study used d_{50} = 0.35 mm with sparse (a = 1.1 m^{-1}, blue circles) and dense (a = 4.9 m^{-1}) canopies. Zhao and Nepf (2021, orange stars) and Yang and Nepf (2019, blue stars) used d_{50} = 0.6 mm. Red dashed line in (a) represents the least squares fit of Equation 4.7. Green and cyan dashed curves in (b) represent the revised TKE-based Meyer-Peter-Müller model in Zhao and Nepf (2021) with corresponding threshold values (0.095 for d_{50} = 0.35 mm and 0.16 for d_{50} = 0.6 mm, respectively), i.e., Equation 4.8.

4.3.3 Prediction of Near-bed Velocity, Turbulence, and Bedload Transport Rate

A prediction for near-bed velocity, turbulence, and sediment transport rate was developed by combining the new sediment transport model (Equation 4.7) with models from several previous studies. In a submerged canopy, the time-mean velocity decays exponentially from a maximum value (U_h) at the top of the canopy (e.g., Nepf, 2012):

$$\bar{u}(z) = U_S + (U_h - U_S)e^{-K_u(h-z)}, \tag{4.9}$$

in which U_S is the velocity within the canopy driven only by the energy slope (subscript 'S') and unaffected by turbulent stress. For $\phi < 0.1$, Equation 14 in Nepf (2012) gives

$$U_S = \sqrt{\frac{2gS}{C_D a}}. \tag{4.10}$$

The coefficient $K_u = (8.7 \pm 1.4)\ C_D a$ describes the decay of the stress-driven velocity component with distance from the canopy top. Ghisalberti (2009, Figure 4b) showed an empirical fit for submerged canopies that

$$U_h - U_S = 2.6u_*, \tag{4.11}$$

in which u_* is the shear velocity at the top of the canopy. If the water surface or bed slope (S) is known, the shear stress can be estimated as

$$u_* = \sqrt{g(H-h)S}, \tag{4.12}$$

so that Equations 4.9 through 4.12 describe the velocity within the canopy.

In the present study, the flume had zero bed slope and the water surface slope was too small to accurately measure, so that S was not available. Instead, u_* was inferred from a two-layer momentum model described in Chen et al. (2013), which defines the average velocity within the canopy (U_{canopy}) and over the canopy (U_{of}, subscript for "overflow"), respectively, in relation to the channel average velocity, U:

$$\begin{cases} \frac{U_{canopy}}{U} = \left[1 - \frac{h}{H}\phi + \sqrt{\frac{C_D a h}{2C(1-\phi)}\left(\frac{H-h}{H}\right)^3}\right]^{-1} \\ \frac{U_{of}}{U_{canopy}} = \frac{1}{H-h}\left[H - \frac{U}{U_{canopy}}h(1-\phi)\right] \end{cases}. \tag{4.13}$$

The coefficient C describes the turbulent stress at the top of the canopy:

$$C = u_*^2 / \left(U_{of} - U_{canopy}\right)^2, \tag{4.14}$$

and for rigid canopies of sufficient density ($ah > 0.1$), $C = (0.07 \pm 0.02)\left(\frac{\delta_e}{H}\right)^{\frac{1}{3}}$. Therefore, the shear velocity at the top of the canopy can be estimated from Equations 4.13 and 4.14:

$$u_* = \sqrt{C}\left(U_{of} - U_{canopy}\right). \tag{4.15}$$

Equations 4.9 – 4.15 together describe the velocity profile $\bar{u}(z)$, from which the near-bed velocity is

$$U_{nb} = \frac{1}{2\text{ cm}} \int_0^{2\text{ cm}} \bar{u}(z)\mathrm{d}z. \tag{4.16}$$

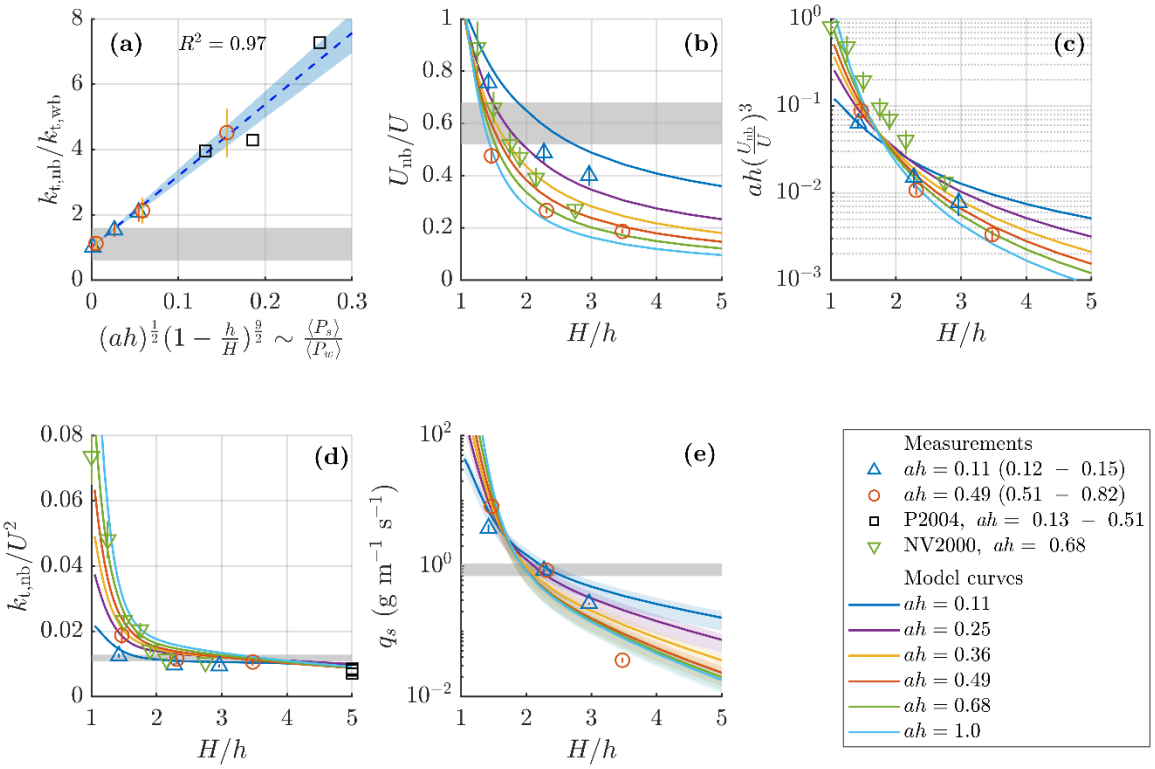

Figure 4-5. (a) Ratio of measured near-bed TKE to predicted sum of bed and wake TKE (Equation 4.24), $\frac{k_{t,nb}}{k_{t,wb}}$, versus parameter $(ah)^{\frac{1}{2}}\left(1-\frac{h}{H}\right)^{\frac{9}{2}}$ representing the ratio of canopy-averaged shear production, $\langle P_s \rangle$, to wake production, $\langle P_w \rangle$ (from Equation 4.23). Gray band represents the range of $\frac{k_{t,nb}}{k_{t,wb}}$ measured in emergent canopies in Zhao and Nepf (2021), and blue line and band represent the average and 95% confidence interval of linear fit. (b) Normalized near-bed velocity U_{nb}/U versus submergence ratio H/h (from Equation 4.16). (c) $ah\,(U_{nb}/U)^3$, product of canopy density ah and cube of normalized near-bed velocity U_{nb}/U, versus submergence ratio H/h. (d) Near-bed TKE normalized by the square of channel-averaged velocity, $k_{t,nb}/U^2$, versus submergence ratio, H/h (from Equation 4.24). (e) Sediment transport rate, q_s, versus submergence ratio, H/h. Data points from this study are blue triangles (a = 1.1 m^{-1}) and red circles (a = 4.9 m^{-1}), and those from Poggi et al. (2004) and Nepf and Vivoni (2000) are black squares and green triangles, respectively. In (b) – (e), solid lines represent model values. In (b) and (d), gray band represents the unvegetated value reported in Ishii (2023), who used the same flume and sediment as in this study. In (e), gray band represents sediment transport rate for unvegetated bed of the same sediment with U = 40 cm/s, based on Ishii (2023, see A3.2 in Appendices). Sediment transport in submerged canopies was predicted from Equation 4.7, using predicted U_{nb} and $k_{t,nb}$. Transparent bands around each curve show variation associated with experimental velocity range 38 cm/s ≤ U ≤ 41 cm/s.

Next, consider the near-bed turbulence, $k_{t,nb}$. Within an emergent vegetation canopy, turbulence can arise from bed shear and the stem wakes (e.g., Nepf, 1999; Stoesser et al., 2010). Modifying the model for emergent canopies (e.g., Zhao & Nepf,

2021), the wake- and bed-generated turbulence within a submerged canopy, $k_{t,wb}$ ("wb" for wake and bed), was written in terms of the near-bed velocity:

$$k_{t,wb} = \underbrace{C_b U_{nb}^2}_{\text{bed-generated}} + \underbrace{\delta_{k_t}\left[\frac{C_{D,form}\, ad}{2(1-\phi)}\right]^{\frac{2}{3}} U_{nb}^2}_{\text{vegetation-generated}}, \quad (4.17)$$

in which $\delta_{k_t} = 0.52 \pm 0.07$ (Zhao & Nepf, 2021), and C_b describes the contribution of bed-generated turbulence. The form drag coefficient was estimated as (Etminan et al., 2017, 2018)

$$C_{D,form} = 0.9C_D = 0.9\left(\frac{1-\phi}{1-\sqrt{2\phi/\pi}}\right)^2\left[1 + 10Re_d^{-2/3}\left(\frac{1-\phi}{1-\sqrt{2\phi/\pi}}\right)^{-2/3}\right], \quad (4.18)$$

which is valid for stem Reynolds number $Re_d = \frac{U_{canopy} d}{\nu} \geq 200$, with kinematic viscosity ν.

Within a submerged canopy, turbulence is also produced in the shear layer at the top of the canopy, and this turbulence may be transported toward the bed by turbulent transport, as discussed in Figure 4-2. As more turbulence is produced by shear production at the top of the canopy, more turbulence can be transported downward to augment the near-bed turbulence, so that it is reasonable to expect the increase in near-bed turbulence, $k_{t,nb}$, above the baseline of wake- and bed-generated turbulence (Equation 4.16) to be proportional to the ratio of shear production to wake production in the canopy, that is, $\frac{k_{t,nb}-k_{t,wb}}{k_{t,wb}} \sim \frac{\langle P_S \rangle}{\langle P_w \rangle}$.

From Zhang et al. (2020), the canopy average wake production is

$$\langle P_w \rangle = \frac{1}{2} C_{D,form} \frac{a}{1-\phi} U_{canopy}^3, \quad (4.19)$$

and the canopy average shear production is

$$\langle P_s \rangle = \frac{1.3}{h} C^{\frac{3}{2}} \left(U_{of} - U_{canopy}\right)^3, \quad (4.20)$$

from which,

$$\frac{\langle P_S \rangle}{\langle P_w \rangle} = 0.65 \frac{C^{\frac{3}{2}}}{ahC_{D,form}} \left(\frac{U_{of}}{U_{canopy}} - 1\right)^3. \quad (4.21)$$

The velocity ratio $\frac{U_{\mathrm{of}}}{U_{\mathrm{canopy}}}$ in Equation 4.21 can be replaced with Equation 4.13. Assuming $C_D \approx 1$ (as expected from Equation 4.18) and $\phi \ll 1$,

$$\frac{U_{\mathrm{of}}}{U_{\mathrm{canopy}}} = 1 + \frac{H}{H-h}\sqrt{\frac{C_D a h}{2C}\left(\frac{H-h}{H}\right)^3}, \tag{4.22}$$

so that

$$\frac{\langle P_s \rangle}{\langle P_w \rangle} \propto (ah)^{\frac{1}{2}}\left(1-\frac{h}{H}\right)^{\frac{9}{2}}. \tag{4.23}$$

This theoretically derived function agreed with measurements (see Figure A3-3).

From Equation 4.23 and assuming $\frac{k_{\mathrm{t,nb}}-k_{\mathrm{t,wb}}}{k_{\mathrm{t,wb}}} \sim \frac{\langle P_s \rangle}{\langle P_w \rangle}$, we expect

$$\frac{k_{\mathrm{t,nb}}}{k_{\mathrm{t,wb}}} = 1 + \delta_{\mathrm{s}}(ah)^{\frac{1}{2}}\left(1-\frac{h}{H}\right)^{\frac{9}{2}}. \tag{4.24}$$

The intercept in Equation 4.24 is unity, because for emergent canopies ($H/h = 1$) the second term is zero, and $k_{\mathrm{t,nb}} = k_{\mathrm{t,wb}}$, because there is no shear production. Equation 4.24 was confirmed using measurements from this study and from Poggi et al. (2004). An optimization of this fit suggested $\delta_{\mathrm{s}} = 22 \pm 2$ (95% CI, Figure 4-5a) and $C_{\mathrm{b}} = 0$ (see A3.3 and Figure A3-5), which implied that the bed turbulence made a negligible contribution to $k_{\mathrm{t,wb}}$ (Equation 4.17). This is consistent with the fact that in the near-bed region, the bed shear production was much smaller than wake production (Figure A3-2). In addition, for both canopies $ah > 0.1$, indicating that stem drag and turbulence were dominant over bed drag and turbulence (see Belcher et al., 2003 and Yang & Nepf, 2019, respectively).

Finally, using the predicted U_{nb} (Equation 4.16) and predicted $k_{\mathrm{t,nb}}$ (Equation 4.24), the bedload transport q_{s} was predicted from Equation 4.7. The modeled and measured values of U_{nb}, $k_{\mathrm{t,nb}}$, and q_{s} had strong agreement (see Figure A3-6). Specifically, modeled U_{nb} matched measurements to within 20%. Modeled and measured $k_{\mathrm{t,nb}}$ agreed within uncertainty. Modeled q_{s} matched measurements within factor 2.

4.3.4 Role of Canopy Density, Submergence Ratio, and Flexibility

The model developed in Section 4.3.3 was used to provide a detailed description of how near-bed turbulence (Figure 4-5d) and sediment transport (Figure 4-5e) vary with canopy density (ah) and submergence (H/h). Assuming a constant channel velocity, two regimes were defined by the degree of submergence. For shallow submergence, $H/h < 2$, canopy shear production is restricted to a region close to the canopy top (small δ_e, see Table 4.1) and the transport of this turbulence into the near-bed region is small compared to the local stem generation. Specifically, for $H/h < 2$, $T_{t,nb}/P_{w,nb} < 0.2$ (Figure A3-4). Therefore, the near-bed turbulence is dominated by stem wake production, which is proportional to a and U_{nb}^3 (Equation 4.19, also Tanino & Nepf, 2008). Although U_{nb}/U decreases with increasing ah, the combination aU_{nb}^3 is positively related to ah (Figure 4-5c, $H/h < 2$), so that near-bed turbulence ($k_{t,nb}/U^2$) increases as canopy density (ah) increases. In this regime, near-bed TKE dominates the channel-scale bedload transport (as discussed in 4.3.2 and A3.2), so that the bedload transport rate decreases with increasing submergence ratio and decreasing canopy density, consistent with the trends in $k_{t,nb}$ (Figure 4-5d and 4-5e, $H/h < 2$). For deeper submergence, $H/h > 2$, the near-bed turbulence is enhanced by turbulent transport, which carries turbulence produced in the canopy shear-layer toward the bed (Figures A3.2 and A3.4). As ah increases, the near-bed velocity decreases, which decreases local wake production (Equation 4.19), but this also increases the velocity shear and thus canopy shear production (Equation 4.20), which contributes to near-bed turbulence via turbulent transport (Figures A3.2 and A3.4). The changes in wake production and turbulent transport are complementary, resulting in $k_{t,nb}/U^2$ that is almost invariant to ah (Figure 4-5d, $H/h > 2$). Because the near-bed TKE is insensitive to ah in this regime, the dependence of sediment transport on near-bed velocity comes into play (see discussion in 4.3.2 around Equation 4.7), so that for $H/h > 2$, cases with higher ah and smaller U_{nb}, yield weaker sediment transport (Figure 4-5e, for $H/h > 2$). Further, in this regime, both $k_{t,nb}/U^2$ and U_{nb}/U decrease to values smaller than that of the unvegetated case (Figure 4-5b and 4-5d), such that sediment transport is reduced to below that of a bare unvegetated bed for $H/h > 2$ (Figure 4-5e).

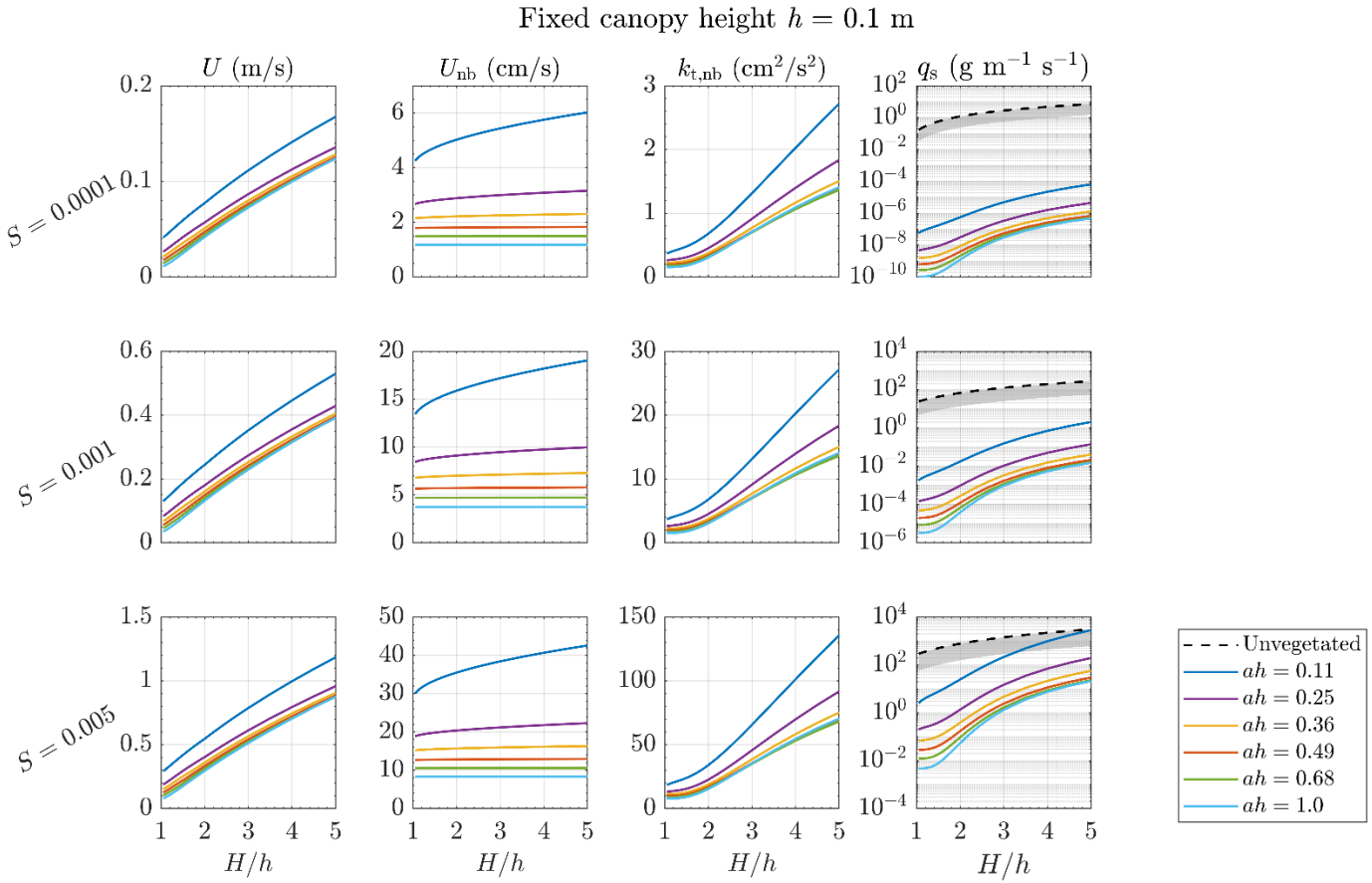

Figure 4-6. Modeled depth-averaged velocity (U), near-bed velocity (U_{nb}), near-bed TKE ($k_{t,nb}$), and sediment transport rate (q_s) under constant hydrodynamic forcing (energy slope, S, from top to bottom: $S = 0.0001$, 0.001, 0.005) in canopies of submerged rigid vegetation. See model details in Section 4.3.3. Canopies had stem diameter $d = 1.3$ cm and height $h = 10$ cm. Bed sediment $d_{50} = 0.35$ mm. Flow depth was varied from $H = 10$ cm to 50 cm, corresponding to the horizontal axis $H/h = 1$ to 5. Solid curves represent model results, with color distinguishing canopy density. Black dashed curves in right-most column show sediment transport rate for bare bed (see A3.2 in Appendices for details). Gray band represents transport rates with bedforms (Wong & Parker, 2006).

The previous paragraph compared conditions with the same channel velocity U as vegetation density and submergence ratio were varied, which is consistent with the present and many previous laboratory studies. Under the same channel velocity but different canopies, the canopy drag could vary with the density and submergence of vegetation, thus producing different water surface or bed slopes (energy slopes). However, in the field, it is often the case that the controlling boundary condition is a constant energy slope (Fagherazzi et al., 1999). With this constraint, the density and submergence of vegetation have a strong influence on the channel velocity, which in turn impacts turbulence and bedload transport. To have a complete picture of field conditions, it is important to consider trends with constant energy slope. Using S (= 1×10^{-4}, 1×10^{-3}, and 5×10^{-3}) to define the friction velocity (Equation 4.12), Equations 4.8, 4.9−4.12, 4.16, 4.17, and 4.24 were used to predict near-bed velocity, turbulence, and bedload transport, with stem diameter d = 1.3 cm, canopy height h = 10 cm, and median grain size d_{50} = 0.35 mm. The canopy density was varied from 0.11 to 1.0, for which canopy shear turbulence is present ($ah > 0.1$).

Figure 4-6 shows how canopy density and submergence ratio control velocity, turbulence, and bedload transport under constant energy slope S. In contrast to conditions constrained to have the same channel velocity (Figure 4-5), with a constant slope, turbulence and bedload transport increase with increasing submergence ratio, reflecting the increase in channel average velocity (Figure 4-6). For the same canopy density (ah), the channel average velocity is lowest for emergent conditions (H/h = 1) and increases as H/h increases (Figure 4-6, first column). However, the near-bed velocity only increases with submergence ratio (H/h) for sparse canopies ($ah < 0.36$, Figure 4-6, second column). For denser canopies ($ah > 0.36$), the penetration of turbulent stress is limited, i.e., $\delta_e = \frac{1}{3}(C_D a)^{-1} < h$, so that the near-bed velocity is only a function of the energy gradient (U_S, Equation 4.10) and independent of H/h. The downward transport of turbulence generated in the canopy shear layer enhances the near-bed TKE. Because shear and shear production increase with the velocity difference, $U-U_{nb}$, $k_{t,nb}$ increases with increasing H/h (Figures 4-6, first through third columns), which in turn leads to increasing sediment

transport with increasing degree of submergence (Figure 4-6, last column). For the same submergence (H/h), as canopy density (ah) and thus drag increases, both the depth-averaged and near-bed flows are reduced. The near-bed turbulence decreases with increasing ah, but reaches a nearly constant value for dense canopies ($ah > 0.36$), corresponding to the trade-off between decreased stem wake production and increased canopy shear production discussed with Figure 4-5. The trends in sediment transport rate reflect the trends in $k_{t,nb}$ and U_{nb}, increasing as H/h increases and ah decreases. It is worth noting that at high submergence ($H/h > 3$), the bedload transport (q_s) reaches a limit for dense canopies such that the curves for $ah > 0.36$ converge. This is because with deep submergence, $\alpha\sqrt{k_{t,nb}} \gg U_{nb}$, so that $f = \frac{\left(U_{nb}+\alpha\sqrt{k_{t,nb}}\right)^2}{\left(\frac{\rho_s}{\rho}-1\right)gd_{50}}$ is dominated by $k_{t,nb}$, which also has convergent behavior for $ah > 0.36$ (Figure 4-6). For comparison, in Figure A3-7, flow depth was held constant, and canopy height was varied for the same range of submergence, $1 \leq H/h \leq 5$, which yielded similar trends as Figure 4-6.

In addition, many submerged aquatic plants are flexible, so that they bend in response to the flow, which reduces their height and frontal area. For a single flexible blade tied to a stem with negligible height, Luhar and Nepf (2011, 2013) proposed a model to predict the ratio of deflected canopy height, h, to the blade length l, which is also the height of the fully erect canopy:

$$\frac{h}{l} = 1 - \frac{1-Ca^{-\frac{1}{4}}}{1+Ca^{-\frac{3}{5}}\left(4+B^{\frac{3}{5}}\right)+Ca^{-2}(8+B^2)}, \tag{4.25}$$

in which the Cauchy number

$$Ca = \frac{1}{2}\frac{\rho C_D b U_{hor}^2 l^3}{EI} \tag{4.26}$$

is the ratio of drag force bending the stem to elastic restoring force which resists bending. The buoyancy parameter

$$B = \frac{|\rho-\rho_{veg}|gbtl^3}{EI} \tag{4.27}$$

is the ratio of buoyant restoring force to elastic restoring force. ρ and ρ_{veg} are the density of water and vegetation, respectively. b is the blade width, t the blade thickness, U_{hor} the

horizontal velocity acting on the blade, g the gravitational acceleration, E the Young's modulus of the blade, and $I = \frac{bt^3}{12}$ the bending moment of inertia of the blade. To characterize the drag reduction by reconfiguration, Luhar and Nepf (2011) also defined an effective blade length, l_{eff}, as the height of erect rigid blade that produces the same total drag as a reconfiguring flexible blade:

$$\frac{l_{\text{eff}}}{l} = 1 - \frac{1-0.9Ca^{-\frac{1}{3}}}{1+Ca^{-\frac{3}{2}}\left(8+B^{\frac{3}{2}}\right)}. \tag{4.28}$$

The equations above can be used to describe the reconfiguration of a submerged canopy, which in turn changes the velocity and TKE within the canopy and the resulting bedload transport. As an example, consider a flexible canopy of *Zostera marina* (eelgrass), a common seagrass. The canopy is sufficiently long, so that the downstream flow is fully developed. We assume no change in the canopy frontal area a during configuration (Razmi et al., 2020). Measurements have shown that blades of *Zostera marina* are close to neutrally buoyant, that is, $\rho_{\text{veg}} \approx \rho$ (Vettori & Marjoribanks, 2021), thus we assume the buoyancy parameter $B = 0$. For the blade geometry and mechanical properties, Young's modulus of the blade $E = 2 \times 10^8$ Pa, blade width $b = 4$ mm, blade thickness $t = 0.3$ mm, blade length $l = 50$ cm (Vettori & Marjoribanks, 2021), and drag coefficient $C_D = 1.95$ (Luhar et al., 2017). For the horizontal velocity acting on the blade, we assume $U_{\text{hor}} = U_{\text{canopy}}$, and Cauchy number Ca, deflected canopy height h_{def}, and effective blade length l_{eff} are solved iteratively. For the erect canopy density al, Luhar et al. (2010) summarized that al ranges from 3.2 to 23.1 for *Zostera marina*, and 0.5 to 40.8 for a range of seagrass species (see Table 3 in Luhar et al., 2010). In this model, we choose $al = 0.5$, 5, and 20 to represent *Zostera marina* and to extend to canopies of other species of flexible vegetation. For a seabed with median grain size $d_{50} = 0.35$ mm (medium sand), and assuming a fixed energy slope $S = 5\times10^{-5}$ based on typical tidal forcing ($S = O(10^{-5}\sim10^{-4})$, e.g., Burke & Stolzenbach, 1983; Leopold et al., 1993; Burchard, 1999; Ensign et al., 2013), we vary the flow depth $H = 0.5$ m to 2 m to examine the impact of flexible canopy on flow and bedload transport. Specifically, before varying the erect canopy density, the model was run to compare with flume results in Le Bouteiller and Venditti (2014), who constructed a nearly neutrally buoyant flexible

canopy with $E = 2 \times 10^8$ Pa, $b = 7.5$ mm, $l = 25.5$ cm, $t = 0.2$ mm, $a = 6$ m^{-1}, leading to $al = 1.5$. Le Bouteiller and Venditti (2014) reported a deflected canopy height $h_{def} = 4.5$ cm and in-canopy velocity $U_{canopy} = 9.4 \pm 7.2$ cm/s (Mean ± SD), whereas the model developed above predicts $h_{def} = 4.3$ cm and $U_{canopy} = 14.8$ cm/s, agreeing with their measurements.

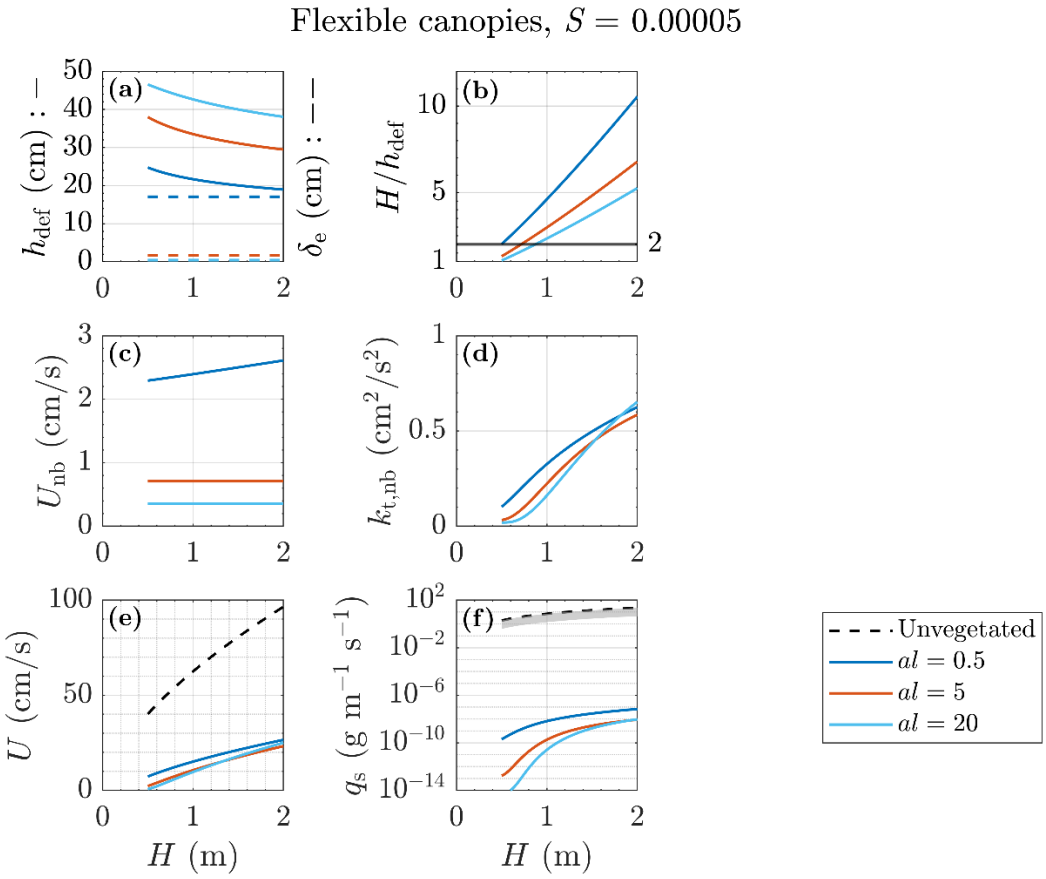

Figure 4-7. Modeled deflected canopy height (h_{def}) and penetration length (δ_e), submergence ratio (H/h_{def}), near-bed velocity (U_{nb}), near-bed TKE ($k_{t,nb}$), depth-averaged velocity (U), and sediment transport rate (q_s) under constant hydrodynamic forcing (constant energy slope $S = 5\times10^{-5}$) in canopies of submerged flexible vegetation. See model details in Section 4.3.3. Canopies had blade elasticity $E = 2 \times 10^8$ Pa, blade width $b = 4$ mm, blade thickness $t = 0.3$ mm, blade length $l = 50$ cm, and erect canopy density $al = 0.5$, 5, and 20. Bed sediment $d_{50} = 0.35$ mm. Flow depth was varied from $H = 0.5$ m to 2 m, corresponding to the horizontal axis. Solid curves represent model results, with color distinguishing canopy density. Black dashed curves in subplots (a) and (f) show bare unvegetated bed scenarios (see A3.2 for details). Gray band represents transport rates with bedforms (Wong & Parker, 2006).

Figure 4-7 shows how flexible canopies of different density respond to the fixed hydrodynamic forcing. First, in response to the flow, flexible canopies exhibit significant reduction in their height (Figure 4-7a). Because sparser canopies are associated with higher in-canopy velocity compared to denser canopies, the blades within the sparser canopies bend more than denser canopies, resulting in lower deflected canopy height (Figure 4-7a). The canopy height decreases by up to 60% for $al = 0.5$ (deep blue curve), and 20% for $al = 20$ (light blue curve). Due to this canopy deflection, as the flow depth H increases, the submergence ratio H/h_{def} also increases, whose degree of increase is greater than the rigid canopies. The sparser the canopy is, the more deflection is observed (Figure 4-7b), associated with greater dominance of near-bed turbulence by the canopy shear production ($H/h_{def} > 2$, black horizontal line in Figure 4-7b; see discussion of Figure 4-5). Second, the trends of near-bed velocity (Figure 4-7c) and turbulence (Figure 4-7d) are generally consistent with those in rigid canopies (Figure 4-6). As H increases, the canopy height is reduced to close to the penetration length for $al = 0.5$ (Figure 4-7a), so that the near-bed region is more subject to the canopy shear vortices, leading to slight increase in its near-bed velocity (Figure 4-7c). For denser canopies ($al = 5$ and 20), the penetration length is much smaller than the canopy height, so that the near-bed velocity is not influenced by canopy shear. The near-bed turbulence increases as H increases because the submergence ratio H/h_{def} also increases, associated with more downward transport of canopy shear turbulence. Third, bedload transport (Figure 4-7f) increases with increasing submergence ratio and decreasing canopy density, reflecting the increase in channel average velocity (Figure 4-7e), which is also consistent with the trends in rigid model canopies. Finally, because it contributes additional drag, the presence of the canopy significantly reduces the channel average velocity. For example, compared with the unvegetated bed, the depth-averaged velocity under the same energy slope $S = 5\times10^{-5}$ is reduced by up to 70% with flexible canopies (Figure 4-7e), reducing sediment transport to negligible (Figure 4-7f).

The model results provide some conclusions relevant to real-world applications. First, the scenarios considered cover a wide range of real field conditions, and in all cases with a constant slope boundary condition the bedload transport was reduced compared to bare beds, supporting the general conclusion that submerged aquatic vegetation reduces

erosion and sediment transport. This is consistent with Le Bouteiller and Vendetti (2014), who observed that bedload transport was reduced within a submerged patch of flexible model seagrass. Second, the saturated sediment transport rate for dense canopies ($ah >$ 0.36 in model rigid canopies, and the model flexible canopies) suggests that there could be an optimal canopy density that maximizes bed protection and habitat creation for a given biomass investment. This can point to an optimum in the price-performance ratio in nature-based erosion control projects. It also suggests a possible energetic optimum for meadow growth.

4.4 Conclusions

Flume experiments in a channel with constant depth-averaged velocity (U) showed that near-bed velocity, turbulence, and bedload transport all decreased as canopy submergence ratio (H/h) increased. However, as canopy density (ah) increased, bedload transport increased in canopies of shallow submergence ($H/h < 2$) but decreased in deeply submerged canopies ($H/h > 2$). As H/h increased, the source of near-bed turbulence shifted from local stem wake production to the turbulence generated in the shear layer at the canopy top. A simple model that relates enhanced near-bed turbulence to the canopy shear was derived to predict near-bed turbulence within a submerged canopy. Bedload transport rate was found to be predominantly correlated with near-bed turbulence but also weakly correlated with near-bed velocity. A flow parameter that incorporates the near-bed velocity and turbulence was shown to predict bedload transport, which can facilitate modeling of coastal and alluvial morphodynamics. The new models were used to explore field conditions with constant water surface or bed slope (S) and flexible vegetation. In the modeled scenarios, for a constant S, bedload transport increase with increasing submergence ratio (H/h) and decreasing canopy density (ah), but is always less than the corresponding bare unvegetated bed condition, illustrating that submerged aquatic vegetation contributes to reducing erosion.

Chapter 4 References

Ancey, C., Davison, A. C., Böhm, T., Jodeau, M., & Frey, P. (2008). Entrainment and motion of coarse particles in a shallow water stream down a steep slope. *Journal of Fluid Mechanics*, 595, 83–114. doi:10.1017/S0022112007008774

Armanini, A., & Cavedon, V. (2019). Bed-load through emergent vegetation. *Advances in Water Resources*, 129, 250–259. doi:10.1016/j.advwatres.2019.05.021

Barbier, E. B., Hacker, S. D., Kennedy, C., Koch, E. W., Stier, A. C. & Silliman, B. R. (2011). The value of estuarine and coastal ecosystem services. *Ecological Monographs*, 81: 169–193. doi:10.1890/10-1510.1

Belcher, S. E., Jerram, N., & Hunt, J. C. R. (2003). Adjustment of a turbulent boundary layer to a canopy of roughness elements. *Journal of Fluid Mechanics*, 488: 369–398. doi:10.1017/S0022112003005019

Burchard, H. (1999). Recalculation of surface slopes as forcing for numerical water column models of tidal flow. *Applied Mathematical Modelling*, 23(10), 737-755. doi:10.1016/S0307-904X(99)00008-6

Burke, R. W., & Stolzenbach, K. D. (1983). *Free Surface Flow Through Salt Marsh Grass*. MIT Sea Grant College Program. https://repository.library.noaa.gov/view/noaa/9839/noaa_9839_DS1.pdf

Celik, A. O., Diplas, P., Dancey, C. L., & Valyrakis, M. (2010). Impulse and particle dislodgement under turbulent flow conditions. *Physics of Fluids*, 22(4), 46601. doi:10.1063/1.3385433

Chen, Z., Jiang, C., & Nepf, H. (2013). Flow adjustment at the leading edge of a submerged aquatic canopy. *Water Resources Research*, 49(9), 5537–5551. doi:10.1002/wrcr.20403

Clarke, S. J. (2002). Vegetation growth in rivers: influences upon sediment and nutrient dynamics. *Progress in Physical Geography: Earth and Environment*, 26(2), 159–172. doi:10.1191/0309133302pp324ra

Conde-Frias, M., Ghisalberti, M., Lowe, R.J., Abdolahpour, M., & Etminan, V. (2023). The Near-Bed Flow Structure and Bed Shear Stresses Within Emergent Vegetation. *Water Resources Research*, 59(4), e2022WR032499. doi:10.1029/2022WR032499

Costanza, R., d'Arge, R., de Groot, R., Farber, S., Grasso, M., Hannon, B., ... & van den Belt, M. (1997). The value of the world's ecosystem services and natural capital. *Nature*, 387(6630), 253–260. doi:10.1038/387253a0

Deitrick, A.R., Ralston, D.K., Esposito, C.R., Baustian, M.M., Burgos, M.B., Courtois, A.J., & Nepf, H. (2024). Vegetation-Generated Turbulence Does Not Impact the Erosion of Natural Cohesive Sediment. *Geophysical Research Letters*, 51(14), e2024GL109730. doi:10.1029/2024GL109730

Einstein, H. A. (1942). Formulas for the Transportation of Bed Load. *Transactions of the American Society of Civil Engineers*, 107(1), 561–577.

Engelund, F., & Hansen, E. (1967). *A monograph on sediment transport in alluvial streams*. Teknisk Forlag.

Ensign, S.H., Doyle, M.W., & Piehler, M.F. (2013). The effect of tide on the hydrology and morphology of a freshwater river. *Earth Surface Processes and Landforms*, 38(6), 655-660. doi:10.1002/esp.3392

Etminan, V., Ghisalberti, M., & Lowe, R. J. (2018). Predicting Bed Shear Stresses in Vegetated Channels. *Water Resources Research*, 54(11), 9187–9206. doi:10.1029/2018WR022811

Etminan, V., Lowe, R. J., & Ghisalberti, M. (2017). A new model for predicting the drag exerted by vegetation canopies. *Water Resources Research*, 53(4), 3179–3196. doi:10.1002/2016WR020090

Fagherazzi, S., Bortoluzzi, A., Dietrich, W.E., Adami, A., Lanzoni, S., Marani, M., & Rinaldo, A. (1999). Tidal networks: 1. Automatic network extraction and preliminary scaling features

from digital terrain maps. *Water Resources Research*, 35(12), 3891-3904. doi:10.1029/1999WR900236

Fagherazzi, S., Bryan, K., & Nardin, W. (2017). Buried Alive or Washed Away: The Challenging Life of Mangroves in the Mekong Delta. *Oceanography*, 30(3), 48–59. doi:10.5670/oceanog.2017.313

Fourqurean, J. W., Duarte, C. M., Kennedy, H., Marbà, N., Holmer, M., Mateo, M. A., ... & Serrano, O. (2012). Seagrass ecosystems as a globally significant carbon stock. *Nature Geoscience*, 5(7), 505–509. doi:10.1038/ngeo1477

Ghisalberti, M. (2009). Obstructed shear flows: similarities across systems and scales. *Journal of Fluid Mechanics*, 641, 51–61. doi:10.1017/S0022112009992175

Huthoff, F., Augustijn, D. C. M., & Hulscher, S. J. M. H. (2007). Analytical solution of the depth-averaged flow velocity in case of submerged rigid cylindrical vegetation. *Water Resources Research*, 43(6), W06413. doi:10.1029/2006WR005625

Ishii, J. (2023). *The influence of current and ripple development on seagrass transplant survival* [Master's thesis, Massachusetts Institute of Technology]. DSpace@MIT. https://dspace.mit.edu/handle/1721.1/151912

Jordanova, A. A., & James, C. S. (2003). Experimental Study of Bed Load Transport through Emergent Vegetation. *Journal of Hydraulic Engineering*, 129(6), 474–478. doi:10.1061/(ASCE)0733-9429(2003)129:6(474)

King, A. T., Tinoco, R. O., & Cowen, E. A. (2012). A k–ε turbulence model based on the scales of vertical shear and stem wakes valid for emergent and submerged vegetated flows. *Journal of Fluid Mechanics*, 701, 1–39. doi:10.1017/jfm.2012.113

Le Bouteiller, C., & Venditti, J. G. (2014). Vegetation-driven morphodynamic adjustments of a sand bed. *Geophysical Research Letters*, 41(11), 3876-3883. doi:10.1002/2014GL060155

Leopold, L., Collins, J., & Collins, L. (1993). Hydrology of some tidal channels in estuarine marshland near San Francisco. *CATENA*, 20(5), 469-493. doi:10.1016/0341-8162(93)90043-O

Liu, C., Shan, Y., & Nepf, H. (2021). Impact of Stem Size on Turbulence and Sediment Resuspension Under Unidirectional Flow. *Water Resources Research*, 57(3), e2020WR028620. doi:10.1029/2020WR028620

Lu, Y., Cheng, N., & Wei, M. (2021). Formulation of bed shear stress for computing bed-load transport rate in vegetated flows. *Physics of Fluids*, 33(11), 115105. doi:10.1063/5.0067851

Luhar, M., Coutu, S., Infantes, E., Fox, S., & Nepf, H. (2010). Wave-induced velocities inside a model seagrass bed. *Journal of Geophysical Research: Oceans*, 115(C12), C12005. doi:10.1029/2010JC006345

Luhar, M., Infantes, E., & Nepf, H. (2017). Seagrass blade motion under waves and its impact on wave decay. *Journal of Geophysical Research: Oceans*, 122(5), 3736-3752. doi: 10.1002/2017JC012731

Luhar, M., Rominger, J., & Nepf, H. (2008). Interaction between flow, transport and vegetation spatial structure. *Environmental Fluid Mechanics*, 8(5-6), 423–439. doi:10.1007/s10652-008-9080-9

Meyer-Peter, E., & Müller, R. (1948). Formulas for Bed Load Transport. In *Proceedings of 2nd meeting of the International Association for Hydraulic Structures Research*, Stockholm, Appendix 2, 39–64.

Moore, K. A. (2004). Influence of Seagrasses on Water Quality in Shallow Regions of the Lower Chesapeake Bay. *Journal of Coastal Research*, 10045, 162–178. doi:10.2112/SI45-162.1

Nardin, W., & Edmonds, D. A. (2014). Optimum vegetation height and density for inorganic sedimentation in deltaic marshes. *Nature Geoscience*, 7(10), 722–726. doi:10.1038/ngeo2233

Nepf, H. M. (1999). Drag, turbulence, and diffusion in flow through emergent vegetation. *Water Resources Research*, 35(2), 479–489. doi:10.1029/1998WR900069

Nepf, H. M. (2012). Flow and Transport in Regions with Aquatic Vegetation. *Annual Review of Fluid Mechanics*, 44(1), 123–142. doi:10.1146/annurev-fluid-120710-101048

Nepf, H. M., & Vivoni, E. R. (2000). Flow structure in depth-limited, vegetated flow. *Journal of Geophysical Research: Oceans*, 105(C12), 28547–28557. doi:10.1029/2000JC900145

Nepf, H., Ghisalberti, M., White, B., & Murphy, E. (2007). Retention time and dispersion associated with submerged aquatic canopies. *Water Resources Research*, 43(4), W04422. doi:10.1029/2006WR005362

Nezu, I., & Rodi, W. (1986). Open-channel Flow Measurements with a Laser Doppler Anemometer. *Journal of Hydraulic Engineering*, 112(5), 335–355. doi:10.1061/(ASCE)0733-9429(1986)112:5(335)

Niño, Y., & Garcia, M. H. (1996). Experiments on particle-turbulence interactions in the near-wall region of an open channel flow: implications for sediment transport. *Journal of Fluid Mechanics*, 326, 285–319. doi:10.1017/S0022112096008324

Nortek. (2021). *How do I enhance Correlation and SNR?* Retrieved January, 15, 2023, from https://support.nortekgroup.com/hc/en-us/articles/360029819951-How-do-I-enhance-Correlation-and-SNR

Paola, C., Twilley, R. R., Edmonds, D. A., Kim, W., Mohrig, D., Parker, G., ... & Voller, V. R. (2011). Natural Processes in Delta Restoration: Application to the Mississippi Delta. *Annual Review of Marine Science*, 3(1), 67–91. doi:10.1146/annurev-marine-120709-142856

Poggi, D., Porporato, A., Ridolfi, L., Albertson, J. D., & Katul, G. G. (2004). The Effect of Vegetation Density on Canopy Sub-Layer Turbulence. *Boundary-Layer Meteorology*, 111(3), 565–587. doi:10.1023/B:BOUN.0000016576.05621.73

Radice, A., & Ballio, F. (2008). Double-average characteristics of sediment motion in one-dimensional bed load. *Acta Geophysica*, 56(3), 654–668. doi:10.2478/s11600-008-0015-0

Raupach, M. R., Finnigan, J. J., & Brunet, Y. (1996). Coherent Eddies and Turbulence in Vegetation Canopies: The Mixing-Layer Analogy. In: Garratt, J.R., Taylor, P.A. (eds) *Boundary-Layer Meteorology 25th Anniversary Volume, 1970–1995* (pp. 351–382). Springer. doi:10.1007/978-94-017-0944-6_15

Razmi, A. M., Chamecki, M., & Nepf, H. M. (2020). Efficient numerical representation of the impacts of flexible plant reconfiguration on canopy posture and hydrodynamic drag. *Journal of Hydraulic Research*, 58(5), 755-766. doi:10.1080/00221686.2019.1671511

Roseberry, J. C., Schmeeckle, M. W., & Furbish, D. J. (2012). A probabilistic description of the bed load sediment flux: 2. Particle activity and motions. *Journal of Geophysical Research: Earth Surface*, 117(F3), F03032. doi:10.1029/2012JF002353

Rubey, W. W. (1933). Settling velocity of gravel, sand, and silt particles. *American Journal of Science*, s5-25(148), 325–338. doi:10.2475/ajs.s5-25.148.325

Salim, S., Pattiaratchi, C., Tinoco, R., Coco, G., Hetzel, Y., Wijeratne, S., & Jayaratne, R. (2017). The influence of turbulent bursting on sediment resuspension under unidirectional currents. *Earth Surface Dynamics*, 5(3), 399–415. doi:10.5194/esurf-5-399-2017

Shan, Y., Zhao, T., Liu, C., & Nepf, H. (2020). Turbulence and Bed Load Transport in Channels With Randomly Distributed Emergent Patches of Model Vegetation. *Geophysical Research Letters*, 47(12), e2020GL087055. doi:10.1029/2020GL087055

Shields, A. (1936). *Anwendung der Aehnlichkeitsmechanik und der Turbulenzforschung auf die Geschiebebewegung* [*Application of similarity mechanics and turbulence research on shear flow*]. Mitteilungen der Preußischen Versuchsanstalt für Wasserbau (in German). 26. Berlin: Preußische Versuchsanstalt für Wasserbau.

Shih, W., & Diplas, P. (2018). A Unified Approach to Bed Load Transport Description Over a Wide Range of Flow Conditions via the Use of Conditional Data Treatment. *Water Resources Research*, 54(5), 3490–3509. doi:10.1029/2017WR022373

Stacey, M. T., Monismith, S. G., & Burau, J. R. (1999). Measurements of Reynolds stress profiles in unstratified tidal flow. *Journal of Geophysical Research: Oceans*, 104(C5), 10933–10949. doi:10.1029/1998JC900095

Stoesser, T., Kim, S. J., & Diplas, P. (2010). Turbulent Flow through Idealized Emergent Vegetation. *Journal of Hydraulic Engineering*, 136(12), 1003–1017. doi:10.1061/(ASCE)HY.1943-7900.0000153

Sukhodolov, A. N., & Sukhodolova, T. A. (2010). Case Study: Effect of Submerged Aquatic Plants on Turbulence Structure in a Lowland River. *Journal of Hydraulic Engineering*, 136(7), 434–446. doi:10.1061/(ASCE)HY.1943-7900.0000195

Sukhodolov, A., & Sukhodolova, T. (2006). Evolution of mixing layers in turbulent flow over submersed vegetation: Field experiments and measurement study. In *River Flow 2006*: *Proceedings of the International Conference on Fluvial Hydraulics, Lisbon, Portugal, 6-8 September 2006* (pp. 525–534), CRC Press.

Sumer, B. M., Chua, L. H. C., Cheng, N.-S., & Fredsøe, J. (2003). Influence of Turbulence on Bed Load Sediment Transport, *Journal of Hydraulic Engineering*, 129(8), 585–596. doi:10.1061/(ASCE)0733-9429(2003)129:8(585)

Tang, H., Wang, H., Liang, D., Lv, S., & Yan, L. (2013). Incipient motion of sediment in the presence of emergent rigid vegetation. *Journal of Hydro-environment Research*, 7(3), 202–208. doi:10.1016/j.jher.2012.11.002

Tanino, Y., & Nepf, H.M. (2008). Lateral dispersion in random cylinder arrays at high Reynolds number. *Journal of Fluid Mechanics*, 600, 339–371. doi:10.1017/S0022112008000505

Tinoco, R.O., & Coco, G. (2018). Turbulence as the Main Driver of Resuspension in Oscillatory Flow Through Vegetation. *Journal of Geophysical Research: Earth Surface*, 123(5), 891–904. doi:10.1002/2017JF004504

Tseng, C., & Tinoco, R. O. (2021). A Two-Layer Turbulence-Based Model to Predict Suspended Sediment Concentration in Flows with Aquatic Vegetation. *Geophysical Research Letters*, 48(3), e2020GL091255. doi:10.1029/2020GL091255

Vettori, D., & Marjoribanks, T. I. (2021). Temporal Variability and Within-Plant Heterogeneity in Blade Biomechanics Regulate Flow-Seagrass Interactions of Zostera marina. *Water Resources Research*, 57(3), e2020WR027747. doi:10.1029/2020WR027747

Wong, M., & Parker, G. (2006). Reanalysis and Correction of Bed-Load Relation of Meyer-Peter and Müller Using Their Own Database. *Journal of Hydraulic Engineering*, 132(11), 1159–1168. doi: 10.1061/(ASCE)0733-9429(2006)132:11(1159)

Wu, H., Cheng, N.-S., & Chiew, Y.-M. (2021). Bed-load Transport in Vegetated Flows: Phenomena, Parametrization, and Prediction. *Water Resources Research*, 57(4), e2020WR028143. doi:10.1029/2020WR028143

Xu, Y., & Nepf, H. (2020). Measured and Predicted Turbulent Kinetic Energy in Flow Through Emergent Vegetation With Real Plant Morphology. *Water Resources Research*, 56(12), e2020WR027892. doi:10.1029/2020WR027892

Xu, Y., Li, D., & Nepf, H. (2022). Sediment Pickup Rate in Bare and Vegetated Channels. *Geophysical Research Letters*, 49(21), e2022GL101279. doi:10.1029/2022GL101279

Yager, E. M., & Schmeeckle, M. W. (2013). The influence of vegetation on turbulence and bed load transport. *Journal of Geophysical Research: Earth Surface*, 118(3), 1585–1601. doi:10.1002/jgrf.20085

Yang, J. Q., & Nepf, H. M. (2018). A Turbulence-Based Bed-Load Transport Model for Bare and Vegetated Channels. *Geophysical Research Letters*, 45(19), 10,428–10,436. doi:10.1029/2018GL079319

Yang, J. Q., & Nepf, H. M. (2019). Impact of Vegetation on Bed Load Transport Rate and Bedform Characteristics. *Water Resources Research*, 55(7), 6109–6124. doi:10.1029/2018WR024404

Yang, J. Q., Chung, H., & Nepf, H. M. (2016). The onset of sediment transport in vegetated channels predicted by turbulent kinetic energy. *Geophysical Research Letters*, 43(21), 11,261–11,268. doi:10.1002/2016GL071092

Zhang, J., Lei, J., Huai, W., & Nepf, H. (2020). Turbulence and Particle Deposition Under Steady Flow Along a Submerged Seagrass Meadow. *Journal of Geophysical Research: Oceans*, 125(5), e2019JC015985. doi:10.1029/2019JC015985

Zhao, T., & Nepf, H. M. (2021). Turbulence Dictates Bedload Transport in Vegetated Channels Without Dependence on Stem Diameter and Arrangement. *Geophysical Research Letters*, 48(21), e2021GL095316. doi:10.1029/2021GL095316

This page intentionally left blank

Chapter 5 Bedform Dynamics in Rigid Submerged Model Canopies

5.1 Introduction

The topographic patterns that form on a mobile sediment bed by unidirectional or oscillatory fluid flows are called bedforms (Southard, 1991; Charru et al., 2013). They are ubiquitous in aeolian environments on Earth (e.g., dunes in a desert; Bagnold, 1941) and other planets (e.g., Mars, Venus, and Titan; Bourke et al., 2010), as well as in subaqueous environments (Best, 2005). Bedforms have scales that are orders of magnitude greater than the grains, varying from centimeters (e.g., subaqueous ripples) to kilometers (e.g., dunes in a desert), and smaller secondary bedforms may be superimposed on the larger primary ones (Charru et al., 2013). Depending on the overlying flow and sediment supply, bedforms can migrate and change their shape (Engelund & Fredsøe, 1982). In some cases, the migration rate of bedforms may be used to estimate bedload transport (van den Berg, 1987). This chapter considers the migrating bedforms formed in the submerged model canopy considered in the laboratory study, and it will not discuss scour holes around individual vegetation elements.

Vegetation and bedforms can coexist in nature, but the interaction between them is complicated. In aeolian environments, vegetation can decelerate the flow and cause particle deposition around it, forming nebkhas (Arabic: نبكة, lit.: small, sandy mound; also known as coppice dunes or phytogenetic dunes) and downwind shadow dunes in aeolian environments (Hesp & Smyth, 2017). In subaqueous environments, vegetation may weaken or suppress the emergence and migration of bedforms by generating or trapping cohesive materials (Parsons et al., 2016), reducing in-canopy velocity (Rominger et al., 2010), and/or enhancing near-bed turbulence to promote sheet flow (Yang & Nepf, 2019).

This chapter describes the bedform generated in a submerged model canopy of finite length. At the leading edge of a submerged canopy, the in-canopy flow is not yet decelerated, so that stem-generated turbulence has a longitudinal maximum at this location, which locally erodes sediment. Initially, the sediment eroded near the leading

edge of a submerged canopy forms a bedform within the canopy at a distance into the canopy at which the in-canopy velocity has been reduced from its magnitude at the leading edge. A similar scour and dune formation near the leading edge of a submerged canopy was also reported in Kim et al. (2015) and Le Bouteiller and Venditti (2014). In this study, over time, the dune moved downstream and was gradually flattened due to the streamwise diffusion of sediment. A similar migration was also captured by Le Bouteiller and Venditti (2014). Because the flume recirculated the sediment, the migrating bedform passed from the downstream back to the upstream part of the test section, repeatedly migrating through the test section. In natural environments without artificial sediment recirculation, this recirculation and reappearance of the bedform within the canopy would not be observed. Nevertheless, the observed phenomenon could be of interest to future flume experiments on bedload transport.

5.2 Methods

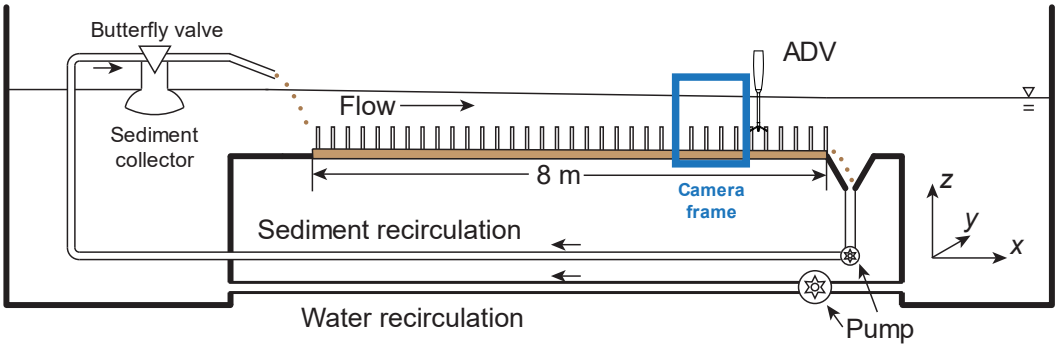

Figure 5-1. Side view of sediment recirculating flume, with sand layer (brown) within an array of submerged cylinders. Brown dots represent sediment in motion. The right-handed coordinates are x (streamwise), y (lateral), and z (vertical). Camera was placed at x = 6.20 m to capture images of side section x = 5.65 to 6.75 m. The dimensions of the glass frame were 110.0 cm (L) x 53.0 cm (H).

A submerged array of cylinders (diameter d = 1.27 cm) in a staggered arrangement was constructed in a 1-m wide and 10.4-m long test section of a sediment recirculating flume (Figure 5-1). The array length (8 m) was sufficient for the velocity

field to reach a fully developed condition (Chen et al., 2013). A sand bed (density ρ_s = 2650 kg/m^3, median grain size d_{50} = 0.35 mm) with an initial thickness of 7.8 ± 0.5 cm was installed along the test section. Initially, the canopy height was h = 10 cm above the top of the sand layer. The dimensionless canopy density was set to ah = 0.11 ($\delta_e = h$, which will be called the sparse canopy) and 0.49 ($\delta_e < h$, which will be called the dense canopy). The targeted channel-averaged velocity U was 40 cm/s, but it varied by up to 15% as the bed level adjusted during specific flow and canopy conditions. The flow depth (H) was varied to produce a range of submergence ratio H/h = 1.5 to 3.5.

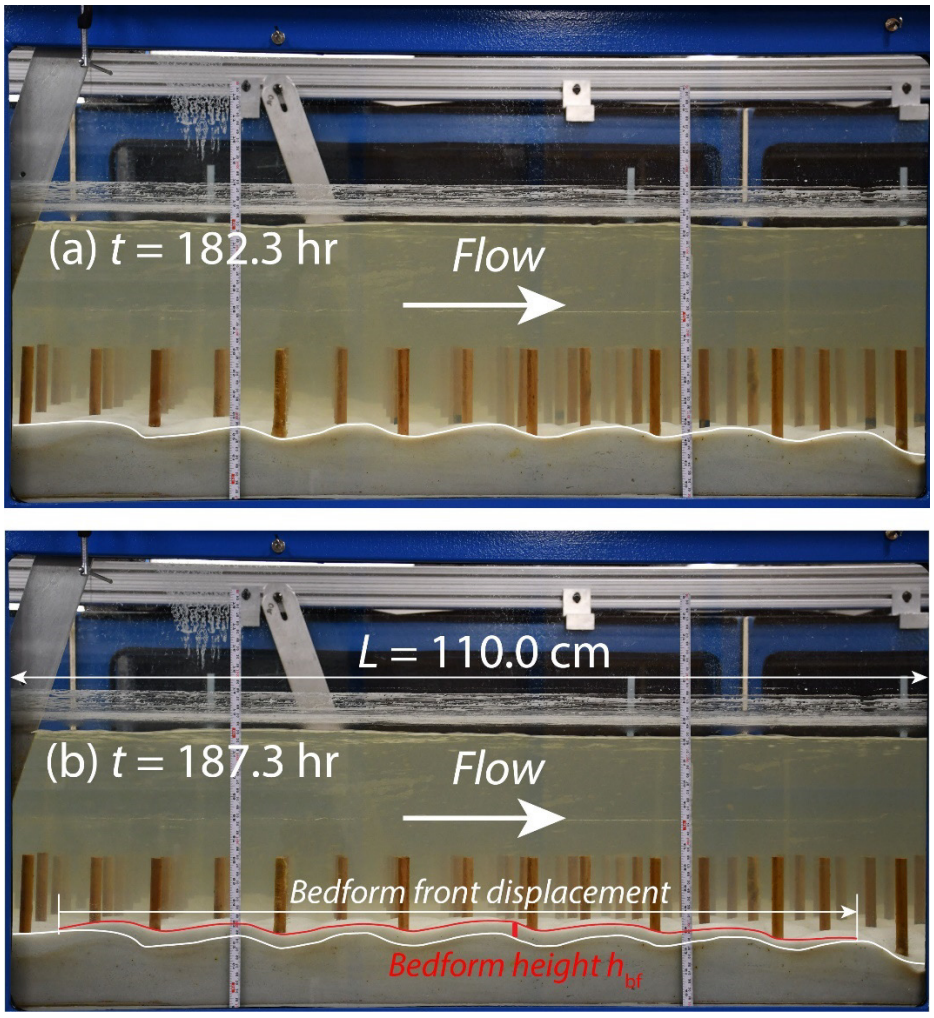

Figure 5-2. Side view of the camera's image frame (dimensions: 110.0 cm (L) x 53.0 cm (H)) of Case S2. The migrating bedform captured within the image frame is marked by the area between white (bed top at t = 182.3 hr) and red (bed top at t = 187.3 hr) curves, with its height h_{bf} marked by a red vertical line.

To observe the bed evolution, a tripod-mounted Canon D7500 camera captured images of a side section (x = 5.65 to 6.75 m) of the channel every 15 min in each run from its start to the end (last sediment transport measurement). The camera view was centered at x = 6.20 m. Because of obstructions in the laboratory, the camera could not be positioned further downstream. For cases with persistent migrating bedforms, camera images were used to determine the bedform position, and height (h_{bf}) and migration rate (c). First, camera images were stepped forward in time until the bedform was observed to enter the upstream edge of the image frame. The image at this time point was set as the reference image and the bed surface was marked by a white curve (Figure 5-2a). Next, the images were stepped forward in time until the bedform front had passed more than 50 cm within the image frame. The bed surface was then marked by a red curve (Figure 5-2b). By overlapping the two images, the migrating bedform was indicated by the area between the white and red curves (Figure 5-2b). The bedform height, h_{bf}, was determined at a position in the image center as the distance between the white and red curves for every cycle available. The bedform migration rate, c, was calculated by dividing the bedform front displacement by the time for the front to migrate over this distance. The standard error was reported as uncertainty for h_{bf} and c.

Depending on the geometry and migration rate of the bedform, the test section may or may not reach an equilibrium state, in which the sediment transport is uniform throughout the test section. However, when present, the bedform migration rate was slow enough, compared to the time needed to run a set of velocity measurements, that one could assume a quasi-equilibrium. Specifically, the study was able to quantify the velocity statistics and sediment transport near the outlet section over a period of sufficiently stationary conditions such that the influence of the migrating bedform could be excluded. The following criteria were used to confirm that local stationary conditions were present. First, the bed elevation at the downstream end of the test section varied by less than 5 mm/hr. Second, the sediment transport varied by less than 15%. This was confirmed using four consecutive measurements of sediment transport rate, and the standard error of this data set should be less than 15% of the set average. For every individual sediment transport rate measurement, sediment was collected by diverting sediment from the recirculation pipe (Figure 5-1) into a mesh bag for 20 min. However, if

the collected sediment weighed more than 50 g, the collection time was then decreased, but to no shorter than 2 min. Each measurement was followed by a 15-min break and was repeated four times to constitute a valid data set. Once the two criteria of locally stationary conditions were met, velocity measurements were performed in the region of stationary conditions. The time to reach this quasi-equilibrium at the measurement position ranged between 30 and 160 hours among all the cases. In cases with weak bedform migration, the quasi-equilibrium state persisted long enough, e.g., more than a day, so that practically this quasi-equilibrium state can be considered an equilibrium state, i.e., local sediment transport rate was uniform everywhere throughout the test section.

5.3 Results and Discussion

The cases were conducted in the following order: S2 (initially flat bed) -> S1 -> S3 -> D3 (initially flat bed) -> D1 -> D2. The sand bed was manually flattened before the first case in each array configuration (sparse S2 and dense D3), so that in these cases the bed evolved from a flat bed with maximum local bed slope smaller than 1/200. To reduce the case run time, for Cases S1, S3, D1, and D2, the sand bed was not flattened but started from the final state of the previous case. It was assumed that given a specific flow rate, the experimental bed would adjust to the same final state regardless of the initial topography.

5.3.1 Initial Bedform Dynamics

The evolution of the channel-scale bedform in Cases S3 (H/h = 3.0) and D3 (H/h = 3.5), with similar submergence ratios, was documented by mobile phone images (Figure A4-1). Because velocity within the canopy was highest at the leading edge, the highest level of turbulence also occurred at the canopy leading edge, producing significant erosion near the leading edge, resulting in a local lowering of the sediment surface over a distance comparable to the adjustment length. The sediment removed from the leading edge initially formed a bedform within the canopy, just downstream of the eroded section at the leading edge. At the same time, the near-bed turbulence within the

canopy, but downstream of the bedform, was also strong enough to generate sediment transport. Sediment mobilized from the downstream end of the canopy was recirculated to the upstream end of the canopy, providing a sediment source into the canopy. At this initial development stage, both the local erosion at the canopy leading edge, and the additional sediment fed from the downstream recirculation contributed to the bedform volume, which increased over time (see Figure 3a1->3a2 and 3b1->3b2). The bedforms had a maximum height comparable with the canopy height.

At the peak of the bedform, the local velocity was enhanced, relative to other locations in the test section, because the water depth and canopy height were locally reduced, resulting in higher channel-average and near-bed velocity. As a result, the sediment transport above the bedform was higher than elsewhere in the canopy, which resulted in the migration of the bedform (see Figure A4-1). Specifically, due to the strong velocity shear near the canopy top, sediment at the bedform top was quickly eroded and resuspended. It was observed that this sediment settled in the wake of bedform as much as two to three canopy heights downstream of the bedform top. In addition, sediment grains rolled down the lee side of the bedform. As a result, the bedform migrated downstream. During migration, the bedforms were flattened by longitudinal sediment diffusivity, becoming just a thin layer of sand that moved over the test section, causing a 1 to 4 cm, cyclical variation in bed elevation and associated changes in sediment transport rate measured at the sediment return at the end of the test section (see Table A4.1).

Table 5.1: Summary of Experimental Cases

Case	#	S1	S2	S3	D1	D2	D3
a	(m^{-1})	1.1	1.1	1.1	4.9	4.9	4.9
h	(cm)	13.3	11.8	10.9	16.7	11.6	10.5
ah	(-)	0.15	0.13	0.12	0.82	0.57	0.51
H	(cm)	18.9	26.8	32.3	24.5	26.8	36.5
H/h	(-)	1.4	2.3	3.0	1.5	2.3	3.5
δ_e	(cm)	6.7	9.5	9.0	7.0	6.5	5.6
$\delta(\delta_e)$	(cm)	0.3	0.4	0.4	1.4	1.0	0.2
q_s	(g m^{-1} s^{-1})	3.8	0.85	0.265	8.2	0.86	0.036
SE(q_s)	(g m^{-1} s^{-1})	0.5	0.06	0.01	0.2	0.02	0.003
Total bedload transport	(g m^{-1} s^{-1})	7.3	1.5	0.265	6.1	0.860	0.036
SE	(g m^{-1} s^{-1})	0.6	0.2	0.010	0.8	0.020	0.003
U	(cm/s)	38.1	41.2	38.9	39.3	45.8	38.4
SE(U)	(cm/s)	1.1	1.3	1.2	2.5	1.8	1.6
U_{canopy}	(cm/s)	32.7	27.0	21.2	26	19.6	12.0
SE(U_{canopy})	(cm/s)	0.9	1.2	1.1	2	1.8	1.2
c	(m/hr)	0.66	0.183	N/A	1.41	N/A	N/A
$\delta(c)$	(m/hr)	0.05	0.009	N/A	0.05	N/A	N/A
h_{bf}	(cm)	1.4	1.6	0	3.5	0	0
$\delta(h_{bf})$	(cm)	0.2	0.2	0	0.4	0	0
Location of initial bedform formation	(cm)	14.5 ± 1.0	63.5 ± 1.0	127.5 ± 1.0	No data	74.0 ± 1.0	75.0 ± 1.0

Notes

(1) Nomenclature

a: Frontal area per unit volume
h: Canopy height
ah: Canopy density
H: Flow depth
H/h: Submergence ratio
δ_e: Penetration length
q_s: Sediment transport rate
U: Channel average velocity
U_{canopy}: Canopy-averaged velocity
c: Bedform migration rate (translation speed of bedform front)
T: Period of bed cycle
h_{bf}: Height of migrating bedform
SE: Standard error

(2) Uncertainties (denoted by $\boldsymbol{\delta}$)

$\frac{\delta a}{a} = \frac{\delta d}{d} = 8\%$, $\delta h = \delta H = 0.5$ cm.

5.3.2 Height of Migrating Bedforms

After the initial formation, the bedform flattened and spread longitudinally as it migrated. Eventually, it became a very long, thin layer, covering a large portion of the text section. At this point, the continued migration of this layer is most clearly observed by the cyclic variation in bed thickness and sediment transport rate. The period and phase of the variation in bed elevation matched the temporal variation of sediment transport, considering the time lag between flow and sediment transport measurements (see Table A4.1), with higher rates of sediment transport correlating with conditions with greater bed thickness, and thus smaller canopy height. This bedform migration and cyclic variation in bed elevation were documented in Cases S1, S2, and D1, but not in Cases S3, D2, and D3. A possible explanation for this difference will be offered later in this section.

For unvegetated beds, van Rijn (1984) described the bedform height produced by steady, unidirectional current, and proposed a transport stage parameter to describe the different regimes of sediment transport:

$$T_{\mathrm{s}} = \frac{\tau_{\mathrm{bs}}}{\tau_{\mathrm{cr}}} - 1, \tag{5.1}$$

which is the excess grain-scale shear stress normalized by the critical stress threshold. Here τ_{cr} is the critical bed shear stress for sediment motion, and $\tau_{\mathrm{bs}} = \rho C_{\mathrm{fs}} U^2$ is the bed shear stress due to grain friction. For $T_{\mathrm{s}} \leq 0$ (no sediment motion) or $T_{\mathrm{s}} \geq 25$ (sheet flow without bedforms), no bedforms will be formed. In between these two regimes, the bedform height, h_{bf}, may be predicted from the empirical relation

$$h_{\mathrm{bf}} = 0.11H \left(\frac{d_{50}}{H}\right)^{0.3} (1 - e^{-0.5T_{\mathrm{s}}})(25 - T_{\mathrm{s}}), \tag{5.2}$$

in which H is the flow depth, and d_{50} the median grain size. Equation 5.2 is accurate to within a factor of 2 (see Figure 2 in van Rijn, 1984). Here, I considered whether this relation would apply on a sand bed with a submerged model canopy.

In this study, the estimated grain Reynolds number $Re_{\mathrm{p}} = \frac{u_* d_{50}}{\nu}$ was slightly above the smooth turbulent flow threshold $Re_{\mathrm{p}} = 5$, so for simplicity, we shall assume that the sediment boundary could be modeled as smooth turbulent, for which the grain friction coefficient can be estimated as follows (Julien, 2010):

$$\frac{1}{\sqrt{C_{\mathrm{fs}}}} = \frac{U}{u_*} = 5.75 \lg\left(\frac{u_* H}{\nu}\right) + 3.25, \tag{5.3}$$

in which u_* is the friction velocity. With U the channel average velocity, Equation 5.3 was used estimate $\tau_{\mathrm{bs}} = \rho C_{\mathrm{fs}} U^2$. Ishii (2023)'s study with the same sediment (d_{50} = 0.35 mm) yielded a dimensionless critical shear stress, $\theta_{\mathrm{cr}} = \frac{\tau_{\mathrm{cr}}}{(\rho_{\mathrm{s}} - \rho) g d_{50}} = 0.012$, with τ_{cr} = 0.068 N/m^2. The bedform height was predicted using this critical stress in Equation 5.2 and τ_{bs} predicted from the depth-averaged velocity. Results are listed in Table 5.2. The predicted bedform height significantly overpredicted the observed bedform height (Figure 5-3a). This suggested that introducing submerged vegetation to a bare bed could suppress the migrating bedforms, as noted previously in Nepf (2012) and Przyborowski et al. (2018).

Bedforms are related to bedload transport and thus near-bed flow conditions. In submerged canopies, the near-bed velocity is smaller than that on an unvegetated bed with the same bed sediment and depth-averaged velocity (see discussions in the previous chapter), so that the energy available to move sediment and shape bedforms is reduced within a submerged canopy, leading to a reduction in bedform height. A more accurate prediction of bedform height might result from using the in-canopy velocity, U_{canopy}, to predict the bed stress as

$$\tau_{\mathrm{bs}} = \rho C_{\mathrm{fs}} U_{\mathrm{canopy}}^2, \tag{5.4}$$

Bedform heights predicted from Equation 5.4 are listed in Table 5.2 and plotted on Figure 5-3b. The new predicted bedform height, using the in-canopy velocity, agrees with measured bedform height within uncertainty, suggesting that the height of bedform in submerged canopies may be predicted with U_{canopy} as input.

Table 5.2: Prediction of bedform height in submerged canopies. The uncertainty of predicted bedform height h_{bf} is factor 2.

Case	S1	S2	S3	D1	D2	D3
	Measured values					
H (m)	0.189	0.268	0.323	0.245	0.268	0.365
U (m/s)	0.381	0.412	0.389	0.393	0.458	0.384
U_{canopy} (m/s)	0.327	0.270	0.212	0.260	0.196	0.120
q_s (g m^{-1} s^{-1})	3.8	0.85	0.265	8.2	0.86	0.036
h_{bf} (m)	0.014	0.016	0	0.035	0	0
$\delta(h_{bf})$ (m)	0.002	0.002	0	0.004	0	0
	Unvegetated beds with U as input					
u_* (m/s)	0.0163	0.0170	0.0158	0.0164	0.0187	0.0155
C_{fs}	0.00183	0.00170	0.00165	0.00174	0.00167	0.00163
Re_p	5.7	6.0	5.5	5.7	6.5	5.4
τ_{bs} (N/m^2)	0.266	0.289	0.250	0.269	0.350	0.240
T_s	2.9	3.3	2.7	3.0	4.1	2.5
h_{bf} (m)	0.053	0.070	0.075	0.064	0.073	0.081
	Unvegetated beds with U_{canopy} as input					
τ_{bs} (N/m^2)	0.196	0.124	0.074	0.118	0.064	0.023
T_s	1.9	0.8	0.1	0.7	<0	<0
h_{bf} (m)	0.044	0.033	0.005	0.028	0	0

Nomenclature:

H: Flow depth
U: Channel average velocity
U_{canopy}: Canopy-averaged velocity
q_s: Sediment transport rate
h_{bf}: Bedform (traversing sand layer) height
u_*: Friction/Shear velocity
C_{fs}: Grain-related bed drag coefficient
$Re_p = \frac{u_* d_{50}}{\nu}$: Particle Reynolds number
τ_{bs}: Grain-related bed skin shear stress
$T_s = \frac{\tau_{bs}}{\tau_{cr}} - 1$: Transport stage parameter

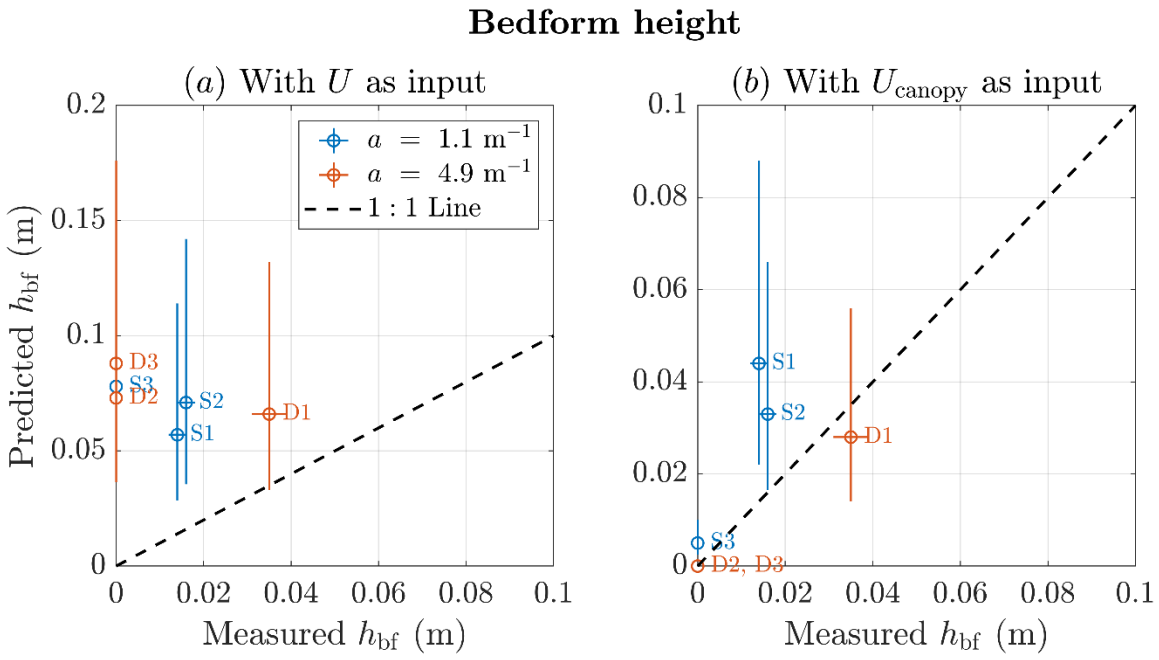

Figure 5-3. Predicted versus measured bedform (migrating sand layer) height in submerged canopies. Error bars denote factor of 2 uncertainty in the van Rijn (1984) model. For the sediment transport rate of each case, refer to Table 5.2 above.

5.3.3 Migrating Bedforms and Sediment Transport

In this study, the initial bedform size, high sediment transport rates, and duration of Cases S1, S2, and D1 resulted in a bedform that passed through the canopy several times, due to the continuous recirculation of sediment in the experimental facility. In contrast, for Cases S3, D2, and D3, the mobilization of sediment was weaker, and the downstream bed elevation varied less than 10% within 24 hrs of the start of velocity measurements. The absence of migrating bedforms is consistent with the modified Equation 5.2, which predicted negligible bedform height in these cases (Figure 5-3b). Specifically, Equation 5.2 predicted that no bedform would develop in Cases D2 and D3, and the bedform height in S3 would be less than a centimeter, which is difficult to detect.

For the cases (S1, S2, and D1) which produced a cyclically appearing bedform, it is reasonable to imagine that if the sand bed evolved from an initially flat condition, due to the region of high turbulence at the canopy leading edge, the upstream bedforms would always form as in Cases S2 and D3 and then spread and flatten to their limit, which is the migrating bedform.

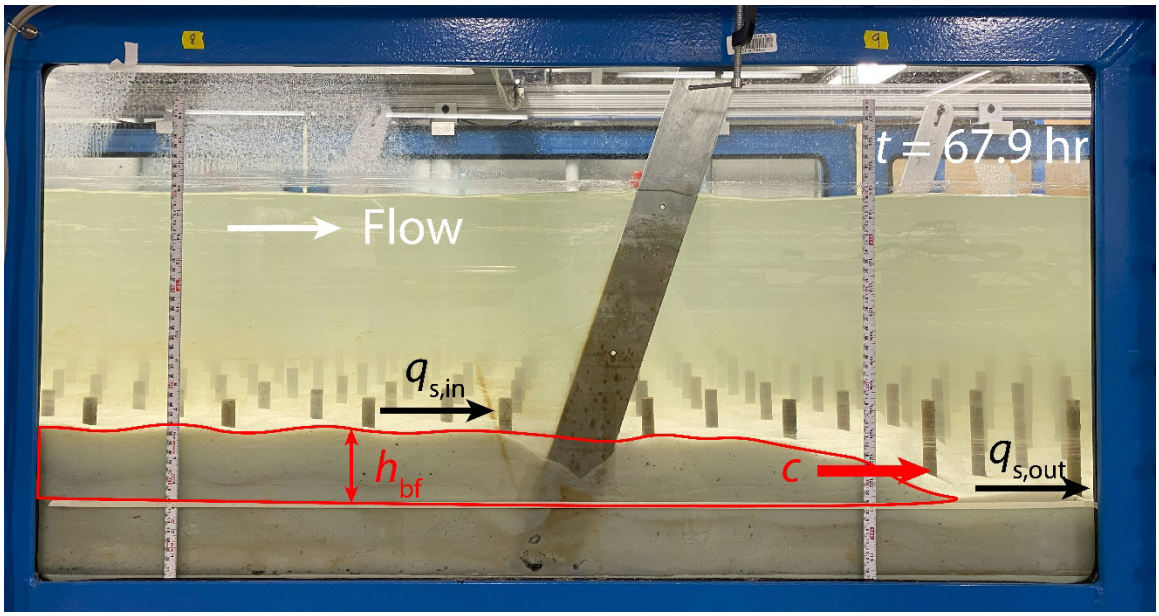

Figure 5-4. Annotated image of bedform migration within the submerged canopy in Case S3. Flow was from the left to the right. Red curves denote the bedform captured within the image frame. h_{bf} and c are the bedform height and migration rate, respectively. $q_{s,in}$ and $q_{s,out}$ represent the sediment transport rate upstream and downstream of the bedform front, respectively.

Sediment transport due to bedform migration may represent the total bedload transport, if rolling and sliding are the dominant mode of transport (van den Berg, 1987; Alvarez & Franklin, 2020). In cases with bedform migration, the local bedload transport upstream and downstream of the bedform front corresponded to the flow conditions upstream and downstream of the front, respectively (see Table A4.1). Specifically, the higher bed upstream of the front was associated with higher near-bed velocity and turbulence, and thus higher bedload transport $q_{s,in}$, as compared to each of these parameters measured downstream of the front, with transport rate $q_{s,out}$. The difference in sediment transport rate up- and downstream of the front describes the migration of the bedform front:

$$q_{s,bf} = q_{s,in} - q_{s,out} = \rho_s(1 - \lambda_p)ch_{bf}, \tag{5.5}$$

in which ρ_s the density of sediment, $\lambda_p = 0.40 \pm 0.02$ the porosity of sediment (Beard & Weyl, 1973), c the bedform migration speed, and h_{bf} the bedform height (Figure 5-4). Equation 5.5 assumes that only bedform migration contributes to the total sediment transport, i.e., it excludes saltation and suspension. Therefore, the difference between the

sediment transport estimated by Equation 5.5 and the sediment transport measured at the channel-scale indicates the relative importance of bedform migration to the total sediment transport.

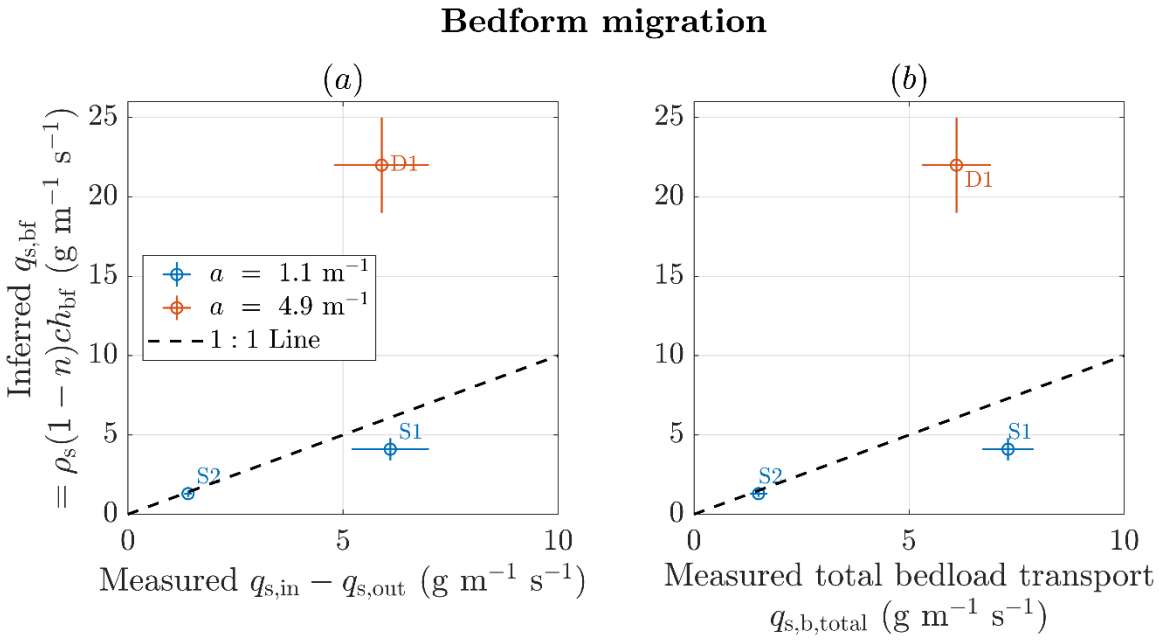

Figure 5-5. Bedload transport rate $q_{s,bf}$, inferred from estimated migration rate, c, using right-most side of Equation 5.5. (a) Versus difference in measured sediment transport between high and low bed stages, and (b) versus measured total bedload transport.

Figure 5-5a compares two estimates of the bedload transport rate due to bedform migration, one being the difference of $q_{s,in}$ and $q_{s,out}$, the other estimated from the bedform migration rate c depicted by camera images. $q_{s,in}$ were calculated as the average of the largest two sediment transport rates of a specific case, whereas $q_{s,out}$ the average of the smallest two. In general, $q_{s,in} - q_{s,out}$ agreed with $q_{s,bf} = \rho_s(1-\lambda_p)ch_{bf}$, within uncertainty, with the exception of S1, in which measured $q_{s,in} - q_{s,out}$ was greater than $q_{s,bf} = \rho_s(1-\lambda_p)ch_{bf}$. This may be attributed to the fact that not all the bedload was associated with bedform migration, as also observed by Yang and Nepf (2019). In this study, we observed intermittent near-bed transport, e.g., observed grain saltation and suspension, which suggests that sediment transport was at the transition of bedload and suspended load (McElroy & Mohrig, 2009). The other exception is Case D1, in which the inferred $q_{s,bf} = \rho_s(1-\lambda_p)ch_{bf}$ is significantly greater than $q_{s,in} - q_{s,out}$, which does not

make physical sense. The cause of this misalignment could be error in the estimates in c and h_{bf}. In this case, as indicated by camera images, scour holes adjacent to the flume walls were more significant than in the other cases, due to the higher canopy density and near-bed turbulence (see Table A4.1). The sidewall scour made it more difficult to define the bedform boundaries, which contributed error to the estimates of c and h_{bf}. Figure 5-5b compares the bedload transport rate due to bedform migration estimated from camera images versus total bedload transport, $q_{\mathrm{s,b,total}}$, which was determined as the average of measured bedload transport rate over the entire bed cycle (see Table A4.1 for instantaneous q_{s} values). The trend is similar to that in Figure 5-5a.

Chapter 5 References

Alvarez, C. A., & Franklin, E. M. (2020). Shape evolution of numerically obtained subaqueous barchan dunes. *Physical Review E*, *101*(1), 012905. doi:10.1103/PhysRevE.101.012905

Bagnold, R. A. (2012). *The physics of blown sand and desert dunes*. Courier Corporation.

Beard, D. C., & Weyl, P. K. (1973). Influence of Texture on Porosity and Permeability of Unconsolidated Sand. The American Association of Petroleum Geologists Bulletin, 57(2): 349–369. doi:10.1306/819A4272-16C5-11D7-8645000102C1865D

Best, J. (2005). The fluid dynamics of river dunes: A review and some future research directions. Journal of Geophysical Research: Earth Surface, 110(F4), F04S02. doi:10.1029/2004JF000218

Bourke, M.C., Lancaster, N., Fenton, L.K., Parteli, E.J., Zimbelman, J.R., & Radebaugh, J. (2010). Extraterrestrial dunes: An introduction to the special issue on planetary dune systems. Geomorphology, 121(1-2), 1-14. doi:10.1016/j.geomorph.2010.04.007

Charru, F., Andreotti, B., & Claudin, P. (2013). Sand Ripples and Dunes. Annual Review of Fluid Mechanics, 45(1), 469-493. doi:10.1146/annurev-fluid-011212-140806

Chen, S., Chan, H., & Li, Y. (2012). Observations on flow and local scour around submerged flexible vegetation. Advances in Water Resources, 43, 28-37. doi:10.1016/j.advwatres.2012.03.017

Chen, Z., Jiang, C., & Nepf, H. (2013). Flow adjustment at the leading edge of a submerged aquatic canopy. *Water Resources Research*, 49(9), 5537–5551. doi:10.1002/wrcr.20403

Engelund, F., & Fredsøe, J. (1982). Sediment Ripples and Dunes. Annual Review of Fluid Mechanics, 14(1), 13-37. doi:10.1146/annurev.fl.14.010182.000305

Hesp, P.A., & Smyth, T.A. (2017). Nebkha flow dynamics and shadow dune formation. Geomorphology, 282, 27-38. doi:10.1016/j.geomorph.2016.12.026

Ishii, J. (2023). *The influence of current and ripple development on seagrass transplant survival* [Master's thesis, Massachusetts Institute of Technology]. DSpace@MIT. https://dspace.mit.edu/handle/1721.1/151912

Julien, P. Y. (2010). *Erosion and Sedimentation* (2nd ed.). Cambridge University Press. doi: 10.1017/CBO9780511806049

Kim, H.S., Kimura, I., & Shimizu, Y. (2015). Bed morphological changes around a finite path of vegetation. Earth Surface Processes and Landforms, 40(3), 375-388. doi:10.1002/esp.3639

Le Bouteiller, C., & Venditti, J. G. (2014). Vegetation-driven morphodynamic adjustments of a sand bed. *Geophysical Research Letters*, 41(11), 3876-3883. doi:10.1002/2014GL060155

McElroy, B., & Mohrig, D. (2009). Nature of deformation of sandy bed forms. Journal of Geophysical Research: Earth Surface, 114(F3), F00A04. doi:10.1029/2008JF001220

Nepf, H. M. (2012). Hydrodynamics of vegetated channels. *Journal of Hydraulic Research*, *50*(3), 262-279. doi:10.1080/00221686.2012.696559

Parsons, D.R., Schindler, R.J., Hope, J.A., Malarkey, J., Baas, J.H., Peakall, J., ... & Thorne, P.D. (2016). The role of biophysical cohesion on subaqueous bed form size. Geophysical Research Letters, 43(4), 1566-1573. doi:10.1002/2016GL067667

Przyborowski, Ł., Łoboda, A. M., & Bialik, R. J. (2018). Experimental investigations of interactions between sand wave movements, flow structure, and individual aquatic plants in natural rivers: A case study of Potamogeton pectinatus L. *Water*, *10*(9), 1166. doi:10.3390/w10091166

Rominger, J.T., Lightbody, A.F., & Nepf, H.M. (2010). Effects of Added Vegetation on Sand Bar Stability and Stream Hydrodynamics. Journal of Hydraulic Engineering, 136(12), 994-1002. doi:10.1061/(ASCE)HY.1943-7900.0000215

Southard, J.B. (1991). Experimental Determination of Bed-Form Stability. Annual Review of Earth and Planetary Sciences, 19(1), 423-455. doi:10.1146/annurev.ea.19.050191.002231

van den Berg, J.H. (1987). Bedform migration and bed-load transport in some rivers and tidal environments. Sedimentology, 34(4), 681-98. doi:10.1111/j.1365-3091.1987.tb00794.x

van Rijn, L. C. (1984). Sediment transport, part III: bed forms and alluvial roughness. *Journal of Hydraulic Engineering*, 110(12), 1733-1754. doi:10.1061/(ASCE)0733-9429(1984)110:12(1733)

Yagci, O., Celik, M.F., Kitsikoudis, V., Ozgur Kirca, V., Hodoglu, C., Valyrakis, M., ... & Kaya, S. (2016). Scour patterns around isolated vegetation elements. Advances in Water Resources, 97, 251-65. doi:10.1016/j.advwatres.2016.10.002

Yang, J.Q., & Nepf, H.M. (2019). Impact of Vegetation on Bed Load Transport Rate and Bedform Characteristics. Water Resources Research, 55(7), 6109-6124. doi:10.1029/2018WR024404

Chapter 6 Conclusions and Suggestions for Future Work

6.1 Thesis Summary

The morphology and distribution of aquatic plants influence the velocity field, turbulence intensity, and bedload transport in wetlands, which impacts the erosion and deposition processes. By combining physical and numerical experiments, this thesis quantified how vegetation geometry impacts velocity and turbulence near the bed, which in turn impacts bedload transport.

Chapter 2 examined turbulence and bedload transport in channels with randomly distributed emergent patches of model vegetation, each with diameter D. With constant channel velocity and total solid volume fraction, TKE and bedload transport decreased with increased clustering, associated with decreasing patch size (D). The channel average TKE better predicted sediment transport than channel average bed shear stress. The experimental results demonstrated that aside from vegetation density, it is also necessary to consider the clustering of vegetation into discrete patches, which occurs at scales typically smaller than a computational grid size. Therefore, sub-grid scale models for bedload transport should consider vegetation distribution.

Chapter 3 explored whether stem diameter and element arrangement (staggered versus random distributions) of emergent model vegetation influenced channel turbulence and bedload transport. When emergent vegetation was not clustered, bedload transport was only a function of channel-scale velocity and solid volume fraction and did not depend on the arrangement or diameter range of individual stems. This was explained by the impulse model for sediment entrainment. The classic Meyer-Peter-Müller bedload transport model was recast in terms of TKE to predict sediment transport in channels with emergent vegetation. In addition, this chapter outlined how to predict the channel average TKE from plant biomass and velocity, offering an important step toward predicting turbulence and sediment transport in vegetation canopies of real morphology in the field.

Chapter 4 explored turbulence and bedload transport in canopies of submerged model vegetation. For constant depth-averaged velocity U, submerged canopies could enhance or reduce bedload transport, depending on their degree of submergence. With increasing submergence H/h, the near-bed velocity and TKE decreased, and the source of near-bed turbulence shifted from individual stem wakes to the shear layer at the canopy top. For high submergence ($H/h > 2$), TKE was insensitive to changes in H/h and dimensionless canopy density ah. Bedload transport was predominantly correlated with near-bed turbulence but also weakly correlated with near-bed velocity, and bedload transport monotonically decreased with increasing H/h. A model to predict near-bed TKE in submerged canopies was developed and used to explore bedload transport under more realistic conditions with constant energy slope and flexible vegetation. In the modeled scenarios, submerged canopies reduce sediment transport compared to unvegetated cases. With a constant energy slope, the channel average velocity increases with decreasing dimensionless canopy density and increasing submergence, which also tend to increase the shear production of turbulence in the canopy shear layer. Because of the important contribution of canopy-shear-generated turbulence, with constant energy slope, the highest sediment transport rates occurred for vegetation with the greatest submergence and the smallest canopy density.

Chapter 5 described the bedform migration observed during the experiments with a submerged model vegetation canopy. Due to the strong turbulence in the flow adjustment region at the canopy leading edge, a bedform was formed downstream of the adjustment length, which later diffused and migrated over the test section. Because sediment was recirculated, the migrating bedform repeatedly passed through the test section causing cyclic temporal variations in the bed elevation and sediment transport rate measured at the end of the test section.

6.2 Future Work

Chapter 2 considered circular patches of emergent model vegetation with a spacing less than six times of the patch diameter, so that the patch-scale turbulence was not generated. If the patch spacing exceeds six times but is less than ten times of the

patch diameter, patch-scale turbulence could be generated (Nicolle & Eames, 2011; Zong & Nepf, 2012), and could also impact the near-bed flow and sediment transport. Moreover, in the field, aquatic vegetation patches may exhibit different shapes, e.g., elliptical (Licci et al., 2019) or polygonal (Schoelynck et al., 2011), that could require a shape factor to be included in turbulence and sediment transport modeling. For example, with the same width, elliptical patches are more streamlined than circular and polygonal patches, thus could generate less pronounced wakes but also longer shear layers on the patch sides. For local, patch-scale hydrodynamic and morphodynamic modeling, it is necessary to solve for the flow field to estimate the sediment transport and consequently patterns of erosion and deposition. However, for reach-scale modeling, it is too computationally expensive to compute the patch-scale hydrodynamics, so the model grid size could be one order of magnitude higher than the patch size. This is when the shape factor could be of benefit to the modelers. Also, the length of patches is a crucial factor for consideration, because the patch must have a length comparable to or longer than the adjustment length to modify the flow field (Chen et al., 2013; Licci et al., 2019). Therefore, the impact of patch spacing, shape, and length should be taken into consideration.

Chapter 3 considered the impact of stem diameter and element arrangement of emergent model vegetation on channel turbulence and bedload transport. The turbulence model used in this chapter included a bed drag coefficient that was defined by a logarithmic profile over an unvegetated bed, which was used to estimate the magnitude of bed-generated turbulence. However, as Yang and Nepf (2019, Figure 4b) suggested, for an emergent canopy with solid volume fraction $\phi > 0.01$, stem wake turbulence is stronger than bed-generated turbulence. TKE budget analysis could have been done to estimate the near-bed shear production $P_{s,nb}$ and wake production $P_{w,nb}$. A ratio of $P_{s,nb}/P_{w,nb} << 1$ would suggest that the bed turbulence is negligible compared to stem wake turbulence, so that the bed turbulence term could be dropped in the turbulence model (e.g., Equation 3.4). Further, when extending the turbulence model to a more complex plant morphology, I assumed a single shape factor for specific plant species (see *Typha* in Section 3.5.3), but Liu et al. (2024) have found that this assumption could alter the prediction of sediment transport by up to an order of magnitude, because the

nonuniform profile of vegetation frontal area led to an accordingly nonuniform velocity profile (Lightbody & Nepf, 2006). Instead, when modeling sediment transport in the field, the plant shape factor should have been defined based on the difference between near-bed and depth-averaged frontal areas.

Chapter 4 developed models that predicted the turbulence and bedload transport in canopies of submerged vegetation. This model can now be used to explore field scenarios. For example, in real systems, the flow depth may vary over days (e.g., flood processes) to decades (e.g., sea level rise). Here is an example that incorporates a time-varying flow depth. Consider a flood process in a river, for which the bed slope is constant over time, so that the flow depth is proportional to the flow rate in the channel. The bed may be bare, or be covered with rigid or flexible submerged canopy, with the same dimensionless canopy density when individual plants are erect. The submerged canopies are assumed sufficiently long, so that the velocity profile is fully developed. The model parameters are listed in Table 6.1. The rigid canopies maintain their height regardless of the water level, whereas the flexible canopies deflect to different degrees in response to the variation in velocity associated with the varying flow depth. The deflection of the canopy increases with increasing channel velocity and decreasing canopy density. Because the model is quasi-steady, the sediment transport trends, in general, agree with the discussions in Chapter 4.3. Specifically, denser canopies and canopies with greater submergence produce weaker bedload transport, which implies that canopies which are denser and more flexible (and thus more pronated) provide more protection to the bed. This calls for further physical and economic analyses of an optimal canopy density for feasible and effective erosion control.

Table 6.1: Parameters in the modeled flood process

Parameter	Symbol (unit)	Rigid canopy	Flexible canopy
Energy slope	S (-)	0.001	
Flow depth	H (m)	0.5 -> 1.5 -> 0.5	
Median grain size of bed sediment	d_{50} (mm)	0.35	
Erect canopy height (blade length in flexible canopies)	h (m)	0.3	
Canopy frontal area per unit volume	a (m^{-1})	0.33, 3.3, 16.7	
Dimensionless canopy density	ah (-)	0.1, 1, 5	
Stem diameter	d (cm)	1.3	N/A
Blade width	w (cm)	N/A	0.4
Blade thickness	t (mm)	N/A	0.3
Young's modulus	E (GPa)	N/A	0.2
Water density	ρ (kg/m^3)	1000	
Blade density	ρ_{veg} (kg/m^3)	N/A	1000
Drag coefficient	C_D (-)	1	1.95

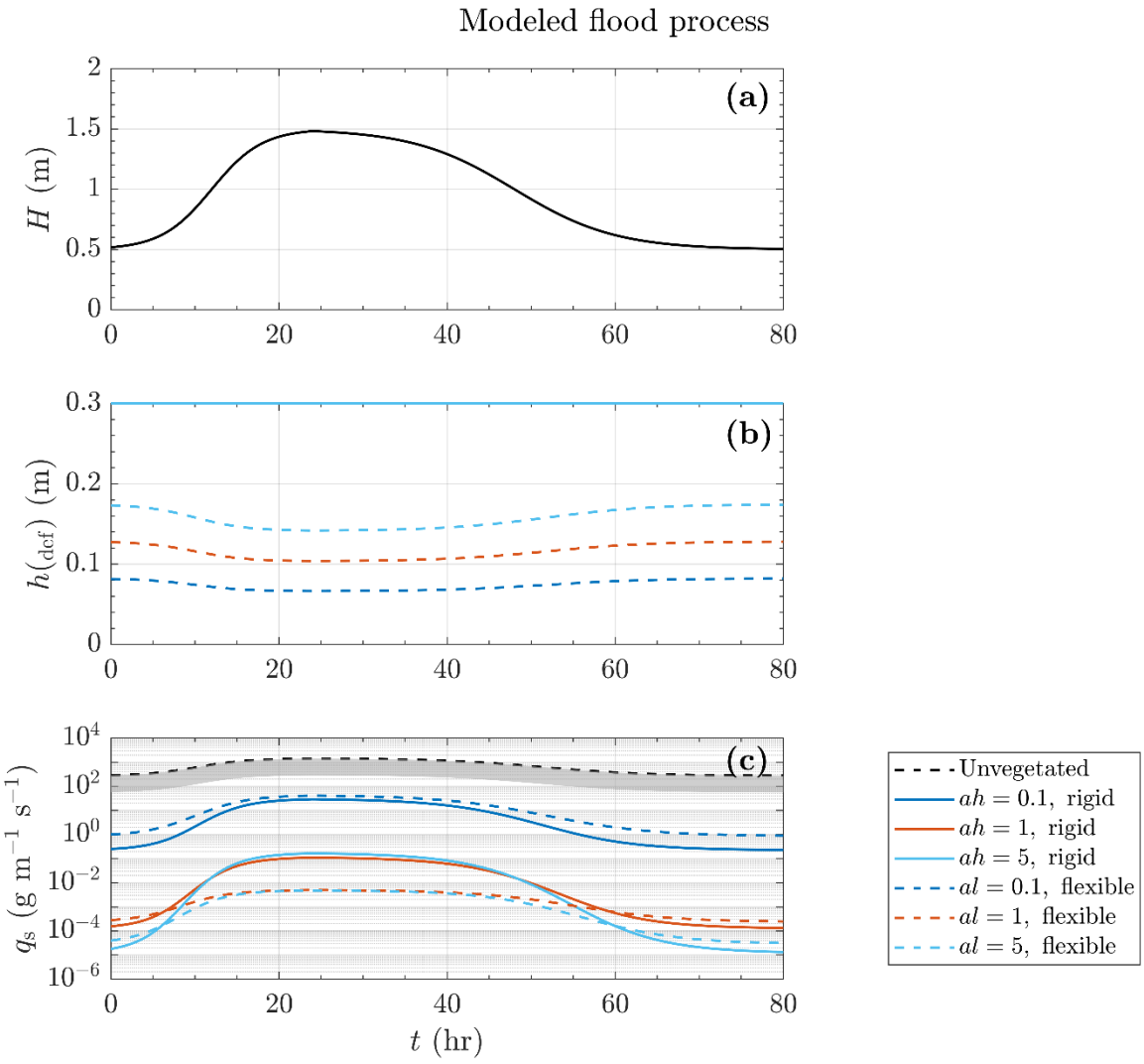

Figure 6-1. Canopy and sediment transport responses to a modeled flood process. Solid lines represent rigid model canopies and dashed lines represent flexible canopies. See Chapter 4.3.4 for model details and Table 6.1 for input parameters. Energy slope $S = 0.001$. Canopy densities are differentiated by colors. (a) Flow depth. (b) Canopy height. For flexible canopies, this represents the deflected canopy height h_{def}. (c) Sediment transport rate. Gray band represents transport rates with bedforms (Wong & Parker, 2006).

Chapter 6 References

Chen, Z., Jiang, C., & Nepf, H. (2013). Flow adjustment at the leading edge of a submerged aquatic canopy. *Water Resources Research*, 49(9), 5537–5551. doi:10.1002/wrcr.20403

Licci, S., Nepf, H., Delolme, C., Marmonier, P., Bouma, T. J., & Puijalon, S. (2019). The role of patch size in ecosystem engineering capacity: a case study of aquatic vegetation. Aquatic Sciences, 81, 1-11. doi:10.1007/s00027-019-0635-2

Liu, C., Shan, Y., He, L., Li, F., Liu, X., & Nepf, H. (2024). Plant morphology impacts bedload sediment transport. *Geophysical Research Letters*, 51(12), e2024GL108800. doi:10.1029/2024GL108800

Luhar, M., & Nepf, H. M. (2011). Flow-induced reconfiguration of buoyant and flexible aquatic vegetation. *Limnology and Oceanography*, 56(6), 2003-2017. doi:10.4319/lo.2011.56.6.2003

Luhar, M., & Nepf, H. M. (2013). From the blade scale to the reach scale: A characterization of aquatic vegetative drag. *Advances in Water Resources*, 51, 305-316. doi:10.1016/j.advwatres.2012.02.002

Nicolle, A., & Eames, I. (2011). Numerical study of flow through and around a circular array of cylinders. *Journal of Fluid Mechanics*, 679, 1-31. doi:10.1017/jfm.2011.77

Schoelynck, J., De Groote, T., Bal, K., Vandenbruwaene, W., Meire, P., & Temmerman, S. (2012). Self-organised patchiness and scale-dependent bio-geomorphic feedbacks in aquatic river vegetation. Ecography, 35(8), 760-768. doi:10.1111/j.1600-0587.2011.07177.x

Yang, J.Q., & Nepf, H.M. (2019). Impact of Vegetation on Bed Load Transport Rate and Bedform Characteristics. Water Resources Research, 55(7), 6109-6124. doi:10.1029/2018WR024404

Zong, L., & Nepf, H. (2012). Vortex development behind a finite porous obstruction in a channel. *Journal of Fluid Mechanics*, 691, 368-391. doi:10.1017/jfm.2011.479

This page intentionally left blank

Appendices

A1 Supporting Information for Chapter 2

(a) D = 6.5 cm, ϕ = 0.24

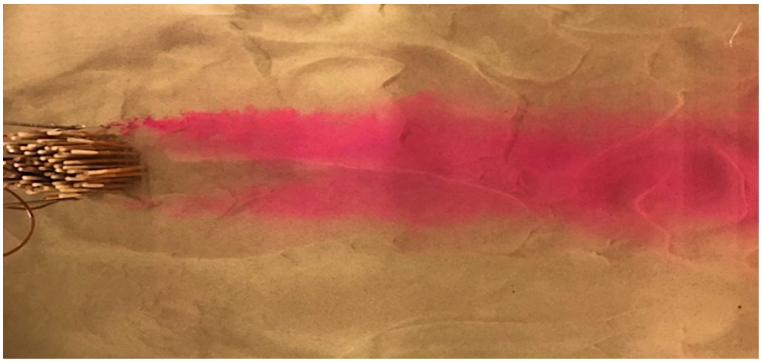

(b) D = 20 cm, ϕ = 0.03

Figure A1-1. Top view of tracer experiments designed to examine the wakes behind individual patches within the channel. Red tracer was injected at mid-depth and at the outer edges of the patch. The channel velocity was U_o = 30.0 ± 0.5 cm/s, and the depth was H = 12 cm. Zong and Nepf (2012) reported that a von Karman vortex street would be present when $\phi \geq 0.04$. A patch with ϕ = 0.03 (subplot b) did not produce a vortex street, consistent with Zong and Nepf (2012). A vortex street was expected for ϕ = 0.24 (subplot a), but was not observed. The presence of neighboring and downstream patches altered the flow sufficiently to prevent the formation of vortices. For shallow flow, the bed friction may also suppress the vortex formation if the stability parameter, $S = C_f D/\mathrm{H}$, is greater than a critical value S_c = 0.2 (Chen and Jirka, 1995). Here, S = 0.002 to 0.007, smaller than the critical value, S_c, suggesting that the bed friction was not the mechanism of vortex suppression.

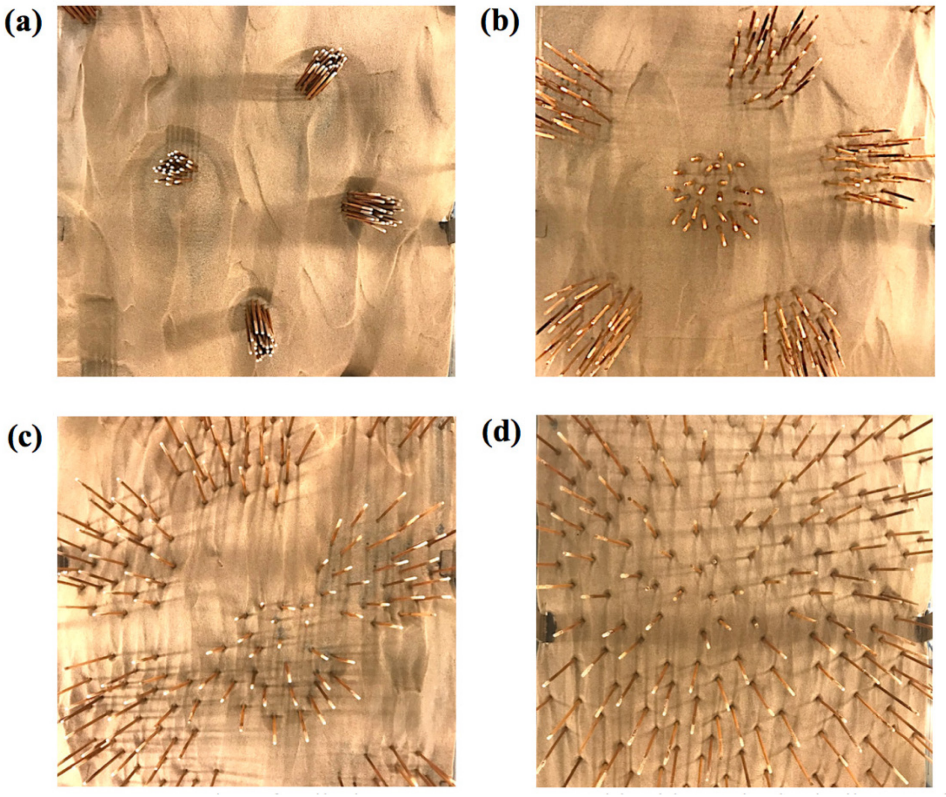

Figure A1-2. Examples of the cylinder arrangements used in this study, for patches with (a) D = 6.5 cm, (b) D = 20 cm, (c) D = 30 cm, and (d) for a uniform random distribution. These four cases had the same the channel-scale solid volume fraction, $\phi_c = 0.005$. The photos were taken after the experiment. The flow was from top to bottom.

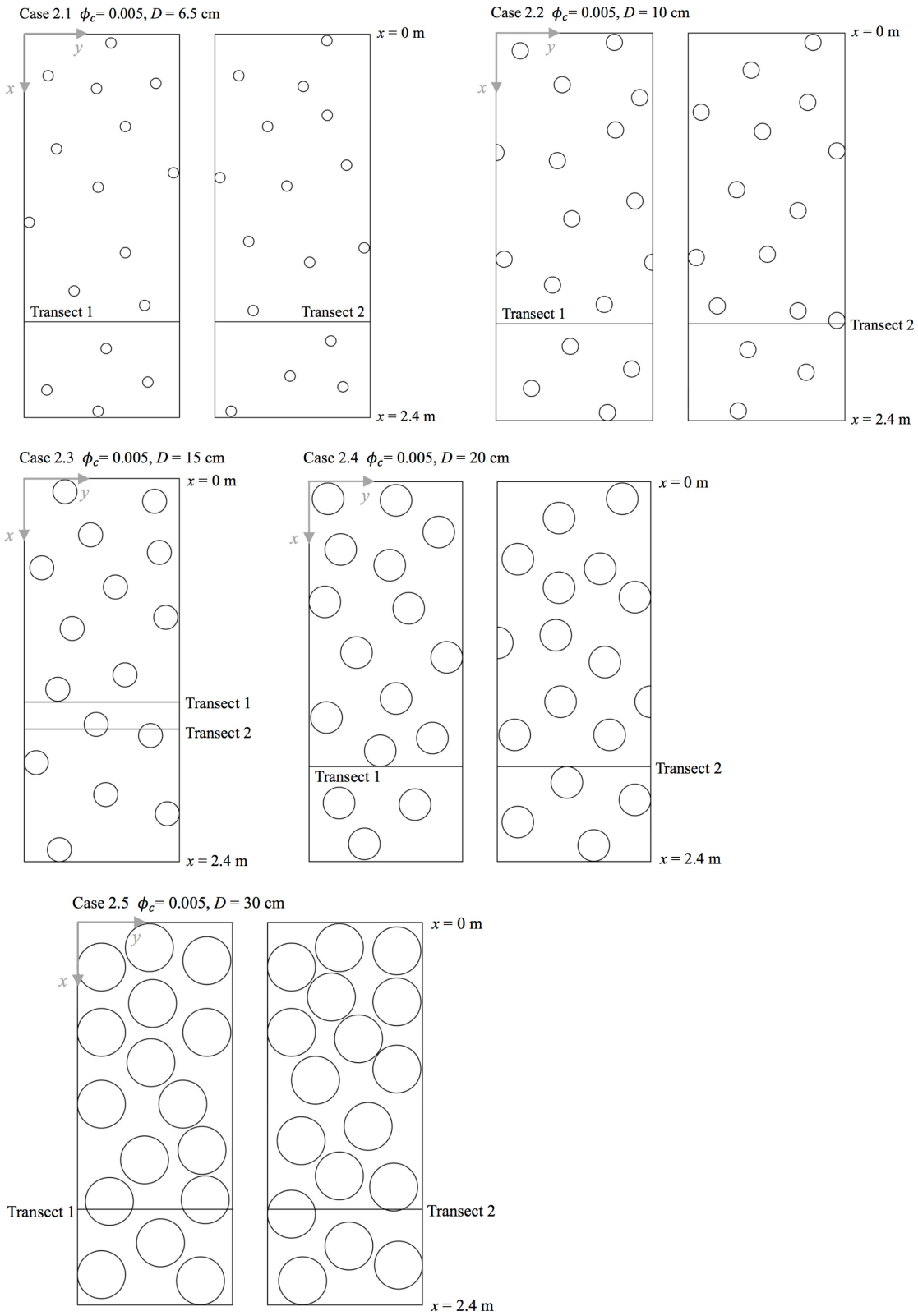

Figure A1-3. Patch distributions for the channel-average solid volume fraction, ϕ_c= 0.005.

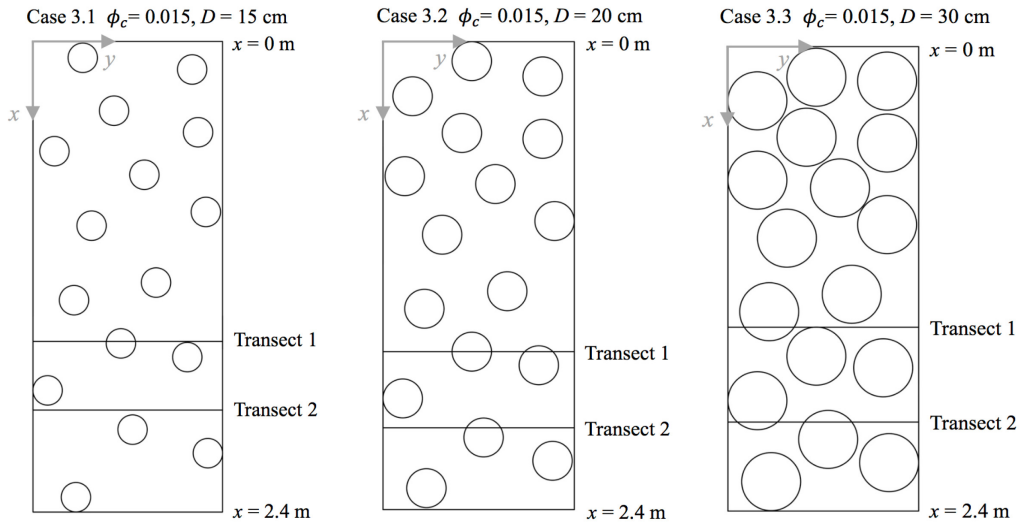

Figure A1-4. Patch distributions for the channel-average solid volume fraction, ϕ_c= 0.015.

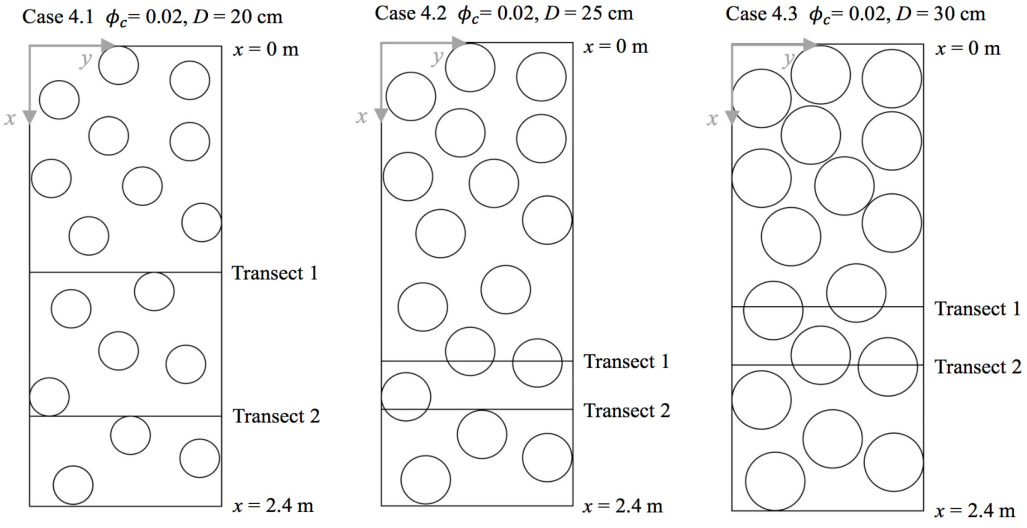

Figure A1-5. Patch distributions for the channel-average solid volume fraction, ϕ_c= 0.02.

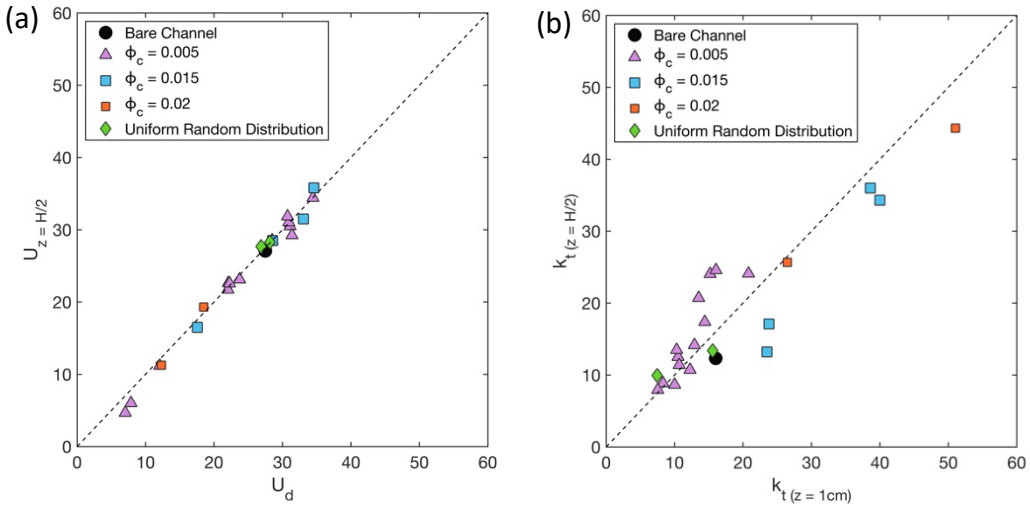

Figure A1-6. (a) Velocity measured at mid-depth ($z = H/2$), $U_{z=H/2}$, compared to depth-averaged velocity, U_d. The ratio of velocity at mid-depth to the depth-averaged velocity was 1.0 ± 0.1. (b) Turbulent kinetic energy measured at mid-depth, $k_{t(z=H/2)}$, and at 1 cm above the bed, $k_{t(z=1\ cm)}$. The ratio of near-bed to mid-depth turbulence, $k_{t(z=H/2)}/k_{t(z=1\ cm)}$, was 1.1 ± 0.3. Both sub-plots include all cases in Table 2.1.

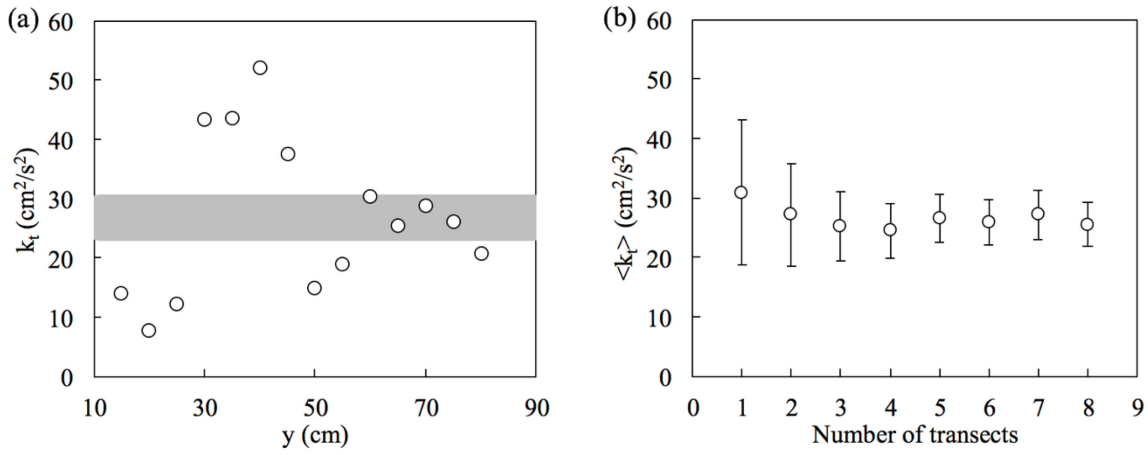

Figure A1-7. (a) Lateral profile of the turbulent kinetic energy, k_t. The horizontal gray bar denotes the average over the transect $k_t = 27 \pm 4$ cm^2/s^2. (b) The cumulative average of turbulent kinetic energy plotted against the number of individual transects included in the average. The individual transects were located at randomly selected longitudinal positions along the channel. The data are from Case 2.4. The spatial mean of k_t achieved a constant value after two transects. The percentage difference between the two-transect average and the average of eight transects was 6 %, indicating that measurements from two transects were sufficient to obtain $\langle k_t \rangle$.

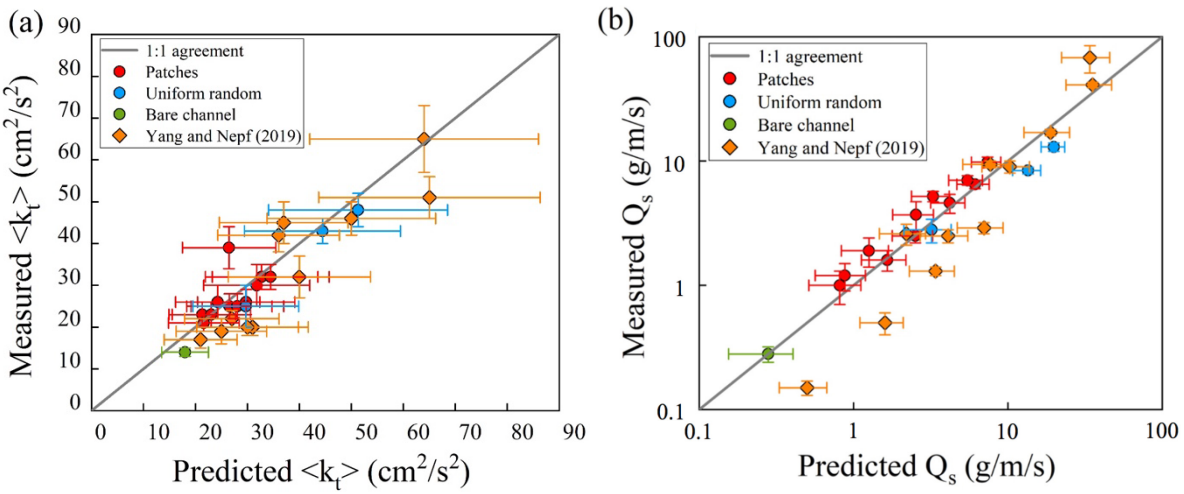

Figure A1-8. (a) Measured (Table 2.1) versus predicted (Equations 2.6 and 2.7) channel-average turbulent kinetic energy, $\langle k_t \rangle$. Uncertainty in the prediction was propagated from uncertainty in γ, C_f and C_d. The scale factor γ = 0.8 ± 0.4 in Equation 2.7 was determined from the least squares fit of all measurements in Table 1. (b) Measured (Table 2.1) versus predicted (Equations 2.2, 2.6, and 2.7) bedload transport. The parameter β = -1.6 ± 0.3 in Equation 2.2 was determined from the minimum mean square error using all cases in Table 1. The legend labels of "Patches", "Uniform random" and "Bare channel" correspond to the patterns listed in Table 2.1. Cases with staggered arrangements of cylinders (diamonds) are from Yang and Nepf (2019).

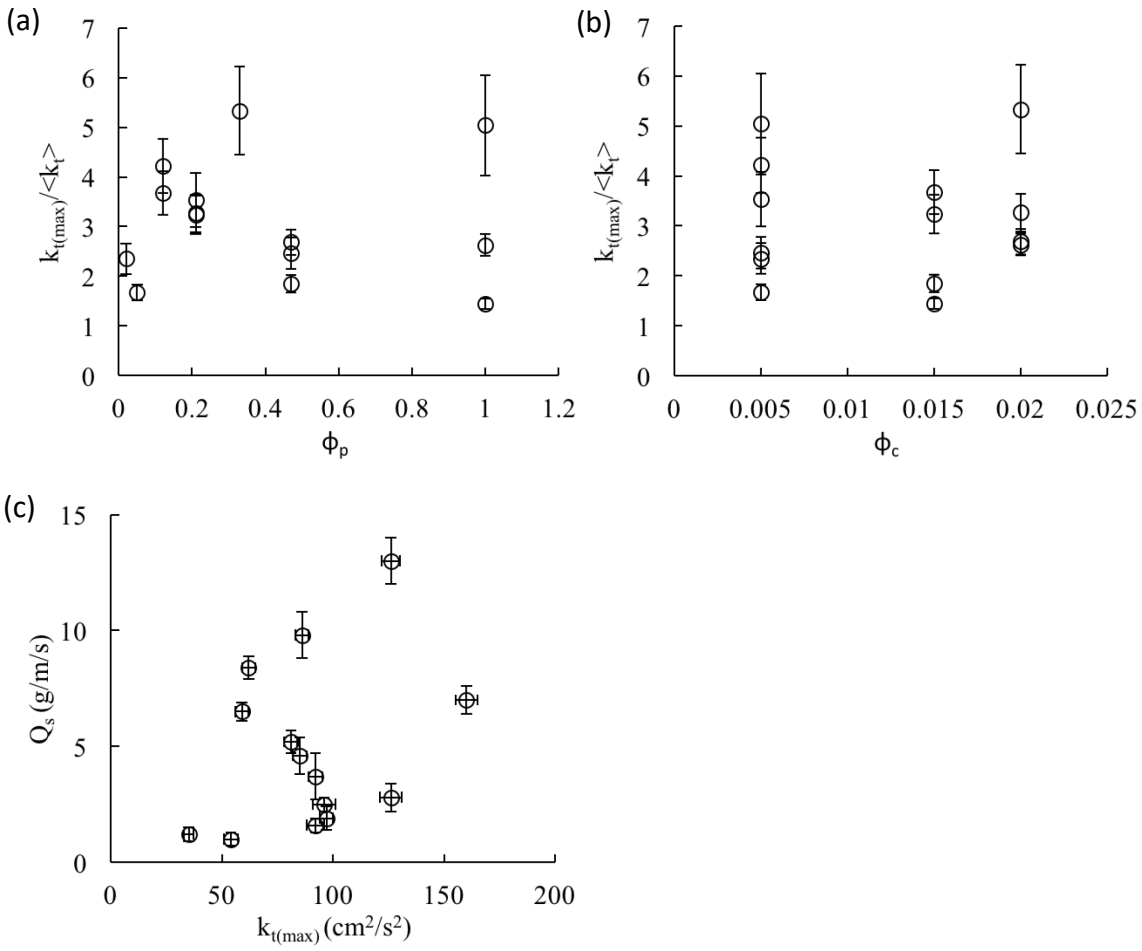

Figure A1-9. The maximum turbulent kinetic energy, $k_{t(max)}$, measured in the channel, normalized by channel-average turbulent kinetic energy, $\langle k_t \rangle$, plotted against (a) the fraction of bed occupied by patches, ϕ_p, and (b) the channel-average solid volume fraction, ϕ_c. The peak turbulence values did not systematically vary with channel-average values. As a result, sediment transport rate per channel width, Q_s, had little dependence on the maximum turbulent kinetic energy, $k_{t(max)}$, as shown in subplot (c). Local peak values in k_t can only impact the channel-scale sediment transport if the peaks occur over a spacing smaller than or equal to the individual sediment excursions. It appears that this condition was not met in our study.

Table A1-1: Transects of time-mean velocity and turbulence kinetic energy *

Patterns	Number	Transects	y (cm)	99	95	90	85	80	75	70	65	60	55	50	45	40	35	30	25	20	15	10	5	1
Bare Channel	case 1.1	transect 1	U (cm/s)		28.0	27.3	30.1	30.2	29.2	29.4	29.0	29.5	30.8	30.5	28.8	28.2	29.5	29.7	28.8	26.4	25.5	24.0	24.5	
		(x = 204 cm)	k_t (cm^2/s^2)		17.9	23.7	19.4	16.1	13.6	10.5	16.4	16.4	11.4	12.0	17.4	15.3	11.0	8.8	9.4	12.9	11.4	15.0	9.9	
Patches	case 2.1	transect 1	U (cm/s)				36.6	36.4	0.3	19.8	27.2	21.9	26.5	29.4	29.1	30.4	13.5	5.2	22.9	31.6				
		(x = 180 cm)	k_t (cm^2/s^2)				10.9	19.2	27.1	54.1	50.1	35.3	28.7	19.3	17.4	20.9	48.2	16.1	34.5	10.5				
		transect 2	U (cm/s)				31.6	30.3	32.9	34.4	34.7	6.0	28.8	34.4	30.9	28.7	29.6	30.9	22.9	12.6				
		(x = 180 cm)	k_t (cm^2/s^2)				15.3	14.2	11.9	9.3	12.0	14.0	40.9	12.5	14.5	17.7	14.6	12.3	29.2	21.9				
	case 2.2	transect 1	U (cm/s)				44.6	44.1	29.0	18.9	22.9	44.1	35.0	27.4	37.5	41.8	40.1	33.4	17.9	10.5				
		(x = 180 cm)	k_t (cm^2/s^2)				24.0	21.5	34.0	14.4	16.5	32.8	35.5	20.7	27.1	24.2	24.2	29.4	20.4	14.0				
		transect 2	U (cm/s)				34.2	35.2	32.5	10.3	9.9	28.7	26.2	18.8	21.4	28.8	27.4	29.0	26.7	8.5				
		(x = 180 cm)	k_t (cm^2/s^2)				10.1	10.7	19.6	12.3	14.0	22.5	32.1	22.9	26.5	16.8	14.4	16.4	30.0	10.4				
	case 2.3	transect 1	U (cm/s)		30.5		30.78	27.1	25.4	23.8	25.7	34.9	30.3	32.1	36.2	35.2	24.1	21.8	20.8				28.1	
		(x = 140 cm)	k_t (cm^2/s^2)		12.7		26.0	29.8	28.5	25.7	26.0	17.7	15.9	14.9	15.4	20.8	14.3	8.4	49.6				11.2	
		transect 2	U (cm/s)		31.5	28.2	32.4	30.1	29.2	27.3	29.0	36.4	33.6	32.2	35.1	31.6	25.9	26.1	18.1	18.1	17.7	30.9	30.9	
		(x = 157 cm)	k_t (cm^2/s^2)		8.5	96.7	16.0	11.5	13.5	14.7	14.5	18.1	18.4	14.8	13.6	25.1	11.8	7.5	20.0	22.4	20.0	91.5	10.5	
	case 2.4	transect 1	U (cm/s)				27.0	26.0	27.1	27.5	35.1	29.6	27.0	19.3	20.2	21.4	22.9	31.6	31.0	28.6				
		(x = 180 cm)	k_t (cm^2/s^2)				20.9	26.0	28.7	25.5	30.5	19.0	15.0	37.6	52.0	43.6	43.5	12.2	7.9	14.0				
		transect 2	U (cm/s)				35.2	30.3	26.0	24.8	26.5	40.5	35.7	29.2	23.7	26.1	32.1	37.0	28.0	29.0				
		(x = 180 cm)	k_t (cm^2/s^2)				19.0	39.4	26.5	28.7	21.3	19.4	12.0	9.7	8.2	7.5	9.6	13.7	50.1	91.6				
	case 2.5	transect 1	U (cm/s)				25.6	20.0	24.7		27.5	28.6	30.9	26.2	29.0	27.5	24.2	23.3	21.1	27.4				
		(x = 180 cm)	k_t (cm^2/s^2)				22.7	93.1	31.9		7.1	10.1	12.0	16.1	19.2	17.4	80.7	96.0	86.0	41.4				
		transect 2	U (cm/s)				27.2		18.2	20.6	28.3	30.3	23.7	26.1	22.3	26.7	26.2	27.0	25.7	22.2				
		(x = 180 cm)	k_t (cm^2/s^2)				66.6		59.6	42.3	36.3	18.4	29.8	26.9	61.1	25.3	26.7	16.2	18.3	41.4				
	case 3.1	transect 1	U (cm/s)		35.9	40.4	17.9	8.0	8.7	19.0	38.9	46.8	28.8	8.3	9.4	5.1	28.5	40.7	35.0	22.4	12.5	20.3	31.5	
		(x = 153 cm)	k_t (cm^2/s^2)		7.1	20.9	33.9	9.4	10.0	27.7	35.5	28.2	92.1	8.8	9.9	17.4	51.4	28.7	23.2	42.0	29.3	41.1	17.4	
		transect 2	U (cm/s)		30.4	34.8	38.8	29.4	12.1	13.6	16.8	39.3	37.7	37.9	41.5	37.4	26.9	28.0	29.1	7.8	9.1	7.4	37.7	
		(x = 188 cm)	k_t (cm^2/s^2)		9.2	24.9	19.7	21.7	13.7	11.1	22.3	36.4	25.7	20.9	15.5	35.0	42.0	45.9	27.8	14.7	9.5	15.7	12.8	
	case 3.2	transect 1	U (cm/s)		37.3	34.8	30.7	35.2	30.0	16.2	18.0	19.2					30.0	15.5	12.9	13.1	13.1	37.9	34.6	
		(x = 159 cm)	k_t (cm^2/s^2)		14.7	66.3	24.5	31.6	38.3	15.2	15.9	15.9					33.3	19.7	17.1	18.7	17.2	81.4	9.7	
		transect 2	U (cm/s)		44.9	35.9	25.3	29.8	23.2	28.9	33.6	31.2	19.6	17.9	23.9	26.6	41.0	38.4	25.7	17.1	14.2	17.3	23.8	
		(x = 198 cm)	k_t (cm^2/s^2)		21.3	44.8	19.4	18.0	15.4	18.1	8.1	12.4	10.4	8.4	12.8	18.1	36.7	34.4	27.4	22.0	30.1	35.7	42.6	
	case 3.3	transect 1	U (cm/s)		36.7	37.8	29.0	26.6	24.7	22.7	19.5	29.7	38.9	38.6	31.6	31.8								
		(x = 145 cm)	k_t (cm^2/s^2)		10.0	33.4	25.2	29.4	42.9	46.2	59.3	39.5	24.3	14.7	12.4	11.7								
		transect 2	U (cm/s)		32.5	32.0	24.6	26.9	24.1	25.2	36.3	34.3	29.1	26.9	26.5	27.5								
		(x = 194 cm)	k_t (cm^2/s^2)		29.4	36.4	40.9	38.5	34.4	33.9	35.0	24.6	29.1	28.4	30.2	28.0								
	case 4.1	transect 1	U (cm/s)	22.7	16.4	10.9	19.5	37.9	41.4	30.1	16.7	15.7	23.1	38.7	17.5	14.9	13.2	18.3	16.3	16.4	24.5	30.8	28.6	31.4
		(x = 120 cm)	k_t (cm^2/s^2)	27.5	15.8	39.2	14.5	44.4	17.7	32.6	10.2	12.6	30.4	36.8	24.1	29.6	33.2	25.2	32.4	14.4	17.8	84.7	15.4	23.3
		transect 2	U (cm/s)	39.2	40.6	18.7	21.5	21.0	23.5	28.2	34.0	34.3	23.5	15.5	18.4	22.5	38.5	30.5						
		(x = 190 cm)	k_t (cm^2/s^2)	8.9	40.2	20.2	38.2	18.6	37.6	22.7	11.0	16.6	12.3	56.5	34.4	10.3	12.4	7.5						
	case 4.2	transect 1	U (cm/s)	36.1	35.8	33.3	28.2	25.3	29.7	16.4	14.0	21.9	11.3	18.7	15.9	24.1	27.9	33.8	19.8	18.8	19.1	23.8	43.4	43.3
		(x = 165 cm)	k_t (cm^2/s^2)	14.4	28.8	36.7	68.0	90.7	28.6	5.6	21.8	6.7	38.3	15.9	51.3	17.5	35.1	17.7	9.1	12.6	11.2	14.6	19.3	19.3
		transect 2	U (cm/s)	42.6	44.8	29.8	24.4	25.9	26.1	28.8	29.3	34.8	28.5	25.4	21.9	21.3	26.7	38.0	32.6	18.9	16.4	26.5	29.0	49.8
		(x = 190 cm)	k_t (cm^2/s^2)	7.2	6.8	36.6	38.6	30.7	30.5	23.4	14.5	10.0	15.0	28.8	15.5	14.2	12.5	18.7	22.3	26.6	22.8	128	160	25.1
	case 4.3	transect 1	U (cm/s)	39.7	39.4	42.8	31.6	31.9	17.5	10.0	17.0	22.1	20.2	8.8	26.4	22.6	28.9	26.4	20.4	18.8	29.4	33.4	42.3	
		(x = 135 cm)	k_t (cm^2/s^2)	28.7	23.6	19.6	10.1	13.9	40.8	60.3	76.2	21.1	22.8	86.4	51.0	36.1	10.4	12.0	33.4	22.1	10.8	11.6	12.7	
		transect 2	U (cm/s)	28.9	26.1	30.8	31.3	21.3	12.1	15.0	11.5	26.3	17.5	26.6	22.2	20.5	27.8	26.0	24.5	21.6	22.0	25.6	40.4	
		(x = 165 cm)	k_t (cm^2/s^2)	37.8	34.7	31.5	82.1	45.4	58.2	16.5	67.0	9.6	33.7	15.0	33.8	40.8	30.9	24.0	14.0	14.5	19.6	25.4	22.7	

*Data with low correlation were excluded, mostly coinciding with position inside patches. Patch distributions are shown in Figures A1.3-A1.5.

A2 Supporting Information for Chapter 3

A2.1. Introduction to the turbulence model (Eqn. 3.4)

In the main text, turbulence within a canopy of cylindrical stems is described by

$$\langle k_\mathrm{t} \rangle = \underbrace{\frac{C_\mathrm{f} U^2}{0.19}}_{k_\mathrm{t,b}} + \underbrace{\delta_{k_\mathrm{t}} \left[\frac{2C_\mathrm{D,form}\,\phi}{\pi(1-\phi)}\right]^{\frac{2}{3}} U^2}_{k_\mathrm{t,v}}, \tag{3.4}$$

which is based on Yang et al. (2016) and assumes that the near-bed TKE is the sum of bed-generated turbulence, $k_\mathrm{t,b}$, and stem-generated turbulence, $k_\mathrm{t,v}$.

The model of stem-generated turbulence was proposed by Tanino and Nepf (2008). This model assumes a local balance between TKE production in the stem wake, P_w, and viscous dissipation, ϵ, which is accurate for emergent vegetation (e.g., Nepf & Vivoni, 2000). TKE production in the stem wake is equal to the rate of work done by form drag on the cylindrical stems (Eqn. 2.8 in Tanino & Nepf, 2008). The viscous dissipation can be written in terms of the turbulent velocity scale $\sqrt{k_t}$ and integral length scale, l_e (e.g., Tennekes and Lumley, 1972).

Specifically, $\epsilon \sim \sqrt{k_t}^3 / l_e$. Using $P_w \approx \epsilon$ and rearranging,

$$\frac{\langle k_t \rangle}{U^2} \sim \left[\frac{2C_\mathrm{D,form}\,\phi}{\pi(1-\phi)} \frac{l_e}{d}\right]^{\frac{2}{3}}. \tag{A2.1}$$

In a sparse array ($\phi < 0.1$ and 0.06 for a regular and random array, respectively), $l_\mathrm{e} \sim d$, with d the stem diameter. Yang et al. (2016, 2018, 2019) and the current study only consider sparse arrays, so $l_\mathrm{e} \sim d$, and stem size is cancelled from Equation A2.1, so that k_t is a function of solid volume fraction, ϕ, but not stem size.

A2.2. Quantitative description of the impulse model

Bedload transport reflects the sum of individual grain dislodgement events (Niño & Garcia, 1996), which depend on both the magnitude, F, and the duration, Δt, of drag and lift forces exerted on the bed (Diplas et al., 2008; Celik et al., 2010), the combination of which is impulse. The force magnitude is proportional to the square of the turbulence intensity, $F \sim {u_{rms}}^2$ (Zanke, 2003), and ${u_{rms}}^2 \sim k_\mathrm{t}$. The duration of a turbulent event depends on the eddy size, l_e, and advection speed, which is generally assumed to be the time-and-spatial-mean velocity, U, according to Taylor's frozen turbulence approximation (Pope, 2000), i.e., $\Delta t \sim l_\mathrm{e}/U$. Within an array, the eddy scale is set by the minimum of the stem diameter, d, and surface-to-surface spacing, Δs, i.e., $l_\mathrm{e} \sim \min\{d, \Delta s\}$ (Tanino & Nepf, 2008). Here we consider a sparse array ($d/\Delta s < 0.56, \phi < 0.1$), for which $l_\mathrm{e} \sim d$, so that larger stems produce larger eddies, which generate turbulence events of longer duration at the bed.

For a constant solid volume fraction and velocity, the cumulative impulse, and thus sediment transport, is not impacted by stem size. Consider two arrays of circular stems with the same solid volume fraction, ϕ, and exposed to the same channel-averaged velocity, U, but consisting of different stem diameter, d (Figure 3-1 in main text). If U is sufficient to generate stem turbulence in both arrays ($Re_\mathrm{d} = \frac{Ud}{\nu} > 120$, Liu & Nepf, 2016), then these arrays have the same turbulence (Eqn. 3.4, given above and in the main text; Yang & Nepf, 2019). For simplicity, we attribute all of the turbulent kinetic energy, k_t, to the main energy-containing eddies with length scale l_e, so that the turbulent velocity fluctuation can be represented by a single sinusoidal associated with l_e and its associated frequency f_e, which has the following streamwise component

$$u'(t) = \sqrt{2}\, u_\mathrm{rms} \sin(2\pi f_e t). \tag{A2.2}$$

The force magnitude is proportional to u'^2, which is plotted in Figure 1c for the two stem sizes. For particle entrainment to occur, the force must exceed a critical value, (${u'_{cr}}^2$ in Figure 3-1c), and the product of force magnitude ($\sim u'^2$) and duration ($\Delta t \sim l_\mathrm{e}/U$) must exceed the critical impulse, I_cr, both of which are functions of grain size (Diplas et al., 2008). Combing these constraints, $u'^2 > {u'_{cr}}^2$ must be experienced for a minimum time, $\Delta t_{min} \sim I_{cr}\,/{u'_{cr}}^2$, to generate particle entrainment. In each eddy cycle, the critical force is exceeded for Δt_1 and Δt_2, in array 1 (Figure 3-1a) and 2 (Figure 3-1b), respectively. If both Δt_1 and Δt_2 are larger than Δt_{min}, it can be shown that for equal turbulence magnitude (Figure 3-1c), the average impulse in exceedance of the critical value is the same in both arrays, because there is a trade-off between number (frequency) and size (duration) of turbulent interactions with the bed. That is, the integral over time represented by the blue and orange shading is the same in arrays 1 and 2 (Figure 3-1c, for mathematical details see A2.3). Assuming the same grain size for both channels, exposure to an equivalent total impulse should produce a similar channel-scale bedload sediment transport. That is, given the same turbulent kinetic energy, bedload transport does not depend on stem diameter.

A2.3. Proof of equal total impulse

The total impulse for Case *n* (n = 1 or 2 in Figure 3-1) is defined by

$$I_{\mathrm{n}} = \int_0^{T_{\mathrm{s}}} [u'(t;n)]^2 H\{[u'(t;n)]^2 - u_{\mathrm{cr}}'^2(n)\} dt, \tag{A2.3}$$

in which T_{s} is the time of interest, and $H(x) = \begin{cases} 0 & x < 0 \\ 1 & x \geq 0 \end{cases}$ is the unit (Heaviside) step function.

Case 1 and 2 have different scales of turbulent eddies with periods $T_1 = \frac{1}{f_{\lambda_1}}$ and $T_2 = \frac{1}{f_{\lambda_2}}$, as depicted in Figure 1. If the duration of interest is sufficiently long ($T_{\mathrm{s}} \gg T_1, T_2$), the remainder of T_{s} divided by T_1 ($T_{\mathrm{s}} \bmod T_1$) or T_2 ($T_{\mathrm{s}} \bmod T_2$) will also be sufficiently small compared with T_{s}, so that we have:

$$T_{\mathrm{s}} \approx N_1 T_1 \approx N_2 T_2, \tag{A2.4}$$

in which N_1 and N_2 are positive integers. In addition, we assume $u_{\mathrm{rms}}(1) = u_{\mathrm{rms}}(2) = u_{\mathrm{rms}} > 0$ and $u_{\mathrm{cr}}'(1) = u_{\mathrm{cr}}'(2) = u_{\mathrm{cr}}' > 0$.

For Case 1, we have:

$$\begin{aligned} I_1 &= \int_0^{T_{\mathrm{s}}} [u'(t;1)]^2 H\{[u'(t;1)]^2 - u_{\mathrm{cr}}'^2(1)\} dt \\ &\approx N_1 \int_0^{T_1} [u'(t;1)]^2 H\{[u'(t;1)]^2 - u_{\mathrm{cr}}'^2(1)\} dt \\ &= 2N_1 u_{\mathrm{rms}}^2 \int_0^{T_1} \sin^2\left(2\pi f_{\lambda_1} t + \varphi_{\lambda_1}\right) H\{[u'(t;1)]^2 - u_{\mathrm{cr}}'^2\} dt \\ &= N_1 u_{\mathrm{rms}}^2 \int_0^{T_1} \left[1 - \cos\left(4\pi f_{\lambda_1} t + 2\varphi_{\lambda_1}\right)\right] H\{[u'(t;1)]^2 - u_{\mathrm{cr}}'^2\} dt. \end{aligned} \tag{A2.5}$$

If $\sqrt{2}u_{\mathrm{rms}} \leq u_{\mathrm{cr}}'$, given $|u'(t;n)| \leq \sqrt{2}u_{\mathrm{rms}}$, $H\{[u'(t;n)]^2 - u_{\mathrm{cr}}'^2\} = 0$ is thus valid for $\forall t \in [0, T_{\mathrm{s}}]$, and the integral $I_1 = I_2 = 0$. This implies we will not observe sediment transport for either case. If $\sqrt{2}u_{\mathrm{rms}} > u_{\mathrm{cr}}'$, the integral in Eqn. A2.5 can be simplified as follows:

$$\begin{aligned} I_1 &\approx N_1 u_{\mathrm{rms}}^2 \int_0^{T_1} \left[1 - \cos\left(4\pi f_{\lambda_1} t + 2\varphi_{\lambda_1}\right)\right] H\{[u'(t;1)]^2 - u_{\mathrm{cr}}'^2\} dt \\ &= N_1 u_{\mathrm{rms}}^2 \int_0^{T_1} \left[1 - \cos\left(4\pi f_{\lambda_1} t\right)\right] H\left\{\left[u'\left(t - \frac{\varphi_{\lambda_1}}{2\pi f_{\lambda_1}}; 1\right)\right]^2 - u_{\mathrm{cr}}'^2\right\} dt \end{aligned}$$

$$= 2N_1 u_{\text{rms}}^2 \int_0^{T_1/2} [1 - \cos(4\pi f_{\lambda_1} t)] H\left\{\left[u'\left(t - \frac{\varphi_{\lambda_1}}{2\pi f_{\lambda_1}}; 1\right)\right]^2 - u_{\text{cr}}'^2\right\} dt. \tag{A2.6}$$

Within the interval $[0, T_1/2]$, the step function $H\left\{\left[u'\left(t - \frac{\varphi_{\lambda_1}}{2\pi f_{\lambda_1}}; 1\right)\right]^2 - u_{\text{cr}}'^2\right\}$ has two discontinuities at $t = T_{1\text{a}}$ and $t = T_{1\text{b}}$. Without loss of generality, let $T_{1\text{a}} < T_{1\text{b}}$ and $u'\left(T_{1\text{a}} - \frac{\varphi_{\lambda_1}}{2\pi f_{\lambda_1}}; 1\right) = u'\left(T_{1\text{b}} - \frac{\varphi_{\lambda_1}}{2\pi f_{\lambda_1}}; 1\right) = u_{\text{cr}}' > 0$, so that

$$\sin(2\pi f_{\lambda_1} T_{1\text{a}}) = \sin(2\pi f_{\lambda_1} T_{1\text{b}}) = \frac{u_{\text{cr}}'}{\sqrt{2} u_{\text{rms}}}, \tag{A2.7}$$

and

$$T_{1\text{a}} = \frac{T_1}{2\pi} \sin^{-1}\left(\frac{u_{\text{cr}}'}{\sqrt{2} u_{\text{rms}}}\right) \in \left(0, \frac{T_1}{4}\right), T_{1\text{b}} = \frac{T_1}{2} - T_{1\text{a}}. \tag{A2.8}$$

Hence,

$$I_1 \approx 2N_1 u_{\text{rms}}^2 \int_0^{\frac{T_1}{2}} [1 - \cos(4\pi f_{\lambda_1} t)] H\left\{\left[u'\left(t - \frac{\varphi_{\lambda_1}}{2\pi f_{\lambda_1}}; 1\right)\right]^2 - u_{\text{cr}}'^2\right\} dt$$

$$= 4N_1 u_{\text{rms}}^2 \int_{T_{1\text{a}}}^{\frac{T_1}{4}} [1 - \cos(4\pi f_{\lambda_1} t)] dt$$

$$= 4N_1 u_{\text{rms}}^2 \left[t - \frac{1}{4\pi f_{\lambda_1}} \sin(4\pi f_{\lambda_1} t)\right]\Bigg|_{T_{1\text{a}}}^{\frac{T_1}{4}}$$

$$= 4N_1 u_{\text{rms}}^2 \left\{\left(\frac{T_1}{4} - \frac{T_1}{2\pi} \sin^{-1}\left(\frac{u_{\text{cr}}'}{\sqrt{2} u_{\text{rms}}}\right)\right) - \frac{T_1}{4\pi}\left\{1 - \sin\left[2 \sin^{-1}\left(\frac{u_{\text{cr}}'}{\sqrt{2} u_{\text{rms}}}\right)\right]\right\}\right\}$$

$$= 4\boldsymbol{N_1 T_1} u_{\text{rms}}^2 \left\{\left(\frac{1}{4} - \frac{1}{2\pi} \sin^{-1}\left(\frac{u_{\text{cr}}'}{\sqrt{2} u_{\text{rms}}}\right)\right) - \frac{1}{4\pi}\left\{1 - \sin\left[2 \sin^{-1}\left(\frac{u_{\text{cr}}'}{\sqrt{2} u_{\text{rms}}}\right)\right]\right\}\right\}. \tag{A2.9}$$

Note: It can be shown that $\sin(2 \sin^{-1} x) = 2x\sqrt{1 - x^2}$, but this is unnecessary here.

Similarly,

$$I_2 \approx 4\boldsymbol{N_2 T_2} u_{\mathrm{rms}}^2 \left\{ \left(\frac{1}{4} - \frac{1}{2\pi} \sin^{-1} \left(\frac{u'_{\mathrm{cr}}}{\sqrt{2} u_{\mathrm{rms}}} \right) \right) - \frac{1}{4\pi} \left\{ 1 - \sin \left[2 \sin^{-1} \left(\frac{u'_{\mathrm{cr}}}{\sqrt{2} u_{\mathrm{rms}}} \right) \right] \right\} \right\}. \quad \text{(A2.10)}$$

Because $T_{\mathrm{s}} \approx N_1 T_1 \approx N_2 T_2$, $I_1 \approx I_2$. That is, the same cumulative impulse is experienced in both channels, so that cumulative impulse is not a function of stem size.

Furthermore, if significant bed sediment entrainment is assumed, the total impulse a sediment grain experiences, I, within the duration of interest, T_{s}, is approximately not dependent on the ratio of the velocity fluctuation, u_{rms}, to the velocity threshold, u'_{cr}. This is granted when $\frac{u_{\mathrm{rms}}}{u'_{\mathrm{cr}}} > 1.34$ so that $\frac{\left| I_{\mathrm{total}} - I_{\mathrm{total}} \left(\frac{u_{\mathrm{rms}}}{u'_{\mathrm{cr}}} \to +\infty \right) \right|}{I_{\mathrm{total}} \left(\frac{u_{\mathrm{rms}}}{u'_{\mathrm{cr}}} \to +\infty \right)} < 0.1$. With this assumption, $I \propto u_{\mathrm{rms}}^2$.

A2.4. Photographs of 1-m-long section within 3-m long array.

Flow direction was from left to right for all images.

Case 1.1
d = 0.64 cm,
ϕ = 0.012,
U = 25.3 ± 0.5 cm/s

Case 2.1
d = 2.5 cm,
ϕ = 0.0051,
U = 38.0 ± 1.1 cm/s

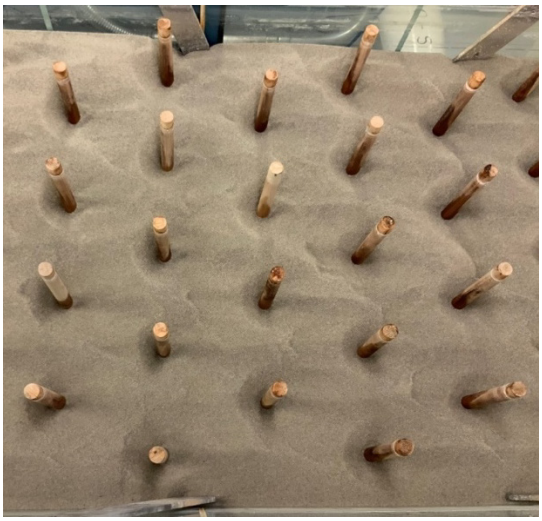

Case 2.7
d = 2.5 cm,
ϕ = 0.012,
U = 33.6 ± 1.2 cm/s

Case 3.4
d = 1.3, 1.9 cm,
ϕ = 0.025,
U = 16.8 ± 0.7 cm/s

Case 4.2
d = 1.3, 1.9, 5.1 cm,
ϕ = 0.025,
U = 33.8 ± 0.6 cm/s

A2.5. Grain size analysis of bed sediment

This study used AGSCO #00N silica sand, which was also used by Yang and Nepf (2018, 2019) and Shan et al. (2020). After the final run, we sampled approximately 300 g of bed sediment, and conducted sieve analysis at MIT Pierce Laboratory. The sieves were cleaned and weighed separately. The sediment sample went through a stack of sieves, fining downward, and the finest composition was collected in a pan at the bottom. Then, the lid of sieve set was closed, and the entire set was shaken for 5 min on a sieve shaker. The sieve set was taken off and disassembled, and we weigh each sieve again to derive the mass of retrieved sediment for each class.

Sieve #	μm	φ	Tare (g)	Bulk (g)	Net (g)	%	Cumulative %
20	850	0.2	410.55	413.70	3.15	1.25	1.25
25	710	0.5	432.17	479.06	46.89	18.61	19.87
30	600	0.7	616.00	696.35	80.35	31.90	51.76
35	500	1.0	553.53	632.28	78.75	31.26	83.03
40	425	1.2	573.94	605.67	31.73	12.60	95.62
45	350	1.5	450.32	455.11	4.79	1.90	97.52
Pan			339.37	345.61	6.24	2.48	100.00

A2.6. Bedload transport prediction

The bed shear stress was predicted using Eqn. 6 in Yang and Nepf (2018):

$$\tau = \begin{cases} \frac{4\rho\nu U}{d} & Re_{\mathrm{d}} < \frac{4}{C_{\mathrm{f}}} \\ \rho C_{\mathrm{f}} U^2 & Re_{\mathrm{d}} \geq \frac{4}{C_{\mathrm{f}}} \end{cases}, \tag{3.10}$$

which reflects the reduction of the viscous sublayer due to vegetation-generated turbulence. The bed drag coefficient was estimated from Julien (2010, Eqn. 6.19c in page 121):

$$C_{\mathrm{f}} = \frac{1}{\left[\frac{1}{\kappa}\ln\left(\frac{2h}{d_{50}}\right)\right]^2}, \tag{A2.11}$$

in which $\kappa = 0.4$ is the von Kármán constant. The measured $C_{\mathrm{f}} = 0.0043 \pm 0.0009$, based on velocity profiles over an unvegetated flat bed in this study, matched Eqn. 3.11. The TKE, k_{t}, was predicted using Eqn. 3.8 with $\delta_{k_{\mathrm{t}}} = 0.52 \pm 0.07$ (95% CI). The settling velocity was calculated using the Rubey (1933) equation

$$w_s = \left[\sqrt{\frac{2}{3} + \frac{36\nu^2}{(\rho_s/\rho - 1)g d_{50}^3}} - \sqrt{\frac{36\nu^2}{(\rho_s/\rho - 1)g d_{50}^3}}\right]\sqrt{(\rho_s/\rho - 1)g d_{50}}, \tag{A2.12}$$

which is accurate to within 30% for the grain sizes considered (Hallermeier, 1981; Dietrich, 1982). The critical shear stress θ_{cr} was extracted from previous data and fitted Shields curves reported in Soulsby (1997) and Whitehouse et al. (2000). The θ_{cr} and $k^*_{\mathrm{t,cr}}$ values are discussed in more detail in Section 3.5.1 in the main text.

In addition, Yang and Nepf (2018) considered the Einstein-Brown (1950) formula to predict sediment transport in model vegetation. The original Einstein-Brown (Einstein, 1950; Brown, 1950) model (blue dashed curve in subplot a)

$$q^*_{\mathrm{s}} = \begin{cases} 2.15e^{-0.391/\theta} & \theta < 0.18 \\ 40\theta^3 & 0.18 \leq \theta \leq 0.52 \\ 15\theta^{1.5} & \theta > 0.52 \end{cases}. \tag{A2.13}$$

was converted to a kt-based model. Specifically, Yang and Nepf (2018) replaced the dimensionless bed shear stress θ with $0.19k_t^*$ (Soulsby, 1983). The converted kt-based Einstein-Brown model (blue dashed curve in subplot b) is:

$$q^*_{\mathrm{s}} = \begin{cases} 2.15e^{-2.06/k^*_{\mathrm{t}}} & k^*_{\mathrm{t}} < 0.95 \\ 0.27{k^*_{\mathrm{t}}}^3 & 0.95 \leq k^*_{\mathrm{t}} \leq 2.74 \\ 1.24{k^*_{\mathrm{t}}}^{1.5} & k^*_{\mathrm{t}} > 2.74 \end{cases}. \tag{A2.14}$$

The plot below is an updated version of Figure 3 in Yang and Nepf (2018), with the addition of data from Armanini and Cavedon (2019), Shan et al. (2020), Wu et al. (2021), and the current study. Yang and Nepf (2018) estimated bed shear stress using their Eqn. 6 (Eqn. 3.10 in this study), and found that turbulent kinetic energy, rather than bed shear stress, was a better predictor for bedload transport rate in vegetated channels.

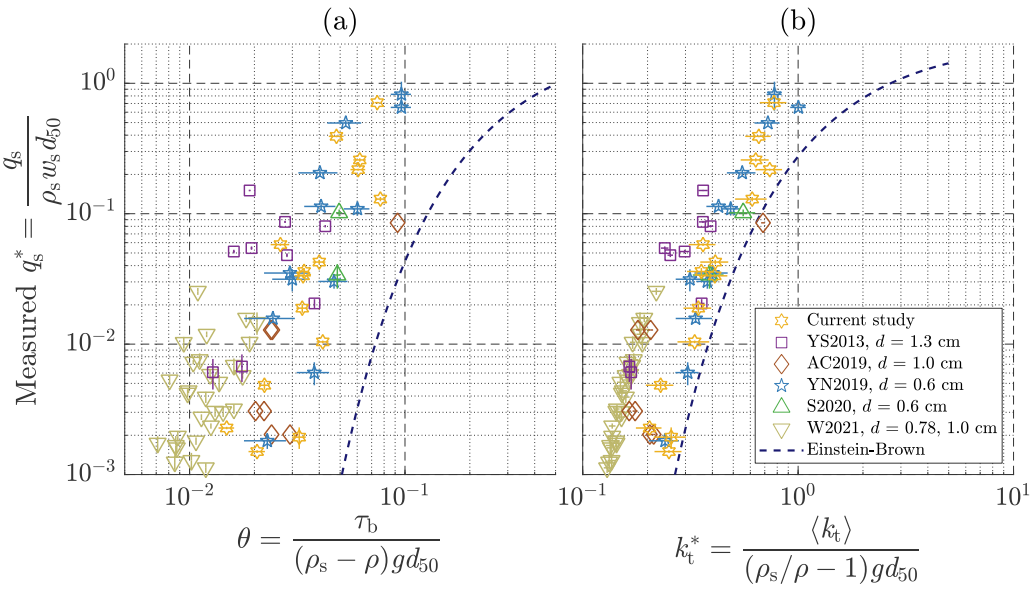

Measured dimensionless sediment transport rate $q_s^* = \frac{q_s}{\rho_s w_s d_{50}}$ versus (a) dimensionless bed stress $\theta = \frac{\tau}{(\rho_s - \rho) g d_{50}}$ predicted using Eqns. 3.10 and A2.11, and (b) dimensionless turbulent kinetic energy $k_t^* = \frac{k_t}{(\rho_s/\rho - 1) g d_{50}}$ predicted using Eqn. 3.8 and $\delta_{k_t} = 0.52 \pm 0.07$ (95% CI). The median grain size was d_{50} = 0.5 mm in the current study and in Yager and Schmeeckle (2013), Armanini and Cavedon (2019), Yang and Nepf (2019), and Shan et al. (2020). For Wu et al. (2021), d_{50} = 0.93 mm. The blue dashed lines represent EB (Eqns. A2.13 & A2.14).

A2.7. Model plants used in Xu and Nepf (2020)

Typha latifolia

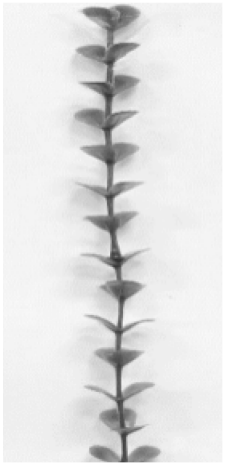

Rotala indica

Data used to produce Figure 4 can be downloaded from:
https://doi.org/10.6084/m9.figshare.12228812.v2

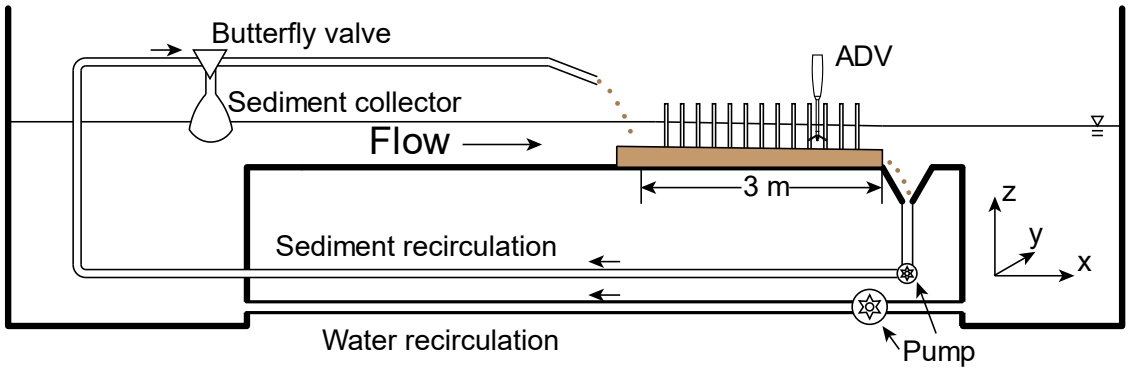

Figure A2-1. Side view of the flume (not to scale).

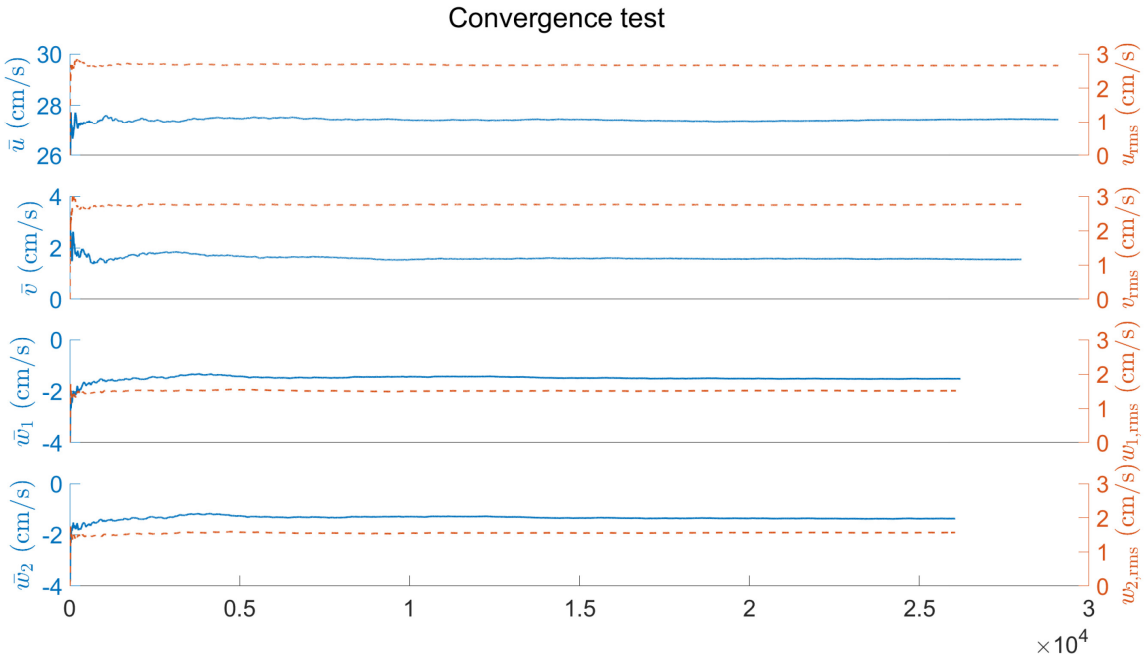

Figure A2-2. Cumulative average of velocity components and root-mean-square values over time, at (x, y, z) = (199 cm, 50 cm, 4 cm) in Case 4.3. The sampling frequency was 200 Hz. Down-looking Vectrino reports two vertical velocities at the same time. All the averages converge at ~6000 sample points (corresponding to a 30-s-long record), but 150-s-long signals were recorded for turbulence analysis with higher resolution.

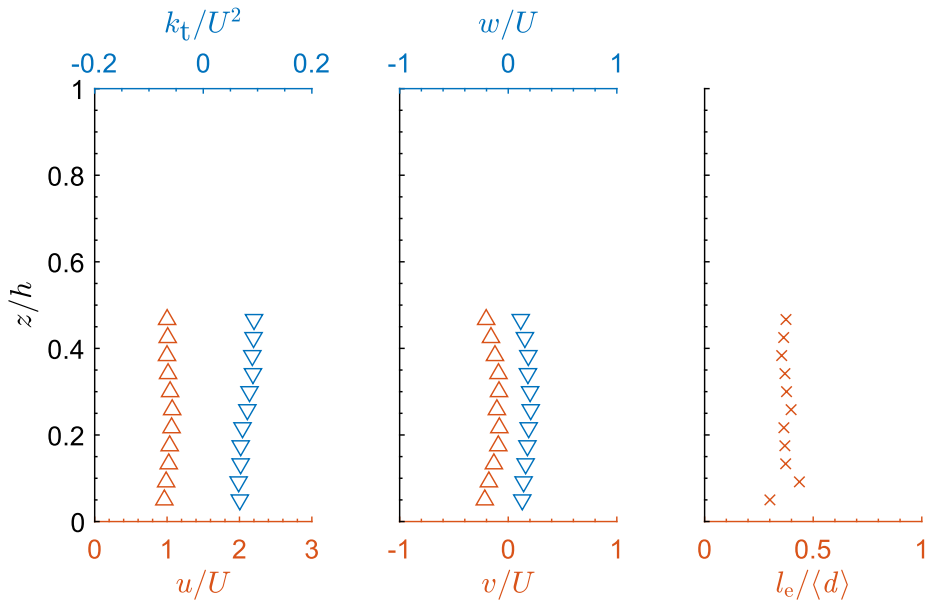

Figure A2-3. Vertical profiles of normalized velocity (u/U, v/U, w/U), normalized TKE (k_t/U^2), and normalized integral length scale ($l_e/\langle d \rangle$) at (x, y) = (245 cm, 55 cm) in Case 4.1. Vertical profiles were measured at the spatial position at which the time-mean velocity matched the spatially and temporally averaged velocity of the transect. The vertical profiles confirmed that mid-depth measurements reasonably represented near-bed conditions (2 cm above the bed).

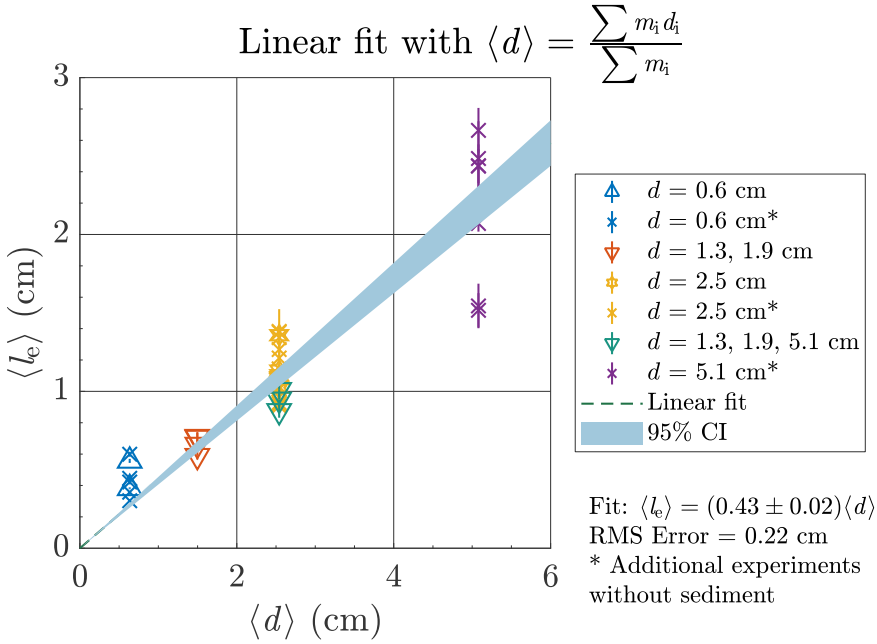

Figure A2-4. Integral length scale versus mean diameter defined as $\langle d \rangle = \frac{\sum_{i=1}^{p} m_i d_i}{\sum_{i=1}^{p} m_i}$. Cases marked by an asterisk were collected without sediment. Each data point is an average taken along one or two lateral transects. Error bars represent the standard error across transect(s).

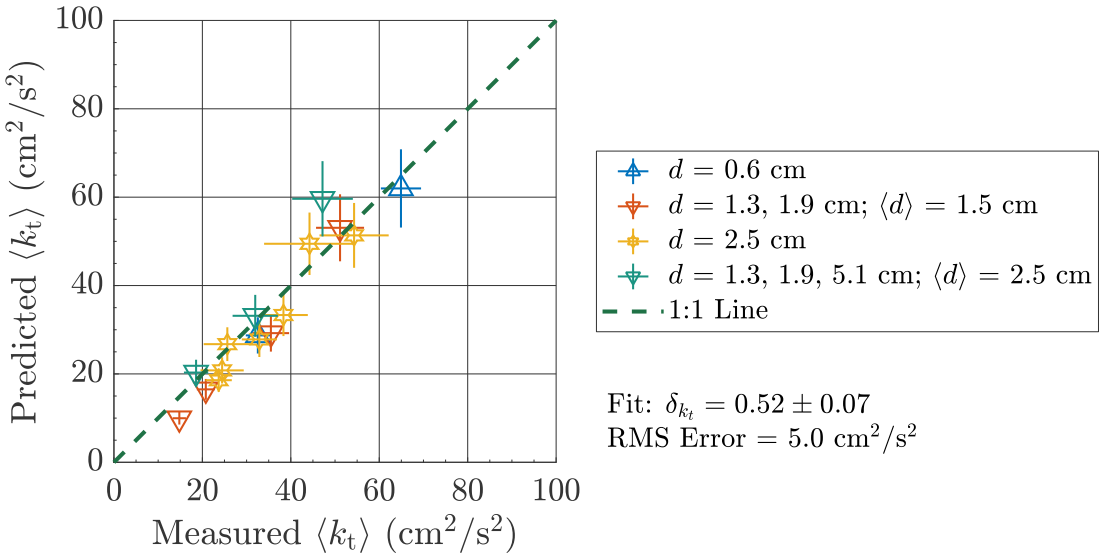

Figure A2-5. Predicted $\langle k_t \rangle$ versus measured $\langle k_t \rangle$. A least-squares fit with data in this study yielded $\delta_{k_t} = 0.52 \pm 0.07$ (95% CI) in Eqn. 3.10. Predicted and measured spatially averaged TKE values are plotted, along with a 1:1 line for reference.

Table A2.1: Nomenclature

Symbol	Unit	Name
$\langle\square\rangle$		Angle brackets; spatial average
$\overline{\square}$		Overbar; temporal average
$'$		Prime; temporal fluctuation
a	m^{-1}	Frontal (submerged) vegetation area per unit volume
C_D	-	Total drag coefficient of vegetation canopy
$C_{D,form}$	-	Form drag coefficient of (model) vegetation canopy
C_f	-	Bed drag coefficient
d	m	Stem diameter (or characteristic width) of vegetation
d_s	m	Grain size of bed sediment
d_{50}	m	Median grain size of bed sediment
F	$m^2\ s^{-2}$	Force magnitude of hydrodynamic force acting on bed sediment, per bed area and per fluid mass
f_e	s^{-1}	Frequency of eddy generation
g	$m\ s^{-2}$	Gravitational acceleration, 9.8 $m\ s^{-2}$
h	m^{-1}	Flow depth
I	$m^2\ s^{-1}$	Impulse of hydrodynamic force acting on bed sediment, per bed area and per fluid mass
k	-	Goring and Nikora (2002)'s velocity threshold in spike removal, 1.5
k_t	$m^2\ s^{-2}$	Turbulent kinetic energy per unit fluid mass, spatially averaged
$k_{t,b}$	$m^2\ s^{-2}$	Bed-generated turbulent kinetic energy
$k_{t,v}$	$m^2\ s^{-2}$	Vegetation-generated turbulent kinetic energy
$k_t^* = \frac{k_t}{(\rho_s/\rho - 1)gd_{50}}$	-	Dimensionless turbulent kinetic energy
$k_{t,cr}^*$	-	Dimensionless critical turbulent kinetic energy
l_e	m	Length scale of turbulent eddies; (local) integral length scale
m	m^{-2}	Number of stems per unit bed area
q_s	$kg\ m^{-1}\ s^{-1}$	Mass sediment transport rate per unit width
$q_s^* = \frac{q_s}{\rho_s w_s d_{50}}$	-	Dimensionless sediment transport rate (Einstein number)
$Re_d = Ud/\nu$	-	Stem Reynolds number
S	-	Surface energy slope
Δs	m	Surface-to-surface spacing between stems
t	s	Time
Δt	s	Duration of hydrodynamic force acting on bed sediment
U	$m\ s^{-1}$	Channel velocity, spatially and temporally averaged
${u_{cr}}'^2$	$m^2\ s^{-2}$	Critical force magnitude for local grain entrainment
u_e	$m\ s^{-1}$	Eddy velocity
u, v, w	$m\ s^{-1}$	Instantaneous velocity component
x, y, z	m	Streamwise, lateral/transverse, and vertical coordinates

$u_{\mathrm{rms}} = \sqrt{\frac{1}{N}\sum_{i=1}^{N}(u')^2}$	m s^{-1}	Root-mean-square velocity component
w_s	m s^{-1}	Settling velocity of sediment
δ_{k_t}	-	Scale factor of vegetation-generated turbulence
ϕ	-	Solid volume fraction of (model) vegetation
ρ_s	kg m^{-3}	Sediment density, 2650 kg m^{-3} for quartz
ρ	kg m^{-3}	Fluid density, 1000 kg m^{-3} for water
τ	kg m^{-1} s^{-2} or N m^{-2}	Bed shear stress, temporally averaged
$\theta = \frac{\tau}{(\rho_s - \rho)gd_{50}}$	-	Dimensionless bed shear stress (Shields number)
θ_{cr}	-	Critical Shields number
κ	-	von Kármán constant, 0.4
λ_a	-	Goring and Nikora (2002)'s acceleration threshold in spike removal, 1
Λ_t	s	(Local) integral time scale
ν	m^2 s^{-1}	Fluid kinematic viscosity, 10^{-6} m^2 s^{-1} for water at 20°C

Table A2.2: Summary of experimental cases

Case #	Arrangement	ϕ	d (cm)	h (cm)	U (cm/s)	$\sigma(U)$ (cm/s)	$\langle k_t \rangle$ (cm^2/s^2)	$\sigma(k_t)$ (cm^2/s^2)	q_s (g m^{-1} s^{-1})	$\sigma(q_s)$ (g m^{-1} s^{-1})	$\langle l_e \rangle$ (cm)	$\sigma(l_e)$ (cm)
1.1	Uniform staggered	0.012	0.64	12.1	25.3	0.5	33	3	2.98	0.19	0.382	0.006
1.2	Uniform staggered	0.012	0.64	12.0	37.4	0.5	65	4	58.7	0.8	0.557	0.013
2.1	Random	0.0051	2.5	10.8	38.0	1.1	44	10	10.7	0.4	1.12	0.03
2.2	Random	0.0051	2.5	11.0	28.0	0.9	26	5	0.86	0.02	0.97	0.05
2.3	Random	0.0051	2.5	11.5	24.6	0.9	24	5	0.16	0.03	0.92	0.04
2.4	Uniform staggered	0.012	2.5	10.7	19.9	0.6	25	3	0.40	0.03	1.35	0.04
2.5	Uniform staggered	0.012	2.5	12.5	24.7	0.8	35	4	1.56	0.12	1.06	0.02
2.6	Uniform staggered	0.012	2.5	12.6	27.0	1.0	41	6	3.52	0.14	1.10	0.02
2.7	Uniform staggered	0.012	2.5	12.5	33.6	1.2	58	8	21.4	0.6	1.100	0.017
3.1	Random	0.025	1.3, 1.9	11.0	13.0	0.6	14.6	1.5	-	-	0.73	0.04
3.2	Random	0.025	1.3, 1.9	10.5	22.3	1.1	31	4	4.79	0.11	0.66	0.03
3.3	Random	0.025	1.3, 1.9	13.0	30.1	1.2	49	5	32.4	0.5	0.72	0.02
3.4	Random	0.025	1.3, 1.9	11.5	16.8	0.7	20	2	0.188	0.004	0.60	0.02
4.1	Random	0.025	1.3, 1.9, 5.1	11.5	19.7	0.9	18	3	0.124	0.003	0.88	0.01
4.2	Random	0.025	1.3, 1.9, 5.1	10.8	33.8	0.6	47	3	18.0	0.3	1.010	0.019
4.3	Random	0.025	1.3, 1.9, 5.1	11.0	25.2	0.5	32	2	2.76	0.08	0.95	0.02

Notes

(a) The sediment used in this study is AGSCO #00N silica sand, d_{50} = 0.6 mm, $\rho_s = 2.65 \times 10^3$ kg/m^3;
(b) All the uncertainties $\sigma()$ represent standard error of measurements;
In Cases 3.1 – 3.4, the amount ratio of 1.3-cm and 1.9-cm cylinders was 9:5; in Cases 4.1 – 4.3, the amount ratio of 1.3-cm, 1.9-cm, and 5.1-cm cylinders was 4:3:3, respectively.

A3 Supporting Information for Chapter 4

A3.1. Near-bed TKE budget

The TKE budget terms were estimated from measured velocity. Wake production was calculated using the local time-mean streamwise velocity:

$$P_{\mathrm{w}} = \frac{1}{2} C_{\mathrm{D}} a \bar{u}^3. \tag{A3.1}$$

Shear production was evaluated as the product of Reynolds stress ($-\overline{u'w'}$) and vertical gradient of streamwise velocity ($\partial\bar{u}/\partial z$), with the latter estimated using a central difference.

$$P_{\mathrm{s}} = -\overline{u'w'}\frac{\partial \bar{u}}{\partial z}. \tag{A3.2}$$

Turbulent transport was estimated as the vertical gradient of vertical TKE flux ($\overline{w'k_{\mathrm{t}}}$):

$$T_{\mathrm{t}} = \frac{\partial \overline{w'k_{\mathrm{t}}}}{\partial z}. \tag{A3.3}$$

The gradients were calculated in MATLAB using gradient() function. The input data was not smoothed. In most cases, wake production was the dominant term in the near-bed region. However, in the dense canopy (Cases 3.1 – 3.3), as the submergence ratio (*H/h*) increased, turbulent transport became more important.

A3.2. Bedload transport rate on an unvegetated bed at same channel conditions

Ishii (2023) studied bare bed conditions in the same channel and with the same sediment (d_{50} = 0.5 mm) as in the present study. She determined the critical channel velocity for incipient motion U = 24.9 ± 0.8 cm/s. At this flow condition, the friction velocity was u_* = 0.0084 ± 0.0014 m/s, based on a logarithmic fit of the velocity profile within 10 cm of the bed. These values defined the bed skin friction coefficient,

$$C_\mathrm{f} = \left(\frac{u_*}{U}\right)^2 = 0.0011 \pm 0.0002 \text{ (95\% CI)}. \tag{A3.4}$$

Based on particle Reynolds number $Re_\mathrm{p} = \frac{u_* d_{50}}{\nu} = 2.9 < 5$, indicating that the flow was smooth turbulent. Consistent with this, Julien (2010)'s skin friction formula

$$\frac{U}{u_*} = 5.75 \lg\left(\frac{u_* H}{\nu}\right) + 3.25 \tag{A3.5}$$

predicted u_* = 0.010 m/s and C_f = 0.0016, which is in reasonable agreement with the measured values. The measured C_f = 0.0011 will be used in the following estimation.

The dimensionless critical bed shear stress is then,

$$\theta_\mathrm{cr} = \frac{\tau_\mathrm{cr}}{(\rho_\mathrm{s}-\rho) g d_{50}} = \frac{\rho C_\mathrm{f} U^2}{(\rho_\mathrm{s}-\rho) g d_{50}} = 0.012. \tag{A3.6}$$

For bare bed (*i.e.*, no vegetation), the Meyer-Peter-Müller (MPM) formula (Meyer-Peter & Müller, 1948) is a well-validated model:

$$q_\mathrm{s}^* = 8(\theta - \theta_\mathrm{cr})^{1.5}\,. \tag{A3.7}$$

Due to a problem with the facility, a direct measurement of sediment transport for a bare bed at 40 cm/s was not possible. Equation A3.7 was used to estimate the bedload transport for a bare bed under flow conditions comparable to the submerged canopy experiments (U = 40 ± 2 cm/s), resulting in q_s = 0.9 ± 0.2 g m^{-1} s^{-1}, which is shown with a gray horizontal band in Figure 4-5e.

A3.3. Sensitivity analysis of bed-shear-generated turbulence

Equation 4.24 from the main text is repeated here for convenience.

$$\frac{k_\mathrm{t,nb}}{k_\mathrm{t,wb}} = 1 + \delta_\mathrm{s}(ah)^{\frac{1}{2}}\left(1 - \frac{h}{H}\right)^{\frac{9}{2}}, \tag{4.24}$$

in which δ_s is the coefficient for near-bed turbulence enhancement by canopy shear production.

Using measured values of near-bed turbulence $k_\mathrm{t,nb}$, a sensitivity analysis (Figure A3-5) was used to find the best fit value for the bed turbulence coefficient, C_b. Specifically, we varied C_b for optimal fit with δ_s = 22 ± 2 (95% CI), which had the highest coefficient of determination, R^2, and the smallest root-mean-square error (RMSE). The best fit value was C_b = 0. This was consistent with the fact that in the near-bed region (z = 0 to 2 cm), the bed shear production was much smaller than wake production (Figure A3-2). In addition, for both canopies, ah > 0.1, indicating that stem drag and turbulence were dominant over bed drag and turbulence (see Belcher et al., 2003 and Yang & Nepf, 2019, respectively).

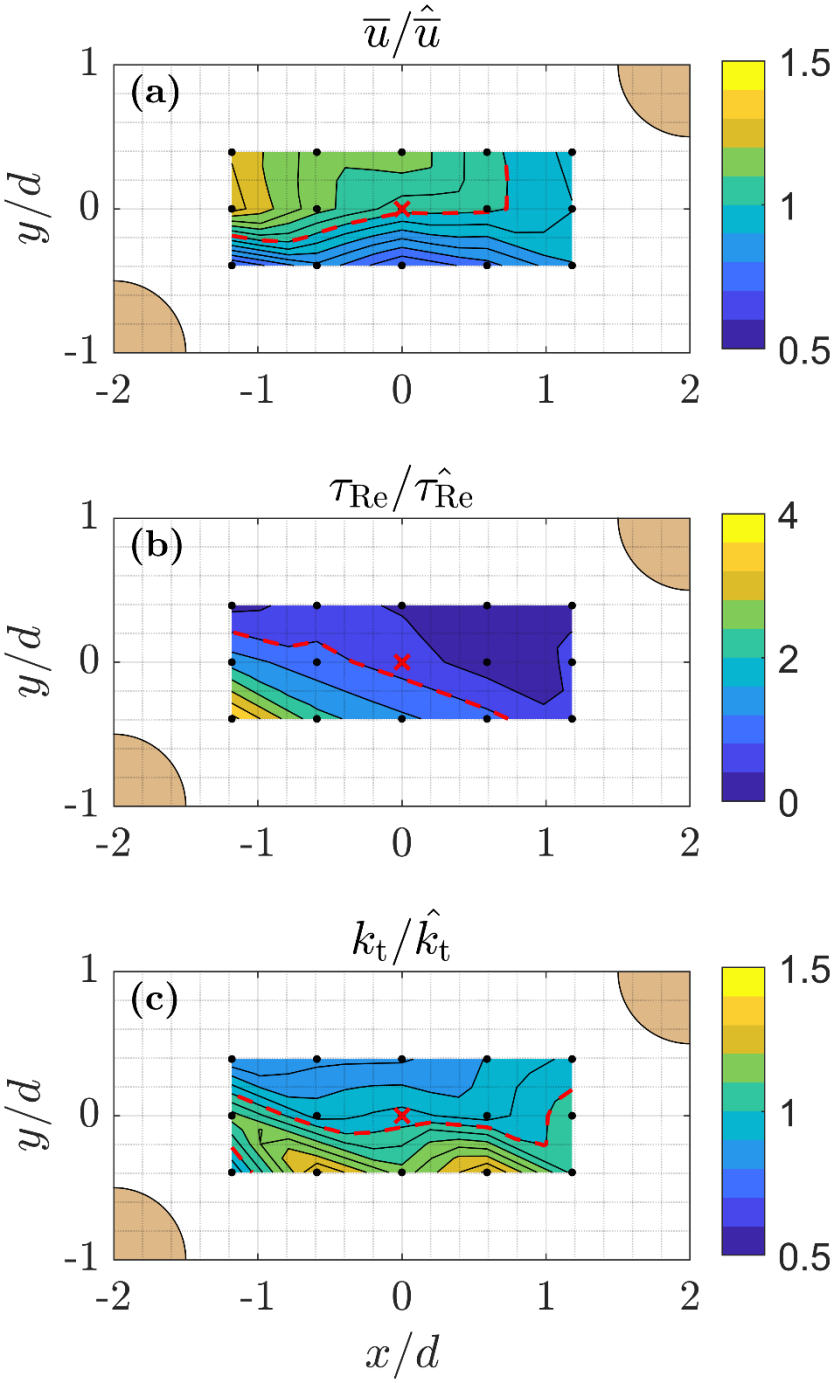

Figure A3-1. Case 2.3 contour plots of near-bed measurements taken in horizontal plane at z = 1.8 ± 0.2 cm relative to average bed level. (a) time-mean velocity, (b) Reynolds stress, and (c) turbulent kinetic energy, each normalized by the horizontal average, indicated by hat. Black dots indicate sampling points. Red cross shows the position of the vertical profile. Brown quarter-circles show position of cylinders. The contours of unity, where the local value matches the horizontal average, are marked with red dashed curves. Flow direction was from left to right.

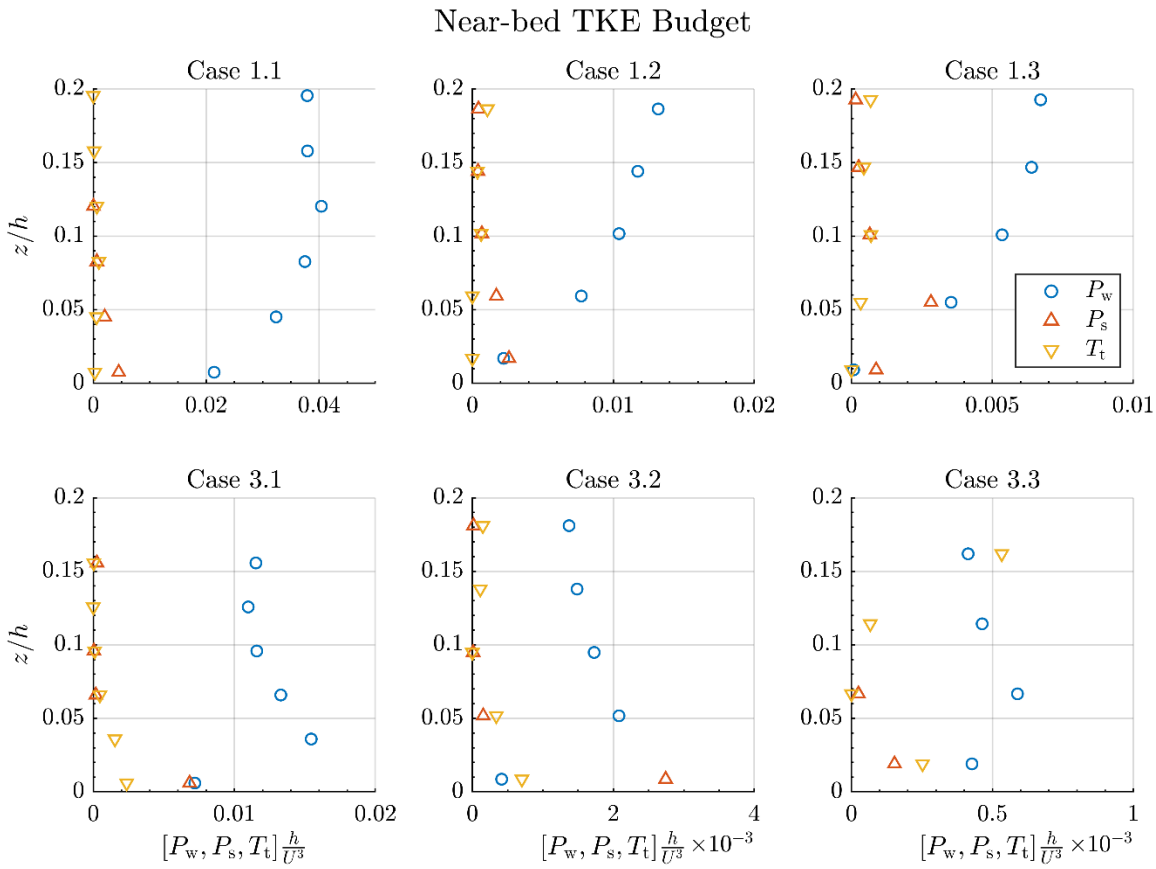

Figure A3-2. Vertical profiles in near-bed region ($z/h < 0.2$) of individual terms in TKE budget: Wake production $P_w = \frac{1}{2} C_D a \bar{u}^3$ (blue circles), shear production $P_s = -\overline{u'w'}\frac{\partial \bar{u}}{\partial z}$ (red upward triangles), and turbulent transport $T_t = \frac{\partial \overline{w'k_t}}{\partial z}$ (orange downward triangles). Note that near-bed shear production was much weaker than wake production for all the cases, except for some points directly at the bed.

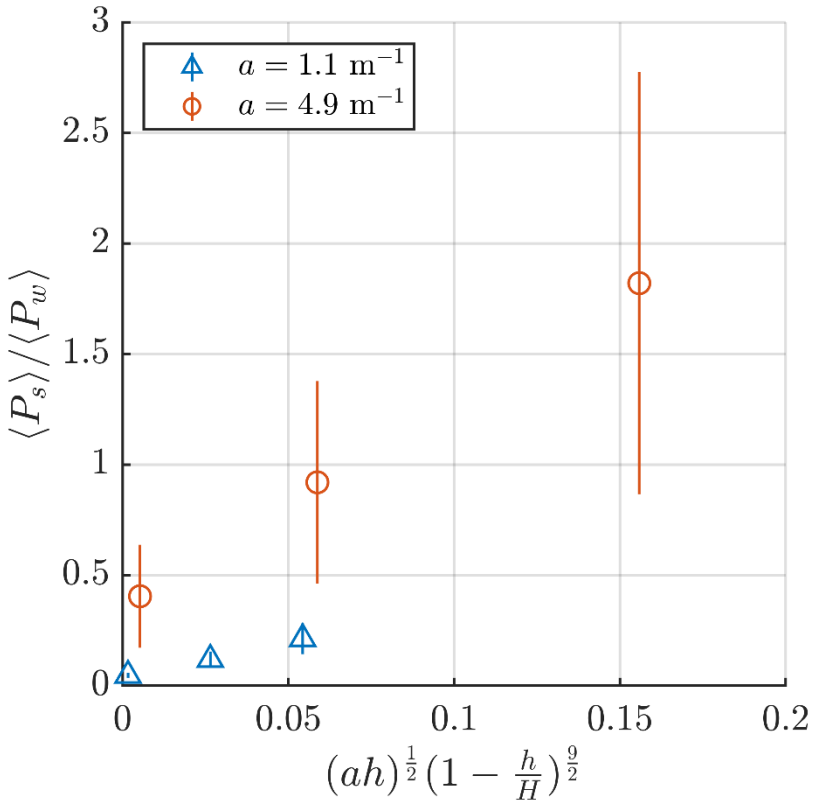

Figure A3-3. Ratio of canopy-averaged shear production $\langle P_s \rangle$ to wake production $\langle P_w \rangle$ versus $(ah)^{\frac{1}{2}}\left(1 - \frac{h}{H}\right)^{\frac{9}{2}}$. Bracket indicates an average over the canopy height. Blue and orange symbols represent sparse (a = 1.1 m^{-1}) and dense (a = 4.9 m^{-1}) cases in this study, respectively. The estimation of shear and wake production is described in section A3.1. This figure supports the theoretically derived dependence of $\langle P_s \rangle / \langle P_w \rangle$ on $(ah)^{\frac{1}{2}}\left(1 - \frac{h}{H}\right)^{\frac{9}{2}}$, which is discussed in the main text leading to Equation 4.21.

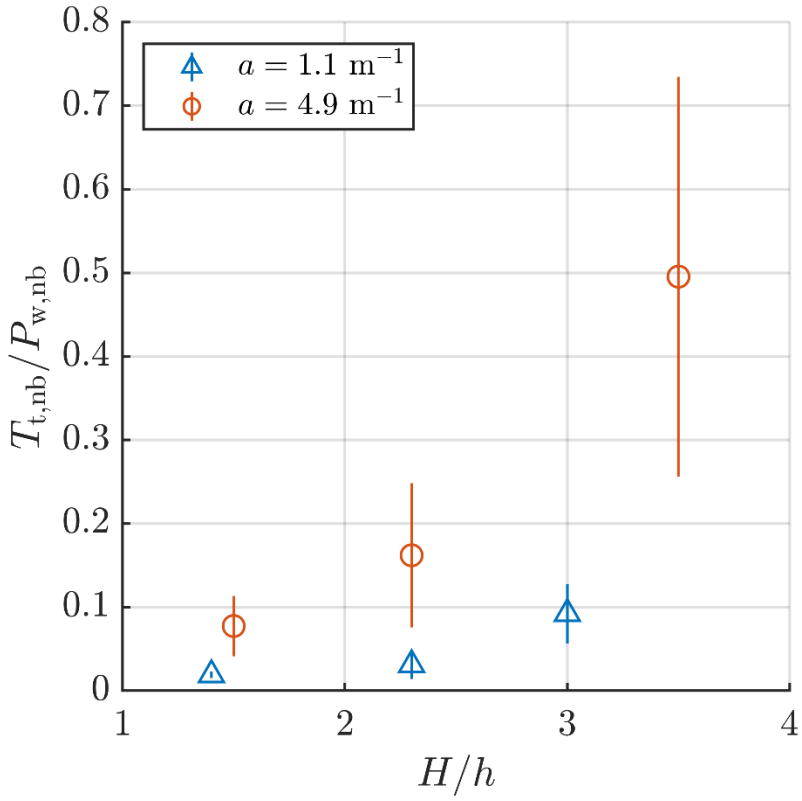

Figure A3-4. Ratio of near-bed turbulent transport ($T_{t,nb}$) to wake production ($P_{w,nb}$) versus submergence ratio (H/h). Blue and orange symbols represent sparse (a = 1.1 m^{-1}) and dense (a = 4.9 m^{-1}) cases in this study, respectively. To estimate the near-bed mean values, the point estimates of T_t and P_w (see section A3.1) were averaged within 2 cm from the bed. For the sparse canopy (a = 4.9 m^{-1}, blue triangles), $T_{t,nb}/P_{w,nb} < 0.1$, showing that near-bed turbulence was dominated by wake production. For the dense canopy (a = 1.1 m^{-1}, red circles), $T_{t,nb}/P_{w,nb}$ increased as depth of submergence increased, suggesting a shift in near-bed turbulence from stem wake production to turbulence generated in the shear layer at the canopy top and transported to the bed by turbulent transport.

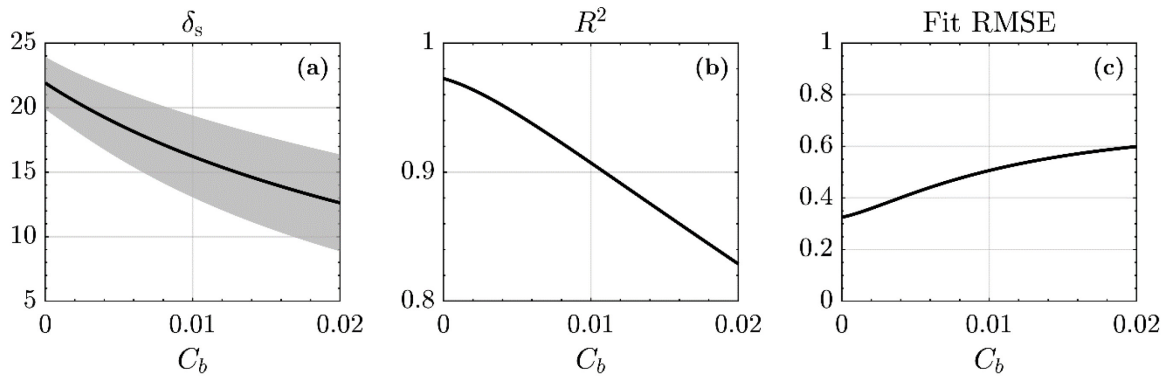

Figure A3-5. Sensitivity analysis to determine the factors δ_s in Equation 4.24 and C_b in Equation 4.17. For each C_b value, a least-squares fit produced a corresponding δ_s in Equation 4.24, which was used to model $\frac{k_{t,nb}}{k_{t,wb}}$ and report R^2 and RMSE values. (a) δ_s value corresponding to each C_b between 0 and 0.02, (b) corresponding coefficient of determination (R^2), and (c) root mean square error (RMSE) of $\frac{k_{t,nb}}{k_{t,wb}}$. The optimal fit, which corresponded to the maximum R^2 and minimum RMSE, was achieved at $C_b = 0$ and $\delta_s = 22 \pm 2$.

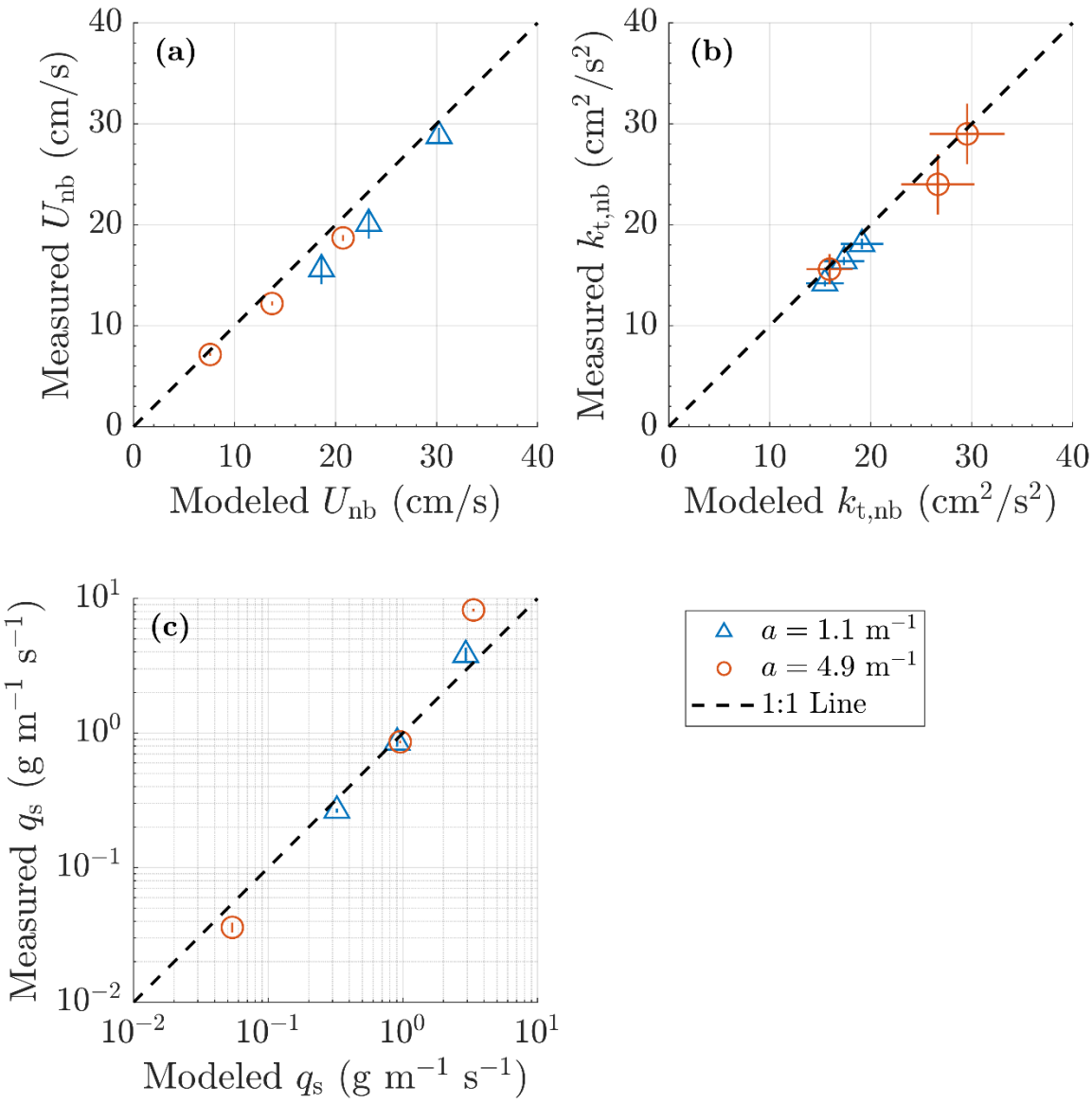

Figure A3-6. Measured versus modeled values of (a) near-bed velocity, (b) near-bed TKE, and (c) bedload transport rate. Blue triangles represent sparse cases (a = 1.1 m^{-1}) and orange circles represent dense cases (a = 4.9 m^{-1}). Near-bed velocity U_{nb} was predicted from Equation 4.16. Near-bed TKE $k_{t,nb}$ was from Equation 4.24. Bedload transport rate qs was from Equation 4.7. Modeled U_{nb} matched measurements to within 20%. Modeled and measured $k_{t,nb}$ agreed within uncertainty. Modeled q_s matched measurements within factor 2.

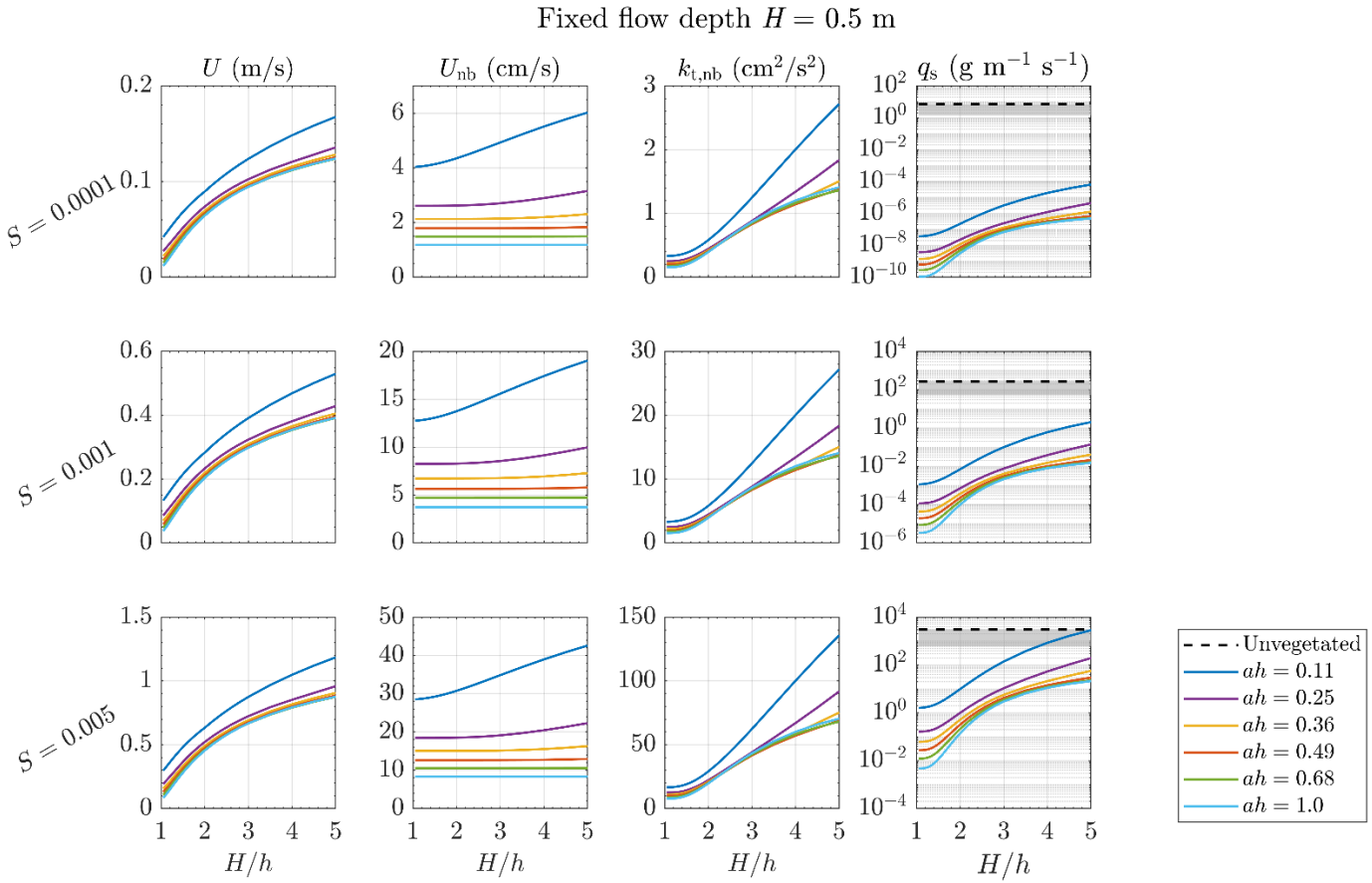

Figure A3-7. Modeled depth-averaged velocity (U), near-bed velocity (U_{nb}), near-bed TKE ($k_{t,nb}$), and sediment transport rate (q_s) under constant hydrodynamic forcing (energy slope, S, from top to bottom: $S = 0.0001$, 0.001, 0.005) and flow depth $H = 50$ cm in canopies of submerged rigid vegetation. See model details in Section 4.3.3. Bed sediment $d_{50} = 0.35$ mm. Canopies had stem diameter $d = 1.3$ cm, with their height varied from $h = 50$ cm to 10 cm, corresponding to submergence ratio $H/h = 1$ to 5. Solid curves represent model results, with color distinguishing canopy density. Black dashed curves in right-most column show sediment transport rate for bare bed (see A3.2 in SI for details). Gray band represents transport rates with bedforms (Wong & Parker, 2006).

A4 Supporting Information for Chapter 5

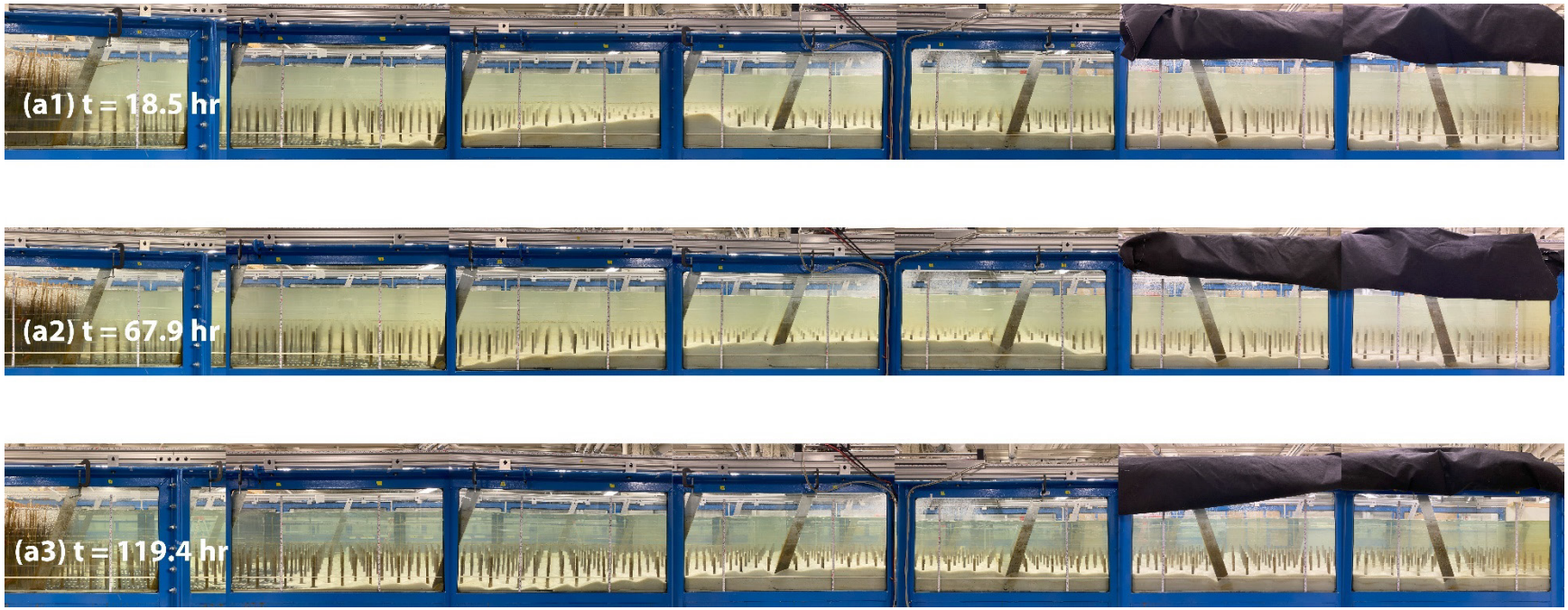

(Continued on next page)

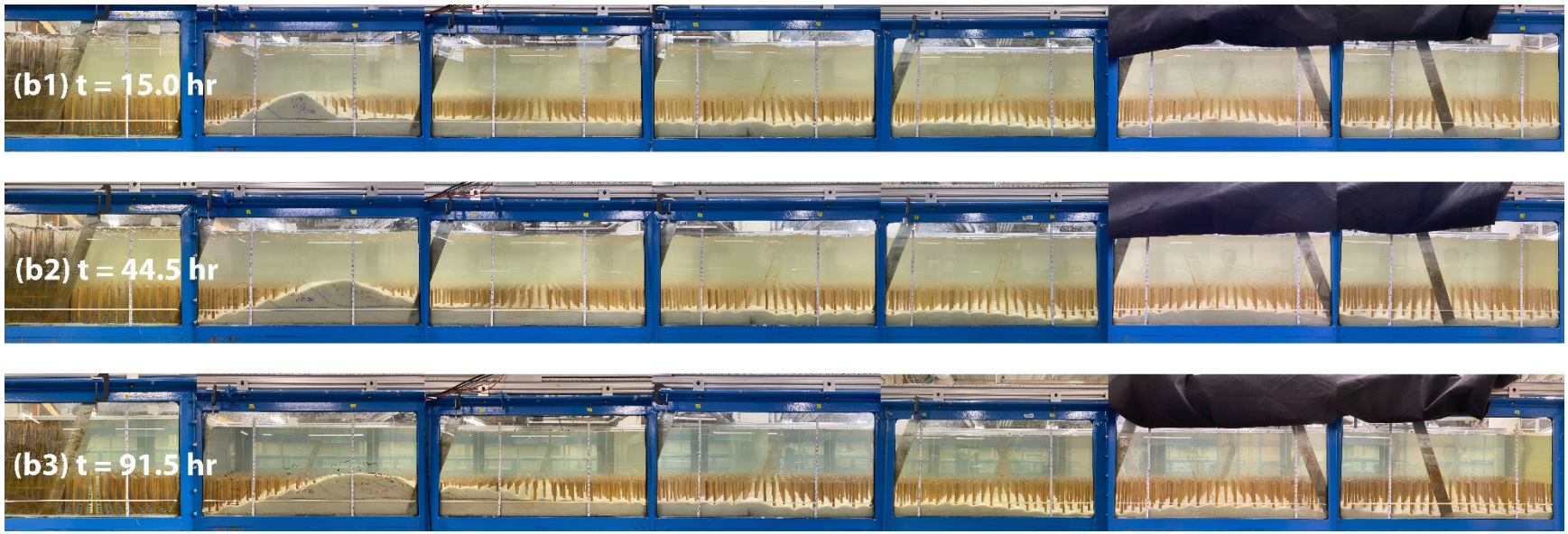

Figure A4-1. Initial evolution of bedform. Flow was from left to right. (a) Case S3, (b) Case D3. White tapes indicate initial flat bed elevation.

Case S1

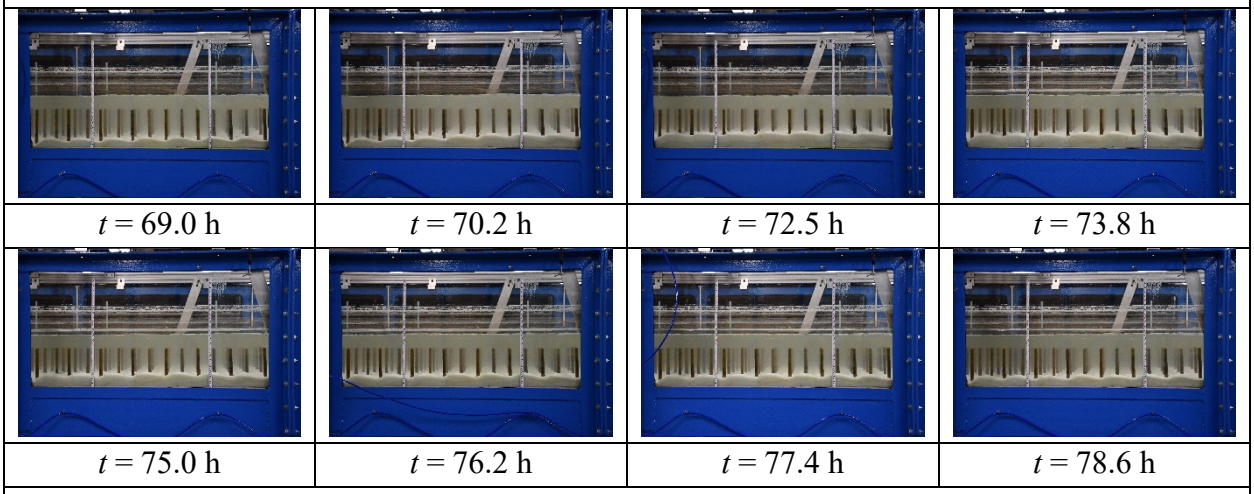

t = 69.0 h	t = 70.2 h	t = 72.5 h	t = 73.8 h
t = 75.0 h	t = 76.2 h	t = 77.4 h	t = 78.6 h

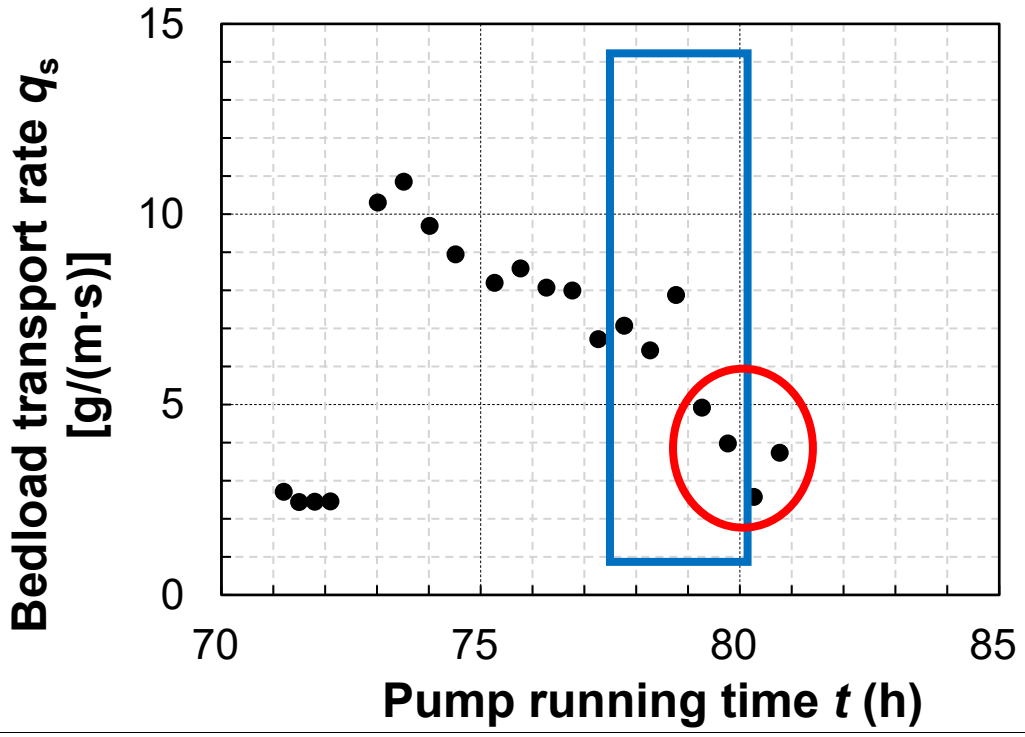

(Continued on next page)

Case S2			
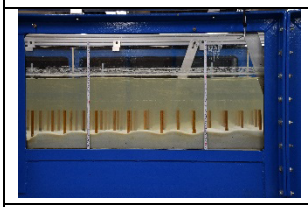	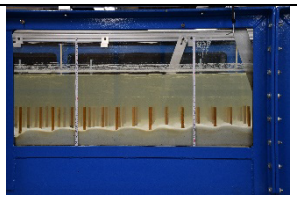	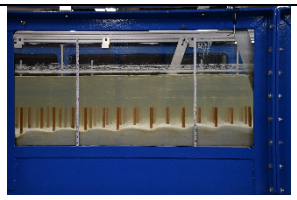	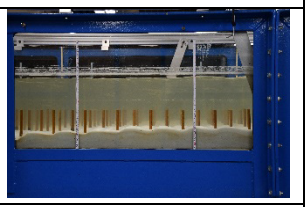
t = 182.3 h	t = 183.3 h	t = 184.3 h	t = 185.3 h
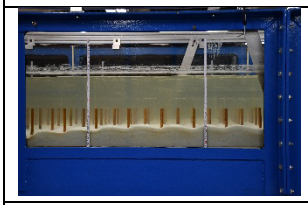	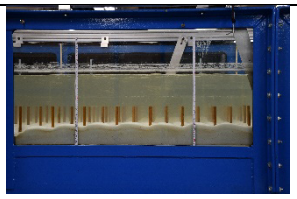	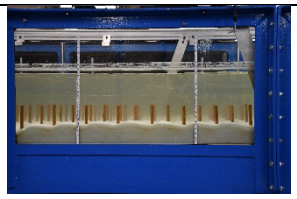	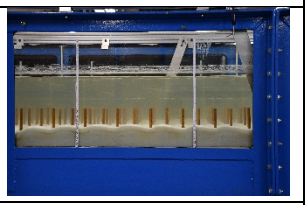
t = 186.3 h	t = 187.3 h	t = 188.0 h	t = 190.0 h
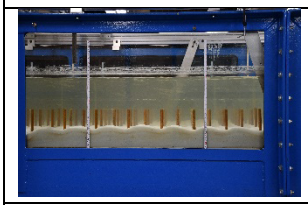	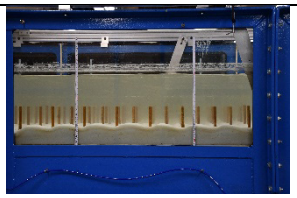	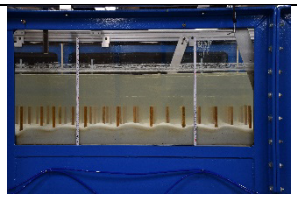	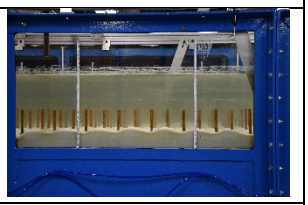
t = 195.1 h	t = 200.1 h	t = 205.0 h	t = 210.0 h
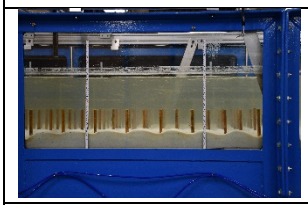	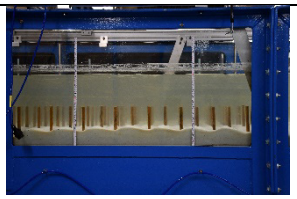	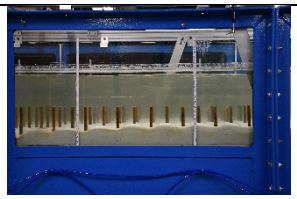	
t = 215.2 h	t = 220.1 h	t = 225.0 h	

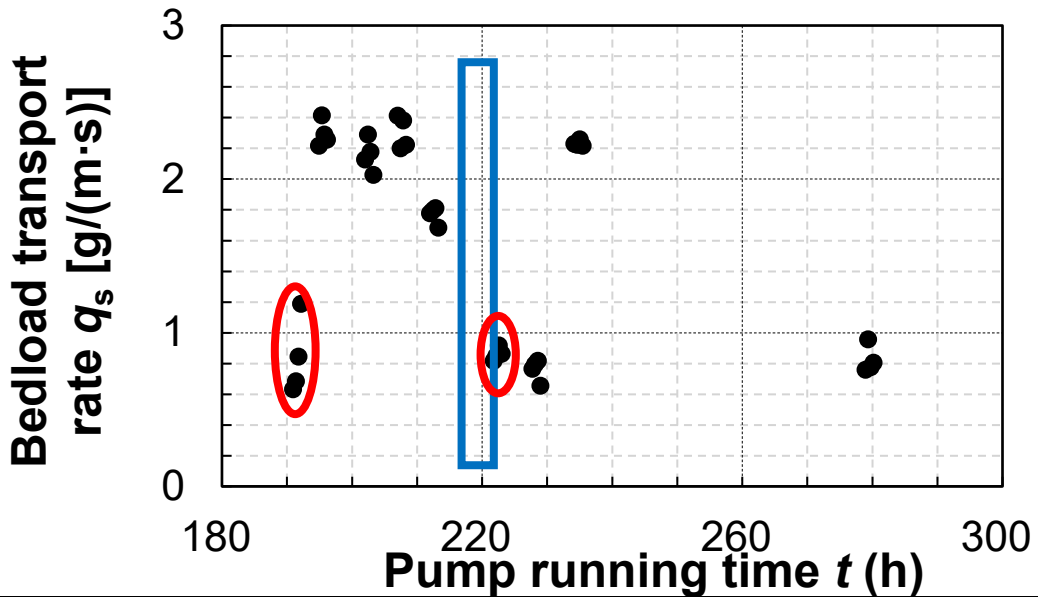

(Continued on next page)

Case S3

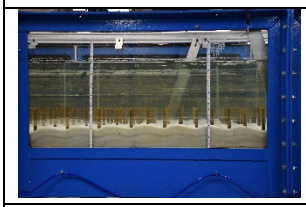
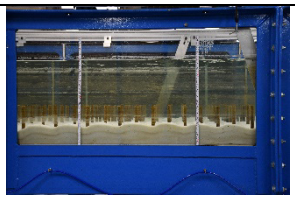
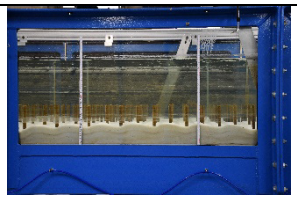
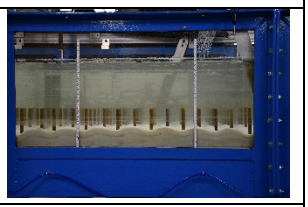

t = 123.0 h	t = 143.0 h	t = 163.0 h	t = 181.5 h

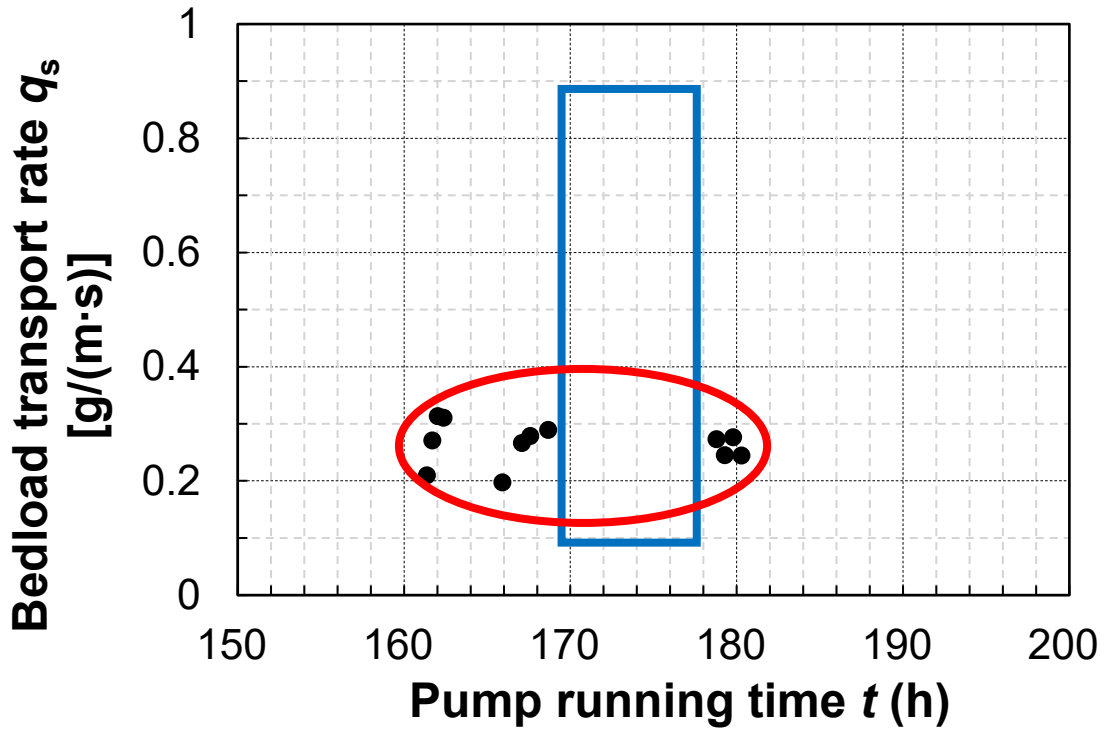

(Continued on next page)

Case D1			
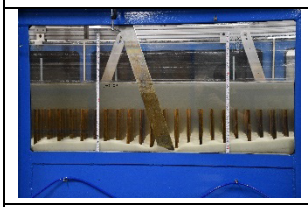		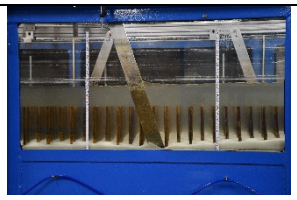	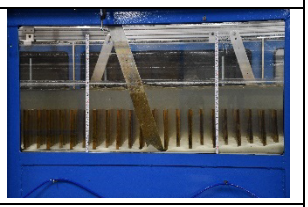
t = 27.3 h	t = 28.0 h	t = 28.8 h	t = 29.6 h
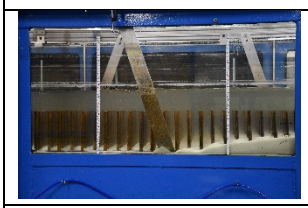	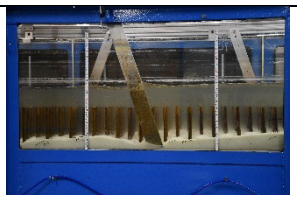	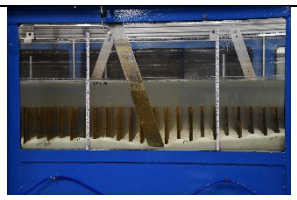	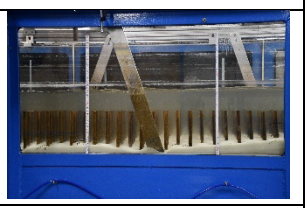
t = 30.3 h	t = 31.3 h	t = 32.1 h	t = 32.6 h

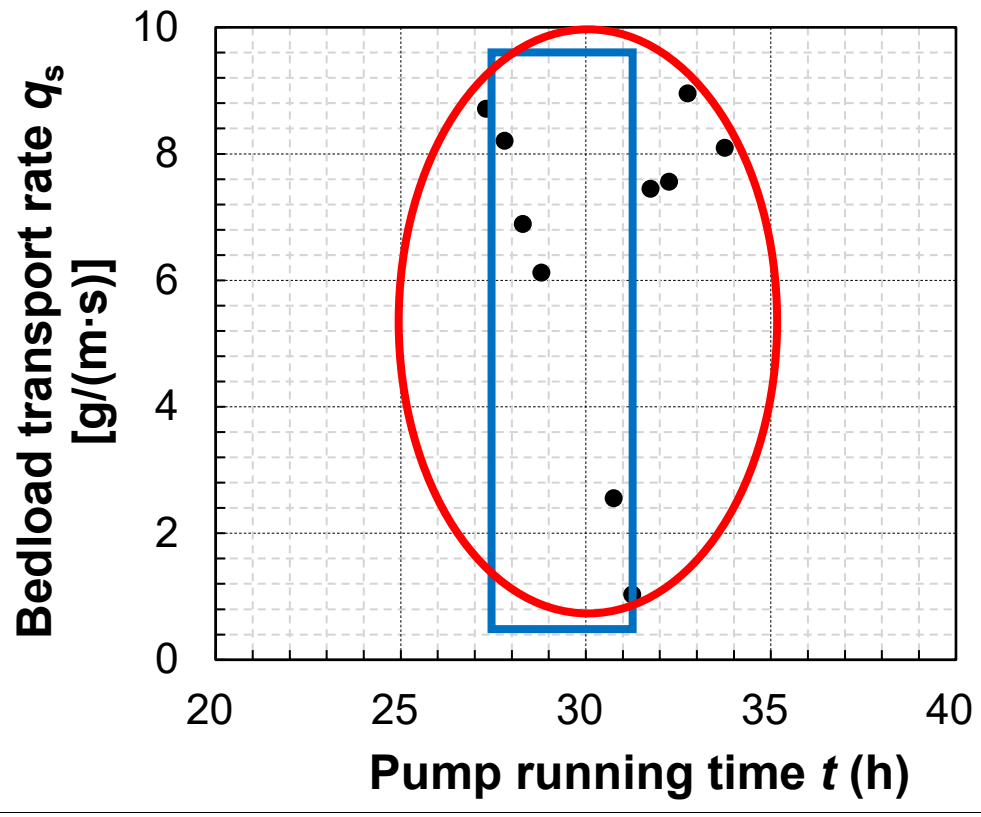

(Continued on next page)

Case D2			
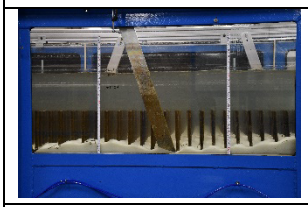	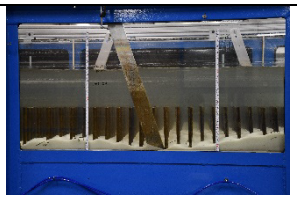	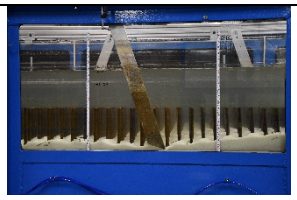	
t = 3.3 h	t = 5.1 h	t = 7.4 h	
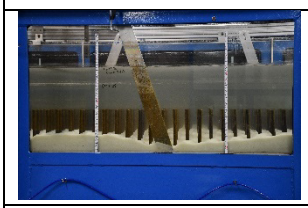	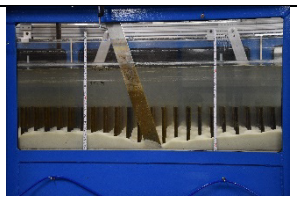	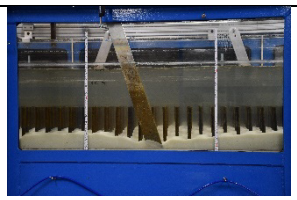	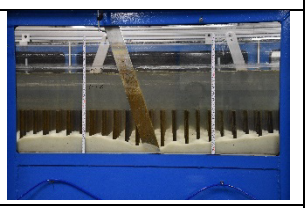
t = 83.5 h	t = 84.5 h	t = 85.5 h	t = 87.0 h
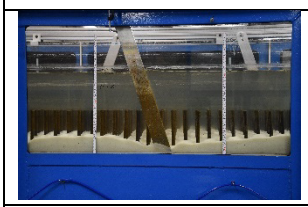		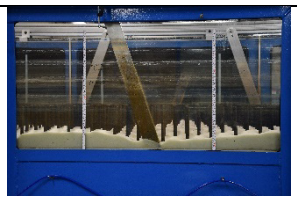	
t = 89.0 h	t = 91.0 h	t = 92.8 h	

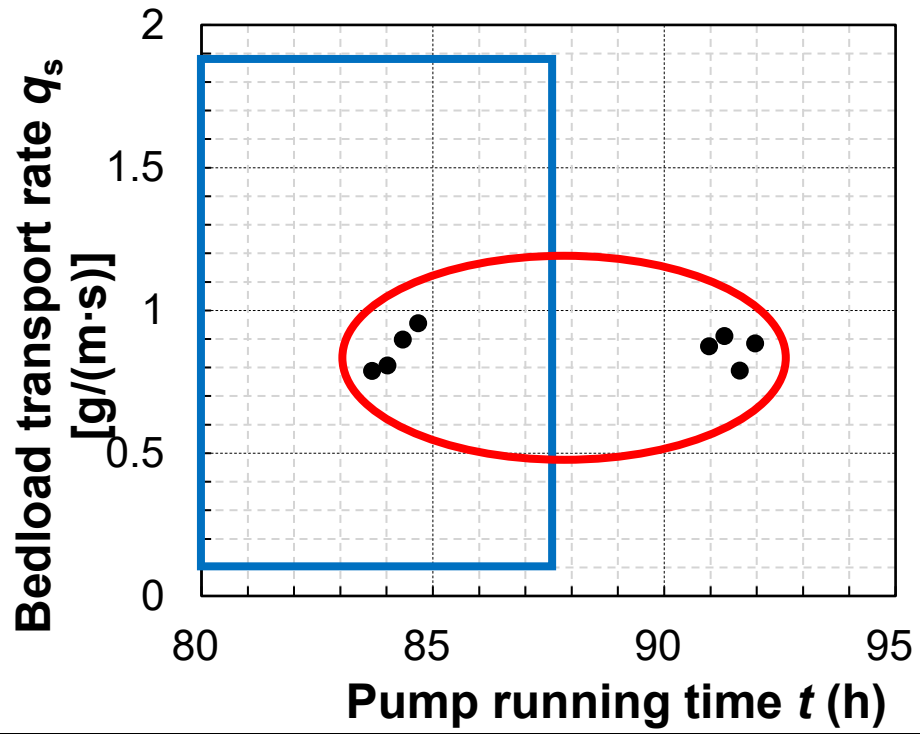

(Continued on next page)

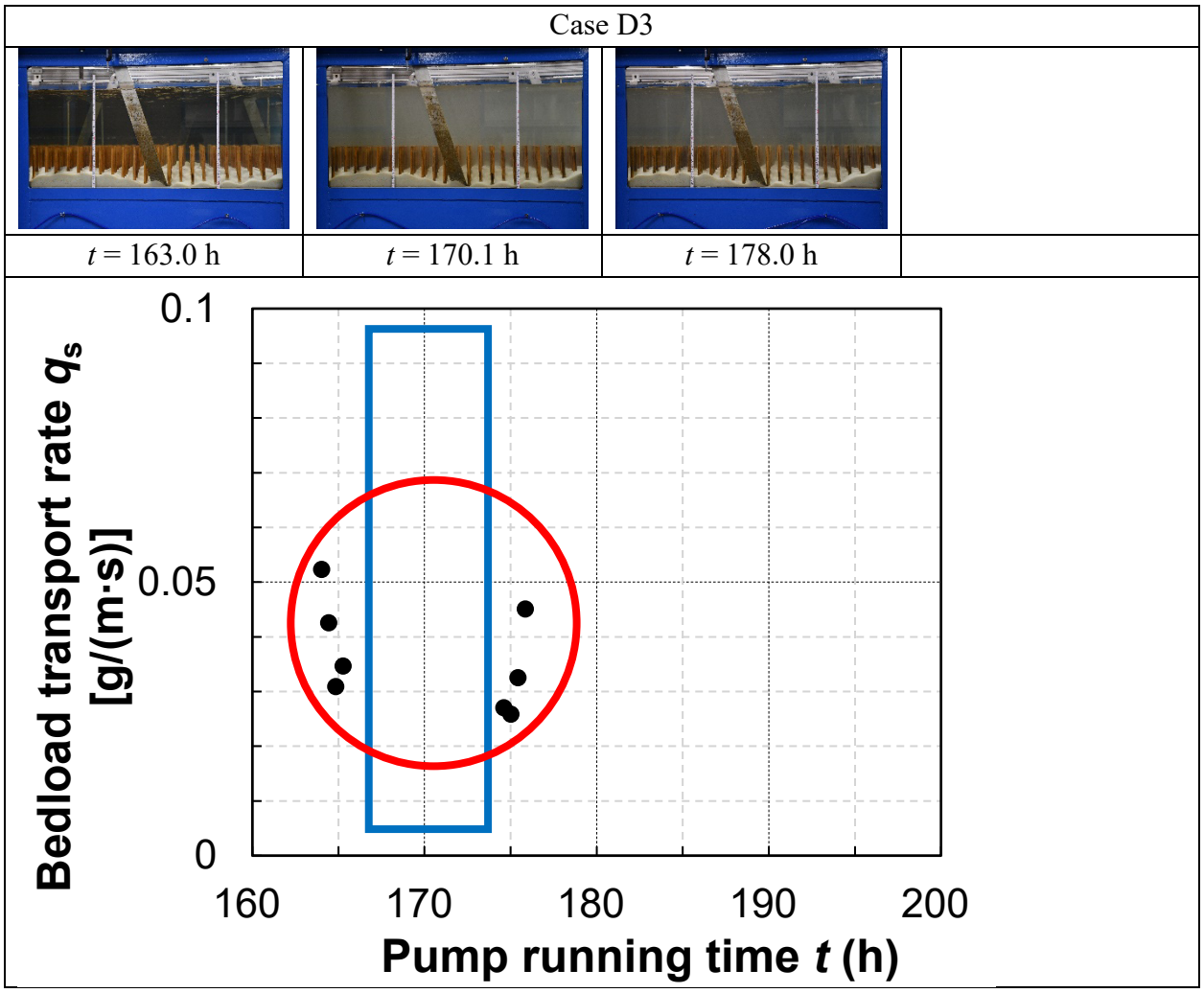

Table A4.1. Gallery of bedform migration and measured instantaneous bedload transport. *t* denotes the cumulative pump running time from the start of case. Blue box represents time interval of flow measurements, and red ovals indicate the individual measurements used to evaluate the sediment transport rate corresponding to the flow measurements. **Flow was from the right to the left.** Note that the left (downstream) edge of the 1.1 m-long image frame, at which the ADV was placed, was 1.3 m upstream of the end of test section, so there was a time lag between the flow measurements and corresponding sediment transport rate.

A5 Final Remarks

The flow data of Chapters 3 and 4, and any updates to the text will be available on:

(Dryad) doi: 10.5061/dryad.r4xgxd2p9

(Google Drive) https://drive.google.com/drive/folders/1RCw6dS4lm4TbCb5SHva-79RINBtwaR5O?usp=sharing

This page intentionally left blank